Exploring the Feasibility of Electrochemical Ammonia Synthesis: From Lab-Scale to Production Plant

Izelaar, B.

Important note
To cite this publication, please use the final published version (if applicable).
Please check the document version above.

Exploring the Feasibility of Electrochemical Ammonia Synthesis: From Lab-Scale to Production Plant

Boaz Izelaar

Exploring the Feasibility of Electrochemical Ammonia Synthesis: From Lab-Scale to Production Plant

Dissertation

for the purpose of obtaining the degree of doctor

at Delft University of Technology

by the authority of the Rector Magnificus, prof.dr.ir. T.H.J.J. van der Hagen,

Chair of the Board for Doctorates

to be defended publicly on

Thursday 14 November at 15:00 o'clock

by

Boaz IZELAAR

Master of Science in Chemical Engineering,

Delft University of Technology, The Netherlands

born in Dirksland, Zuid-Holland, The Netherlands

This dissertation has been approved by the promotors.

Composition of the doctoral committee:

Rector Magnificus	chairperson
Dr. R. Kortlever	Delft University of Technology, promotor
Prof. dr. ir. W. de Jong	Delft University of Technology, promotor
Prof. dr. F. M. Mulder	Delft University of Technology, promotor

Independent members:

Prof. dr. G. Mul	University of Twente
Dr. P. Ngene	Utrecht University
Prof. dr. ir. A. Urakawa	Delft University of Technology
Prof. dr. ir. C. A. Ramirez-Ramirez	Delft University of Technology
Prof. dr. R. Pecnik	Delft University of Technology, reserve member

Cover design by Tirza Izelaar with OpenArt AI

An electronic version of this dissertation is available at

http://repository.tudelft.nl/.

"In 1909 Carl Bosch perfected a process invented by Fritz Haber which used methane and steam to pull nitrogen out of the air and turn it into fertilizer on an industrial scale, replacing the massive quantities of bird poop that had previously been needed to return nitrogen to depleted soils. Those two chemists top the list of the 20th-century scientists who saved the greatest number of lives in history, with 2.7 billion."

- Stephen Pinker

"It is the responsibility of scientists never to suppress knowledge, no matter how awkward that knowledge is, no matter how it may bother those in power; we are not smart enough to decide which pieces of knowledge are permissible and which are not."

- Carl Sagan

"Many individuals are doing what they can. But real success can only come if there is a change in our societies and in our economics and in our politics."

- David Attenborough

Contents

Summary

Ammonia can be used as a global energy carrier to connect the geographically divided landscape of renewable energy sources. Unfortunately, the current ammonia production process of the century old fossil-fuel based Haber-Bosch process is not sustainable and is responsible for approximately 1.2% of the global anthropogenic CO_2 emissions. The most polluting part of the process is the hydrogen generation step by either coal gasification or the more common steam methane reforming. The majority of the emissions can be cut down by replacing this step by water electrolysis often referred to as the electrified Haber-Bosch. An alternative technology for sustainable ammonia production, which is still in its infancy, is ammonia synthesis via the electrochemical reduction of nitrogen (NRR), requiring a proton source and electrons from renewable electricity. The following NRR approaches are prominently reported in the literature: (i) NRR in aqueous based electrolytes at ambient conditions (aqueous NRR), (ii) NRR at elevated temperatures with a solid oxide electrolyte, (iii) Li-mediated NRR in non-aqueous electrolytes at room temperature (Li-NRR). The main aim of this thesis is to identify and understand which of the above-mentioned electrochemical ammonia routes are the most promising for future application.

Aqueous NRR is generally perceived to be a challenging reaction because it competes with the hydrogen evolution reaction, the difficult activation of N_2, and the poor N_2 mass transport in aqueous solutions due to its low solubility. Additionally, reported ammonia concentrations are in the parts per million range, which is of the same order of magnitude as ammonia from adventitious sources. Small quantities of nitrogen oxide (NO_x) species were also observed during aqueous NRR experiments and can be electroreduced into ammonia at more positive potentials than N_2. Both adventitious NH_3 and NO_x are problematic and can interfere with the genuine quantification of ammonia that could stem from N_2 reduction.

Fe- and Mo-based carbides were recently reported as active aqueous NRR electrocatalysts. Most of these literature reports did not include adequate control experiments to confirm NRR as the source of the observed NH_3 unambiguously. This motivated us to critically assess the NRR catalytic activity of the most promising Fe- and Mo-based carbides in Chapter 2. Herein, a strict experimental protocol was implemented to minimize the NH_3 and NO_x background levels to a bare minimum. This gives us the opportunity to identify a promising NRR catalyst or label it as a false positive. The successful synthesis of α-Mo_2C decorated carbon nanosheets, α-Mo_2C nanoparticles, θ-Fe_3C nanoparticles, and χ-Fe_5C_2 nanoparticles were confirmed by X-ray diffraction, scanning and transmission electron microscopy, X-ray photoelectron and Mössbauer spectroscopy. Multiple electrochemical techniques, such as cyclic voltammetry and chronoamperometry were applied, but there was no sign of NRR activity. The quantified ammonia concentrations did not exceed the pre-estimated background level, which suggests that the origin of ammonia stems from other sources.

These results are in contradiction with earlier literature reports and indicate that Mo- and Fe-carbides are not active towards the NRR. This work emphasizes the importance of implementing a strict experimental protocol to distinguish between an active catalyst and a false positive result.

Over recent years, the majority of the publications in the aqueous NRR field implemented all recommended control experiments (including Ar blank tests and isotope labelled $^{15}N_2$-gas) and improved their experimental protocols. Yet, the reported reaction selectivities and ammonia production rates are in most cases not reproducible. The main issue is that the efficacy of the purification and cleaning procedures are often not reported or demonstrated. Additionally, it remains unclear how severe these impurities are and how they individually contribute to the overall ammonia background level. Moreover, the main source of all these impurities is poorly understood. Chapter 3 presents a systematic impurity screening of commonly used lab materials and gases during aqueous NRR and non-aqueous Li-mediated NRR experiments. More importantly, the effectiveness of earlier proposed cleaning strategies is re-evaluated and further optimized. It was found that $^{15}N_2$ gas is contaminated and can only be purified with certified gas filters, while the commonly adopted liquid scrubbers fail to eliminate impurities. The accumulation of atmospheric NO_x on ambient exposed lab materials is unavoidable and can be prevented by storing materials in gloveboxes or desiccators. To remove impurities that are already present, treatments with water, alkaline solutions, or heat can be considered. The proposed methods equip the experimentalist with specific guidelines and tools to perform more reliable NRR experiments.

Li-mediated NRR in non-aqueous electrolytes has progressed tremendously in recent years, where many independent laboratories have irrevocably confirmed that ammonia is generated from activated nitrogen gas. However, the current understanding of the reaction mechanism and potentials is limited because electrochemical measurements are often performed with quasi reference electrodes (QREs). The redox potentials of these QREs such as a bare Ag or Pt wire, are poorly defined and unstable in non-aqueous Li-NRR environments. Partially delithiated lithium iron phospate (LFP) was recently identified by other research groups as a versatile reference electrode material for non-aqueous electrochemistry, and was adopted in Chapter 4 to investigate the relationship between the applied potential and the Li-NRR performance. Cyclic voltammetry was also performed with 2 M LiTFSI under different reaction conditions (Ar or N_2 with or without EtOH) and did not show any peaks besides Li plating and stripping, suggesting that both the N_2 activation and protonation steps are chemical by nature. With 2 M Li bis(trifluoromethanesulfonyl)imide (LiTFSI) dissolved in 0.1 M EtOH/THF and 20 bar of N_2 pressure, the FE_{NH3} remained below 15% after chronoamperometry measurements at potentials above -3.23 V vs. SHE and increased to 50% and remained constant at potentials ≤ -3.43 V vs. SHE. The current response was unstable at potentials more negative than -4.03 V vs. SHE and resulted in a lower NH_3 production rate. The current stability was significantly improved by implementing 1 M LiTFSI, but at the cost of relatively lower Faradaic efficiencies and NH_3 production rates

at more negative potentials. The solid electrolyte interphase in all three potential regimes were physically characterized post-mortem by X-ray photoelectron spectroscopy (XPS) to determine the chemical composition. The results indicate that SEIs are significantly enriched with LiF. The ratio of inorganic/organic compounds changes with the potential but does not solely explain the trend between the applied potential and the Li-NRR performance. Changes in the morphology of the electrode surface structure were not investigated in the present study, but might give more insights into the relationship between applied potential and the performance parameters, which will be subject of a forthcoming study.

Currently, there is a lack of knowledge in the electrochemical ammonia field regarding the process design, energy consumption and techno-economic feasibility of a large scale electrochemical NH_3 process plant, including upstream and downstream separation units, heat integration and storage. Chapter 5 presents comprehensive conceptual process models of direct and indirect NRR pathways at ambient and elevated temperatures, including Li-mediated NRR at a small-scale ammonia production plant with a capacity of 91 tonnes per day. These models were compared with steam methane reforming (SMR) Haber-Bosch as the best available technology and electrified Haber-Bosch as the benchmark for green ammonia production. The levelized cost of ammonia (LCOA) of aqueous NRR at ambient conditions may only become comparable with SMR Haber-Bosch at very optimistic electrolyzer performance parameters (FE > 80% at $j \geq 0.3$ A cm^{-2}) and electricity prices (< $0.024 per kWh). When considering the LCOA, both high temperature NRR and Li-mediated NRR are not economically comparable with SMR Haber-Bosch within the tested variable ranges. High temperature NRR is very capital intensive due the requirement of a heat exchanger network, more auxiliary equipment, and an additional water electrolyzer (considering the indirect route). For Li-mediated NRR, the high lithium plating potentials, ohmic losses and the requirement for a source of H_2, limits its commercial competitiveness with SMR Haber-Bosch. This incentivises the search for materials beyond lithium. For the considered systems, the electrified Haber-Bosch, especially with a flexible proton exchange membrane electrolyzer for H_2 production, remains the only compelling electrochemical route towards green ammonia.

Samenvatting

Ammoniak kan worden gebruikt als mondiale energiedrager en kan het geografisch verdeelde landschap van hernieuwbare energiebronnen met elkaar verbinden. Helaas is het huidige ammoniakproductieproces, het Haber-Bosch proces dat fossiele brandstoffen verbruikt, niet duurzaam. Hierdoor is de ammoniaksector verantwoordelijk voor ongeveer 1.2% van de mondiale antropogene CO_2-uitstoot. Het meest vervuilende gedeelte van het proces is de stap van waterstofproductie door steenkoolvergassing of stoomreforming van aardgas. De grootste emissiewinst kan worden behaald door deze stap te vervangen door waterelektrolyse, wat ook wel de elektrificatie van het Haber-Bosch proces wordt genoemd. Een alternatieve technologie voor duurzame ammoniakproductie, die nog in de kinderschoenen staat, is de ammoniaksynthese via de elektrochemische reductie van stikstof (NRR). Hiervoor zijn een protonenbron en elektronen van hernieuwbare elektriciteit nodig. In de literatuur wordt NRR bij verschillende condities onderzocht, voornamelijk: (i) NRR in waterig elektrolyt bij omgevingstemperatuur (waterige NRR), (ii) NRR bij verhoogde temperaturen met een vaste stof elektrolyt gebaseerd op oxides, (iii) NRR via lithium in een organisch elektrolyt op kamertemperatuur (Li-NRR). Het hoofddoel van dit proefschrift is het identificeren en begrijpen welke van de hierboven genoemde elektrochemische ammoniakroutes veelbelovend zijn voor toekomstige toepassingen.

NRR in waterig elektrolyt wordt over het algemeen gezien als een uitdaging, omdat het concurreert met de waterstofproductiereactie van waterelektrolyse terwijl N_2 activatie moeilijk is. Ook wordt het trage massatransport van N_2 in waterige oplossingen door de lage oplosbaarheid gezien als een probleem. Bovendien zijn de via NRR verkregen gerapporteerde ammoniakconcentraties in de literatuur in micro molariteit, wat in dezelfde marge ligt als sporen van ammoniakconcentraties uit de omgeving. Kleine hoeveelheden stikstofoxides (NO_x) zijn ook waargenomen tijdens de NRR-experimenten en kunnen bij een elektrisch potentiaal, die positiever is dan voor N_2, gereduceerd worden in ammoniak. Zowel externe NH_3 als NO_x zijn problematisch en kunnen interfereren met de kwantificering van ammoniak door de NRR.

Fe- en Mo-gebaseerde carbiden zijn onlangs gerapporteerd als actieve waterige NRR-elektrokatalysatoren. Het overgrote deel van deze literatuurrapporten bevatten geen adequate beschrijving van uitgevoerde controle-experimenten. Daarom is het lastig om NRR als de bron van de geobserveerde NH_3 vast te stellen. Dit motiveerde ons om de katalytische activiteit van de meest veelbelovende Fe- en Mo-carbiden te reproduceren. De uitvoering hiervan, behaalde resultaten en discussie worden besproken in Hoofdstuk 2. Hierin is een strikt experimenteel protocol geïmplementeerd zodat het NH_3 en NO_x achtergrondniveau tot een absoluut minimum kan worden beperkt. Dit geeft ons de mogelijkheid om daadwerkelijk actieve NRR-katalysator te identificeren of deze te bestempelen als een vals-positief resultaat. De succesvolle synthese van α-Mo_2C gedecoreerde koolstofnanovellen, α-

Mo$_2$C nanodeeltjes, θ-Fe$_3$C nanodeeltjes en χ-Fe$_5$C$_2$ nanodeeltjes werden bevestigd door röntgendiffractie, elektronenmicroscopie, röntgen foto-elektronenspectroscopie en Mössbauer-spectroscopie. Verschillende elektrochemische technieken zijn toegepast, zoals cyclovoltammetrie en chronoamperometrie, maar er bleek geen teken van NRR-activiteit te zijn. De gekwantificeerde ammoniakconcentraties kwamen niet boven het achtergrondniveau uit, wat erop wijst dat de oorsprong van ammoniak uit andere bronnen voortkomt. Deze resultaten zijn in tegenspraak met eerdere literatuurrapporten en geven aan dat Mo- en Fe-carbiden niet actief zijn voor NRR. Dit hoofdstuk benadrukt het belang van het implementeren van een strikt experimenteel protocol zodat onderscheid gemaakt kan worden tussen een actieve katalysator en een vals-positief resultaat.

De afgelopen jaren heeft het merendeel van de publicaties in het vakgebied van waterige NRR de aanbevolen controle-experimenten (Ar en ^{15}N$_2$-gas) en strengere experimentele protocollen geïmplementeerd. Toch zijn de gerapporteerde waarden wat betreft de reactieselectiviteit en ammoniak productiesnelheid niet reproduceerbaar. Het belangrijkste probleem is dat de effectiviteit van de gebruikte zuiverings- en reinigingsstappen niet worden gerapporteerd of getest. Bovendien blijft het onduidelijk hoe hoog de concentratie van de stikstofhoudende onzuiverheden zijn en hoe deze individueel bijdragen aan het algehele ammoniakachtergrondniveau. Tevens is het ongewis waar all deze onzuiverheden precies vandaan komen. Hoofdstuk 3 presenteert een systematische "screening" van laboratoriummaterialen en gassen op stikstof onzuiverheden die men gebruikt tijdens waterige NRR en niet-waterige Li-NRR experimenten. Hierin wordt ook de effectiviteit van eerder voorgestelde schoonmaakstrategieën opnieuw geëvalueerd en geoptimaliseerd. We hebben vastgesteld dat het ^{15}N$_2$-gas verontreinigd is en alleen kan worden gezuiverd met gecertificeerde (eventueel commerciële) gasfilters, omdat zelfgemaakte gaswassers niet adequaat genoeg zijn. De ophoping van atmosferische NO$_x$ en NH$_3$ op laboratoriummaterialen die blootgesteld zijn aan de omgeving is onvermijdelijk en kan worden voorkomen door de materialen op te slaan in handschoenenkastjes of exsiccatoren. De materialen die al verontreinigd zijn, kunnen worden behandeld met water, alkalische oplossingen of warmte om stikstof onzuiverheden te verwijderen. De ontwikkelde methoden besproken in dit hoofdstuk voorzien de experimentele onderzoeker van specifieke richtlijnen en hulpmiddelen om betrouwbaardere NRR-experimenten uit te voeren.

Het Li-NRR vakgebied heeft de afgelopen jaren enorme vooruitgang geboekt, waarbij onafhankelijke laboratoria onherroepelijk hebben vastgesteld dat ammoniak afkomstig is van geactiveerd stikstofgas. Desalniettemin wordt het reactiemechanisme niet volledig begrepen, omdat de elektrochemische experimenten vaak worden uitgevoerd met quasi-referentie-elektroden (QRE'en). De redoxpotentialen van deze QRE'en, zoals een Ag- of Pt-draad, zijn slecht gedefinieerd en onstabiel tijdens een Li-NRR experiment. Lithiumijzerfosfaat (LFP) is onlangs geïdentificeerd door andere onderzoeksgroepen als een veelzijdig referentie-elektrodemateriaal voor elektrochemie in niet-waterige elektrolyten en

wordt in hoofdstuk 4 gebruikt om de relatie tussen het potentiaal en de Li-NRR-prestaties te onderzoeken. Cyclovoltammetry werd ook uitgevoerd met 2 M Li bis(trifluormethaansulfonyl)imide (LiTFSI) onder verschillende reactieomstandigheden (Ar of N_2 met of zonder EtOH) en vertoonde alleen een piek associërend met Li^+ reductie en oxidatie. Dit wijst erop dat zowel de N_2 activatie, als de protoneringsreactie chemisch van aard zijn. Met 2 M LiTFSI opgelost in 0.1 M EtOH/THF en 20 bar N_2-druk bleef de FE_{NH3} onder de 15% na chronoamperometrie metingen bij een potentiaal boven -3.23 V vs. SHE, en steeg naar 50% en bleef constant bij potentialen ≤ -3.43 V vs. SHE. De stroom werd onstabiel bij potentialen negatiever dan -4.03 V vs. SHE, wat resulteerde in een lagere NH_3-productiesnelheid. De stabiliteit van de stroom verbetert aanzienlijk wanneer 1 M LiTFSI wordt geïmplementeerd, maar dit gaat ten koste van een relatief lagere Faradisch efficiëntie en NH_3-productiesnelheden bij negatievere potentialen. De grenslaag van het vaste stof elektrolyt (SEI) op de elektrode werden gekarakteriseerd *post-mortem* door röntgenfoto-elektronenspectroscopie (XPS) om de chemische bestandsdelen te bepalen. De SEI's waren allen aanzienlijk verrijkt met LiF. De verhouding anorganische/organische componenten nam licht toe als functie van het potentiaal, maar dit is geen duidelijke verklaring voor de afhankelijk van het potentiaal en de Li-NRR prestaties. Veranderingen in de morfologie van de oppervlaktestructuur van de elektrode is in de huidige studie niet onderzocht, maar kan inzichten geven in de relatie tussen het potentiaal en de prestaties van het Li-NRR systeem. Dit wordt het onderwerp van een vervolgstudie.

Momenteel bestaat er op het gebied van elektrochemische ammoniak een gebrek aan kennis over het procesontwerp, het energieverbruik en de techno-economische haalbaarheid van een grootschalige elektrochemische NH_3 productiefabriek, inclusief voorbehandeling- en de scheidingsstappen, warmte-integratie en opslag. Hoofdstuk 5 presenteert uitgebreide conceptuele procesmodellen van directe en indirecte NRR-processen bij omgevingstemperatuur en verhoogde temperaturen, inclusief Li-NRR in een kleinschalige ammoniakfabriek met een capaciteit van 91 ton per dag. Deze modellen werden vergeleken met het Haber-Bosch proces gebaseerd op stoom reforming van aardgas (SMR) als de best beschikbare technologie en geëlektrificeerde Haber-Bosch als maatstaf voor de productie van groene ammoniak. De genivelleerde kosten van ammoniak (LCOA) van waterige NRR bij de omgevingstemperatuur kunnen alleen concurreren met SMR Haber-Bosch bij zeer optimistische investeringskosten van de elektrolyser (FE_{NH_3} > 80% bij j ≥ 0.3 A cm-2) en elektriciteitsprijzen (< $0.024 per kWh). Zowel NRR bij hoge temperatuur als Li-NRR zijn niet economisch rendabel binnen de aangenomen investeringskosten en energieprijzen. NRR bij hoge temperaturen is zeer kapitaalintensief vanwege de behoefte aan een uitgebreid warmtewisselaarnetwerk, procesapparatuur en een extra waterelektrolyser (wat betreft de indirecte route). Voor Li-NRR, maken de hoge lithium reductie cel potentialen, ohmse verliezen en een extra waterstof bron, het proceseconomisch onaantrekkelijk ten opzichte van SMR Haber-Bosch. Hierdoor moeten andere materialen geïdentificeerd worden die bij een gunstiger potentiaal dan lithium, N_2 kunnen activeren. Voor de onderzochte processen is de geëlektrificeerde variant van het

Haber-Bosch proces met een flexibele proton-doorlaatbaar-membraan waterelektrolyzer tot nu toe de beste elektrochemische route voor de productie van groene ammoniak.

1

Introduction

1.1   General Introduction

Anthropogenic greenhouse gas (GHG) emissions have led to an unprecedented increase of the average global surface temperature by approximately 1.1°C between 1900-2020 (see Figure 1a).[1] As a consequence, global warming leads to more weather and climate extremes in already observable forms, such as prolonged heat waves, heavy precipitation, droughts and tropical cyclones. Therefore, GHG mitigation strategies must be implemented to prevent further rise of the average global temperature. Unfortunately, the current climate agreements for 2030 between national governments (announced in 2021) are not sufficient to keep the average global temperature below 1.5°C, but will likely exceed 2°C within the 21st century.[2] To prevent a scenario beyond 2°C and limit catastrophic climate events, GHG emission must be gradually reduced to net zero by 2050 (see Figure 1b).
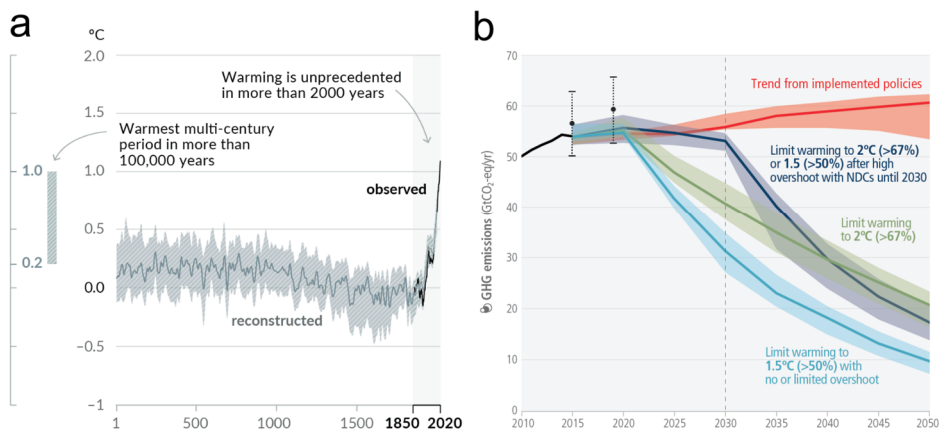
Figure 1. (a) Change in global surface temperature (b) Projected global GHG emissions over 2015-2050 with the implementation of different policies. NDC stands for Nationally Determined Contributions. Reprinted from IPCC under the Creative Commons CC BY-NC-ND license.[1,2]

The main GHGs are carbon dioxide (CO_2), methane (CH_4) and nitrous oxide (N_2O). Figure 2 illustrates that the majority of the global emissions are related to the energy sector (73%) via the combustion of fossil fuels for electricity generation, industrial and residential heating, and transportation, emitting staggering amounts of carbon dioxides (CO_2). Specific manufacturing and chemical industries account for roughly 5% of the global emissions by forming CO_2 as a by-product. The majority of CH_4 emissions are fugitive (6%), which means that they are released during the extraction of oil and gas and pipeline leakage due to poor maintenance practices on pipeline infrastructure.[3] During the oil extraction process in remote areas, residual CH_4 is vented or flared on-site when gas transportation is too costly.[4] N_2O is mainly emitted by the agricultural sector through volatilization of fertilized soil and the decomposition of stored animal manure.[5] Livestock, mainly ruminants, also emit CH_4 because of their digestion system. This shows that each sector contributes differently to the global emissions, hence there will be no "one size fits all" solution, but a combination of

multiple decarbonization strategies that has to be implemented in order to prevent global warming.
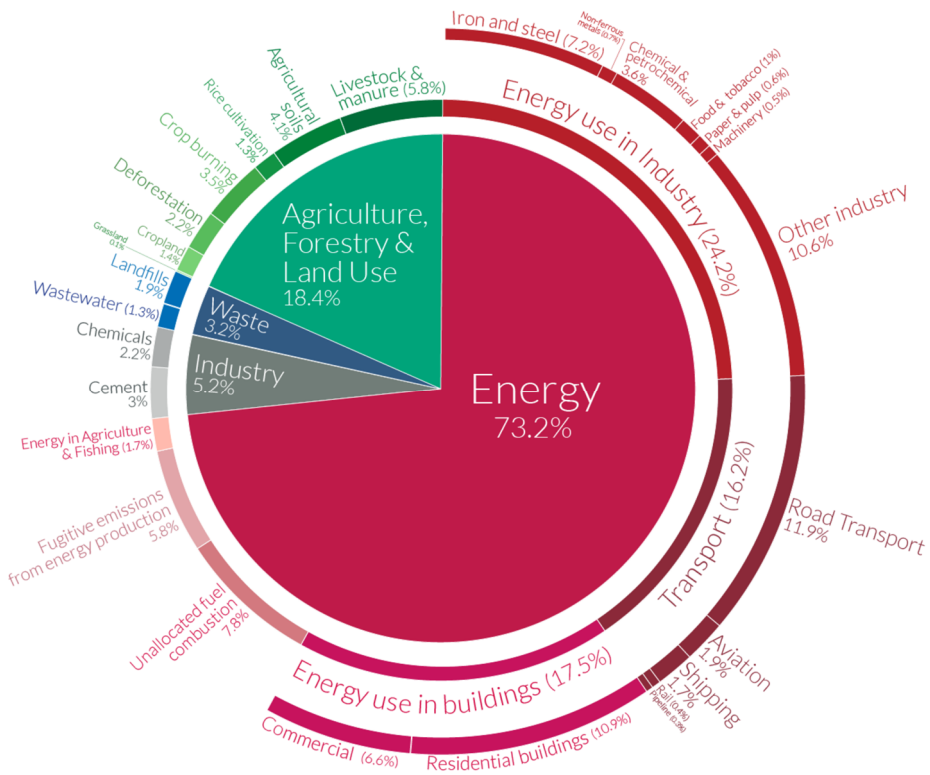
Figure 2. Global GHG emissions by sector in 2016. Reprinted from Our World in Data under the Creative Commons CC BY license.[3]

1.1.1 Mitigation Strategies for the Energy Sector

The strategy for the decarbonization of the energy sector is divided into three main principles: (i) improvement in the energy efficiency, (ii) direct use of renewable energy and (iii) indirect use of renewable energy.[6] Renewable energy will be mainly in the form of electrical energy generated by power technologies based on hydro, wind (onshore and offshore), solar (photovoltaic and thermal), tide, biomass and geothermal.[7] The availability, and feasibility of these technologies depend mainly on geographic space and location. Table 1 indicates that the current production cost of electricity from onshore wind and solar PV decreased to an electricity price below $0.05 per kWh, which surpasses the cost fossil fuel-based power generation.[7,8] Renewable heat will be indirectly produced from renewable electricity. A suitable power-to-heat technology depends on the quality of the heat (supply temperature).[9]

Table 1. Total installed costs, capacity factor and levelized cost of electricity trends of different renewable energy technologies between 2010 and 2022. Reprinted from IRENA under the Creative Commons CC BY license.[7]

	Total installed costs			Capacity factor			Levelised cost of electricity		
	(2022 USD/kW)			(%)			(2022 USD/kWh)		
	2010	2022	Percent change	2010	2022	Percent change	2010	2022	Percent change
Bioenergy	2 904	2 162	-26%	72	72	1%	0.082	0.061	-25%
Geothermal	2 904	3 478	20%	87	85	-2%	0.053	0.056	6%
Hydropower	1 407	2 881	105%	44	46	4%	0.042	0.061	47%
Solar PV	5 124	876	-83%	14	17	23%	0.445	0.049	-89%
CSP	10 082	4 274	-58%	30	36	19%	0.380	0.118	-69%
Onshore wind	2 179	1 274	-42%	27	37	35%	0.107	0.033	-69%
Offshore wind	5 217	3 461	-34%	38	42	10%	0.197	0.081	-59%

Low quality heat (≤80°C) is mainly used for commercial and residential buildings heating, which is done conventionally by natural gas fired boilers, coal or biomass fired stoves.[9,10] Electric heat pumps are poised as promising renewable alternatives (if they are powered by renewable technologies) and can reach efficiencies above 100%.[11] The main downside of the implementation of heat pumps is their high investment costs and the requirement of high insulation levels, which can be challenging for old buildings (>40 years).

Heat demand for the manufacturing industry is more than two-thirds of their total energy consumption.[12] Refineries and other chemical processes, such as distillation, reforming, cracking or reactors in operation require medium-to-high quality heat (80 – 1000°C).[13] Manufacturing industries, such as steel and glass use even temperatures above 1000°C. Conventionally, this heat is supplied by high pressure steam from a methane-fed boiler or a natural gas fired furnace. Up to 350°C, electrically-driven boilers can substitute conventional steam boilers, reaching efficiencies between 95-99%.[14] TNO indicates that electric boilers can be implemented on large scales with capacities beyond 70 MW. The duty of these boilers can be reduced if low-temperature surplus heat is upgraded to high quality process heat by renewable electricity driven industrial heat pumps with a coefficient of performance (COP) between 1.5-13.[6]

For temperatures above 350°C, heat can in principle be supplied by gas fired or electric furnaces. A potential solution would be to replace the fossil feedstock with green fuels, such as biogas, H_2 and carbon-based fuels, derived directly or indirectly from water electrolysis. However, the economics and energy efficiency of power-to-fuel-to-heat strategies must be carefully evaluated because it comprises several conversion steps, which typically involves energy losses and extra costs. Electric furnaces based on induction, conduction, resistance, arc or infrared heating are examples of heating types that can be tailer-made for a specific industrial process.[15] Most types of electric furnaces and boilers are already mature

technologies, but heat from fossil resources remain cheaper. For now, electric furnaces are only implemented within very specific process steps when there is simply no cheaper alternative, as in the steel and aluminium industries.[15,16]

Most of the renewable energy sources for electricity generation are intermittent, which also affects the indirect production of heat. Capacity factor (CF) is a performance indicator for the actual annually delivered power as a percentage of the maximum output. Table 1 shows the CF for each technology, wherein solar PV and onshore wind have relatively low CFs of 17% and 37%, respectively. In order to establish a continuous flow of renewable energy, the energy mix has to be diversified. For instance, solar and wind can be combined with technologies that have a higher CF, such as biomass (77%) or geothermal (85%) to ensure a constant grid baseload, but this will be challenging. Therefore, energy storage technologies are necessary to stabilize the grid, and minimize the peak-valley demand ratio to prevent fluctuations of electricity prices.

1.1.2 Energy Storage Technologies

Energy storage technologies are generally classified in electrochemical, chemical, mechanical and thermal based systems, wherein each technology is unique and suitable for specific applications based on its costs, scalability, capacity, discharge rate and power rating (see Figure 3).[17] Pumped hydro storage is by far the most implemented storage technology and harvests the potential energy of water flowing from a high altitude reservoir to a lower reservoir via a turbine. In case excess renewable energy is available, the water from the lower reservoir is pumped back. The power rating can range between 1 MW up to 3 GW with an approximate cycle efficiency of 70-85%. Although still in the development stage, compressed air energy storage (CAES) is another example of a mechanical storage system, wherein air is compressed into underground cavities in porous rock bed or salt caverns. The cycle efficiency is comparable with pumped hydro (70%). These storage technologies are however limited to a region's specific geology.[18,19]

Batteries store energy in the form of electrical charge inside porous electrodes, separated by an electrolyte that can be solid or liquid. Li-ion based batteries are most commonly implemented, in for instance; portable consumer electronics, hybrid and full electric vehicles. Dwindling manufacturing costs of Li-ion batteries have paved the way towards large scale stationary storage facilities with capacities up to 250-750 MW for grid balancing, which have been proven to be economically attractive.[20,21] Battery systems are quite compact, flexible in terms of positioning and have a high cycling efficiency (energy efficiency ~ 90%).

Redox flow batteries are promising for large scale stationary storage. The main difference between a redox flow and a conventional battery is that the charge is not stored in the electrodes, but in the electrolyte. Consequently, its gravimetric power (W kg^{-1}) is almost two orders of magnitude lower than Li-ion batteries.[22] However, the total energy capacity of the

redox flow batteries can be increased by upscaling the volume of the electrolyte storage tanks. This also induces an economic benefit because the manufacturing costs of larger volumetric storage tanks will be relatively cheaper than battery electrodes. Unfortunately, the current market price of vanadium limits its economic potential. Alternative redox couples based on Zn-Br$_2$ or hybrid Fe-V flow batteries are much cheaper and could pave the way for commercial implementation.[23]
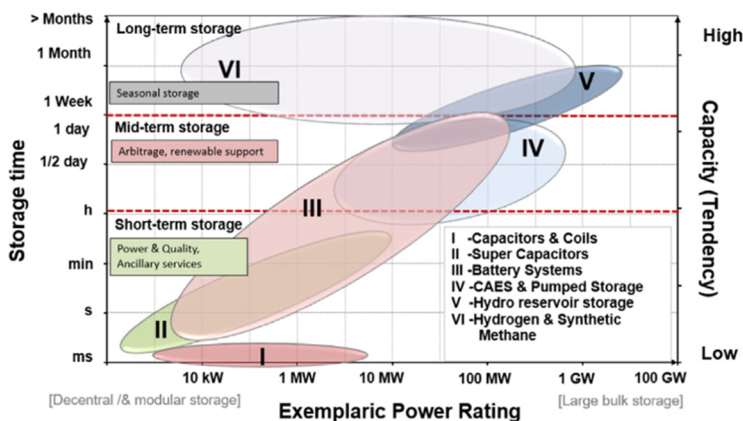
Figure 3. A comparison between energy storage technologies based on capacity, discharge time and power rating. Reprinted (adapted) with permission from Baumann et al.[24] Copyright 2024 Elsevier.

Thermal energy storage systems can be based on electrically heating a medium, with preferably a decent thermal conductivity and heat capacity, in an insulated environment. A Rankine cycle is often integrated to extract the heat for electricity generation.[25] Water has good thermal properties, but is temperature limited. Therefore, molten salts or even metals up to their melting point are used as a storage medium. Using specific phase change materials is also strategy to use their latent heat for thermal storage. Latent heat storage systems have a much higher energy density, which allows a more compact reservoir ideal for residential heating.[25] Thermal storage energy systems are generally considered cheap technologies that can be easily upscaled. The downside is that the cycle efficiency is with 30-60% on the low side, mainly due to heat dissipation and losses in the Rankine cycle. Hydrides have been mainly explored for hydrogen storage, but can also be used for thermal energy storage purposes. These systems typically contain several different hydride species with high and low-enthalpies. Upon heating by solar or surplus electricity, high-enthalpy hydrides (TiH$_2$, MgH$_2$, or MgFeH$_2$) release H$_2$, which are adsorbed and stored in low-enthalpy hydrides (Na$_3$AlH$_6$, LaNi$_5$H$_6$).[26] This process can be reversed to re-obtain the heat.

The discussed energy storage technologies are all suited for stabilizing and balancing regional or domesticated energy systems, ranging from hours-to-days for batteries and thermal energy storage, and days to weeks for pumped hydro and CAES. For seasonal storage, the conversion of renewable energy into chemical bonds, such as hydrogen or other high energy dense fuels, has been poised as one of the most prominent strategies. Water electrolysis is the backbone of this approach and requires electricity to split water into two separate product streams of hydrogen and oxygen. Hydrogen must be stored under high pressure due to its low volumetric energy density, but can be re-utilized into electricity via a fuel cell.

1.1.3 Water Electrolysis

Water electrolysis is based on a two electrode system, separated by a membrane to prevent H_2 and O_2 mixing (Figure 4). The electrochemical potential is the main driving force and is 1.23 V at standard conditions. Energy losses in the form of overpotentials vary greatly among different cell configurations. Alkaline water electrolysis is considered as a mature technology and is commercially available, using mainly earth abundant electrode materials, such as nickel and iron to suppress the investment costs. Unfortunately, commercial alkaline water electrolyzers (AEL) are limited to current densities up to 0.2-0.4 A cm^{-2} due to energy losses.[27] Acidic water electrolysis in a proton exchange membrane electrolyzer (PEMEL) are more energy efficient at current densities up to 2 A cm^{-2}. Until now, only expensive materials, such as Pt and IrO$_x$, show good performance and can resist corrosion in acidic electrolytes. Flexibility in power level is considered to be higher for PEMEL than for AEL, which is important for storage of variable renewable power levels. Hence there is a trade-off between the equipment and operational costs to select the most optimal electrolyzer configuration.
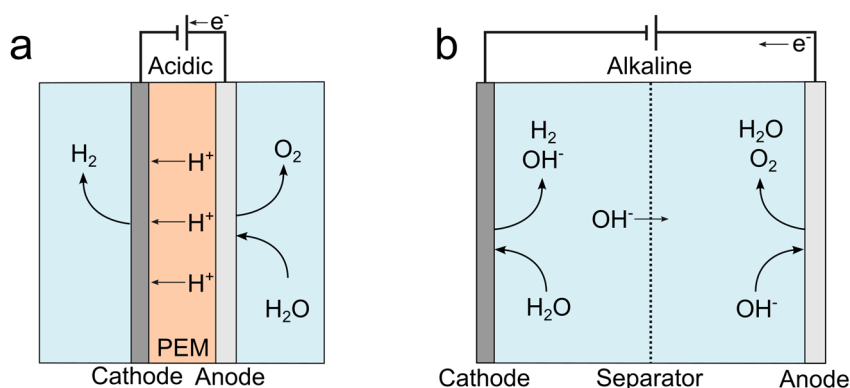
Figure 4. Schematic overview of water electrolysis in (a) acidic and (b) alkaline electrolytes.

1.1.4 Ammonia as a Future Energy Carrier

The renewable energy landscape will be geographically divided, with regions having an abundance of wind, solar or hydro. Therefore, there is a necessity for the global transportation of renewable energy over land and sea. The most probable scenario to accomplish this is to use high energy dense liquid fuels for global scale storage and transportation, that has to be produced on-site with renewable energy via either direct or indirect electrolysis based processes. Liquified H_2 (LH_2) derived from water electrolysis has been considered as a potential energy carrier, as it has one of the highest gravimetric energy densities (33.3 kWh kg^{-1}) among liquid fuels.[28] Additionally, it can be easily converted into gaseous H_2 and further utilized in a fuel cell. However, the significant energy costs associated with reaching the cryogenic -253 °C hydrogen liquefaction temperature (30-40% of H_2 LHV), along with additional boil-off losses during transportation, may render LH_2 unsuitable.[29] Hydrogen carriers, such as artificial carbon-based fuels (formic acid and methanol), metal hydrides and NH_3 are seen as promising alternatives. Among these, NH_3 stands out due to its unique properties. For instance, NH_3 contains significantly more H_2 (17.65%) than MeOH (12.5%) and formic acid (4.4%).[30,31] Although the liquid energy density of NH_3 (15.6 MJ/L) and MeOH (15.97 MJ/L) are similar, the future costs of MeOH are presumed to be higher when CO_2 from direct air capture is used as a feed.[4] Methanol is however an irreplacible base chemical in the chemical industry, and will serve other purposes within the energy market. NH_3 liquefaction occurs at mild conditions, either by pressurization up to 10 bar at room temperature, or refrigeration up to -33°C at atmospheric pressure. This minimizes energy loss during transportation and storage. Already existing NH_3 infrastructure, including production and storage facilities, can accelerate the transition towards NH_3 as a global energy vector.

1.1.5 Ammonia Market

NH_3 ranks among the largest produced synthetic chemicals in the world with an annual market size of ~180 Mt, total market capitalization of around $76 billion USD and an expected annual growth of 3-5%.[32,32] Figure 5 shows that the majority of NH_3 (80%) is processed into N-based fertilizers such as urea and ammonium nitrate, where the latter is mainly used for the production of explosives (5%). Other applications are in the manufacturing of cleaning detergents, pharmaceuticals, rubber and other polymers (15%).[34,35]
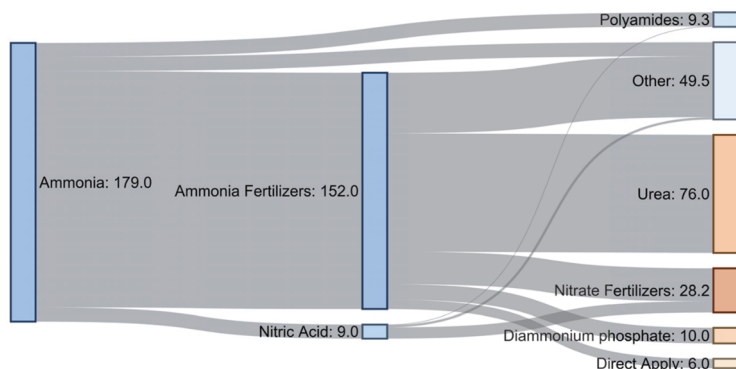
Figure 5. Sankey diagram of the global mass flow of ammonia and its derivatives in million tonnes per year. Reprinted (adapted) with permission from Lim et al.[35] Copyright 2024 American Chemical Society.

1.1.6 Current Ammonia Production Process

The vast majority of NH_3 is produced by the thermochemical Haber-Bosch process following reaction Equation 1. Nitrogen fixation is one of the most challenging reactions in the field of chemistry. The inert nature of the N_2 molecule is related to the absence of a permanent dipole moment and its strong bond-dissociation energy (945 kJ mol^{-1}). For Haber-Bosch synthesis, only a handful of transition metals such as Fe, Ru and Os are known to be active nitrogen catalysts at elevated temperatures (300-500 °C). Unfortunately, high operating temperatures promote NH_3 dissociation instead of formation. Hence, higher pressures (200-300 atm) are used to shift the equilibrium towards products, reaching NH_3 conversions up to 15-20%.[36,37]

$$N_2 + 3\,H_2 \rightarrow 2\,NH_3 \tag{1}$$

Due to these intensive process conditions, the ammonia sector consumes vast amounts of energy (~1% in the world), and requires substantial capital investments, with costs reaching $USD billions for large scale plants (>2000 tNH$_3$ per day) to minimize the investment costs.[38] The downside of these centralized plants are the increasing transportation costs, especially to remote areas. However, small scale plants do exist catering to local markets with regional price agreements.[39]

The most energy efficient method for NH_3 production is steam methane reforming (SMR) for H_2 feed production coupled to the Haber-Bosch synthesis loop. An overview of the main process components are illustrated in Figure 6a. SMR Haber-Bosch has a significant carbon footprint as it releases 1.22 tCO$_2$ per tNH$_3$ alongside additional emissions related to burning fuel, natural gas extraction and other losses.[40] Approximately 1.2% of the anthropogenic CO_2 emissions are caused by the NH_3 sector, necessitating a transition to greener production alternatives meet the net-zero emissions goal in 2050.[41] A significant cut on emissions can be accomplished if the SMR or coal gasification plant is substituted by greener alternatives,

such as water electrolysis (Figure 6b). This "electrified" version of the Haber-Bosch process, first implemented in 1928 (Rjukan, Norway), was discontinued in the 1960's when SMR became more competitive, is poised for a comeback.[42] Mainly due to the decreasing costs for renewable electricity from onshore wind and solar photovoltaics.[7] Moreover, the expected decline in manufacturing costs of AEL and PEMEL (decreasing 3.0% and 4.8% each year),[43] further enhances the competitiveness for the electrified Haber-Bosch in the near future.[40,44,45]

Figure 6. Schematic process flow diagram of (a) the conventional SMR Haber-Bosch and (b) the electrified Haber-Bosch processes. The lines indicated in dark blue, light blue, yellow, grey and purple represent steam, air, process gas, electricity and ammonia. Reprinted from Smith et al. under the Creative Commons CC BY license.[40]

1.1.7 Electrochemical Ammonia Synthesis

Alternative technologies for sustainable NH_3 production are based on the electrochemical reduction of nitrogen (NRR) by protons from water (or another source) and electrons from renewable electricity. NRR can in theory operate at ambient conditions, thereby saving energy and costs on plant equipment, such as compressors and heat exchangers.[46] Another promising approach is that NRR can be operated at elevated temperatures in a solid-oxide electrolyzer, harvesting waste heat from the chemical industry to produce ammonia at higher energy efficiencies. Nitrogen reduction via electroplated lithium with ethanol as a proton source has recently been identified as a new alternative for electrochemical ammonia production.

The next section highlights the current understanding of different approaches for electrochemical ammonia synthesis, discusses the research challenges and noteworthy achievements. The final part of this chapter presents the aim of this thesis, the main research questions and the overall outlook of the forthcoming chapters.

1.2 Theory

The following subsections will discuss the theory of the electrochemical nitrogen reduction reaction and relevant literature from the field. The theory section is divided into the three different approaches; NRR in aqueous electrolytes at ambient conditions, high temperature NRR, and NRR via an activate mediator in organic electrolytes.

1.2.1 NRR in Aqueous Electrolytes at Ambient Conditions
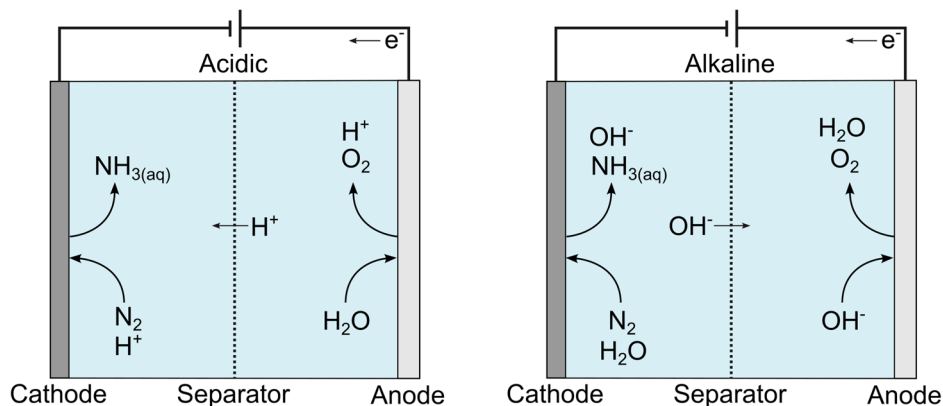
Figure 7. Schematic overview of an H-cell with aqueous NRR and OER in acidic (left) and alkaline (right) conditions.

Electrochemical NRR in an aqueous based electrolyte has obtained significant research interest over the past two decades. Figure 7 shows a basic representation of a electrochemical cell in acidic and alkaline conditions, where NRR occurs at the cathode and water oxidation (OER) at the anode. Both half-reactions of NRR and OER are pH dependent and are summarized in Equations 2-5 with the overall reaction and standard equilibrium potential in Equation 6.

$$N_2 + 6\,H^+ + 6\,e^- \leftrightarrow 2\,NH_3 \;\; (NRR, pH = 0) \;\; E^0 = 0.057 \text{ V vs. RHE} \tag{2}$$

$$3\,H_2O \leftrightarrow 1.5\,O_2 + 6\,H^+ + 6\,e^- \;\; (OER, \; pH = 0) \;\; E^0 = 1.229 \text{ V vs. RHE} \tag{3}$$

$$N_2 + 6\,H_2O + 6\,e^- \leftrightarrow 2\,NH_3 + 6\,OH^- \;\; (NRR, \; pH = 14) \;\; E^0 = 0.057 \text{ V vs. RHE} \tag{4}$$

$$6\,OH^- \leftrightarrow 1.5\,O_2 + 3\,H_2O + 6\,e^- \;\; (OER, \; pH = 14) \;\; E^0 = 1.229 \text{ V vs. RHE} \tag{5}$$

$$N_2 + 3\,H_2O \leftrightarrow 2\,NH_3 + 1.5\,O_2 \;\;\; E^0_{rxn} = 1.172 \text{ V} \tag{6}$$
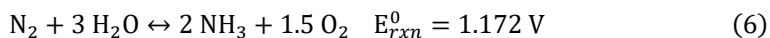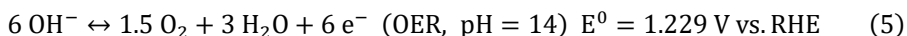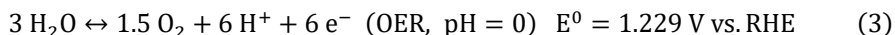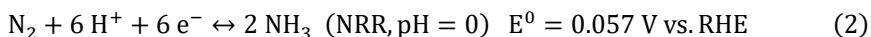
NRR requires six proton-coupled electron transfer steps and can react via either a dissociative or associative reaction mechanism (Figure 8) depending on the metal and surface structure (flat or steps).[37]

First-principles density functional theory is often employed to get an estimation of the favourable mechanism and the rate determining step by calculating and comparing the adsorption energies between the intermediates and the substrate. Theoretical work mentions that the Haber-Bosch reaction (see Equation 1) follows a dissociative pathway, where dinitrogen dissociates in two surface bounded nitrogen radicals *N that react independently with co-adsorbed protons and electrons until ammonia desorption occurs. N_2 dissociation has the slowest kinetics, but is not considered as a difficult reaction step on for instance iron and ruthenium under the appropriate conditions.[46] The same holds for H_2 dissociation as being a more facile reaction step. The hydrogenation reaction of the *N species, thus forming *NH and *NH_2 species requires the highest thermodynamic barrier because the N and H bonding on the catalyst surface is very strong and has to be overcome. Therefore, the Haber-Bosch reactor typically operates between $300 - 500$ °C to increase the N_2 dissociation rate and activate the hydrogenation steps.
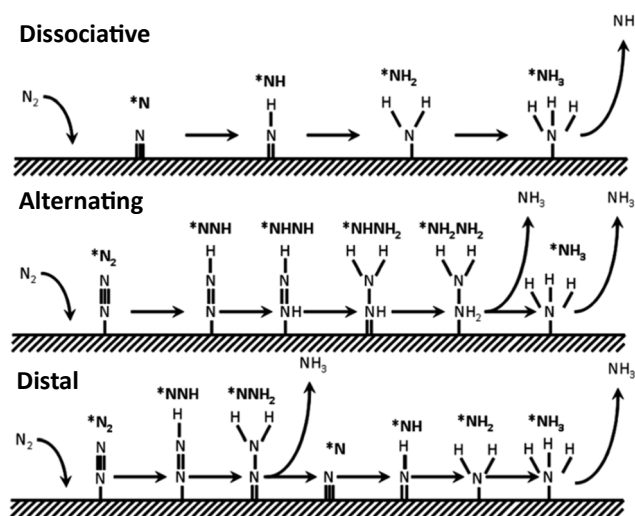
Figure 8. Dissociative (top) and associative nitrogen activation mechanisms, where the middle represents the alternating associative and bottom the distal associative pathway. Reprinted (adapted) with permission from Van der Ham et al.[36] Copyright 2024 Royal Society of Chemistry.

In the associative mechanism, dinitrogen is not dissociated, but cleaves as *N_2 on the catalyst surface. Both the N atoms in adsorbed *N_2 react with protons and electrons to form *N_2H, *NHNH, *$NHNH_2$, and *NH_3 intermediates in the alternating associative mechanism. The distal pathway is similar, but releases NH_3 after *NNH_2 is formed leaving an *N on the surface, which is further hydrogenated into a second NH_3 molecule. Theoretical studies point out that the distal pathway is energetically more favourable over the alternating

pathway because the *NNH$_2$ and *N intermediates require a lower kinetic barrier then *NHNH and *NHNH$_2$.[36] As mentioned previously, the *N$_2$ dissociation step (in the dissociative mechanism) is very slow and requires a higher temperature to increase the reaction rate. Therefore, catalyst materials that favour the dissociation mechanism are perhaps not suitable for NRR at ambient conditions.

Side Reactions

Diazene and hydrazine are important intermediates in the associative reaction mechanism and might be produced (Equation 7 and 8) as side products during NRR.[36] Therefore, most experimental studies include quantification tests for hydrazine detection, but has until now not been observed.[47]

$$N_2 + 4\,H^+ + 4\,e^- \leftrightarrow N_2H_4(g) \quad E^0 = -0.33 \text{ V vs. RHE} \tag{7}$$

$$N_2 + 2\,H^+ + 2\,e^- \leftrightarrow N_2H_2(g) \quad E^0 = -1.10 \text{ V vs. RHE} \tag{8}$$
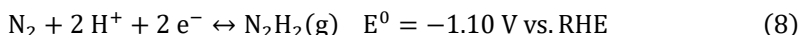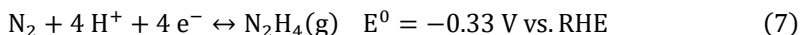
The hydrogen evolution reaction (HER) is the main parasitic side reaction because HER occurs at a similar standard equilibrium potential (E^0 = 0 V vs. RHE) as NRR (E^0 = 0.057 V vs. RHE). It is however expected that NRR has an additional overpotential of at least 0.4 V to overcome all kinetic barriers of the intermediate reaction steps.[36,37,48] HER in both acidic and alkaline electrolyte follow either a Volmer-Heyrovsky or Volmer-Tafel mechanism (see Table 2). This means that HER has only one intermediate, which indicates that the activation barrier in comparison to NRR is significantly lower. Therefore, in order to find an active catalyst for NRR, the material in question should favour N over H adsorption.

Table 2. Half-reactions and reaction mechanisms of HER in acidic and alkaline electrolytes.

Acidic conditions	
$2\,H^+ + 2\,e^- \leftrightarrow H_2$	
Volmer step	$H^+ + e^- \rightarrow H_{ads}$
Tafel step	$2H_{ads} \rightarrow H_2$
Heyrovsky step	$H^+ + H_{ads} + e^- \rightarrow H_2$
Alkaline conditions	
$2\,H_2O + 2\,e^- \leftrightarrow H_2 + 2\,OH^-$	
Volmer step-water dissociation	$2H_2O + 2e^- \rightarrow 2H_{ads} + 2OH^-$
Tafel step	$2H_{ads} \rightarrow H_2$
Heyrovsky step	$H_2O + H_{ads} + e^- \rightarrow H_2 + OH^-$

Norskov and coworkers have applied Density Functional Theory (DFT) calculations on various transitional metals to find catalysts with the optimum *N binding energy (binding neither too strong nor too weak) as a function of the limiting overpotential. Figure 9 indicates that Fe, Rh, Ru, Ir, Co, Ni and to some extent Mo are close to the top of the volcano. However, most of these metals, especially the platinum group metals (Rh, Ru, Ir) are known

to be excellent HER catalysts.[49] This means that the adsorption strength of *H is more favourable over *N (as indicated in the grey area in Figure 9). The NRR activity of these materials were also examined experimentally, but only quantified H_2 as the main product.[47,50] The volcano plot indicates that only a few materials (Sc, Y, Ti and Zr) have a higher affinity to N-binding. So far, no experimental studies have irrevocably confirmed that these materials are active towards nitrogen reduction to ammonia.

The effect of pH on the NRR kinetics is rarely discussed in literature. For HER in an alkaline electrolyte, the hydrogen intermediate (*H) comes from the dissociation of water, which introduces an additional barrier. This explains why the HER activity is roughly 2-3 orders of magnitude lower in alkaline media.[51] The most active catalysts in alkaline conditions are Ir, Ru and Pt-based alloys, which are all supreme over Pt.[52] This could indicate that NRR activation stands a better chance in alkaline environments, where new classes of materials may become interesting.[48]
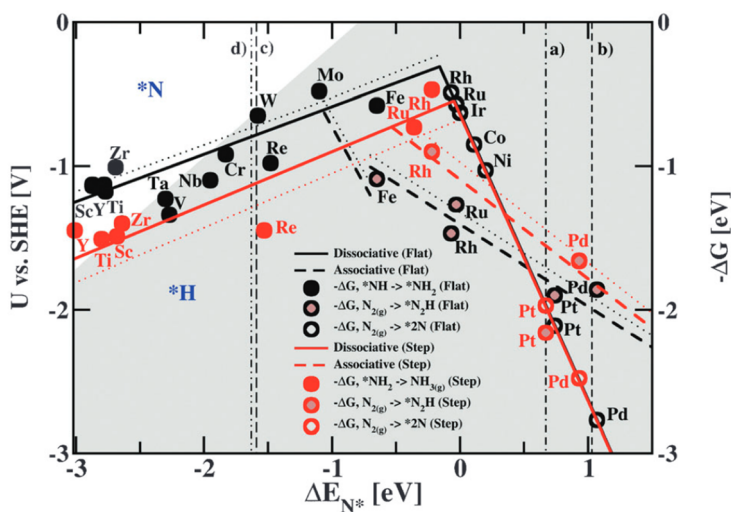
Figure 9. Volcano diagram of different transition metals with a flat (black) and step (red) configuration for the NRR. Associative mechanism is indicated as a dotted line and the dissociative as a flat line. The volcano plot indicates the minimum overpotential required to overcome the potential limiting step as a function of the *N binding strength. The metals in the grey indicate that adsorption of *H is more favorable than *N. This means that selectivity issues towards the formation H_2 can be expected. Reprinted (adapted) with permission from Skúlason et al.[37] Copyright 2024 Royal Society of Chemistry.

Impurities

Most experiments are performed in a small electrochemical cell at current densities between 0.01-10 mA cm^{-2}. As a consequence, the quantification range of ammonia concentrations are often in the parts per million (ppm) range, which is at similar levels as ammonia from external sources, such as the ambient air, lab ware, consumables, cell

components, catalysts materials and feed gasses.[47] This questions rather ammonia is artificially produced by nitrogen fixation or is coming from external sources.

Different nitrogen oxide (NO_x) species from external sources have also been labelled as potential impurities because they can be electroreduced into ammonia and are generally more labile than N_2 as illustrated in Figure 10. For long, NO_x has been (and still is) an unforeseen contaminant in the research community, which doubts many old and recently published results.[53] It is therefore essential to quantify the NO_x concentration during or after an electrochemical experiment, which still remains a rare practise.

Extensive experimental protocols have been published to identify or rule out any effects of impurities.[47,54,55] The following three control experiments are advised as mandatory. At first, an argon blank test under electrochemical operation reveals potential impurities from the internal cell components, such as the electrolyte, membrane and catalytic material. Secondly, an experiment run at open-circuit conditions while purging with reactant gas can identify any labile species in the N_2 feed. At last, isotope labelled $^{15}N_2$-gas must be used to confirm a nitrogen active catalyst through the quantification $^{15}NH_3$. Nuclear magnetic resonance spectroscopy is generally used to distinguish between $^{15}NH_3$ and $^{14}NH_3$. It is important to note that $^{15}N_2$-gas is available at lower purities (99%) and contains ppm levels of $^{15}NH_3$ or $^{15}NO_x$ species.[56] Therefore, it is important to purify the gas by using a certified gas filter prior introducing it into the cell.
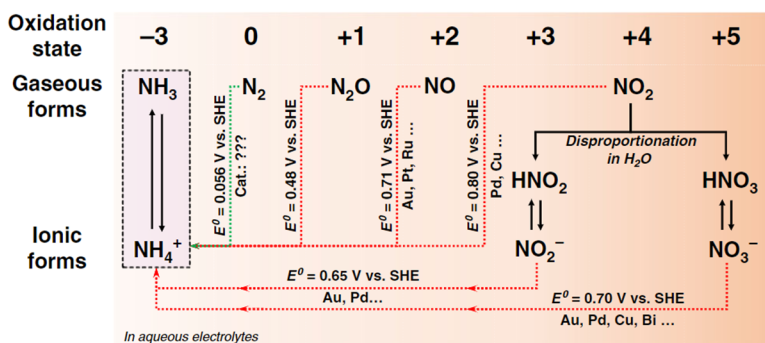
Figure 10. Different electrochemical synthesis routes towards NH_3 via N_2 and NO_x species including their apparent standard equilibrium potentials. Reprinted from Choi et al.[53] under the Creative Commons CC BY license.

Mass Transport

The solubility of nitrogen gas in aqueous solutions is considerably low and might be another reason why nitrogen activation at ambient conditions is challenging. Most fundamental electrochemical research is performed in a H-cell configuration, whereby the mass transport is limited by the solubility of the reactants. Strategies to overcome this is by using different cell configurations based on gas-diffusion electrodes or high pressure cells.[57,58] Another

approach is to switch towards organic based electrolytes with a higher nitrogen solubility, such as ionic liquids or fluorinated aprotic solvents.[59,60] These strategies have been tried, but without success.[61,62]

1.2.2 Nitrogen Reduction at Elevated Temperatures

High temperature electrocatalysis can be beneficial to overcome the kinetic barrier for nitrogen activation. Nitrogen reduction at elevated temperatures is typically done in a solid oxide electrolysis cell (SOEC) with a solid ceramic electrolyte in the middle, an anode and cathode, forming together a membrane electrode assembly (MEA) (see Figure 11). The solid electrolyte has to be chemically and mechanically stable, electronically insulating and ionic conductive at temperatures up to 650 °C. Proton conducting perovskite, such as $BaCe_{0.9}Y_{0.1}O_{3-\delta}$ (BCY), $BaZr_{0.8}Y_{0.2}O_{3-\delta}$ (BZY) or composites ($BaZr_{0.8}Ce_{0.1}Y_{0.1}O_{3-\delta}$) are the most promising for NRR.[63,64] Proton transport occurs by the Grotthuss mechanism where proton hopping occurs via neighbouring free oxygen atoms in the perovskite. AgPd catalysts show the best ammonia production rates (10^{-8}-10^{-10} mol cm^{-2} s^{-1}) and FE (50-80%) between a temperature range of 400-600 °C. Non-noble catalysts, such as Fe, Ni, FeMoN, CoMoN and VN show also promising production rates (~10^{-9} mol cm^{-2} s^{-1}), but have been inferior in terms of selectivity towards NRR compared to AgPd.[63-65]
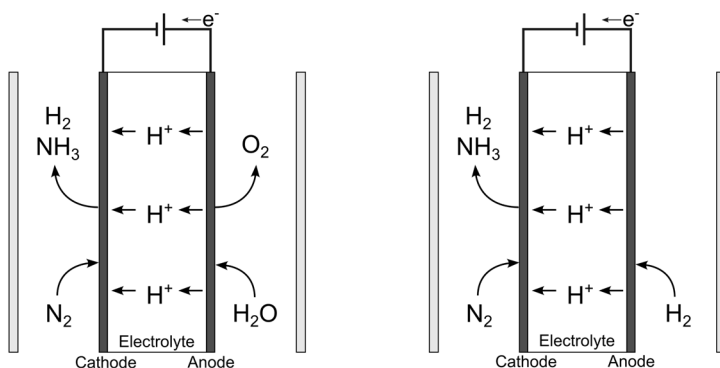
Figure 11. Schematic drawing of high temperature NRR in a proton conducting solid oxide electrochemical cell with steam oxidation (left) and hydrogen oxidation (right).

One of the problems of operating at high temperatures is the loss of produced ammonia due to ammonia decomposition, which is circumvented in the Haber-Bosch reactor by increasing the pressure. Another issue is that SOEC is in practise not compatible with steam oxidation because it breaks down the anode materials. Steam oxidation requires a minimum cell voltage of 1.2 V, which also accelerates degradation of all SOEC components. This means that hydrogen must be used as a feed stock, which is from an energy efficiency and commercial point of view most likely not desirable.

1.2.3 Nitrogen Reduction via a Mediated Activator

An alternative approach towards electrochemical ammonia synthesis is based on nitrogen activation through a reactive mediator, such as metallic reduced lithium or calcium. The working principle is outlined in Figure 12 and deviates from a classical electrocatalytic approach as was discussed in section 1.2.1 and 1.2.2, but has more similarities to Li-ion batteries. During operation, Li-ions in an organic based electrolyte are electroplated to Li metal on a substrate by applying a negative reduction potential (< -3 V vs. SHE). N_2 gas dissolved in the solution reacts spontaneously with Li metal to form a lithium nitride (Li_3N). Ethanol acts as a proton donor and reacts with Li_3N to form NH_3. The Li_3N hydrogenation steps seems to be chemical in nature, wherein Li plating is the only electrochemical step (Equation 9-11).[66] However, it is unclear what exactly happens with the Li metal and ethoxide after the NRR. If Li plating is the only electrochemical step, then Li metal dissolution (into Li^+) in the form of a cyclic mechanism seems evident. Otherwise, a significant amount of isolated patches of "dead" Li metal would accumulate on the electrode, resulting in a thick visible surface layer, which is not always observed in the literature.[67] There is evidence that $EtOH/EtO^-$ is operating as a proton shuttle, wherein EtO^- is re-protonated at the anode via solvent or hydrogen oxidation.[68,69] Another possibility is that the Li_3N protonation steps are electrochemical by nature, wherein an initial deposited Li layer functions as an electrocatalyst (see Equations 12-14).
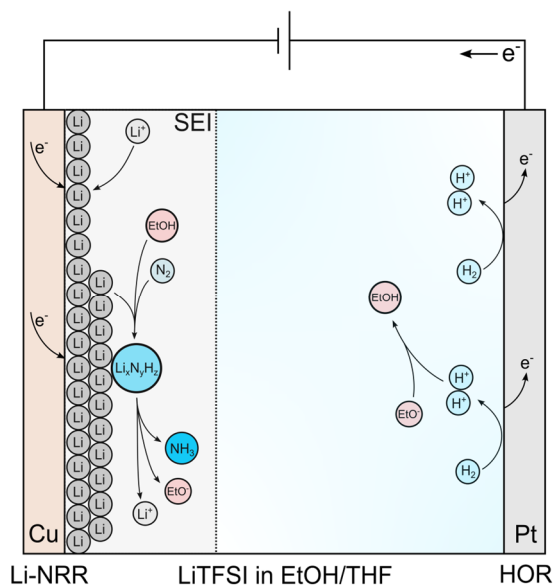
Figure 12. Schematic of a typical Li-NRR electrochemical cell with hydrogen oxidation at anode.

Cycling mechanism

$$Li^+ + e^- \leftrightarrow Li^0 \qquad (9)$$

$$6\,Li^0 + N_2 \rightarrow 2\,Li_3N \qquad (10)$$

$$Li_3N + 3\,EtOH \rightarrow NH_3 + 3\,Li^+ + 3\,EtO^- \qquad (11)$$
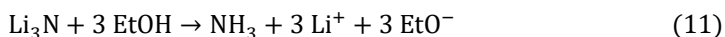
Electrochemical mechanism

$$Li_3N + EtOH + e^- \rightarrow LiNH + EtO^- \qquad (12)$$

$$Li_3NH + EtOH + e^- \rightarrow LiNH_2 + EtO^- \qquad (13)$$

$$Li_3NH_2 + EtOH + e^- \rightarrow Li^0 + NH_3 + EtO^- \qquad (14)$$
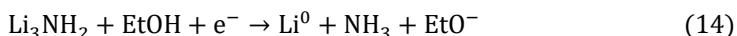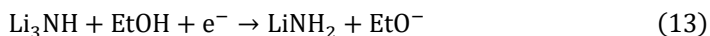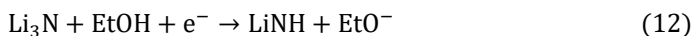
All these reactions occur in a solid electrolyte interphase (SEI), which is combination of organic and inorganic lithium compounds affiliated with the species in the organic electrolyte. The SEI is formed naturally when there is freshly plated Li metal on the electrode. The SEI functions as a protective layer between the electrolyte and Li metal, but also controls the diffusive mass transport of the proton shuttle and nitrogen gas to the surface of the Li metal.[67] The latter is important for the selectivity of the reaction. The composition of the SEI can be altered by additives, Li-salt anions, electrolyte concentrations and organic solvents. Recently, it was found that high concentrations of fluorine based electrolytes (2M $LiBF_4$ and 2M LiTFSI) could form a compact and uniform SEI layer of predominantly LiF. As a result, FE and NH_3 rate above 95% and 200 nmol s^{-1} cm^{-2} were obtained by two independent studies.[70,71] Besides the SEI, the concentration of the proton shuttle and dissolved nitrogen in the electrolyte plays also an important role in reaching high selectivity's. The optimum EtOH concentration for a three electrode autoclave cell is 0.1 M in THF, wherein the reaction rate is H^+ limited below and N_2 limited above 0.1 M EtOH in THF.[68,71] During the latter, the formation of H_2 by ethanol hydrolysis will be one of the side reactions. Other side reactions are most likely related to the formation of the SEI or growth of "dead" lithium.[68,73-75] Other proton donors, such as alcohols with lower and higher alkane chains, phenols and phosphonium were examined previously. The exact correlation between the proton donor type and the Li-NRR performance remains disputed. It seems that the diffusion constant, the pKa and the thickness of the SEI by proton donor decomposition all have an effect on the performance. [74,75] Some claim that EtOH remain the most prominent proton donor, while others find PrOH, BuOH,[73] or PhOH more suitable for Li-NRR.

Most experiments are performed in a small batch-type three electrode autoclave cell with ethanol as a sacrificial proton donor, which is simply not scalable. Chorkendorff and coworkers developed a continuous flow cell with two compartments for the N_2 and H_2 feed and a third for the electrolyte.[69] N_2 and H_2 gases are fed into the electrolyte through stainless steel mesh gas diffusion electrodes based on the initial work of Lazouski et al.[76] Although

the system runs at a low current density (-4 mA cm^{-2}), the flow cell is already selective reaching a Faradaic efficiency of 61%.

For a long time is has been thought that only Li can activate N_2, until Ca has been experimentally identified as another mediator.[77] DFT calculations show that the N_2 dissociation barrier on metallic Ca is low and can occur at room temperature following a similar mechanism as Li.[77,78] Stable Ca plating was only achieved using $Ca(BH_4)_2$ and $Ca[B(hfip)_4]_2$, while not with $Ca(ClO_4)_2$ and $Ca(BF_4)_2$. This indicates that Ca-NRR is more sensitive towards the composition of the electrolyte, with in particular the anion species.

Albeit exciting to observe progress in the NRR mediated field, there are many things still unknown. The exact reaction mechanism is poorly understood, although it is somewhat accepted that nitrogen dissociation by the mediator is a chemical reaction by nature. Perhaps the potential dependency as a function of the selectivity and reaction rate can give some mechanistic insights. However, a pseudo reference electrode is commonly applied, which is not reliable for a potential screening. This also limits the determination of the actual energy efficiency of a Li-NRR system.

1.3   Research Questions and Thesis Outline

Based on the previous discussion of the current challenges in the field, the following research questions were contrived and addressed throughout this thesis:

- Is there a catalyst that is electrochemically active towards the NRR in an aqueous based electrolyte at ambient conditions?
- How reliable are previous literature reports without performing the necessary control experiments?
- What is the main source of origin of encountered NH_3 and NO_x impurities?
- What are the best methods to limit the effect of N impurities during NRR experiments?
- Is the performance of the Li-mediated NRR affected by different applied potentials?
- What is the energy efficiency of a Li-NRR electrolyzer?
- Will the electrochemical synthesis of ammonia be economically competitive with the electrified or methane-fed Haber-Bosch synthesis?

The main aim of this thesis is to identify and understand which of the electrochemical ammonia approaches as discussed in section 1.2 are the most promising for future application. Transition metal carbides were earlier reported as promising NRR catalysts in aqueous electrolytes. The activity of these materials is revisited in Chapter 2, wherein a strict experimental protocol was implemented to limit the effect of impurities during the electrochemical measurements. Regarding the material synthesis, nanoparticles of molybdenum and iron carbides were prepared by earlier developed carburization methods and further verified by physical characterization methods, such as X-ray diffraction, X-ray

photoelectron spectroscopy, Mössbauer spectroscopy and electron microscopy. Chapter 3 is entirely dedicated to the identification and elimination of external sources of NH_3 and NO_x. Commonly used cell components, lab ware, solvents, salts and feed gases are screened to obtain insights into which sources are most severe. Additionally, the efficacy of several cleaning strategies is also revised to improve the current protocols. Li-NRR is discussed in Chapter 4, where an in-house made three electrode autoclave cell is used to study the effect of potential on the selectivity and NH_3 production rate at 20 bar N_2 pressure. The SEIs are physically characterized by X-ray photoelectron spectroscopy to obtain information about the composition. Chapter 5 discusses a comprehensive techno-economic model, wherein conceptual process designs of different NRR pathways are developed and their economic feasibility compared with the electrified and methane fed Haber-Bosch process. The main conclusions and recommendations of this thesis are summarized in Chapter 6.

1.4 References

1   Masson-Delmotte, V. *et al.* Climate Change 2021: The Physical Science Basis. Contribution of Working Group I to the Sixth Assessment Report of the Intergovernmental Panel on Climate Change. (2021).

2   Lee, H. *et al.* IPCC, 2023: Climate Change 2023: Synthesis Report, Summary for Policymakers. Contribution of Working Groups I, II and III to the Sixth Assessment Report of the Intergovernmental Panel on Climate Change [Core Writing Team, H. Lee and J. Romero (eds.)]. IPCC, Geneva, Switzerland. (2023).

3   Ritchie, H. *Sector by sector: where do global greenhouse gas emissions come from?* , <https://ourworldindata.org/ghg-emissions-by-sector> (2020).

4   International Energy Agency. *Gas Flaring*, <https://www.iea.org/energy-system/fossil-fuels/gas-flaring> (2023).

5   Huijsmans, J. F. & Schils, R. L.   (International Fertiliser Society).

6   Schlosser, F. *et al.* Large-scale heat pumps: Applications, performance, economic feasibility and industrial integration. *Renewable and Sustainable Energy Reviews* **133**, 110219 (2020).

7   International Rewenable Energy Agency (IRENA). Renewable power generation costs in 2022. (2022).

8   International Rewenable Energy Agency (IRENA). Future of Solar Photovoltaic: Deployment, investment, technology, grid intergration and socio-economic aspects (A global Energy Transformation: paper). (2019).

9   van Leeuwen, R. P., De Wit, J. & Smit, G. J. M. Review of urban energy transition in the Netherlands and the role of smart energy management. *Energy conversion and management* **150**, 941-948 (2017).

10   Lowes, R., Woodman, B. & Fitch-Roy, O. Policy change, power and the development of Great Britain's Renewable Heat Incentive. *Energy Policy* **131**, 410-421 (2019).

11   Philibert, I. E. A.-C. Renewable Energy for Industry: From green energy to green materials and fuels. (2017).

12   Zuberi, M. J. S., Hasanbeigi, A. & Morrow, W. Electrification of industrial boilers in the USA: potentials, challenges, and policy implications. *Energy Efficiency* **15**, 70 (2022).

13   Marc Marsidi, Luuk Beurskens & Uslu, A. The role of renewable heat technologies in industry - a review of Dutch sectoral industry roadmaps. (2018).

14   Marsidi, M. *Technology Factsheet - Electric Industrial Boiler*, <https://energy.nl/wp-content/uploads/electric-industrial-boiler-7.pdf> (2018).

15   Schüwer, D. & Schneider, C. Electrification of industrial process heat: long-term applications, potentials and impacts. (2018).

16   Lee, B. & Sohn, I. Review of innovative energy savings technology for the electric arc furnace. *Jom* **66**, 1581-1594 (2014).

17   Gür, T. M. Review of electrical energy storage technologies, materials and systems: challenges and prospects for large-scale grid storage. *Energy & Environmental Science* **11**, 2696-2767 (2018).

18   Valera-Medina, A. & Banares-Alcantara, R. *Techno-economic challenges of green ammonia as an energy vector*. (Academic Press, 2020).

1

19   Wu, S., Salmon, N., Li, M. M.-J., Bañares-Alcántara, R. & Tsang, S. C. E. Energy decarbonization via green H2 or NH3? *ACS Energy Letters* **7**, 1021-1033 (2022).

20   InnoEnergy. *Fast-growing grid scale stationary battery storage*, <https://www.eba250.com/fast-growing-grid-scale-stationary-battery-storage/> (2021).

21   Maisch, M.   (pv magazine, 2018).

22   Dunn, B., Kamath, H. & Tarascon, J.-M. Electrical energy storage for the grid: a battery of choices. *Science* **334**, 928-935 (2011).

23   Scott, A. in *Chemical & Engineering News* Vol. 101   (ACS, 2023).

24   Baumann, M., Weil, M., Peters, J. F., Chibeles-Martins, N. & Moniz, A. B. A review of multi-criteria decision making approaches for evaluating energy storage systems for grid applications. *Renewable and Sustainable Energy Reviews* **107**, 516-534 (2019).

25   Luo, X., Wang, J., Dooner, M. & Clarke, J. Overview of current development in electrical energy storage technologies and the application potential in power system operation. *Applied energy* **137**, 511-536 (2015).

26   Wang, Q., Guo, J. & Chen, P. The power of hydrides. *Joule* **4**, 705-709 (2020).

27   Buttler, A. & Spliethoff, H. Current status of water electrolysis for energy storage, grid balancing and sector coupling via power-to-gas and power-to-liquids: A review. *Renewable and Sustainable Energy Reviews* **82**, 2440-2454 (2018). https://doi.org:10.1016/j.rser.2017.09.003

28   Sartbaeva, A., Kuznetsov, V., Wells, S. A. & Edwards, P. Hydrogen nexus in a sustainable energy future. *Energy & Environmental Science* **1**, 79-85 (2008).

29   Chatterjee, S. Limitations of Ammonia as a Hydrogen Energy Carrier for the Transportation Sector. (2021). https://doi.org:10.1021/acsenergylett.1c02189

30   Energy, U. D. o. *Alternative Fuels Data Center - Fuel Properties Comparison*, <https://afdc.energy.gov/fuels/properties?fuels=ME> (

31   Eppinger, J. r. & Huang, K.-W. Formic acid as a hydrogen energy carrier. *ACS Energy Letters* **2**, 188-195 (2017).

32   Food and Agriculture Organization of the United Nations. World Fertilizer Trends and Outlook to 2022. (2019).

33   IMARC. Ammonia Market: Global Industry Trends, Share, Size, Growth, Opportunity and Forecast 2023-2028. (2022).

34   International Energy Agency. Ammonia Technology Roadmap - Towards more sustainable nitrogen fertiliser production (2021).

35   Lim, J., Fernández, C. A., Lee, S. W. & Hatzell, M. C. Ammonia and nitric acid demands for fertilizer use in 2050. *ACS Energy Letters* **6**, 3676-3685 (2021).

36   Van Der Ham, C. J. M., Koper, M. T. M. & Hetterscheid, D. G. H. Challenges in reduction of dinitrogen by proton and electron transfer. *Chemical Society Reviews* **43**, 5183-5191 (2014). https://doi.org:10.1039/c4cs00085d

37   Skúlason, E. *et al.* A theoretical evaluation of possible transition metal electro-catalysts for N2 reduction. *Physical Chemistry Chemical Physics* **14**, 1235-1245 (2012). https://doi.org:10.1039/c1cp22271f

38   Soloveichik, G. Electrochemical synthesis of ammonia as a potential alternative to the Haber–Bosch process. *Nature Catalysis* **2**, 377-380 (2019).

39   Brown, T. *The capital intensity of small-scale ammonia plants*, <https://www.ammoniaenergy.org/articles/the-capital-intensity-of-small-scale-ammonia-plants/> (2018).

40   Smith, C., Hill, A. K. & Torrente-Murciano, L. Current and future role of Haber-Bosch ammonia in a carbon-free energy landscape. *Energy and Environmental Science* **13**, 331-344 (2020). https://doi.org:10.1039/c9ee02873k

41   Arias, P. *et al.* Climate Change 2021: the physical science basis. Contribution of Working Group I to the Sixth Assessment Report of the Intergovernmental Panel on Climate Change; technical summary. (2021).

42   Smolinka, T., Bergmann, H., Garche, J. & Kusnezoff, M. in *Electrochemical power sources: fundamentals, systems, and applications* 83-164 (Elsevier, 2022).

43   Glenk, G. & Reichelstein, S. Economics of converting renewable power to hydrogen. *Nature Energy* **4**, 216-222 (2019).

44   Michael Nayak-Luke, R. & Bañares-Alcántara, R. Techno-economic viability of islanded green ammonia as a carbon-free energy vector and as a substitute for conventional production †. *Cite this: Energy Environ. Sci* **13**, 2957-2957 (2020). https://doi.org:10.1039/d0ee01707h

45   Cesaro, Z., Ives, M., Nayak-Luke, R., Mason, M. & Bañares-Alcántara, R. Ammonia to power: Forecasting the levelized cost of electricity from green ammonia in large-scale power plants. *Applied Energy* **282**, 116009-116009 (2021). https://doi.org:10.1016/J.APENERGY.2020.116009

46   Rod, T. H., Logadottir, A. & Nørskov, J. K. Ammonia synthesis at low temperatures. *The Journal of Chemical Physics* **112**, 5343-5347 (2000).

47   Andersen, S. Z. *et al.* A rigorous electrochemical ammonia synthesis protocol with quantitative isotope measurements. *Nature* **570**, 504-508 (2019). https://doi.org:10.1038/s41586-019-1260-x

48   Dražević, E. & Skúlason, E. Are There Any Overlooked Catalysts for Electrochemical NH3 Synthesis—New Insights from Analysis of Thermochemical Data. *iScience* **23**, 101803-101803 (2020). https://doi.org:10.1016/j.isci.2020.101803

49   Seh, Z. W. *et al.* Combining theory and experiment in electrocatalysis: Insights into materials design. *Science* **355**, eaad4998 (2017).

50   Suryanto, B. H. R. *et al.* MoS 2 Polymorphic Engineering Enhances Selectivity in the Electrochemical Reduction of Nitrogen to Ammonia. *ACS Energy Letters* **4**, 430-435 (2019). https://doi.org:10.1021/acsenergylett.8b02257

51   Zheng, Y., Jiao, Y., Vasileff, A. & Qiao, S. Z. The hydrogen evolution reaction in alkaline solution: from theory, single crystal models, to practical electrocatalysts. *Angewandte Chemie International Edition* **57**, 7568-7579 (2018).

52   McCrum, I. T. & Koper, M. T. The role of adsorbed hydroxide in hydrogen evolution reaction kinetics on modified platinum. *Nature Energy* **5**, 891-899 (2020).

53   Choi, J. *et al.* Identification and elimination of false positives in electrochemical nitrogen reduction studies. *Nature Communications* **11**, 1-10 (2020). https://doi.org:10.1038/s41467-020-19130-z

54   Greenlee, L. F., Renner, J. N. & Foster, S. L. The Use of Controls for Consistent and Accurate Measurements of Electrocatalytic Ammonia Synthesis from Dinitrogen. *ACS Catalysis* **8**, 7820-7827 (2018). https://doi.org:10.1021/acscatal.8b02120

55   Du, H. L., Gengenbach, T. R., Hodgetts, R., Macfarlane, D. R. & Simonov, A. N. Critical Assessment of the Electrocatalytic Activity of Vanadium and Niobium Nitrides toward Dinitrogen Reduction to Ammonia. *ACS Sustainable Chemistry and Engineering* **7**, 6839-6850 (2019). https://doi.org:10.1021/acssuschemeng.8b06163

56   Dabundo, R. *et al.* The Contamination of Commercial 15N2 Gas Stocks with 15N–Labeled Nitrate and Ammonium and Consequences for Nitrogen Fixation Measurements. *PLOS ONE* **9**, e110335-e110335 (2014). https://doi.org:10.1371/JOURNAL.PONE.0110335

57   Kolen, M., Ripepi, D., Smith, W. A., Burdyny, T. & Mulder, F. M. Overcoming nitrogen reduction to ammonia detection challenges: the case for leapfrogging to gas diffusion electrode platforms. *ACS catalysis* **12**, 5726-5735 (2022).

58   Wang, Y. *et al.* Highly selective NH3 synthesis from N2 on electron-rich Bi0 in a pressurized electrolyzer. *Proceedings of the National Academy of Sciences* **120**, e2305604120 (2023).

59   Zhou, F. *et al.* Electro-synthesis of ammonia from nitrogen at ambient temperature and pressure in ionic liquids. *Energy and Environmental Science* **10**, 2516-2520 (2017). https://doi.org:10.1039/c7ee02716h

60   Kang, C. S. M., Zhang, X. & Macfarlane, D. R. High Nitrogen Gas Solubility and Physicochemical Properties of [C4mpyr][eFAP]-Fluorinated Solvent Mixtures. *Journal of Physical Chemistry C* **123**, 21376-21385 (2019). https://doi.org:10.1021/acs.jpcc.9b06000

61   Hodgetts, R. Y., Du, H. L., MacFarlane, D. R. & Simonov, A. N. Electrochemically Induced Generation of Extraneous Nitrite and Ammonia in Organic Electrolyte Solutions During Nitrogen Reduction Experiments. *ChemElectroChem* **2**, 1-10 (2021). https://doi.org:10.1002/celc.202100251

62   Kolen, M. *et al.* Combinatorial Screening of Bimetallic Electrocatalysts for Nitrogen Reduction to Ammonia Using a High-Throughput Gas Diffusion Electrode Cell Design. *Journal of The Electrochemical Society* **169**, 124506 (2022).

63   Kyriakou, V., Garagounis, I., Vasileiou, E., Vourros, A. & Stoukides, M. Progress in the Electrochemical Synthesis of Ammonia. *Catalysis Today* **286**, 2-13 (2017). https://doi.org:10.1016/j.cattod.2016.06.014

64   Fernandez, C. A. *et al.* Opportunities for intermediate temperature renewable ammonia electrosynthesis. *Journal of Materials Chemistry A* **8**, 15591-15606 (2020). https://doi.org:10.1039/d0ta03753b

65   Kyriakou, V., Garagounis, I., Vourros, A., Vasileiou, E. & Stoukides, M. An Electrochemical Haber-Bosch Process. *Joule* **4**, 142-158 (2020). https://doi.org:10.1016/j.joule.2019.10.006

66   Bjarke Valbæk Mygind, J. *et al.* Is Ethanol Essential for the Lithium-Mediated Nitrogen Reduction Reaction? *ChemSusChem* **16**, e202301011 (2023).

67   Andersen, S. Z. *et al.* Increasing stability, efficiency, and fundamental understanding of lithium-mediated electrochemical nitrogen reduction. *Energy & Environmental Science* **13**, 4291-4300 (2020). https://doi.org:10.1039/d0ee02246b

68   Du, H.-L. *et al.* The chemistry of proton carriers in high-performance lithium-mediated ammonia electrosynthesis. *Energy & Environmental Science* **16**, 1082-1090 (2023).

69   Fu, X. *et al.* Continuous-flow electrosynthesis of ammonia by nitrogen reduction and hydrogen oxidation. *Science* **379**, 707-712 (2023).

70   Du, H.-L. *et al.* Electroreduction of nitrogen at almost 100% current-to-ammonia efficiency. *Nature* **609**, 722-727 (2022). https://doi.org:10.1038/s41586-022-05108-y

71   Li, S. *et al.* Electrosynthesis of ammonia with high selectivity and high rates via engineering of the solid-electrolyte interphase Electrosynthesis of ammonia with high selectivity and high rates via engineering. *Joule* **6**, 2083-2101 (2022). https://doi.org:10.1016/j.joule.2022.07.009

72   Lazouski, N., Schiffer, Z. J., Williams, K. & Manthiram, K. Understanding Continuous Lithium-Mediated Electrochemical Nitrogen Reduction. *Joule* **3**, 1127-1139 (2019). https://doi.org:10.1016/j.joule.2019.02.003

73   Lazouski, N. *et al.* Proton Donors Induce a Differential Transport Effect for Selectivity toward Ammonia in Lithium-Mediated Nitrogen Reduction. *ACS Catalysis* (2022). https://doi.org:10.1021/ACSCATAL.2C00389

74   McShane, E. J. *et al.* Quantifying Influence of the Solid-Electrolyte Interphase in Ammonia Electrosynthesis. *ACS Energy Letters* **8**, 4024-4032 (2023).

75   Chorkendorff, I. *et al.* Phenol as Proton Shuttle and Buffer for Lithium-mediated Ammonia Electrosynthesis. (2023).

76   Lazouski, N., Chung, M., Williams, K., Gala, M. L. & Manthiram, K. Nonaqueous gas diffusion electrodes for rapid ammonia synthesis from nitrogen and water. *Nature Catalysis* (2020). https://doi.org:10.1038/s41929-020-0455-8

77   Fu, X. *et al.* Calcium-mediated nitrogen reduction for electrochemical ammonia synthesis. *Nature Materials*, 1-7 (2023).

78   Tort, R. *et al.* Searching for the Rules of Electrochemical Nitrogen Fixation. *ACS Catalysis* **13**, 14513-14522 (2023).

1

2

Revisiting the Electrochemical Nitrogen Reduction on Molybdenum and Iron Carbides: Promising Catalysts or False Positives?

Abstract

The electrochemical dinitrogen reduction reaction (NRR) has recently gained much interest as it can potentially produce ammonia from renewable intermittent electricity and replace the Haber−Bosch process. Previous literature studies report Fe- and Mo-carbides as promising electrocatalysts for the NRR with activities higher than other metals. However, recent understanding of extraneous ammonia and nitrogen oxide contaminations have challenged previously published results. Here, we critically assess the NRR performance of several Fe- and Mo-carbides reported as promising by implementing a strict experimental protocol to minimize the effect of impurities. The successful synthesis of α-Mo$_2$C decorated carbon nanosheets, α-Mo$_2$C nanoparticles, θ-Fe$_3$C nanoparticles, and χ-Fe$_5$C$_2$ nanoparticles was confirmed by X-ray diffraction, scanning and transmission electron microscopy, and X-ray photoelectron and Mössbauer spectroscopy. After performing NRR chronoamperometric tests with the synthesized materials, the ammonia concentrations varied between 37 and 124 ppb and are in close proximity with the estimated ammonia background level. Notwithstanding the impracticality of these extremely low ammonia yields, the observed ammonia did not originate from the electrochemical nitrogen reduction but from unavoidable extraneous ammonia and NOx impurities. These findings are in contradiction with earlier literature studies and show that these carbide materials are not active for the NRR under the employed conditions. This further emphasizes the importance of a strict protocol in order to distinguish between a promising NRR catalyst and a false positive.

2.1 Introduction

The activation of diatomic nitrogen has been one of the greatest challenges in nitrogen-related chemistry.[1,2] This is inherently related to the inert nature of the nitrogen molecule due to its high bond-dissociation energy, absence of a dipole moment, and low proton and electron affinity.[3] Despite the inert nature, diazotrophic microorganisms successfully fixate nitrogen and play a key role in enriching the soil.[4] However, due to the growing world population and the high demand for food, additional nitrogen containing nutrients in the form of artificial ammonia-based fertilizers must be provided to the soil. The majority of the ammonia produced worldwide is synthesized by the Haber−Bosch process (H-B), wherein energy intensive reaction conditions (T = 300−500 °C, P = 150−300 bar) are needed to activate dinitrogen.[2] The ammonia industry consumes approximately 1% of the global energy demand and emits roughly 0.75% of the anthropogenic CO_2 emissions (assuming 1.9 $t_{CO_2} \, t_{NH_3}^{-1}$),[5,6] which is motivating the search for more energy efficient and sustainable alternatives.

The electrochemical nitrogen reduction reaction (NRR), wherein dinitrogen, water, and electrons from renewable sources react to form ammonia, has recently gained significant scientific interest and has been proposed as a potential replacement for the fossil fuel-based H-B.[7,8] NRR systems at high (>500 °C) and intermediate (100−500 °C) temperatures have proven to be successful in terms of faradaic efficiency (FE ⩾ 75%) and NH_3 yield (⩾ 4.5 nmol s^{-1} cm^{-2}).[9] Nevertheless, the present high temperature NRR systems tend to have a low energy efficiency compared to H-B.[10,11] Therefore, it would be beneficial to perform the NRR under ambient conditions. Significant FEs have been reported with iron electrocatalysts in ionic liquids and organic electrolytes by suppressing the parasitic hydrogen evolution reaction (HER).[12,13] However, the use of organic electrolytes is likely to be less economically feasible compared to aqueous electrolytes due to complex scalability, safety issues, high costs, and intense energy requirements.[8,14] Unfortunately, the kinetics under ambient conditions in aqueous electrolytes are sluggish and many attempts in examining transition metals, such as Au, Fe, Mo, Ru, Rh, and Re, as potential electrocatalysts for the NRR have resulted in low FEs (<1%) and ammonia yields (<0.1 nmol s^{-1} cm^{-2}).[15,16]

The active site of the nitrogenase enzyme, the biologic pathway for nitrogen fixation, is the FeMo-cofactor. The FeMo-cofactor contains a six iron atomic trigonal prism with a carbon-centered position. Each iron is bound to three sulfur atoms, with an additional iron and molybdenum in apical positions.[2,17] Attempts to mimic the FeMo-cofactor initiated investigation into Fe- and Mo-based heterogeneous NRR catalysts, such as carbides and sulfides. Both Mo_2C and MoS_2 show noble metal like properties, due to similar d-band configurations as Pt.[18] Therefore, they can act as cheap and robust catalytic substitutes for many applications, including water electrolysis, water gas shift reaction, and ammonia decomposition.[19] Despite the fact that these materials are good HER catalysts, several density functional theory studies have predicted favorable nitrogen binding energies.[19–21]

Experimental results are somewhat distinct; nitrogen reduction experiments with amorphous 2H-MoS$_2$ and metallic 1 T-MoS$_2$ did not produce quantities of ammonia exceeding the background level,[12,21] while other studies report reasonable FEs and ammonia yields using FeS$_2$, Mo$_2$C, and Fe$_3$C, thereby labeling these materials as promising NRR catalysts.[22–24]

The electrochemical NRR field is plagued by questionable results, mainly due to the large impact of extraneous ammonia sources on experiments performed on a small scale. Ammonia stemming for other sources can erroneously be assigned to ammonia synthesized by the NRR, which can lead to false positives. Ammonia impurities can be minimized by a proper experiment design and can be identified by applying the right control experiments, such as argon and open-circuit blank tests and ultimately ^{15}N$_2$-labeled experiments. Recently, nitrogen oxides have been identified as another source of contamination, as these species are more easily reduced to ammonia than dinitrogen in the NRR.[25] The majority of the recently published studies have applied blank tests, but performing quantitative ^{15}N$_2$-labeled experiments and monitoring nitrogen oxide species are done sporadically.[25] As a consequence, a handful of research groups have tried to reproduce electrocatalysts initially labeled as promising, such as Fe, Bi, Au, VN, CoMo, Mo$_2$N, and MoS$_2$,[16,21,26–30] but discovered that the quantified ammonia must originate from sources other than the NRR. Here, we critically assess the electrocatalytic NRR activity of molybdenum and iron carbides, where more than 10 independent literature reports claim to observe superior or excellent catalytic performance.[23,24,31–38] In the present work, α-Mo$_2$C nanodots from Cheng et al. (reported as the most promising carbide catalyst) are reproduced and compared with α-Mo$_2$C nanoparticles as a benchmark.[23] Additionally, nanostructured θ-Fe$_3$C and χ-Fe$_5$C$_2$ are synthesized and examined for their NRR activity. A key aspect of this work is the implementation of a strict protocol, which is designed to minimize the level of extraneous contamination,[15,25] allowing genuine quantification of ammonia produced by the NRR.

2.2 Experimental Section

2.2.1 Materials

Materials and chemicals were purchased from Sigma Aldrich, if not indicated otherwise. Ultrapure water (Millipore Milli-Q IQ 7000) was used for catalyst synthesis, electrolyte preparation, and cleaning procedures. Concentrated sulfuric acid (95−98 wt % H_2SO_4, trace metal purity) was used for glassware acid cleaning and diluted for other purposes. High purity N_2, Ar, and H_2 (99.999%, Linde) were used for electrochemical experiments and material synthesis.

2.2.2 Molybdenum and Iron Carbide Synthesis

Mo_2C Nanodot-Decorated Carbon Nanosheets. Mo_2C nanodots (Mo_2C NS) were synthesized by a molten-salt synthesis procedure as reported in detail elsewhere.[23] In short, a mixture of 1 mL of water and 4 mL of ethanol (96%, VWR) was mixed in a beaker and continuously heated and stirred on a hotplate. Once the mixture reached 70 °C, 0.4 g of bis(acetylacetonato)dioxomolybdenum(VI) and 0.14 g of sucrose (99.5%) were added. After the mixture turned green, an excess amount of sodium chloride (99.5%) was added until a green crystalline slurry was formed. The slurry was directly transferred to a ceramic boat and placed inside a tubular furnace (Blue, Lenton), where the specimen was heated to its carburization temperature under an Ar atmosphere (T_{carb} = 800 °C, heating rate = 5 °C min^{-1}), kept constant at this temperature for 2 h and the furnace cooled down to room temperature naturally. The resulting black catalyst/salt mixture was excessively rinsed with ultrapure water to remove the sodium chloride. The residue was filtrated (Durapore 100 nm, Merck) and dried in an oven at 80 °C overnight.

α-Mo_2C Nanoparticles. Gómez-Marín and Ticianelli reported a procedure for the synthesis of porous Mo_2C nanoparticles (Mo_2C NP) that was replicated here.[39] In a typical procedure, 0.15 g of Vulcan VC-72 (Cabot) was mixed with 0.51 g of MoO_3 (99.9%) in a beaker containing 30 mL of ethanol. The dispersion was heated to 60 °C overnight while continuously stirring to evaporate the ethanol completely. The powder was transferred to a ceramic boat for carburization inside a tubular furnace under 10 vol % H_2:Ar. The precursor was heated to 725 °C for 30 min with a slow heating rate (1 °C min^{-1}) and cooled down to room temperature.

Mesoporous Fe_3C. A combined hard-templating and carburization method developed by Kraupner and coworkers was used to create a mesoporous Fe_3C structure with a high surface area.[40] In brief, 0.5 g of $FeCl_3$ (99.9%) was dissolved in 1 g of 40 wt% SiO_2 in H_2O (Ludox AS40) in a borosilicate test tube. Additionally, 0.728 g of 4.5-dicyanoimidazole (99%) was added and stirred through the suspension and sonicated for 30 min to achieve a homogeneous yellow-colored thick slurry paste. The paste was transferred to a ceramic boat and

carburized inside a tubular furnace at 700 °C (heating rate 2 °C min^{-1}) for 2 h under an Ar atmosphere and cooled down to room temperature.

χ-Fe$_5$C$_2$ Nanoparticles. The principle of thermal decomposition of Fe(CO)$_5$ is a common used strategy to synthesize iron carbides and is discussed in detail elsewhere.[41] A mixture of 0.2 g of polyvinylpyrrolidone (PVP, 40000 g mol^{-1}) and 1 mL of Fe(CO)$_5$ (99.99%) was inserted in a homemade air-tight reactor consisting of Swagelock tubes and adapters (Figure A1). The reactor was purged with Ar at a flowrate of 20 mL min^{-1} for approximately 10 min to remove residual oxygen, and immediately afterward, all Swagelock adapters were closed. The reactor was positioned inside a muffle furnace programmed with T_{carb} at 300 °C (heating rate 2.3 °C min^{-1}) for a duration of 24 h.

2.2.3 Characterization

X-ray Diffraction (XRD). Samples were deposited on a Si510 zero background wafer and positioned inside a Bruker D8 Advance diffractometer in Bragg-Brentano geometry equipped with a graphite monochromator, a Vantec position sensitive detector, a variable divergence slit, and a 5 mm height scatter screen. Co $K\alpha$ radiation (λ = 0.1789 nm) was used to avoid incident beam fluorescence effects on the Fe carbides. During each acquisition, steps with a size of 0.038° and 5 s per step were measured over a 10-110° 2ϑ range. Bruker DiffracSuite.EVA v6.0 was used to subtract the background, correct small displacements, and strip the $K\alpha 2$ contribution from the patterns to enable crystallite size (D_{XRD}) estimation with the Scherrer equation (Equation 1), where λ is the wavelength, and κ the shape factor taken as 1. Peak shapes were assumed Gaussian, and the full width at half maximum, in this case β, was additionally corrected for instrumental line broadening effects.

$$D_{XRD} = \frac{\kappa\lambda}{\beta\cos\vartheta} \tag{1}$$

Mössbauer spectroscopy. Transmission ^{57}Fe Mössbauer spectra were collected at room temperature with a conventional constant-acceleration spectrometer with a ^{57}Co(Rh) source. Velocity calibration was carried out using an α-Fe foil. The Mössbauer spectra were fitted using the Mosswinn 4.0 program.[42]

X-ray Photoelectron Spectroscopy (XPS). A Thermo Scientific Kα spectrometer with a monochromatic Al Kα excitation source was used to acquire X-ray photoemission spectroscopy (XPS) spectra. The base pressure inside the analysis chamber was about 2 x 10^9 mbar. HR-XPS spectra were recorded using a 400 μm spot size, 0.1 eV step size, and 50 eV pass energy (200 eV for survey). All spectra were charge corrected to the C 1s adventitious carbon (284.8 eV). Sub-surface layers were measured with a depth-profile by argon ion etching (1000 eV) in between XPS measurements. The obtained XPS spectra were deconvoluted with CasaXPS v2.3 software.

Inductively Coupled Plasma Atomic Emission Spectroscopy (ICP-OES). The materials were dispersed in 35 vol% HNO_3 overnight to dissolve the carbides. The samples were further diluted with 3 vol% HNO_3 with an amount depending on the expected metal content. All ICP-OES measurements were performed on a SPECTRO ARCOS measured against an external calibration, with a typical detection limit of 10 ppb.

Scanning Electron Microscopy (SEM). Prior to analysis, the aluminum cylindrical sample holder was washed in isopropanol in an ultrasonic bath for approximately 2 min. An isopropanol based catalyst ink was drop-casted on the sample holder and positioned in a 25 mm working distance. The SEM measurements were executed on a Jeol JSM 6500F instrument at an acceleration voltage of 15 kV, coupled with an energy dispersed X-ray analysis detector (Ultradry, Thermo Scientific).

Transmission Electron Microscopy (TEM). A dispersion of catalyst and isopropanol was drop-casted on a TEM grid with a holey carbon film on a copper 400 mesh (EM-resolutions). All materials were analyzed with a JEOL JEM1400plus TEM at a 120 kV acceleration voltage using a single-tilt specimen holder. The TEM was equipped with a TVIPS TemCam-F416R high resolution camera based on a custom designed CMOS architecture. ImageJ was used to estimate the particle size distribution.

2.2.4 Electrochemical Measurements

A Biologic VSP-300 potentiostat in combination with EC-Lab software was used for all electrochemical measurements. The uncompensated resistance (R_u) of the system (the resistance between the reference electrode (RE) and working electrode (WE)) was measured before each cyclic voltammetry (CV) and chronoamperometry (CA) measurement. R_u was determined with potentiostatic electrochemical impedance spectroscopy at open-circuit potential, with a frequency range between 200 kHz and 0.1 Hz. The distance between the origin and the first line intersection on the Z_{Real}-axes within the Nyquist plot represents R_u and was extracted by manual data fitting. Subsequently, the EC-Lab build-in IR compensation allowed 85% R_u compensation without adding to much distortion to the CV and CA results. Only for the CA experiments, the other 15% R_u was compensated after the measurement by using Equation 2.

$$V_{100\%} = V_{85\%} - (iR_u)_{15\%} \qquad (2)$$

A polyether ether ketone (PEEK) three-electrode cell design adapted from the Jaramillo group was used for all electrochemical experiments.[43] It consisted of two separate compartments that accommodate 5 mL of electrolyte and 3 mL of gas headspace. An additional plate was added to the overall cell design (Figure A2), which fixated the WE. A leak-free Ag/AgCl micro reference electrode (Innovative Instruments, LF-1-45) was used for potential control, wherein all potentials were recalculated versus the reversible hydrogen electrode scale following Equation 3.

$$E_{RHE} = E_{Ag/AgCl} + E^0_{Ag/AgCl} + 0.059*pH \qquad (3)$$

A Pt foil (50 x 50 x 0.025 mm, 99.99%, Mateck) functioned as the anode and was rinsed with water and flame annealed before each experiment. A fresh sheet of membrane (Celgard 3401) was used for every run, thereby preventing accumulation of NH_3. The WE was prepared by drop-casting 3 droplets of 10 µL of a freshly prepared catalyst ink (2 mg_{cat} mL^{-1}, 950 µL 2-propanol (98%, VWR) and 50 µL of Nafion 117-containing solution (5 wt%)) on a carbon paper disk (1 cm^2, Toray carbon paper, Aesar) with a loading of 0.06 mg cm^{-2} and stored under vacuum once prepared. The WE was soaked in a fresh 1 M KOH (99.95%), 0.1 M KOH, 0.5 M Li_2SO_4 or 0.05 M H_2SO_4 solution before it was fixated in the cell by a glassy carbon plate (25 x 25 x 1 mm, HTW). The back of the glassy carbon was taped with a Cu strip (AT528, 10 mm width, RS Components) and connected to the potentiostat wires. The catholyte was saturated by purging N_2 or Ar for 30 min before each experiment. After cyclic voltammetry and chronoamperometric measurements, aliquots of both catholyte and anolyte were collected with a syringe and transferred to several test tubes for further quantification.

2.2.5 Minimizing Effects of Impurities

Feed gas contamination in the form of NH_3 and NO_x in both high purity Ar and N_2 have been reported previously.[15,25] In order to remove residual contaminants, a certified commercial gas filter (Entegris GPUS35FHX) was installed upstream of the electrochemical cell (see Figure A3). The cell components were always acid cleaned with 10 vol% H_2SO_4 for at least 1 h and rinsed with ultrapure water prior to each experiment. Syringes, needles, pipet tips, and sample tubes were also excessively washed with ultrapure water and dried under Ar flow before use. A microporous membrane (Celgard 3401) with a gas repellent coating was selected as a more suitable separator compared to the more commonly used Nafion membrane to avoid accumulation of ammonia contaminations as was reported previously.[15,44,45] A downstream acidified liquid trap is often used to measure volatile ammonia that could potentially be present in the effluent gas. As NH_3 dissolves very well in aqueous electrolytes ($\sim$500 g L^{-1}), this suggests that low concentrations of NH_3 readily dissolves in the used electrolyte. This means that an acid trap is often redundant and can potentially be an extra source of contamination.[15] Therefore, we did not incorporate a downstream acidified trap in the experimental design.

Precursors and catalysts containing nitrogen species are potential sources of impurities and should be avoided.[28,30] The selection criteria for our catalyst synthesis procedures was mainly motivated by minimizing the use of N-containing precursors. The Mo_2C nanoparticles and Mo_2C nanodots do not contain N-based materials for the preparation, while the use of N−C compounds was unavoidable for the synthesis of iron carbide nanomaterials. The latter motivated us to use a catalyst loading of 0.06 mg cm^{-2} to minimize the effects of the N−C precursor during the electrochemical experiments. We used a method adopted from Chen et al. to monitor impurities in our materials,[26] such as catalyst powders, membranes, carbon

paper, and Pt foil. Strategies to effectively remove impurities will be discussed in a future study.[46]

Li-salts are notorious for containing trace levels of NO_x–species as was previously reported by Li et al.[47] Therefore, Li_2SO_4 is suspected of having these labile N-species and the suggested thermal annealing step was implemented to remove trace impurities. For the annealing step, the as received Li_2SO_4 (99.5%) was transferred to a tubular furnace and thermally annealed at 800 °C for 4 h in Ar with a heating rate of 10 °C min^{-1} before preparing a solution.

2.2.6 Ammonia and Nitrite Quantification

Ammonia was quantified by the Berthelot reaction.[48] In a routine analysis, a volume of 1.33 mL of either 1 M KOH, 0.1 M KOH, 0.5 M Li_2SO_4, or 0.05 M H_2SO_4 was neutralized with dilute concentrations of H_2SO_4 or KOH. Then, phenol nitroprusside and alkaline hypochlorite (0.2 wt % sodium hypochlorite in an alkaline solution) were both added in an amount equal to 25 vol % of the neutralized solution. The mixture was stirred thoroughly on a vortex shaker. After 30 min of incubation time, the solution color and its intensity differed from light green to dark blue with increasing NH_3 content. The samples were transferred to PMMA cuvettes (10 × 10 × 30 mm) for further analysis with the UV–Vis spectrophotometer (Hach DR6000). For constructing a calibration line, a series of six different concentrations of NH_4Cl (99.99%) in 1 M KOH, 0.1 M KOH, 0.5 M Li_2SO_4, and 0.05 M H_2SO_4 were prepared with respective concentrations of 0.01, 0.05, 0.1, 0.5, 1, and 2 ppm. The fitted calibration lines shown in Figure A4 were reproducible and resulted in the following linear relationships: A_{1MKOH} = $0.5642\,C_{NH_3}$ - 0.0045 with R^2 = 0.9997, $A_{0.1MKOH}$ = $0.7279\,C_{NH_3}$ - 0.001 with R^2 = 0.9999, $A_{0.5MLi_2SO_4}$ = $0.7992C_{NH_3}$ - 0.0033 with R^2 = 0.9997, $A_{0.05MH_2SO_4}$ = $0.6613C_{NH_3}$ - 0.00405 with R^2 = 0.9997.

The concentration of NO_2^- was quantified by the photometric Griess test. A commercially available Griess reagent mixture was used with a detection range between 0.007 and 3.28 ppm NO_2^- (Spectroquant, Merck). Typically, a sample of 2 mL of 0.1 M KOH was neutralized with 168 μL of 0.5 M H_2SO_4. Subsequently, 30 mg of the Griess reagents were added and mixed with the solution with an incubation time of 10 min. Five different concentrations of 0.02, 0.05, 0.1, 0.5, 1 ppm KNO_2 in 0.1 M KOH were prepared to construct a calibration line with a perfect linear fit: $A = 0.8071C_{NO_2^-}$ - 0.0001 and R^2 = 1 (Figure A5). The UV-Vis spectroscopic measurements to detect ammonia and NO_2^- were always performed versus a blank 0.1 M KOH electrolyte stock solution, to exclude the influence of electrolyte background contaminations.

2.3 Results and Discussion

2.3.1 Material Characterization

The X-ray diffraction patterns of Mo_2C NS, Mo_2C NP, Fe_3C and Fe_5C_2 are shown in Figure 1. The Mo_2C samples (Figure 1a) show three sharp peaks at 40.2, 44.3, and 46.1° that are identical to the reference spectrum of α-Mo_2C (PDF 04-003-0962). Three other peak features at 30.3, 43.2, and 63.0° suggest the existence of MoO_2 (PDF 04-013-3645) in the Mo_2C NS sample. This is most likely related to an incomplete carbothermal reduction of the molybdenum oxide precursor, which was not observed for the Mo_2C NP. The "hill-like" peak between 20 and 25° is typical for amorphous carbon and reflects its dominant presence in the Mo_2C NS, Fe_3C, and Fe_5C_2 samples.[49] The peaks between 45 and 60° in Figure 1b correspond to orthorhombic iron carbide (θ-Fe3C, PDF 00-035-0772). The formation of other Fe oxidation states, such as reduced Fe (53.3°), Fe_3O_4 (41.3, 35, 74.2°), and Fe_2O_3 (38.6°) are inevitable by-products of the carburization process.[41,50] Also, small fractions of Fe_3O_4 (41.4° and 74°) were identified in Figure 1c after the thermal decomposition of $Fe(CO)_5$,[41] while the multiplet between 49 and 55° is very typical for χ-Fe_5C_2 (PDF 01-080-4102). The average crystallite size was calculated with the Scherrer equation (Equation 1) and summarized in Table A1.

The fitted Mössbauer spectrum of the Fe_3C sample (Figure 2a) shows a sextuplet with an isomer shift (*IS*) of 0.19 mm s^{-1}, and a hyperfine field of 20.8 T. θ-Fe_3C is identified as the major spectral contributor (67%).[51] Additionally, a metallic Fe sextuplet (*IS* = −0.004 mm s^{-1}, 33 T) was clearly observed and is in agreement with the sharp peak at 53.3° in the Fe_3C diffractogram. A doublet indicates a quadrupole peak splitting, which means the absence of magnetic field spin coupling. This indicates the presence of (super)paramagnetic Fe^{3+} nanostructures. It is difficult to allocate the specific Fe^{3+} phase, as multiple subdoublets can be superimposed in one doublet.[52] However, the low intensity XRD peaks of Fe_2O_3 suggests that the doublet contains mostly nanostructured Fe_3O_4. The presumably low quantities of Fe_2O_3 are covered by a sextet (*IS* = 0.31 mm s^{-1}, 49.3 T); therefore, it is unlikely that Fe_2O_3 has a spectral contribution in the doublet. Three sextuplets (*IS* = 0.27, 0.21, and 0.16 mm s^{-1} with B_{hyp} = 21.7, 18.1, and 10.3 T) covered 78% of the spectral area in Figure 2b, which were attributed to the three iron lattice sites in the Fe_5C_2 crystal structure.[53,54] Fe_3O_4 has a small spectral contribution located in the outer spectrum with an octahedral (*IS* = 0.28 mm s^{-1}, 49.1 T) and a tetrahedral site (*IS* = 0.71 mm s^{-1}, 46 T).[55] Fe_2O_3 was not identified in the Fe_5C_2 diffractogram, which again suggests that the doublet is nanostructured Fe_3O_4. In conclusion, the Mössbauer data confirms the synthesis of the intended Fe_3C and Fe_5C_2 compounds with limited amounts of iron and iron oxide species. The remainder of the Mössbauer data is summarized in Table A2.
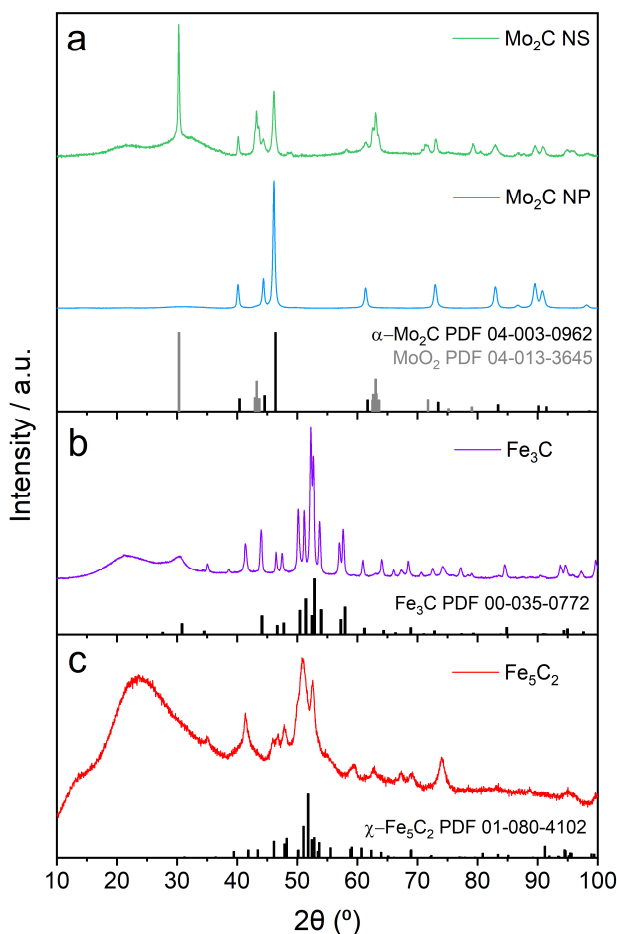
Figure 1. X-ray diffractions patterns of (a) Mo_2C NS (green) and Mo_2C NP (blue) with the α-Mo_2C (PDF 04-003-0962, black) and MoO_2 (PDF 04-013-3645, gray) reference patterns. The patterns in (b) and (c) represent Fe_3C (purple) and Fe_5C_2 (red) with the corresponding θ-Fe_3C (PDF 00-035-0772, black) and χ-Fe_5C_2 (PDF 01-080-4102, black) reference patterns.

Mössbauer spectroscopy and XRD give information about the bulk phase of the material. XPS is surface sensitive and gives information regarding the surface phase and composition. The Mo_2C XPS survey scans (Figure A6a,b) contain peaks of Mo 3d, Mo 3p, C 1s and O 1s, from which the high-resolution scans of the Mo 3d photoelectrons (Figure 3a,b) were deconvoluted to identify different Mo oxidation states. The Mo 3d orbital has a spin−orbit Mo $3d_{5/2}$-Mo $3d_{3/2}$ doublet with a 3/2 peak intensity ratio that is separated by a binding energy of 3.15 eV. The full width at half-maximum (FWHM) was kept constant for each doublet during the deconvolution process. It is often ambiguous to assign an oxidation state to Mo_2C; therefore, it is often denoted in an aggregated term as Mo^{0-3+}.[56] The presence of

Mo_2C surface bonded species was confirmed by the small Mo $3d_{5/2}$ peaks at 229.3 and 228.2 eV for both Mo_2C NS and Mo_2C NP, respectively.[34,57] Other peaks at binding energies 232.5 and 235.5 eV for both Mo carbide materials are identified as MoO_3 and must be solely present in the thin surface layers as MoO_3 was not identified in the diffractograms. These spontaneously formed metal oxide surface layers are inevitable due to exposure to ambient air. Post-mortem XPS analyses confirmed that the majority of the surface layer was Mo_2C.[23,58] This suggests that the Mo-oxide species are reduced during electrochemical reduction. Moreover, it is expected that the trans-passive Mo-oxide layers are not stable in alkaline conditions and form soluble MoO_4^{2-} even at moderate reduction potentials.[59,60]
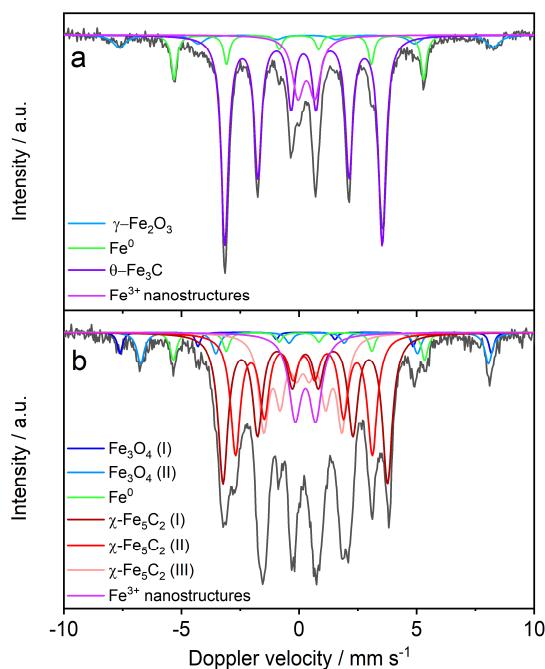
Figure 2. Room temperature transmission ^{57}Fe Mössbauer spectra in the (a) prepared Fe_3C sample with a large intensity sextet (purple) identified as θ-Fe_3C and (b) synthesized Fe_5C_2 powder with three intense sextets of χ-Fe_5C_2 (I maroon, II red, III salmon).

The Fe $2p_{3/2}$ peak was used to identify different Fe oxidation states. The broad peak between 714 and 709 eV contains a complex convolution of multiple subpentuplets of Fe_2O_4, Fe_3O_4, and FeOOH species, which all overlap in this region. We fitted one pentuplet as a general Fe-oxide term as indicated in Figure 3c,d by taking XPS reference data such as FWHM, relative peak area, and binding energies from Biesinger et al.[61] For iron carbide, the majority of the surface is covered with a thin Fe-oxide layer. According to the Pourbaix diagram for Fe, this oxide-layer is reduced by applying mild reduction potentials.[62] The presence of a single peak at 708.4 eV for Fe_3C and 708.6 eV for Fe_5C_2 is identified as the Fe carbide phase.

Only Fe_5C_2 has an additional sharp metallic Fe peak at 707.2 eV. The low signal-to-noise ratio for the Fe_5C_2 Fe 2p spectra indicates a low Fe quantity (<1 at%), which is also reflected in a low intensity Fe oxide peak in the O 1s spectra (Figure A7e). From a depth profiling test (Figure A8), it becomes clear that the Fe 2p signal increases with a longer etching time, while the intensities of the O 1s and N 1s spectra decreases. This indicates that the top surface layer is covered with adventitious species due to atmospheric exposure.
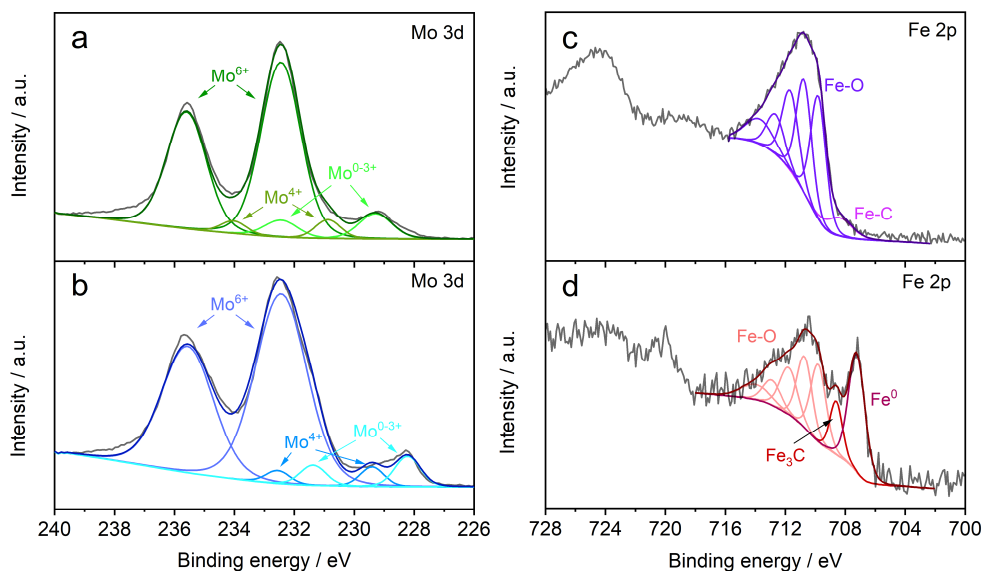
Figure 3. X-ray photoelectron spectroscopy Mo 3d and Fe 2p spectra with deconvoluted peaks in (a) Mo_2C NS (green) and (b) Mo_2C NP (blue), (c) orthorhombic Fe_3C (purple), and (d) Fe_5C_2 (red).

The elemental Mo and Fe content in all metal carbides were analyzed by ICP-OES and are summarized in Table A3. The ICP-OES results revealed that the bulk concentrations of Mo and Fe are significantly higher with respect to the surface concentrations estimated by XPS. This suggests that the surface adsorption of advantageous species by air exposure is not only observed for Fe_5C_2 but also for the other metal carbides.

The Mo_2C NS are clearly visible in Figure 4a,e and confirm a successful synthesis. TEM imaging (Figure A9a) reveals that a relatively large proportion of the sample consists of undecorated carbon nanosheets. This explains why the majority of the surface composition, analyzed by XPS, is predominantly carbon (Table A4). The existence of Mo_2C nanodots (<20 nm), as proposed by Wang and coworkers, was not observed in our TEM analysis.[23] Despite the magnification limitations of the low-resolution TEM, distinguished nano-particles up to 5–10 nm were detectable in other metal carbide samples, indicating that Mo_2C nanodots of the order 10–20 nm should be visible. In Figure 4e and Figure A9b, regions with a higher contrast indicate a layer of aggregated Mo_2C, with an average crystallite size (D_{XRD}) of 35 nm.

The SEM–EDX results (Figures A10 and A11) support this observation and show that the carbon sheet is indeed covered with a nanocrystalline layer of Mo_2C.
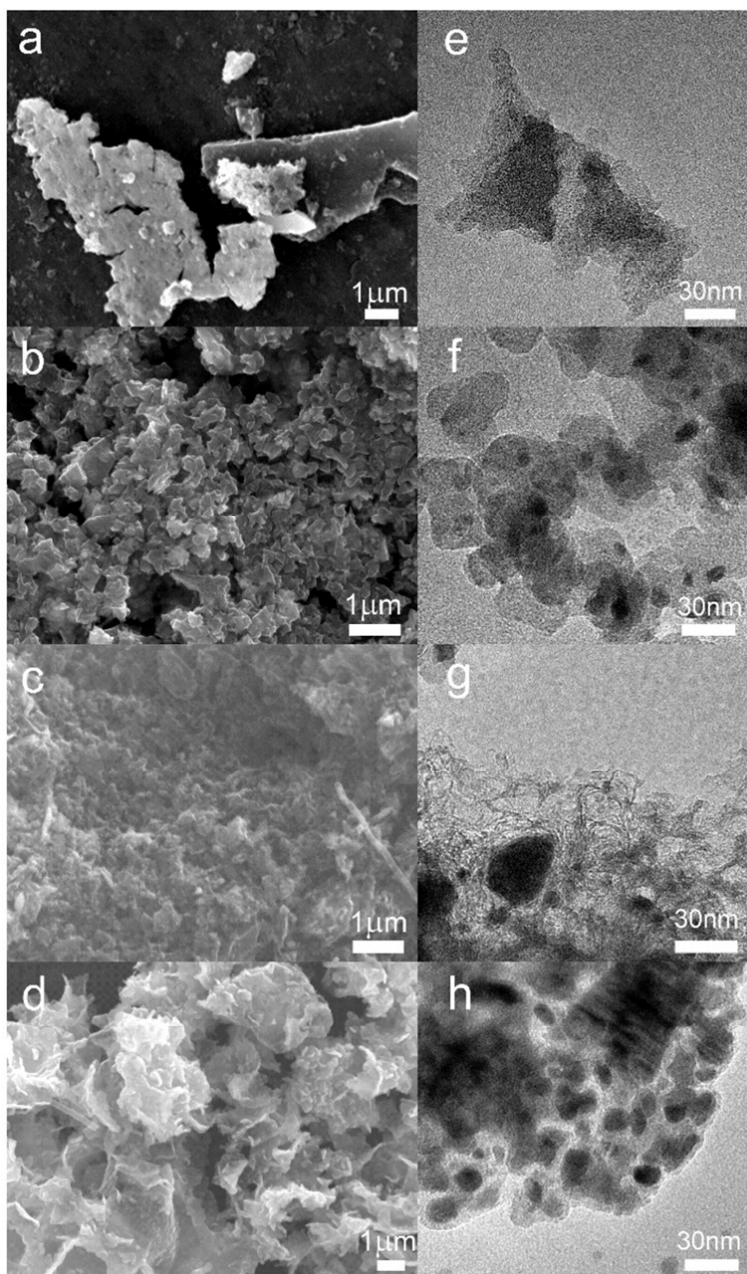
Figure 4. Scanning and transmission electron micrographs of (a, e) Mo_2C NS, (b, f) Mo_2C NP on a carbon support, (c, g) Fe_3C, and (d, h) Fe_5C_2.

The successful synthesis of Mo_2C NP on a carbon support was confirmed by TEM (Figure 4f and Figure A12). The particle size, D_{TEM}, was distributed between 10 and 50 nm, which is in agreement with the average crystallite size (D_{XRD} = 21 nm). The SEM images in Figure 4b and Figure A13 show a mesoporous morphology with a large surface area. The overall Mo_2C surface distribution is homogeneous as was confirmed by the SEM–EDX mapping (Figure A14). The carbon precursor in combination with the inert SiO_2 nanoparticles stimulates the spherical growth of nanosized Fe_3C particles and prevents it from forming larger aggregates. Most Fe_3C particles were between 40 and 60 nm. The Fe_3C sample contained nanosized hollow features as visible in Figure 4c,g and confirmed the successful removal of SiO_2 during the 1 M KOH treatment. The absence of the SiO_2 nanoparticles after the treatment was further supported by Fourier transform infrared spectroscopy (Figure A15).

Small and isolated Fe_5C_2 spherical nanoparticles with a narrow size distribution are observed in Figure 4d and Figure A16 (D_{TEM} is 5–35 nm and D_{XRD} is 11 nm). This highlights that PVP successfully stabilizes the nanoparticles from agglomeration during the carbothermal reduction of $Fe(CO)_5$. The material has a microporous structure (Figure A17b) with a high surface area because of the polymeric nature of the support. In contrast to the low Fe content measured in the first ~10 nm thick surface layer, well distributed and significant Fe concentrations were detected in the bulk surface layers (~1 μm) by SEM–EDX mapping (Figure A18), which supports the XPS depth profiling and ICP-OES results (Figure A8).

2.3.2 Electrochemical Characterization

The current-potential (*I–V*) relationship of each material was investigated by executing multiple CV cycles at a scan rate of 20 mV·s^{-1} in a N_2 presaturated electrolyte to estimate the onset potential and an expected potential window for the NRR. A possible pH dependency on the Mo_2C activity of the NRR was investigated by executing CV in 0.05 M H_2SO_4 (pH = 1), 0.5 M Li_2SO_4 (pH = 8.3), 0.1 M KOH (pH 13), and 1 M KOH (pH 14). The stability of Fe-carbides in acidic-to-neutral conditions is low as the material tends to dissolve.[63] Therefore, we decided to only use 0.1 M and 1 M KOH for the evaluation of the Fe-carbides. Mo_2C is generally stable in both acidic and alkaline environments, allowing CV measurements in all electrolytes.[58,64] The uncompensated resistance (R_u), measured with open-circuit electrochemical impedance spectroscopy was consistent for each material tested and ranged between 25 and 30 Ω for 0.1 M KOH, 3 and 4 Ω for 1 M KOH, 12 and 13 Ω for 0.5 M Li_2SO_4, and 24 Ω for 0.05 M H_2SO_4 (Figure A19). These quantities for Ru are below the acceptable range of the R_u compensator used for all electrochemical measurements.
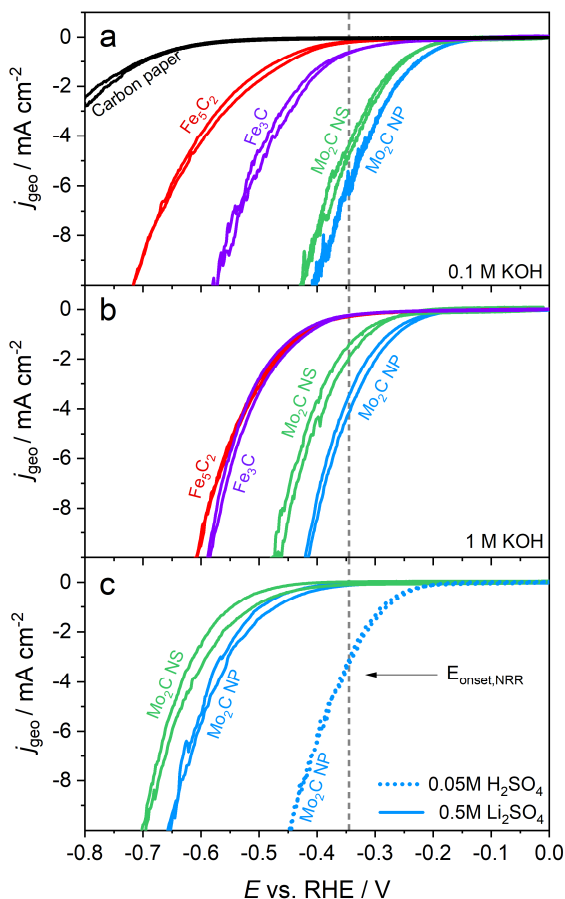
Figure 5. Cyclic voltammograms (6th cycle) at 20 mV·s^{-1} for Mo$_2$C NS (green), Mo$_2$C NP (blue), Fe$_3$C (purple), Fe$_5$C$_2$ (red), and carbon paper (black) in (a) 0.1 M KOH, (b) 1 M KOH, (c) 0.5 M Li$_2$SO$_4$, and 0.05 M H$_2$SO$_4$. The gray dotted line at −0.345 V vs. RHE represents the theoretically estimated onset potential for the NRR.

Figure 5 shows that all metal carbide I−V relationships in acidic, neutral, and alkaline conditions display an increase in with open-circuit electrochemical impedance spectroscopy was consistent for each material tested and ranged between 25 and 30 Ω for 0.1 M KOH, 3 and 4 Ω for 1 M KOH, 12 and 13 Ω for 0.5 M Li$_2$SO$_4$, and 24 Ω for 0.05 M H$_2$SO$_4$ (Figure A19). These quantities for R_u are below the acceptable range of the R_u compensator used for all electrochemical measurements. Figure 5 shows that all metal carbide I−V relationships in acidic, neutral, and alkaline conditions display an increase in current density at increasingly more negative potentials, characteristic for an HER I−V profile. Other distinctive reduction peaks that might be identified as the NRR were not observed in the voltammetry measurements. In addition to this, there was no indication of a metal oxide reduction peak

within the examined potential window, which suggests that the metal oxide surface layer is removed immediately. Mo_2C NP reaches higher current densities compared to Mo_2C NS at all pH values, which could be explained by a larger electrochemical surface area due to the mesoporous structure of Mo_2C NP. Another explanation might be the higher Mo_2C loading content in Mo_2C NP, since the ICP-OES analysis resulted in a higher concentration of elemental Mo in Mo_2C NP.

The onset potential is used to indicate the minimum activation potential of a redox reaction in cyclic voltammograms.[65] A theoretical approximation of the NRR onset potential in alkaline media can be calculated using the equilibrium potential and the activation overpotential. First-principles density functional theory calculations suggest that the minimum overpotential for the NRR is approximately −0.4 V, due to scaling relationships between intermediates.[2,66] The NRR equilibrium potential was calculated by equilibrium thermodynamics and is 0.054 V vs. RHE, which results in a minimum required onset potential (E_{onset}, NRR) of −0.35 V vs. RHE. Here, we estimated the experimental onset for different pH values by plotting the first derivative of the voltammogram (dj/dE) versus the applied potential (Figure A20). The lift-off point where the slope of the dj/dE curve starts to increase is set as the E_{onset}.

For 0.1 M and 1 M KOH, we do not see clear evidence for an alkaline pH effect for Mo_2C materials as both Mo_2C NP and NS have a similar I−V curve at both KOH concentrations. The onset potential for Mo_2C NP of −0.11 V vs. RHE is similar for both electrolytes and is in agreement with earlier observations.[64] Moreover, the onset potentials for Fe_3C and Fe_5C_2 are also similar and varied between −0.22 and −0.23 V vs. RHE for both 0.1 M and 1 M KOH. The I−V relationship in Figure 5c for Mo_2C in 0.5 M Li_2SO_4 is remarkably different showing a more negative onset potential of −0.28 V vs. RHE and −0.32 V vs. RHE for Mo_2C NP and NS, respectively. As a consequence, the activation overpotential at −10 mA·cm^{-2} for Mo_2C NP is −0.25 V lower than in alkaline conditions, which can be related to the low availability of either protons or hydroxide ions. At acidic conditions (pH = 1), Mo_2C NP displays a similar I−V relationship with respect to alkaline conditions, which highlights the unique properties of Mo_2C showing similar catalytic activity in both acidic and alkaline conditions.[64] However, the onset potential is slightly more negative (−0.17 V vs. RHE), indicating that the catalyst is more active in alkaline conditions.

E_{onset} for Mo_2C is above the theoretically estimated threshold in both acidic and alkaline pH, where the current density $E_{onset,NRR}$ is roughly −4 mA·cm^{-2} for Mo_2C NP. From this analysis, it is unlikely that the NRR is a dominant contributor to the I−V profile of Mo_2C because the HER kinetics are more facile in these conditions. Interestingly, E_{onset} for Mo_2C in 0.5 M Li_2SO_4 is below $E_{onset,NRR}$ and suggests that operating at near-neutral conditions might be ideal for the NRR. It is important to note that Cheng and coworkers reported high NH_3 yields with Mo_2C NS using the same electrolyte.[23] For Fe_3C and Fe_5C_2, the majority of the I−V profile exceeds $E_{onset,NRR}$, suggesting that both iron carbides might be promising catalysts for the NRR.

The NRR activity of the metal carbides was qualitatively screened by measuring the ammonia concentration after executing 40 scans of cyclic voltammetry with a scan rate of 20 mV s^{-1}. The results are summarized in Figure A21 and show that NH$_3$ concentrations for Mo$_2$C in acidic-neutral pH is close to the detection limit <30 ppb, while levels up to 100 ppb were observed in alkaline conditions. Operating at alkaline conditions is therefore more beneficial for studying the NRR, and subsequently, the main electrochemical experiments herein were performed in alkaline conditions.

To ultimately verify Mo- and Fe-carbides as conceivable NRR catalysts, a series of 2 h chronoamperometry (CA) measurements were performed at five different potentials in a N$_2$-saturated 0.1 M KOH electrolyte. The current densities for the metal carbides are stable in alkaline conditions as illustrated in Figure A22. As a comparison, two additional CA measurements in Ar-saturated electrolytes were performed with Mo$_2$C, which gave slightly higher current densities for two potentials. The difference in current density is however rather small and can be caused by slight variations in the experiments. This observation was also made elsewhere,[28] questioning the reliability of N$_2$ vs. Ar voltammetry and CA experiments as an initial indicator for successful dinitrogen reduction.

2.3.3 NRR Measurements

CA measurements were used to further assess the activity toward the NRR. After each CA, aliquots of both catholyte and anolyte were taken from the cell for further quantification of NH$_3$ and NO$_2^-$. The amount of quantified NH$_3$ after each experiment varied between 37 and 123 ppb with no particular trend linking ammonia concentration and applied potential over time. A 2 h open circuit potential (OCV) test with a N$_2$-saturated electrolyte was used to obtain insights on the amount of impurities coming from either the feed gas stream or surface adsorbed species inside the cell. The OCV results for Mo$_2$C reveal a similar NH$_3$ concentration as obtained with the chronoamperometry experiments. The impact of feed gas impurities can be excluded due to the installed certified gas filter (<100 ppt) in front of the cell. It is more likely that adsorbed NH$_3$ in the cell components is released during the OCV experiments and inevitably during the NRR measurements. Long term CA experiments with an Ar-saturated electrolyte are useful to study the possible release of N-impurities from the catalyst and other cell components exposed to the electrolyte under electrochemical conditions. For Mo$_2$C, three CA experiments with Ar-saturated electrolyte at −0.20, −0.31, and −0.44 V vs. RHE resulted in a somewhat lower NH$_3$ content (80, 53, and 60 ppb) compared to experiments with N$_2$-saturated electrolytes. Again, it is deemed unlikely that purified Ar (and N$_2$) introduces feed gas impurities. Therefore, this observation suggests that the Ar gas flowing through the electrolyte stripped a small part of the dissolved NH$_3$ from the electrolyte. Nevertheless, both the N$_2$ OCV and Ar CA experiments indicate that the majority of the quantified NH$_3$ is not from the NRR but originates from contaminations. Additional control experiments with ^{15}N$_2$-labeled gas were not performed since the observed NH$_3$ concentrations were below or approximating the background level.

Small quantities of NO_2^- were detected after all CA experiments, suggesting that a part of the quantified NH_3 potentially stems from NO_x reduction. Jiao and coworkers observed that the electrochemical reduction of NO_x forms multiple N-products, such as ammonia, hydroxylamine, N_2, and N_2O depending on the transition metal.[67] Pt is more selective toward NH_3, which was also supported by Koper and coworkers who made a similar observation for NO_3-electroreduction on Pt.[68] Mo_2C has similar noble metal-like properties as platinum;[69] therefore, it is reasonable to assume that NO_x species are reduced to ammonia at the investigated potentials. Fe_3C is also an efficient nitrate reduction electrocatalyst, where a previous study reported faradaic efficiencies (*FE*) higher than 90% to NH_3 at moderate reduction potentials.[70]
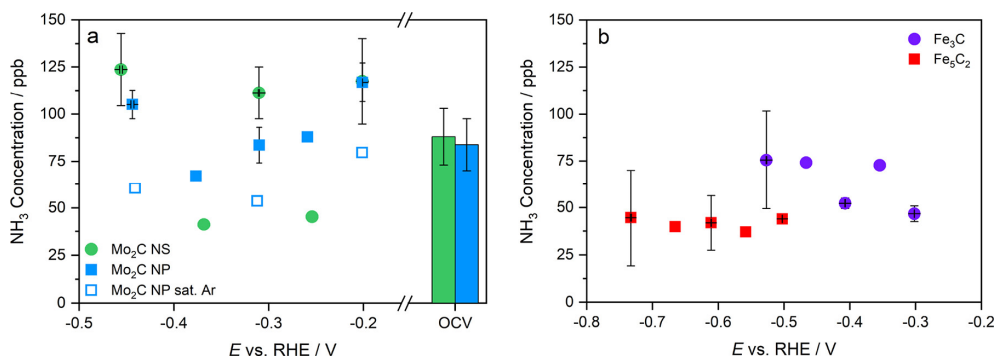
Figure 6. NH_3 concentration measured from the electrolyte after two hour CA experiments in 0.1 M KOH. (a) Mo_2C NS (green, spherical) and Mo_2C NP in N_2 (blue, rectangular) and Ar (open rectangular). (b) Fe_3C (purple, spherical) and Fe_5C_2 (red, rectangular). The data points with the error bars were done in duplicates.

Despite the thorough cleaning efforts for every part of the cell, a well-established background level of both NH_3 and NO_2^- was always observed after each experiment. We decided to analyze the removal efficiencies of our cleaning methods (elaborated in the caption of Figure A23) and found that NH_3 was sufficiently removed by simply rinsing with water. Surprisingly, significant quantities of released NO_2^- were detected that originated from the Celgard 3401 membrane, carbon paper, and Pt foil. This is a valuable observation, as two previous studies advised substituting the Nafion membrane with a microporous Celgard membrane to reduce NH_3 contaminations.[15,45] Our results indicate that NO_2^- is not only a surface adsorbed species but is also present in the inner membrane and carbon paper structure and is problematic to remove. Generally, the amount of released NO_2^- depends mainly on the exposed surface area, meaning that it can be lowered significantly by optimizing the cell design. Investigating the origin of the observed NO_x impurities is out of the scope of the present work and will be addressed in an upcoming study.[46]

2.3.4 Literature Comparison

Previous studies using Mo- and Fe-carbides as NRR electrocatalysts are shown in a comparative overview (Figure 7a), including our own observations. It becomes clear that both our Fe_3C and Fe_5C_2 quantified NH_3 yields are within the NH_3 background level. The Mo_2C catalysts exceed this threshold slightly, but with a significant NO_x background, it becomes unlikely that any nitrogen reduction to NH_3 occurred. The study of Cheng and coworkers outperformed our Mo_2C NS, observing a 240 times higher NH_3 yield.[23] This motivated us to execute a direct comparison by increasing the catalyst loading to 3 mg·cm⁻² and using 0.5 M Li_2SO_4. The chronoamperometry measurements were comparable, but our NH_3 concentrations were below 100 ppb and close to the earlier defined background level as displayed in Figure 6. This is additional proof that Mo_2C cannot be perceived as a promising NRR catalyst.

The majority of the earlier published literature observed orders of magnitude higher yields and FEs compared to this work. Firstly, all the literature studies shown in the overview did not quantify or consider NO_x as an influential factor on their measured NH_3 content. Secondly, the impurities in the feed gas stream were not removed by the installment of a certified gas filter. This is especially important when performing $^{15}N_2$-isotope labeled experiments as traces of ^{15}N-labeled impurities ($^{15}NH_3$ and $^{15}NO_x$) have been identified in several $^{15}N_2$-gas bottles.[15,25,71,72] Before using Li-based electrolytes for NRR experiments, Li-salts must be thermally annealed at 800 °C under inert conditions to remove trace levels (>1 ppm) of NO_x^- impurities.[47] We followed this procedure, while others, including Cheng et al., did not consider this extraneous source of impurities, and this might be one of the main factors contributing to their high NH_3 yields.[23,31,36] As final point, the Nafion membrane commonly applied in these studies is known for the uptake and release of NH_3 during electrochemical experiments.[15] Substituting the Nafion membrane with another membrane is not straightforward as we detected a significant amount of NO_2^- in the microporous membranes (Celgard 3401), but selecting a suitable treatment method is advised.[73]

Control experiments become even more essential when catalysts have a high N-content, such as metal nitrides, N-doped supports, or leftover NO_x/NH_3 traces from the catalyst synthesis. Evidence was found that for catalysts with a high N content, such as VN and Nb_4N_5, the decomposition of the N atomic lattice in acidic media released significant amounts of NH_4^+ during the initial stages of the electrochemical experiment.[28] Similar observations were also reported for Mo_2N.[30] Additionally, several commercially available metal oxide powders, such as Fe_2O_3 and Bi_2O_3, released a large amount of NO_x impurities. This eventually led to the retraction of a study, as it was proven that the origin of observed NH_3 was from NO_x reduction and not the NRR.[26,74] Therefore, we decided to analyze the N-content of all four materials by XPS and UV–Vis spectroscopy (method described in the SI). The N 1s spectra of Mo_2C could not be identified because of overlapping peak features with the Mo 3p orbital. Nevertheless, the absence of N KLL Auger peaks in both Mo_2C NS and NP XPS surveys (Figure A6a,b) indicate that the N-content might be negligible. Figure A7c,f shows two distinct N 1s

peaks for Fe_3C (398.3 and 399.9 eV) and Fe_5C_2 (398.9 and 400.1 eV), suggesting pyridinic N−C and pyrrolic N−C bonds from the precursor (4.5-dicyanoimidazole and PVP).[75] Nevertheless, the samples were exposed to air before XPS analysis, indicating that the peaks could be also from adventitious N species, such as −NH2, which have similar binding energies.[75–77] It is therefore challenging to assign these peaks to a specific N functional group. From the spectrophotometric analysis (Figure A25), directly performed after the material synthesis, it becomes clear that NH_3 impurities from an unidentifiable source were present in all catalysts (Mo_2C NS = 8.9 μmol_{NH_3} gcat^{-1}, Mo_2C NP = 16.5 μmol_{NH_3} gcat^{-1}, Fe_3C = 21.9 μmol_{NH_3} gcat^{-1}, Fe_5C_2 = 4.5 μmol_{NH_3} gcat^{-1}). This effect was suppressed by using a low catalyst loading (0.06 mg) for each experiment. In the case of the most contaminated sample, the expected release of NH_3 from 0.06 mg Fe_3C is limited to a negligible 1.3 nmol. Nevertheless, the NRR measurements performed with 3 mg Mo_2C NS did not result in an increase in the NH_3 concentration. It remains unlikely that impurities in the catalyst resulted in exceptionally high NH_3 yield reported by Cheng et al.[23] This suggests that other factors lead to their positive result.

The NH_3 partial current density, j_{NH_3}, is a useful performance indicator, wherein cases with j_{NH_3} smaller than 100 μA cm^{-1} are too low to be promising. From a back-of-the-envelope calculation, we estimated that the NH_3 concentration at j_{NH_3} = 100 μA cm^{-1} is in the 1 ppm order of magnitude range assuming typical parameters, such as A_{WE} = 1 cm^2, $V_{catholyte}$ = 20 mL, and t_{CP} = 1 h. These levels of NH_3 can easily be reached when the earlier mentioned sources of contamination are not identified or even considered. This has implications on the reliability and usefulness of reporting the FE, wherein the focus should be initially on j_{NH_3} or the NH_3 yield rate. From Figure 7b, it becomes clear that most literature studies did not exceed 100 μA cm^{-1}, while a FE > 20% was reported (see Table A4). Therefore, we suggest that future publications explicitly report the NH_3 partial current density as the main catalyst performance indicator.

Interestingly, the role of metal carbides is also under debate for hydrazine oxidation.[78] Fe−N−C catalysts are common used catalysts for this reaction and contain iron carbides because of the high temperature pyrolysis required for the synthesis. Early studies claimed that Fe_3C plays an active role in the reaction,[79,80] while a recent study revealed the true role of Fe_3C by executing a rigorous comparison study between Fe−N−C materials with different amounts of Fe_3C.[78] This approach led to the conclusion that Fe_3C is mostly inactive for hydrazine oxidation, and should be removed by nonoxidizing acid solutions. This is yet another example of how a rigorous and well-designed experimental procedure can aid in clarifying the activity of electrocatalysts for reactions in the nitrogen cycle.
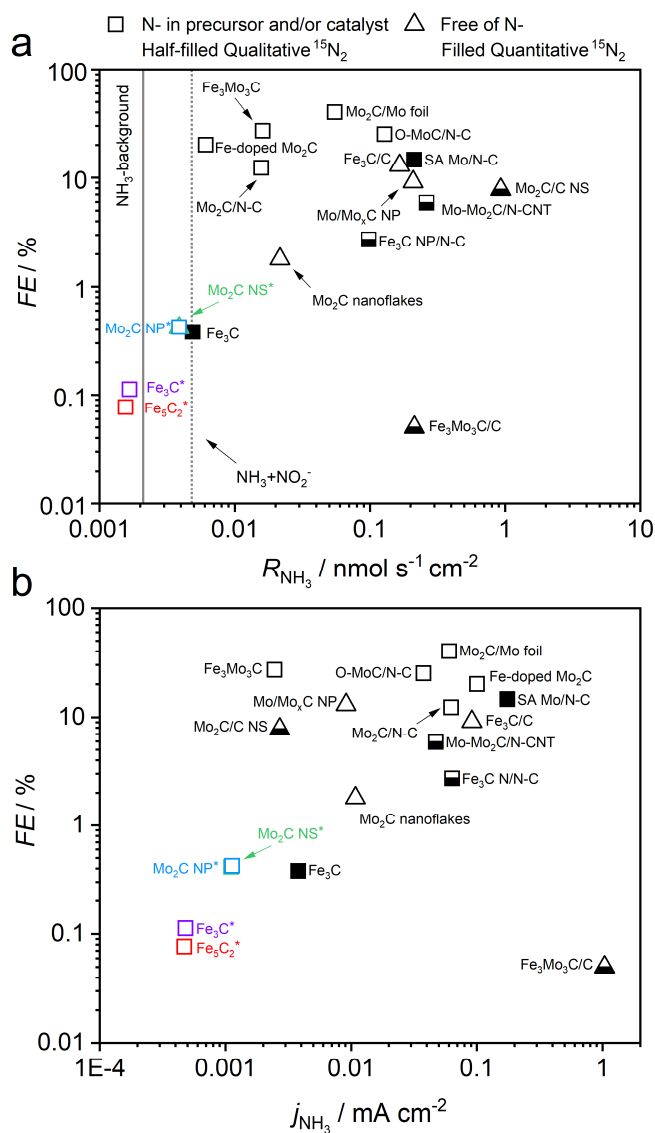
Figure 7. Literature overview of recently published NRR studies using Mo- and Fe-carbides as electrocatalysts differentiated by either high N-source in the support or used during synthesis (square) and free of N-source (triangular). The symbols are filled in case of quantitative $^{15}N_2$-labeled experiments and half-filled if analyzed qualitatively. Our own results are included as Mo_2C NS* (green), Mo_2C NP* (blue), Fe_3C* (purple), and Fe_5C_2* (red). (a) Faradaic efficiency vs. NH_3 yield with thick line (gray) indicates the estimated NH_3 background level and the dotted line presents a hypothetical background level including the measured NO_2^- from Figure A24. (b) Faradaic efficiency versus the j_{NH_3}. More details regarding the literature studies included in the figure can be found in Table A4.

2.4 Conclusion

Nanostructured molybdenum carbide and iron carbide were reported earlier as promising electrochemical nitrogen reduction catalysts. In this study, the NRR activity of both molybdenum and iron carbide materials were reassessed with the implementation of a strict experimental protocol that allowed us to reduce the effects of extraneous impurities to a bare minimum and identify false positives. The successful synthesis of nanostructured Mo_2C, Fe_3C, and Fe_5C_2 was confirmed by X-ray diffraction, scanning and transmission electron microscopy, and X-ray photoelectron and Mössbauer spectroscopy. The current–potential relationship of the metal carbides is characteristic for the HER, where the current increases with increasing negative overpotential. Moreover, specific reduction peaks that could be related to the NRR were not identified. NH_3 quantification was done after 40 scans of cyclic voltammetry, where we indeed measured NH_3 (50–100 ppb) for both Mo_2C and Fe_5C_2 in alkaline conditions. To further assess the NRR catalytic activity of molybdenum and iron carbides, we performed a series of 2 h chronoamperometry measurements at different potentials in N_2-saturated 0.1 M KOH. For Mo_2C NP and NS, the NH_3 concentration was between 41 and 124 ppb, exceeding the NH_3 background level (84–88 ppb) for potentials at −0.2, −0.31, and −0.46 V vs. RHE. We noticed that the yield earlier reported by Cheng et al. was considerable higher than measured with our Mo_2C NS.[23] A direct comparison by performing chronoamperometry experiments with an increased loading (3 mg cm^{-2}) and 0.5M Li_2SO_4 did not result in elevated NH_3 concentrations. This is additional proof that Mo_2C cannot be conceived as a promising NRR catalyst. The NO_x content after the NRR, Ar, and OCV blank tests revealed NO_2^- concentrations in the same order of magnitude (55–122 ppb). This implies that NH_3 arises from NO_2^- reduction and not from the NRR. These NO_2^- impurities originated from the Celgard membrane, since we found that the membrane, even after rinsing excessively with water, released a considerable amount of NO_2^- impurities (109 ± 31 ppb). This emphasizes the importance of NO_x monitoring, which is often overlooked in the literature and might result in a false positive. The quantified NH_3 from the iron carbide catalysts did not exceed the NH_3 background level, indicating that these materials are not active for the NRR. With our experimental approach, we succeeded in establishing a minimized and reproducible background level that allowed us to critically assess promising NRR catalysts. We believe that our methods and detailed analysis will equip researchers entering the field with clear guidelines to perform NRR experiments in a more reliable manner.

2.5 References

2

1 MacLeod, K. C.; Holland, P. L. Recent developments in the homogeneous reduction of dinitrogen by molybdenum and iron. *Nature Chemistry* **2013**, *5* (7), 559-565.

2 Van Der Ham, C. J. M.; Koper, M. T. M.; Hetterscheid, D. G. H. Challenges in reduction of dinitrogen by proton and electron transfer. *Chemical Society Reviews* **2014**, *43* (15), 5183-5191.

3 Rösch, B.; Gentner, T.; Langer, J.; Färber, C.; Eyselein, J.; Zhao, L.; Ding, C.; Frenking, G.; Harder, S. Dinitrogen complexation and reduction at low-valent calcium. *Science* **2021**, *371* (6534), 1125-1128.

4 Zhu, X.; Zhang, W.; Chen, H.; Mo, J. Impacts of nitrogen deposition on soil nitrogen cycle in forest ecosystems: A review. *Acta Ecologica Sinica* **2015**, *35* (3), 35-43.

5 Nørskov, J. C., J.; Miranda, R.; Fitzsimmons, T.; Stack, R. Sustainable Ammonia Synthesis –Exploring the scientific challenges associated with discovering alternative, sustainable processes for ammonia production. U.S. Department of Energy: Dulles, Virginia, 2016.

6 Ritchie, H. R., M. *CO and Greenhouse Gas Emissions*. Our World in Data, 2020. https://ourworldindata.org/co2-and-other-greenhouse-gas-emissions. (accessed 2022 31 of March).

7 Greenlee, L. F.; Renner, J. N.; Foster, S. L. The Use of Controls for Consistent and Accurate Measurements of Electrocatalytic Ammonia Synthesis from Dinitrogen. *ACS Catalysis* **2018**, *8* (9), 7820-7827.

8 MacFarlane, D. R.; Cherepanov, P. V.; Choi, J.; Suryanto, B. H. R.; Hodgetts, R. Y.; Bakker, J. M.; Ferrero Vallana, F. M.; Simonov, A. N. A Roadmap to the Ammonia Economy. *Joule* **2020**, 1-20.

9 Kyriakou, V.; Garagounis, I.; Vasileiou, E.; Vourros, A.; Stoukides, M. Progress in the Electrochemical Synthesis of Ammonia. *Catalysis Today* **2017**, *286*, 2-13.

10 Wang, M.; Khan, M. A.; Mohsin, I.; Wicks, J.; Ip, A. H.; Sumon, K. Z.; Dinh, C.-T.; Sargent, E. H.; Gates, I. D.; Kibria, M. G. Can sustainable ammonia synthesis pathways compete with fossil-fuel based Haber–Bosch processes? *Energy & Environmental Science* **2021**, *14* (5), 2535-2548.

11 Fernandez, C. A.; Hortance, N. M.; Liu, Y.-H.; Lim, J.; Hatzell, K. B.; Hatzell, M. C. Opportunities for intermediate temperature renewable ammonia electrosynthesis. *Journal of Materials Chemistry A* **2020**, *8* (31), 15591-15606.

12 Zhou, F.; Azofra, L. M.; Ali, M.; Kar, M.; Simonov, A. N.; McDonnell-Worth, C.; Sun, C.; Zhang, X.; Macfarlane, D. R. Electro-synthesis of ammonia from nitrogen at ambient temperature and pressure in ionic liquids. *Energy and Environmental Science* **2017**, *10* (12), 2516-2520.

13 Suryanto, B. H. R.; Kang, C. S. M.; Wang, D.; Xiao, C.; Zhou, F.; Azofra, L. M.; Cavallo, L.; Zhang, X.; Macfarlane, D. R. Rational Electrode-Electrolyte Design for Efficient Ammonia Electrosynthesis under Ambient Conditions. *ACS Energy Letters* **2018**, *3* (6), 1219-1224.

14 König, M.; Vaes, J.; Klemm, E.; Pant, D. Solvents and Supporting Electrolytes in the Electrocatalytic Reduction of CO2. *iScience* **2019**, *19*, 135-160.

15   Andersen, S. Z.; Čolić, V.; Yang, S.; Schwalbe, J. A.; Nielander, A. C.; McEnaney, J. M.; Enemark-Rasmussen, K.; Baker, J. G.; Singh, A. R.; Rohr, B. A.; et al. A rigorous electrochemical ammonia synthesis protocol with quantitative isotope measurements. *Nature* **2019**, *570* (7762), 504-508.

16   Suryanto, B. H. R.; Wang, D.; Azofra, L. M.; Harb, M.; Cavallo, L.; Jalili, R.; Mitchell, D. R. G.; Chatti, M.; MacFarlane, D. R. MoS 2 Polymorphic Engineering Enhances Selectivity in the Electrochemical Reduction of Nitrogen to Ammonia. *ACS Energy Letters* **2019**, *4* (2), 430-435.

17   Einsle, O.; Tezcan, F. A.; Andrade, S. L. A.; Schmid, B.; Yoshida, M.; Howard, J. B.; Rees, D. C. Nitrogenase MoFe-Protein at 1.16 Å Resolution: A Central Ligand in the FeMo-Cofactor. *Science* **2002**, *297* (5587), 1696-1700.

18   Michalsky, R.; Zhang, Y. J.; Medford, A. J.; Peterson, A. A. Departures from the adsorption energy scaling relations for metal carbide catalysts. *Journal of Physical Chemistry C* **2014**, *118* (24), 13026-13034.

19   Matanovic, I.; Garzon, F. H. Nitrogen electroreduction and hydrogen evolution on cubic molybdenum carbide: A density functional study. *Physical Chemistry Chemical Physics* **2018**, *20* (21), 14679-14687.

20   Li, Q.; Qiu, S.; He, L.; Zhang, X.; Sun, C. Impact of H-termination on the nitrogen reduction reaction of molybdenum carbide as an electrochemical catalyst. *Physical Chemistry Chemical Physics* **2018**, *20* (36), 23338-23343.

21   Du, H.-L.; Hodgetts, R. Y.; Chatti, M.; Nguyen, C. K.; Macfarlane, D. R.; Simonov, A. N. Is Molybdenum Disulfide Modified with Molybdenum Metal Catalytically Active for the Nitrogen Reduction Reaction? *Journal of The Electrochemical Society* **2020**, *167* (14), 146507-146507.

22   Du, H.; Yang, C.; Pu, W.; Zeng, L.; Gong, J. Enhanced Electrochemical Reduction of N 2 to Ammonia over Pyrite FeS_2 with Excellent Selectivity. *ACS Sustainable Chemistry & Engineering* **2020**, *8* (28), 10572-10580.

23   Cheng, H.; Ding, L. X.; Chen, G. F.; Zhang, L.; Xue, J.; Wang, H. Molybdenum Carbide Nanodots Enable Efficient Electrocatalytic Nitrogen Fixation under Ambient Conditions. *Advanced Materials* **2018**, *30* (46), 1-7.

24   Peng, M.; Qiao, Y.; Luo, M.; Wang, M.; Chu, S.; Zhao, Y.; Liu, P.; Liu, J.; Tan, Y. Bioinspired $Fe_3C@C$ as Highly Efficient Electrocatalyst for Nitrogen Reduction Reaction under Ambient Conditions. *ACS Applied Materials and Interfaces* **2019**, *11* (43), 40062-40068.

25   Choi, J.; Suryanto, B. H. R.; Wang, D.; Du, H. L.; Hodgetts, R. Y.; Ferrero Vallana, F. M.; MacFarlane, D. R.; Simonov, A. N. Identification and elimination of false positives in electrochemical nitrogen reduction studies. *Nature Communications* **2020**, *11* (1), 1-10.

26   Chen, Y.; Liu, H.; Ha, N.; Licht, S.; Gu, S.; Li, W. Revealing nitrogen-containing species in commercial catalysts used for ammonia electrosynthesis. *Nature Catalysis* **2020**, 1-7.

27   Choi, J.; Choi, J.; Du, H. L.; Du, H. L.; Nguyen, C. K.; Nguyen, C. K.; Suryanto, B. H. R.; Simonov, A. N.; Simonov, A. N.; MacFarlane, D. R.; et al. Electroreduction of Nitrates, Nitrites, and Gaseous Nitrogen Oxides: A Potential Source of Ammonia in Dinitrogen Reduction Studies. *ACS Energy Letters* **2020**, *5* (6), 2095-2097.

28   Du, H. L.; Gengenbach, T. R.; Hodgetts, R.; Macfarlane, D. R.; Simonov, A. N. Critical Assessment of the Electrocatalytic Activity of Vanadium and Niobium Nitrides toward Dinitrogen Reduction to Ammonia. *ACS Sustainable Chemistry and Engineering* **2019**, *7* (7), 6839-6850.

29   Yu, W.; Buabthong, P.; Read, C. G.; Dalleska, N. F.; Lewis, N. S.; Lewerenz, H.-J.; Gray, H. B.; Brinkert, K. Cathodic NH_4^+ leaching of nitrogen impurities in CoMo thin-film electrodes in aqueous acidic solutions. **2020**. *4* (10), 5080-5087.

30   Hu, B.; Hu, M.; Seefeldt, L.; Liu, T. L. Electrochemical dinitrogen reduction to ammonia by Mo2N: catalysis or decomposition? *ACS Energy Letters* **2019**, *4* (5), 1053-1054.

31   Qin, B.; Li, Y.; Zhang, Q.; Yang, G.; Liang, H.; Peng, F. Understanding of nitrogen fixation electro catalyzed by molybdenum–iron carbide through the experiment and theory. *Nano Energy* **2020**, *68*, 104374.

32   Zhang, Y.; Hu, J.; Zhang, C.; Cheung, A. T. F.; Zhang, Y.; Liu, L.; Leung, M. K. H. Mo2C embedded on nitrogen-doped carbon toward electrocatalytic nitrogen reduction to ammonia under ambient conditions. *International Journal of Hydrogen Energy* **2021**, *46* (24), 13011-13019.

33   Ba, K.; Wang, G.; Ye, T.; Wang, X.; Sun, Y.; Liu, H.; Hu, A.; Li, Z.; Sun, Z. Single Faceted Two-Dimensional Mo 2 C Electrocatalyst for Highly Efficient Nitrogen Fixation. **2020**. *10* (14), 7864-7870.

34   Liu, Y.; Zhu, X.; Zhang, Q.; Tang, T.; Zhang, Y.; Gu, L.; Li, Y.; Bao, J.; Dai, Z.; Hu, J. S. Engineering Mo/Mo2C/MoC hetero-interfaces for enhanced electrocatalytic nitrogen reduction. *Journal of Materials Chemistry A* **2020**, *8* (18), 8920-8926.

35   Wang, T.; Kou, Z.; Zhang, J.; Wang, H.; Zeng, Y. J.; Wei, S.; Zhang, H. Boosting Faradic efficiency of dinitrogen reduction on the negatively charged Mo sites modulated via interstitial Fe doping into a Mo2C nanowall catalyst. *Chemical Engineering Journal* **2021**, *417*, 127924-127924.

36   Qu, X.; Shen, L.; Mao, Y.; Lin, J.; Li, Y.; Li, G.; Zhang, Y.; Jiang, Y.; Sun, S. Facile Preparation of Carbon Shells-Coated O-Doped Molybdenum Carbide Nanoparticles as High Selective Electrocatalysts for Nitrogen Reduction Reaction under Ambient Conditions. *ACS Applied Materials & Interfaces* **2019**, *11* (35), 31869-31877.

37   Cong, L.; Yu, Z.; Liu, F.; Huang, W. Electrochemical synthesis of ammonia from N_2 and H $_2$O using a typical non-noble metal carbon-based catalyst under ambient conditions. *Catal. Sci. Technol* **2019**, *9*, 1208-1208.

38   Biswas, A.; Bhardwaj, S.; Boruah, T.; Dey, R. S. Electrochemical ammonia synthesis: Fundamental practices and recent developments in transition metal boride, carbide and nitride-class of catalysts. *Materials Advances* **2022**, 3, 5207.

39   Gómez-Marín, A. M.; Ticianelli, E. A. Analysis of the electrocatalytic activity of α-molybdenum carbide thin porous electrodes toward the hydrogen evolution reaction. *Electrochimica Acta* **2016**, *220*, 363-372.

40   Kraupner, A.; Markus, A.; Palkovits, R.; Schlicht, K.; Giordano, C. Mesoporous Fe3C sponges as magnetic supports and as heterogeneous catalyst. *Journal of Materials Chemistry* **2010**, *20* (29), 6019-6022.

2

41   Snovski, R.; Grinblat, J.; Sougrati, M. T.; Jumas, J. C.; Margel, S. Synthesis and characterization of iron, iron oxide and iron carbide nanostructures. *Journal of Magnetism and Magnetic Materials* **2014**, *349*, 35-44.

42   Klencsar, Z. Mössbauer spectrum analysis by evolution algorithm. *Nuclear Instruments and Methods in Physics Research Section B: Beam Interactions with Materials and Atoms* **1997**, *129* (4), 527-533.

43   Kuhl, K. P.; Cave, E. R.; Abram, D. N.; Jaramillo, T. F. New insights into the electrochemical reduction of carbon dioxide on metallic copper surfaces. *Energy & Environmental Science* **2012**, *5* (5), 7050-7059.

44   Cai, X.; Iriawan, H.; Yang, F.; Luo, L.; Shen, S.; Shao-Horn, Y.; Zhang, J. Interaction of Ammonia with Nafion and Electrolyte in Electrocatalytic Nitrogen Reduction Study. *The Journal of Physical Chemistry Letters* **2021**, *12* (29), 6861-6866.

45   Liu, H.; Zhang, Y.; Luo, J. The removal of inevitable NOx species in catalysts and the selection of appropriate membrane for measuring electrocatalytic ammonia synthesis accurately. *Journal of Energy Chemistry* **2020**, *49* (x), 51-58. DOI: 10.1016/j.jechem.2020.01.029.

46   Izelaar, B.; Ripepi, D.; van Noordenne, D. D.; Jungbacker, P.; Kortlever, R.; Mulder, F. M. Determining sources of NO_x and NH_3 impurities and removal strategies for reliable electrochemical NRR. *In Submission* **2022**.

47   Li, L.; Tang, C.; Yao, D.; Zheng, Y.; Qiao, S. Z. Electrochemical Nitrogen Reduction: Identification and Elimination of Contamination in Electrolyte. **2019**, *4* (9), 2111-2116.

48   Weatherburn, M. W. Phenol-Hypochlorite Reaction for Determination of Ammonia. *Analytical Chemistry* **1967**, *39* (8), 971-974.

49   Kyotani, T.; Nagai, T.; Inoue, S.; Tomita, A. Formation of new type of porous carbon by carbonization in zeolite nanochannels. *Chemistry of materials* **1997**, *9* (2), 609-615.

50   Kim, J. H.; Ju, H.; An, B.-S.; An, Y.; Cho, K.; Kim, S. H.; Bae, Y.-S.; Yoon, H. C. Comparison between Fe2O3/C and Fe3C/Fe2O3/Fe/C Electrocatalysts for N2 Reduction in an Alkaline Electrolyte. *ACS Applied Materials & Interfaces* **2021**, acsami.1c20807-acsami.20801c20807.

51   Kniep, B.; Constantinescu, A.; Niemeier, D.; Becker, K. D. An in-situ Mössbauer study of the formation of cementite, Fe_3C. *Zeitschrift fur Anorganische und Allgemeine Chemie* **2003**, *629* (10), 1795-1804.

52   Muxworthy, A. R.; Schmidbauer, E.; Petersen, N. Magnetic properties and Mössbauer spectra of urban atmospheric particulate matter: A case study from Munich, Germany. *Geophysical Journal International* **2002**, *150* (2), 558-570.

53   Kuivila, C. S.; Butt, J. B.; Stair, P. C. Characterization of surface species on iron synthesis catalysts by X-ray photoelectron spectroscopy. *Applied Surface Science* **1988**, *32* (1-2), 99-121.

54   Malina, O.; Jakubec, P.; Kašlík, J.; Tuček, J.; Zbořil, R. A simple high-yield synthesis of high-purity Hägg carbide (χ-Fe_5C_2) nanoparticles with extraordinary electrochemical properties. *Nanoscale* **2017**, *9* (29), 10440-10446.

2

55   Goya, G. F.; Berquó, T. S.; Fonseca, F. C.; Morales, M. P. Static and dynamic magnetic properties of spherical magnetite nanoparticles. *Journal of Applied Physics* **2003**, *94* (5), 3520-3528.

56   Choi, J. G.; Choi, D.; Thompson, L. T. Surface properties of high-surface-area powder and thin film molybdenum nitrides treated in H2 and H2S. *Applied Surface Science* **1997**, *108* (1), 103-111.

57   Wan, C.; Regmi, Y. N.; Leonard, B. M. Multiple phases of molybdenum carbide as electrocatalysts for the hydrogen evolution reaction. *Angewandte Chemie* **2014**, *126* (25), 6525-6528.

58   Seh, Z. W.; Fredrickson, K. D.; Anasori, B.; Kibsgaard, J.; Strickler, A. L.; Lukatskaya, M. R.; Gogotsi, Y.; Jaramillo, T. F.; Vojvodic, A. Two-Dimensional Molybdenum Carbide (MXene) as an Efficient Electrocatalyst for Hydrogen Evolution. *ACS Energy Letters* **2016**, *1* (3), 589-594.

59   Saji, V. S.; Lee, C. W. Molybdenum, molybdenum oxides, and their electrochemistry. *ChemSusChem* **2012**, *5* (7), 1146-1161.

60   Nishimoto, M.; Muto, I.; Sugawara, Y.; Hara, N. Morphological Characteristics of Trenching around MnS Inclusions in Type 316 Stainless Steel: The Role of Molybdenum in Pitting Corrosion Resistance. *Journal of The Electrochemical Society* **2019**, *166* (11), C3081-C3089.

61   Biesinger, M. C.; Payne, B. P.; Grosvenor, A. P.; Lau, L. W. M.; Gerson, A. R.; Smart, R. S. C. Resolving surface chemical states in XPS analysis of first row transition metals, oxides and hydroxides: Cr, Mn, Fe, Co and Ni. *Applied Surface Science* **2011**, *257* (7), 2717-2730.

62   Townsend, H. E. Potential-pH diagrams at elevatedtemperature for the system Fe-H2O. *Corrosion Science* **1970**, *10* (5), 343-358.

63   Xu, W.; Street, S. R.; Amri, M.; Mosselmans, J. F. W.; Quinn, P. D.; Rayment, T.; Davenport, A. J. In-Situ Synchrotron Studies of the Effect of Nitrate on Iron Artificial Pits in Chloride Solutions. *Journal of The Electrochemical Society* **2015**, *162* (6), C243-C250.

64   Vrubel, H.; Hu, X. Molybdenum boride and carbide catalyze hydrogen evolution in both acidic and basic solutions. *Angewandte Chemie - International Edition* **2012**, *51* (51), 12703-12706.

65   Bard, A. J.; Inzelt, G.; Scholz, F. *Electrochemical dictionary*; Springer, 2012.

66   Skúlason, E.; Bligaard, T.; Gudmundsdóttir, S.; Studt, F.; Rossmeisl, J.; Abild-Pedersen, F.; Vegge, T.; Jónsson, H.; Nørskov, J. K. A theoretical evaluation of possible transition metal electro-catalysts for N2 reduction. *Physical Chemistry Chemical Physics* **2012**, *14* (3), 1235-1245.

67   Ko, B. H.; Hasa, B.; Shin, H.; Zhao, Y.; Jiao, F. Electrochemical Reduction of Gaseous Nitrogen Oxides on Transition Metals at Ambient Conditions. *Journal of the American Chemical Society* **2022**, *144* (3), 1258-1266.

68   Dima, G. E.; De Vooys, A. C. A.; Koper, M. T. M. Electrocatalytic reduction of nitrate at low concentration on coinage and transition-metal electrodes in acid solutions. *Journal of Electroanalytical Chemistry* **2003**, *554-555* (1), 15-23.

69   Zheng, W.; Cotter, T. P.; Kaghazchi, P.; Jacob, T.; Frank, B.; Schlichte, K.; Zhang, W.; Su, D. S.; Schüth, F.; Schlögl, R. Experimental and theoretical investigation of

molybdenum carbide and nitride as catalysts for ammonia decomposition. *Journal of the American Chemical Society* **2013**, *135* (9), 3458-3464.

70 Wang, Y.; Zhang, L.; Niu, Y.; Fang, D.; Wang, J.; Su, Q.; Wang, C. Boosting NH3 production from nitrate electroreduction via electronic structure engineering of Fe_3C nanoflakes. *Green Chemistry* **2021**, *23* (19), 7594-7608.

71 Hodgetts, R. Y.; Du, H. L.; MacFarlane, D. R.; Simonov, A. N. Electrochemically Induced Generation of Extraneous Nitrite and Ammonia in Organic Electrolyte Solutions During Nitrogen Reduction Experiments. *ChemElectroChem* **2021**, *2*, 1-10.

72 Dabundo, R.; Lehmann, M. F.; Treibergs, L.; Tobias, C. R.; Altabet, M. A.; Moisander, P. H.; Granger, J. The Contamination of Commercial $^{15}N_2$ Gas Stocks with ^{15}N–Labeled Nitrate and Ammonium and Consequences for Nitrogen Fixation Measurements. *PLOS ONE* **2014**, *9* (10), e110335-e110335.

73 Hanifpour, F.; Sveinbjörnsson, A.; Canales, C. P.; Skúlason, E.; Flosadóttir, H. D. Preparation of Nafion Membranes for Reproducible Ammonia Quantification in Nitrogen Reduction Reaction Experiments. *Angewandte Chemie International Edition* **2020**, *59* (51), 22938-22942.

74 Licht, S.; Cui, B.; Wang, B.; Li, F.-F.; Lau, J.; Liu, S. Ammonia synthesis by N2 and steam electrolysis in molten hydroxide suspensions of nanoscale Fe2O3. *Science* **2014**, *345* (6197), 637-640.

75 Hueso, J. L.; Espinós, J. P.; Caballero, A.; Cotrino, J.; González-Elipe, A. R. XPS investigation of the reaction of carbon with NO, O_2, N_2 and H_2O plasmas. *Carbon* **2007**, *45* (1), 89-96.

76 Chastain, J.; King Jr, R. C. Handbook of X-ray photoelectron spectroscopy. *Perkin-Elmer Corporation* **1992**, *40*, 221.

77 Bertóti, I. Characterization of nitride coatings by XPS. *Surface and Coatings Technology* **2002**, *151-152*, 194-203.

78 Burshtein, T. Y.; Aias, D.; Wang, J.; Sananis, M.; Farber, E. M.; Gazit, O. M.; Grinberg, I.; Eisenberg, D. Fe–N–C electrocatalysts in the oxygen and nitrogen cycles in alkaline media: the role of iron carbide. *Physical Chemistry Chemical Physics* **2021**, *23* (47), 26674-26679.

79 Wu, Z. Y.; Xu, X. X.; Hu, B. C.; Liang, H. W.; Lin, Y.; Chen, L. F.; Yu, S. H. Iron carbide nanoparticles encapsulated in mesoporous Fe-N-doped carbon nanofibers for efficient electrocatalysis. *Angewandte Chemie* **2015**, *127* (28), 8297-8301.

80 Jiang, W.-J.; Gu, L.; Li, L.; Zhang, Y.; Zhang, X.; Zhang, L.-J.; Wang, J.-Q.; Hu, J.-S.; Wei, Z.; Wan, L.-J. Understanding the high activity of Fe–N–C electrocatalysts in oxygen reduction: Fe/Fe3C nanoparticles boost the activity of Fe–N x. *Journal of the American Chemical Society* **2016**, *138* (10), 3570-3578.

Appendix A

Appendix Figures
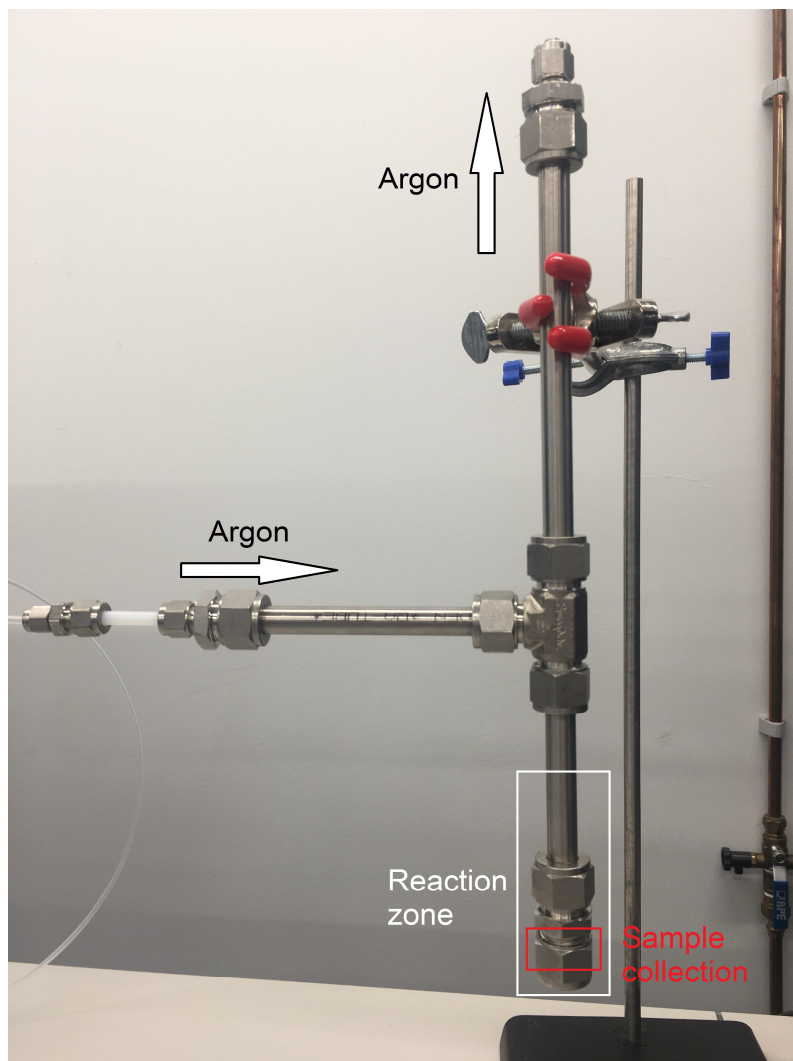
Figure A1. Homemade gas-tight reaction chamber from Swagelock stainless steel tubes and adapters for the synthesis of χ-Fe$_5$C$_2$. Polyvinylpyrrolidone was mixed with iron(0) pentacarbonyl in the reaction zone as indicated. After the thermal-decomposition process, the reactor was depressurized and the sample was collected from the bottom part of the reactor.
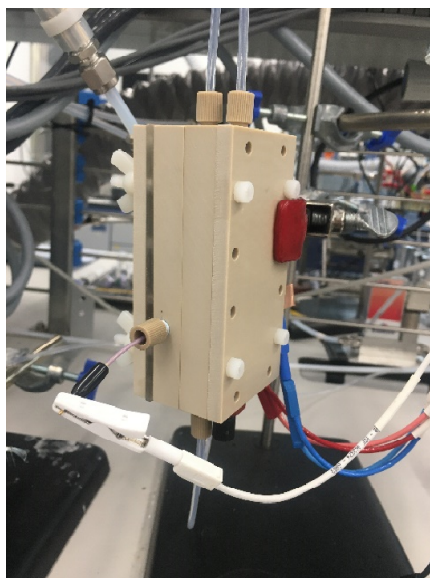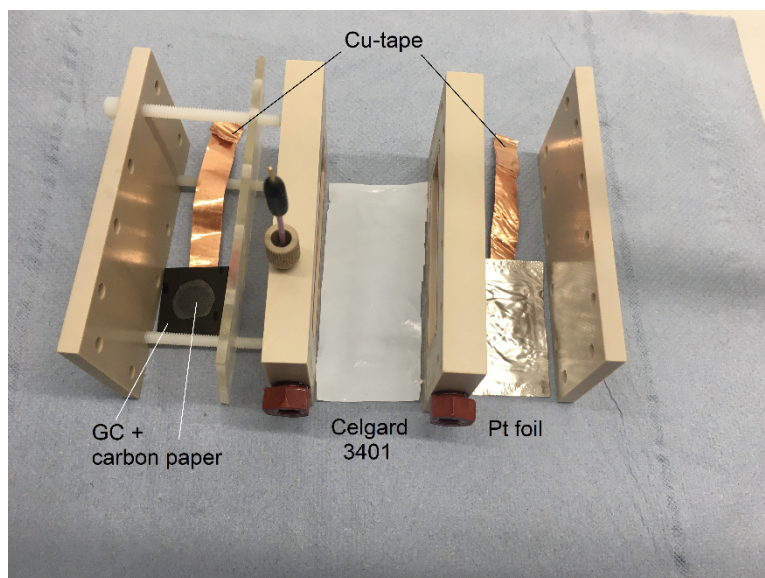
Figure A2. (top) Photograph of the PEEK cell body adapted from the Jaramillo group and its components.[1] (bottom) The assembled cell connected to the potentiostat.
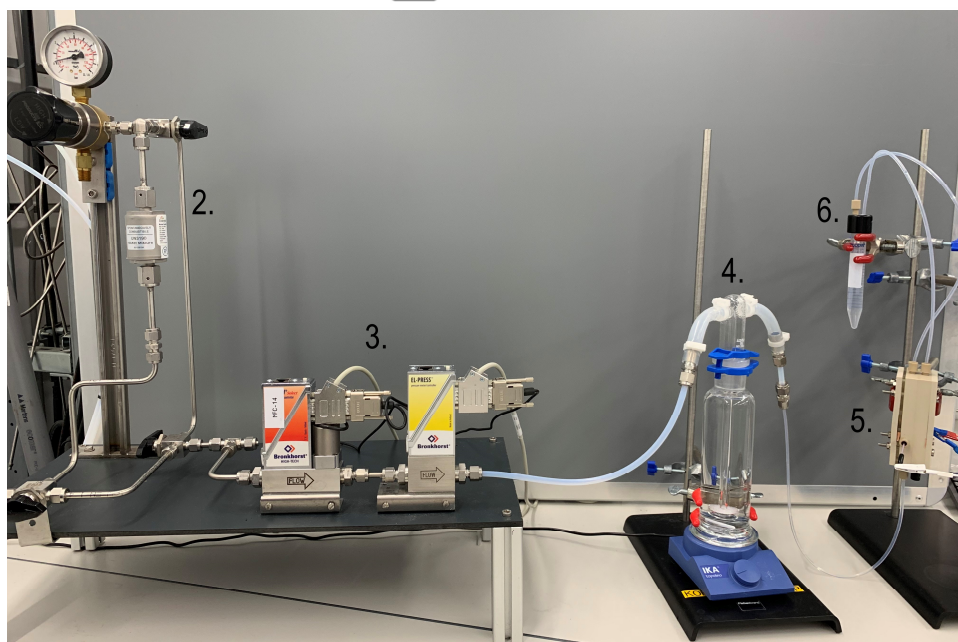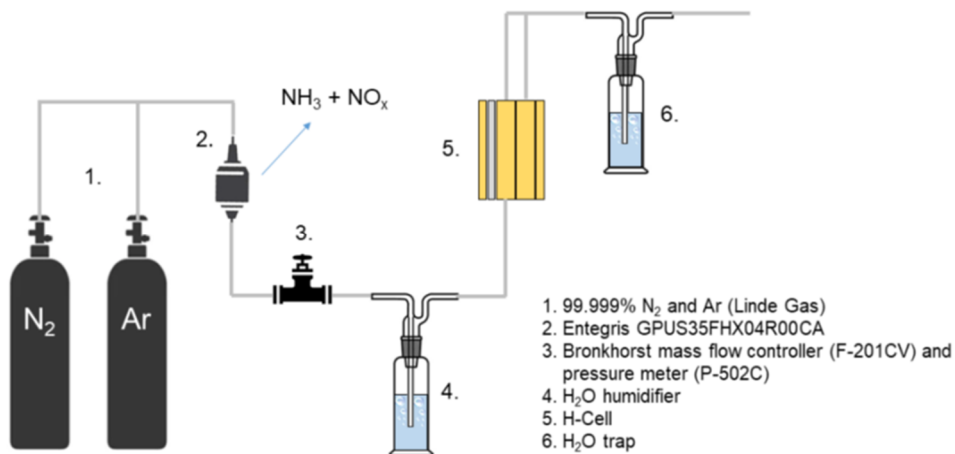
Figure A3. Photograph of the experimental setup including enumerated labels (bottom) and an explanatory schematic (top).
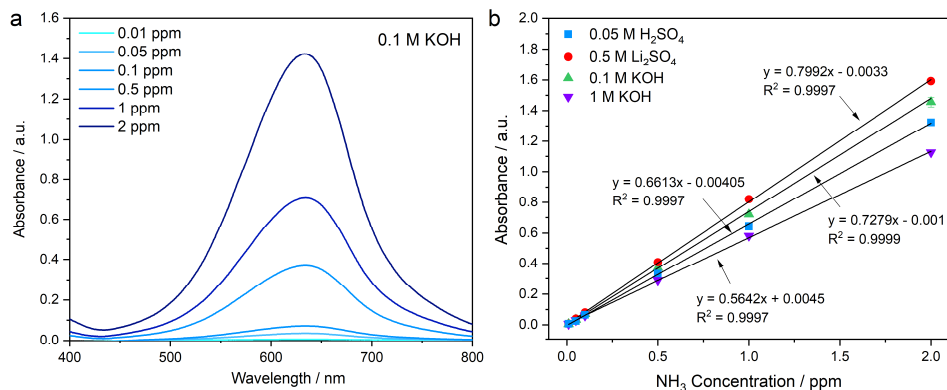
Figure A4. (a) UV-Vis spectra of 0 – 2 ppm NH_3 concentrations in 0.1 M KOH with a maximum absorbance at 633 nm, and is also representative for other pH. (b) NH_3 calibration lines for 0.05 M H_2SO_4, 0.5 M Li_2SO_4, 0.1 M KOH and 1 M KOH, where 0.1 M KOH is performed in duplicates.
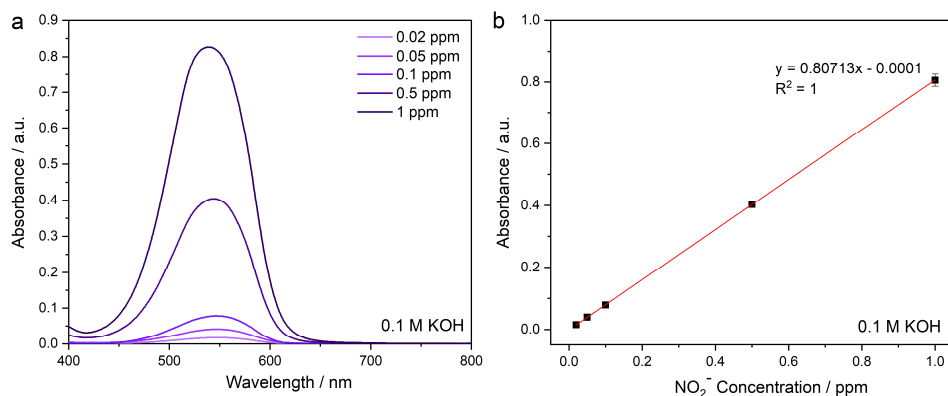
Figure A5. (a) UV-Vis spectra of 0 – 1 ppm NO_2^- concentrations in 0.1 M KOH with a maximum absorbance at 544 nm. (b) NO_2^- calibration line in 0.1 M KOH done in duplicates.
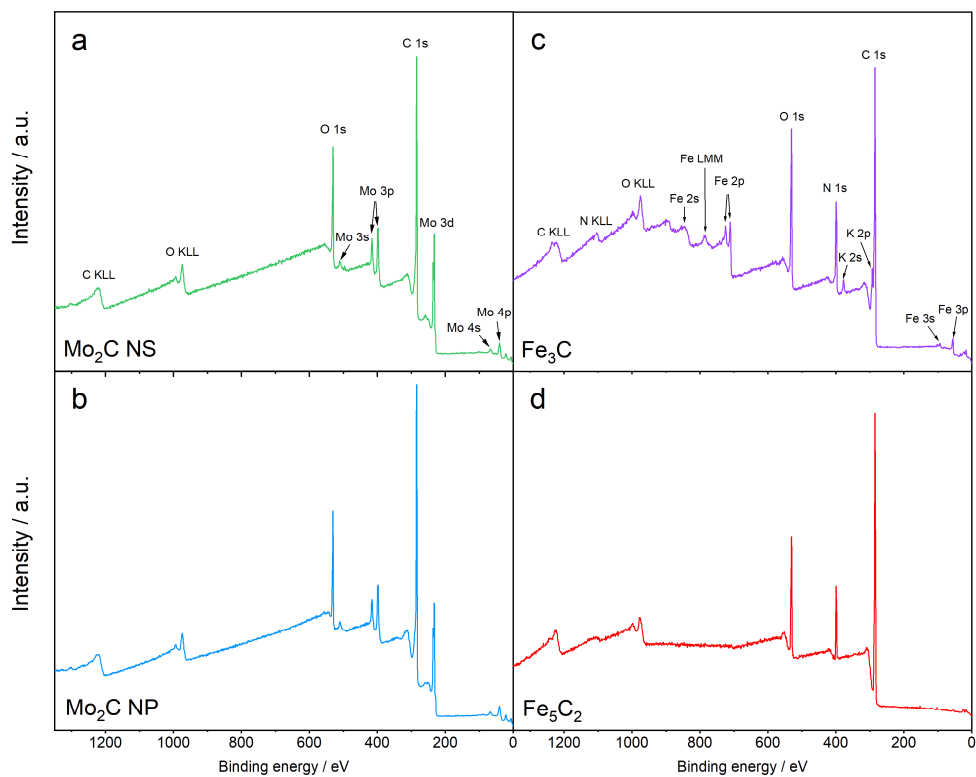
Figure A6. XPS survey of (a) Mo_2C NS, (b) Mo_2C NP, (c) Fe_3C and (d) Fe_5C_2 with peak allocation including auger peaks. The peaks were identified by the CasaXPS v2.3 database and ref [2].
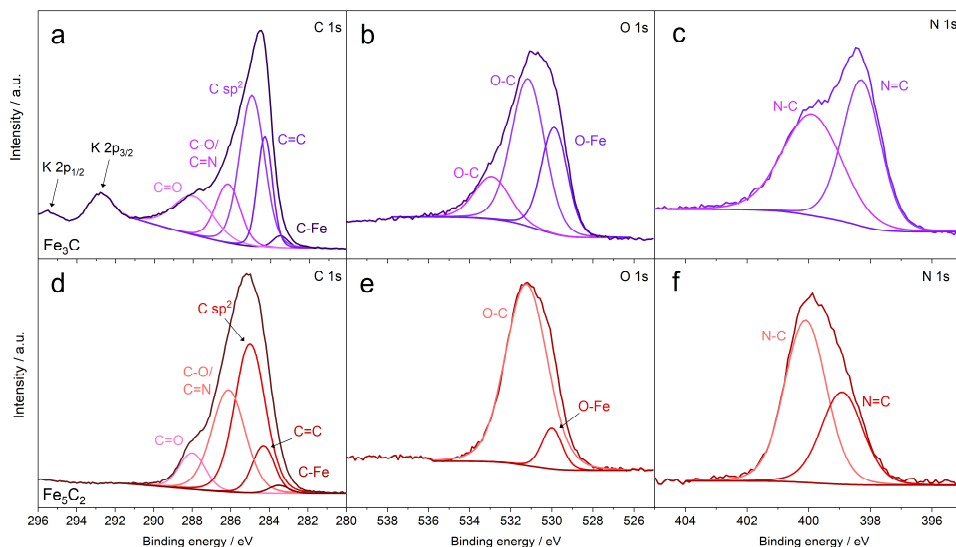
Figure A7. XPS spectra (a,d) C 1s, (b,e) O 1s, (c,f) N 1s of Fe_3C (purple) and Fe_5C_2 (red). Similar features as for the Mo_2C spectra, such as the absence of a clear carbide peak between 283-284 eV in the C 1s spectra and the identification of a Fe-oxide peak in the O 1s spectra due to air exposure. Two additional peaks in (a) at 292.8 eV and 295.5 eV were identified as K $2p_{1/2}$ and K $2p_{3/2}$, which are residual from the KOH wash.
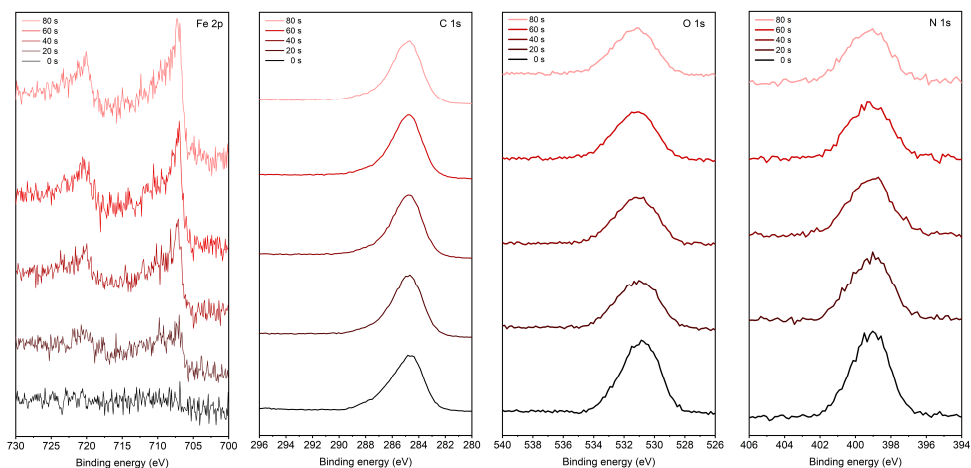
Figure A8. XPS depth profiling of Fe_5C_2 by in situ Ar^+ etching.
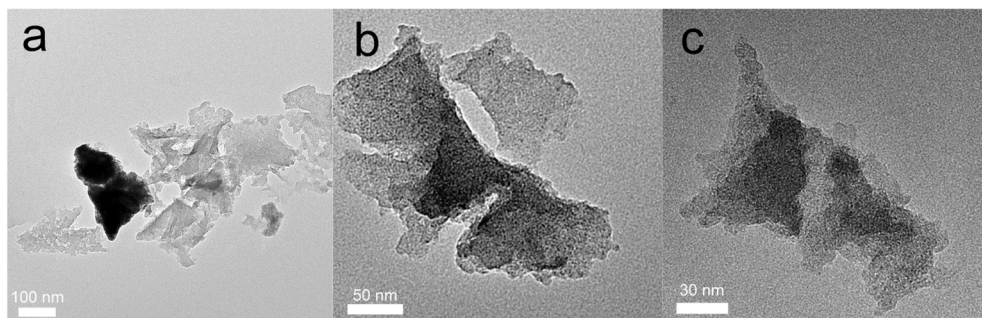
Figure A9. Transmission electron micrographs of various Mo$_2$C NS at different magnifications.
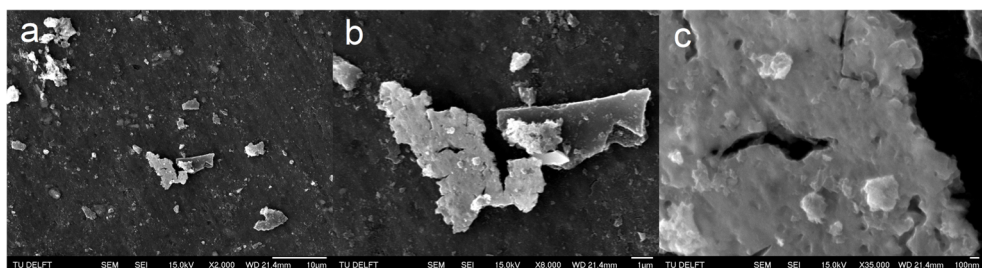
Figure A10. Scanning electron micrographs of one particular Mo$_2$C NS at different magnifications.
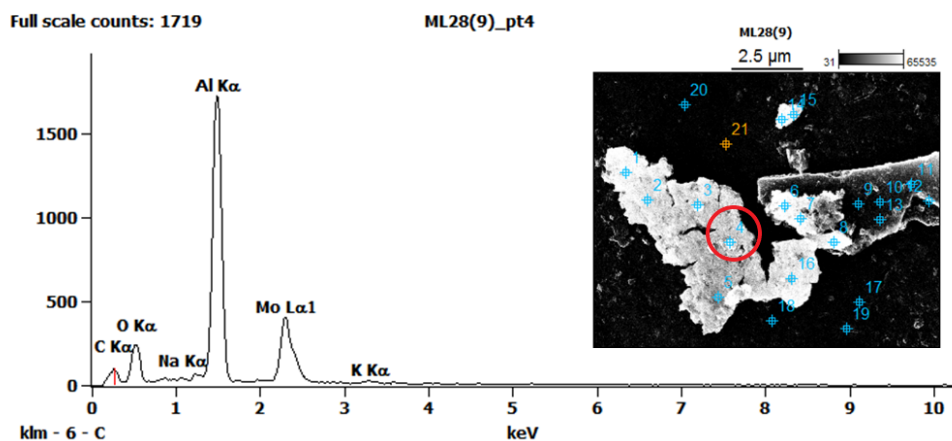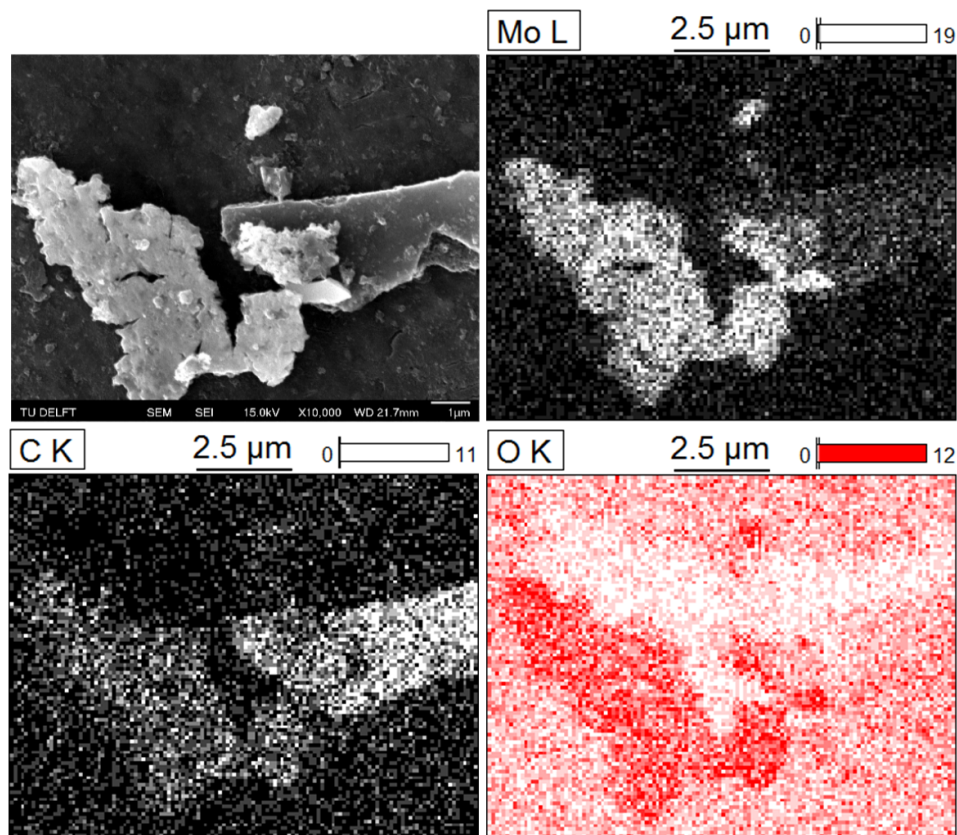
Figure A11. Energy-dispersive X-ray spectroscopy analysis of a Mo$_2$C NS. The spectra obtained by the point and shoot method at location 4 indicate a C, O and Mo peak at 0.28, 0.53 and 2.29 keV, respectively. The large peak at 1.49 keV is identified as the Al background signal from the supporting disc.
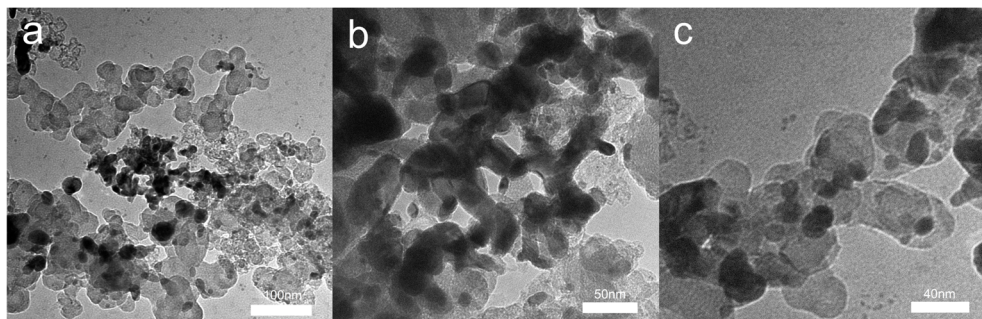
Figure A12. Transmission electron micrographs of Mo$_2$C NP anchored on a carbon support at different magnifications.
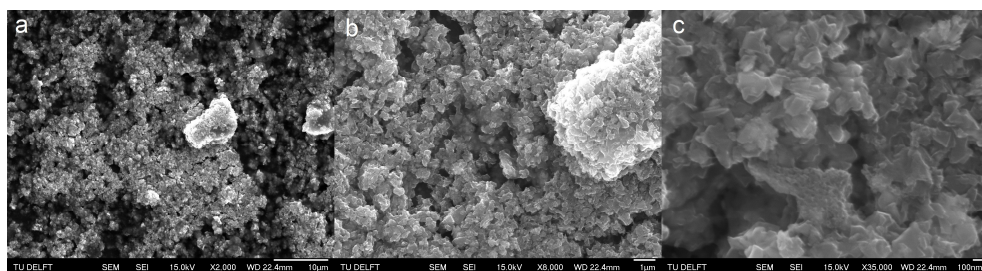
Figure A13. Scanning electron micrographs of the supported Mo$_2$C NP at different magnifications.
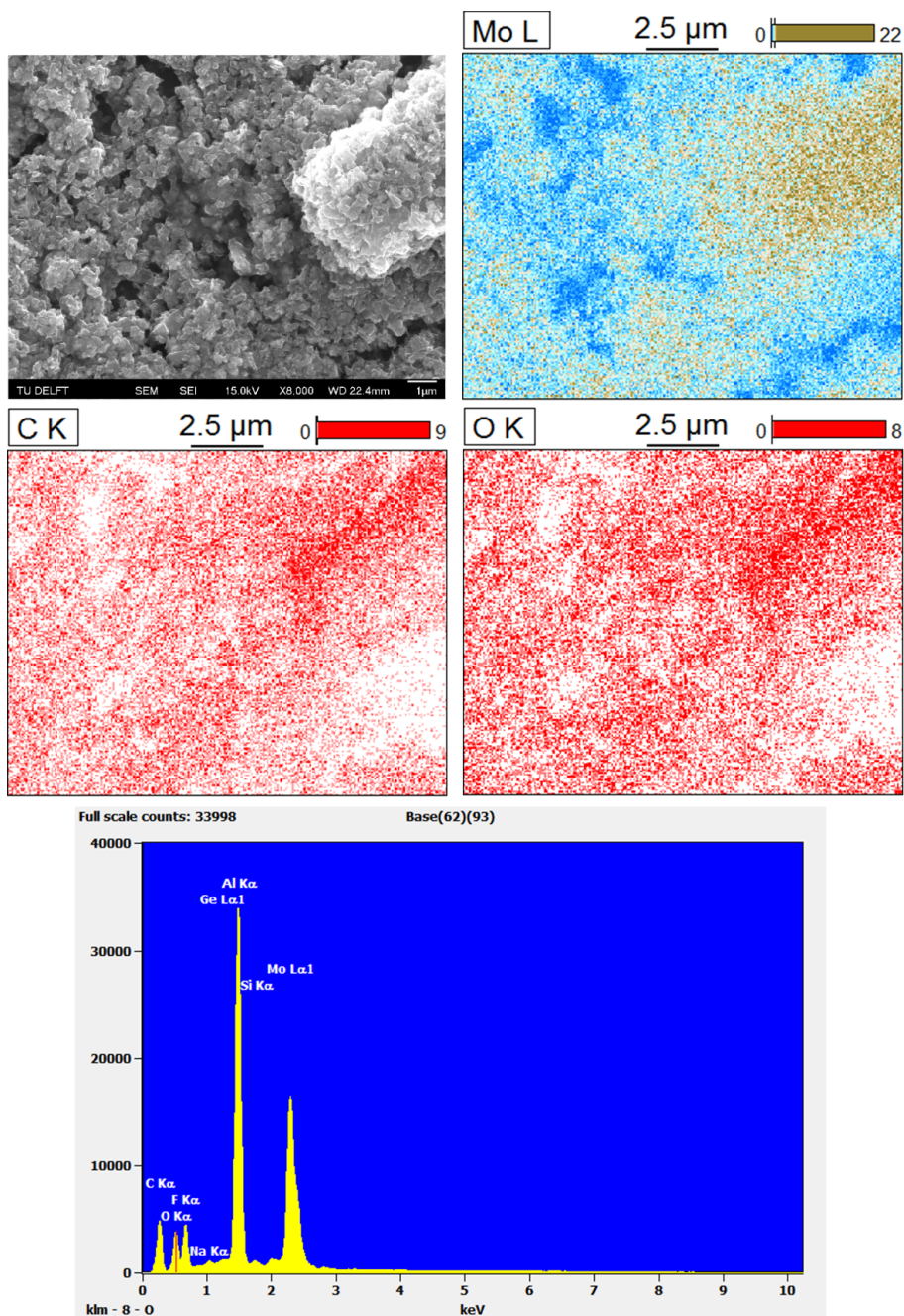
Figure A14. Energy-dispersive X-ray element mapping and spectra of Mo$_2$C NP. The EDX peaks at 0.28, 0.53 and 2.29 keV are assigned to C, O and Mo. The feature between 0.6-0.7 keV might be identified as F, but its origin remains unclear. The large peak at 1.49 keV is identified as the Al background signal from the supporting disc.
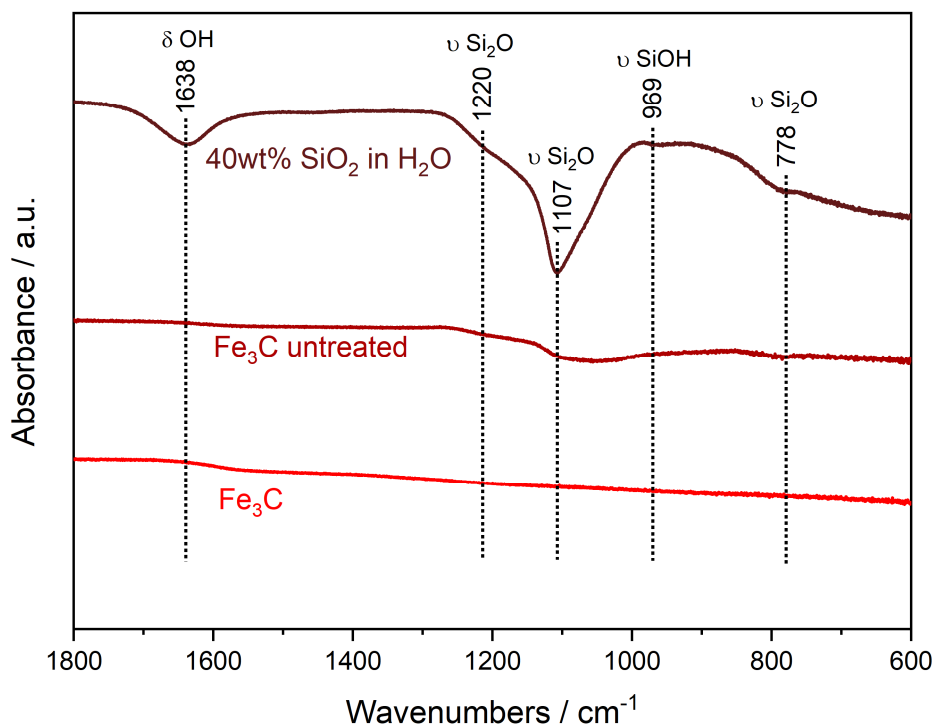
Figure A15. Attenuated total reflectance Fourier transform infrared (ATR-FTIR) spectroscopy was performed with a Thermo Scientific Nicolet iS50 FTIR spectrometer. The recorded spectra are 40wt% SiO_2 in H_2O (wine) as reference, Fe_3C without alkaline treatment (maroon) and Fe_3C treated with 1 M KOH (red). The shoulder feature at 1220 cm^{-1} and 1107 cm^{-1} from the reference spectra are both seen as asymmetric Si-O-Si stretching. Another small feature at 778 cm^{-1} is symmetric Si-O-Si stretching.[3] The spectra of the untreated Fe_3C is slightly bend in these regions and suggests the presence of the SiO_2 colloidal particles in the Fe_3C after the carburization procedure. The treated Fe_3C (red) did not show characteristic Si peaks, meaning that the Si phase was successfully removed.
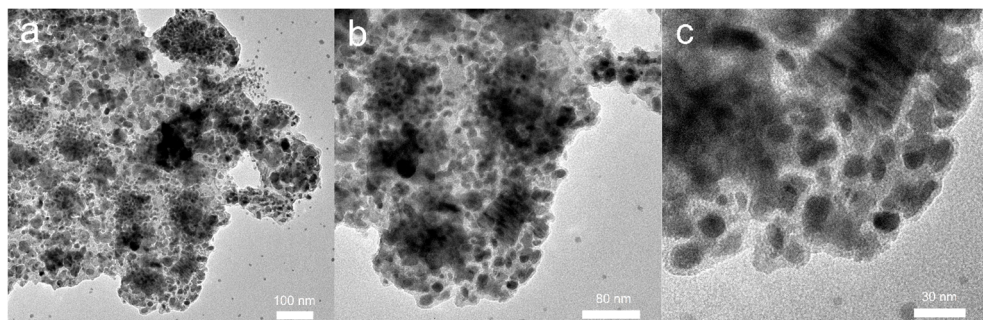
Figure A16. Transmission electron micrographs of Fe$_5$C$_2$ nanoparticles with increasing magnification from left to right.
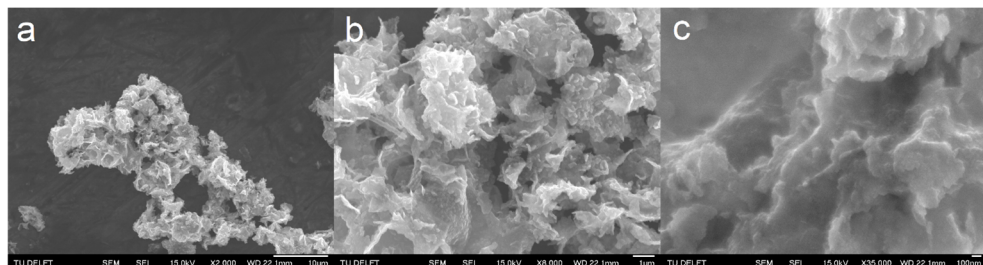
Figure A17. Scanning electron micrographs of Fe$_5$C$_2$ at different magnifications.
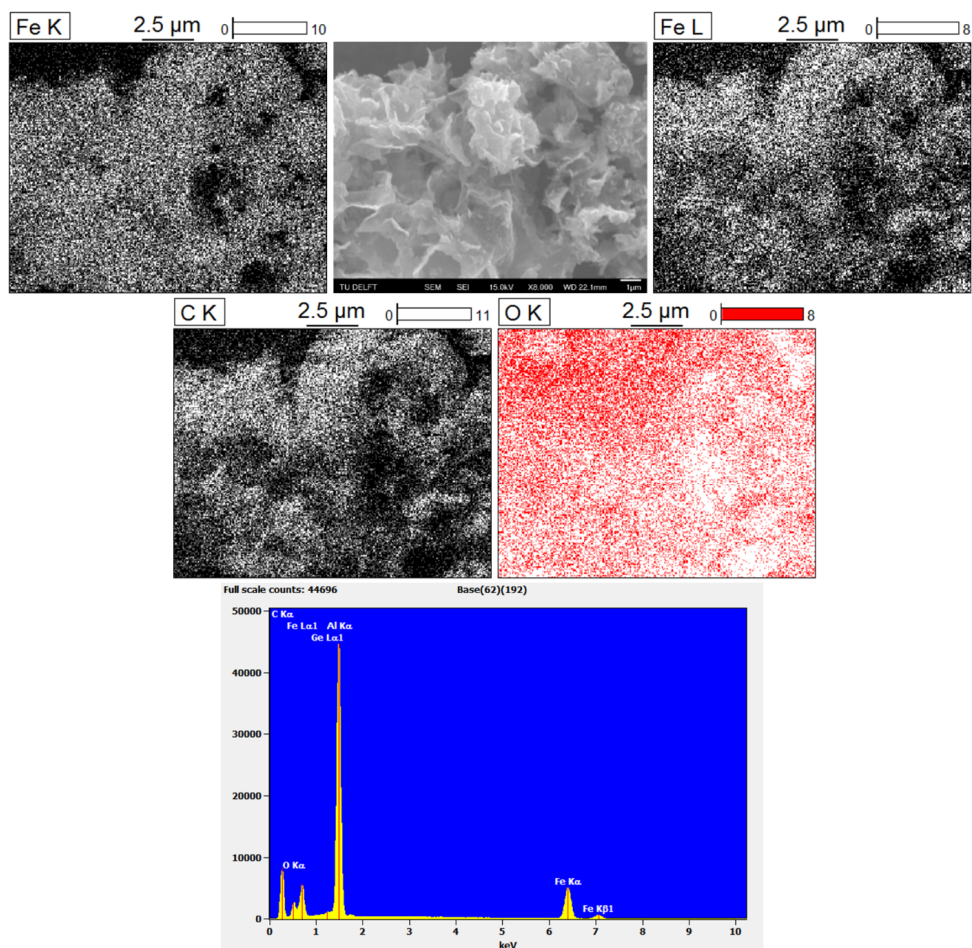
Figure A18. Energy-dispersive X-ray element mapping and spectra of Fe_5C_2. The spectra peaks between 0-1 keV are identified as C, O and Fe. Both the mapping and spectra show a sufficient distribution of Fe throughout the sample, which suggests that only the surface layer of materials contains a low quantity of Fe as observed by XPS. The large peak at 1.49 keV is identified as the Al background signal from the supporting disc.
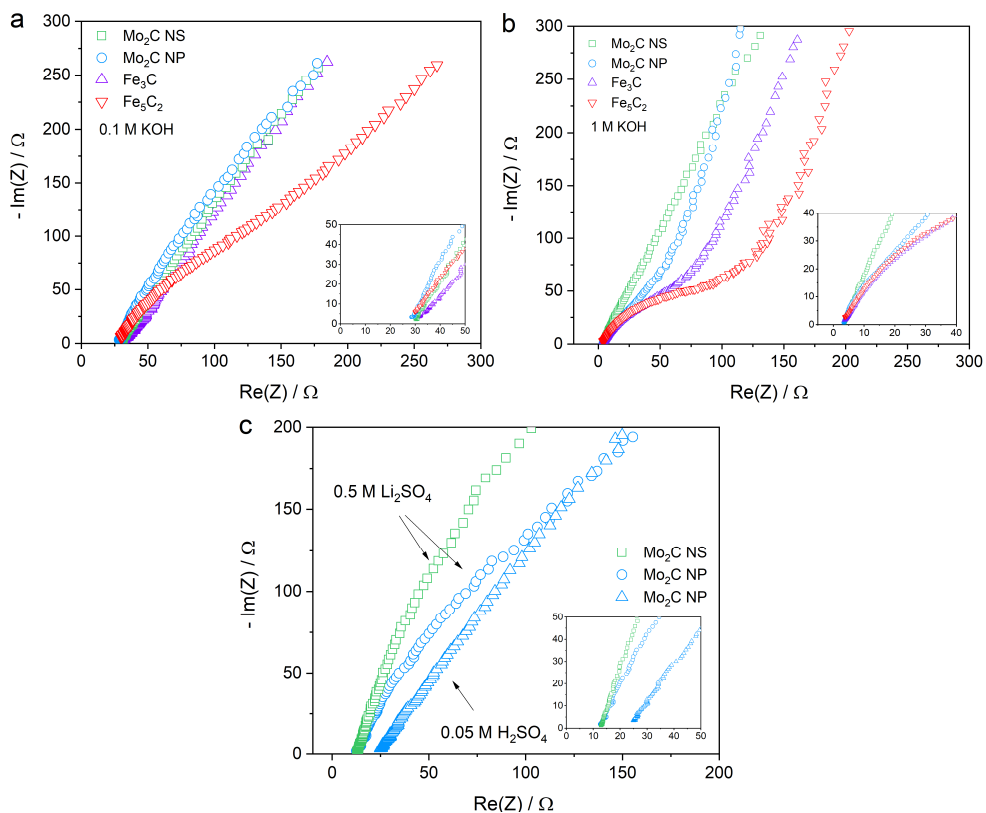
Figure A19. Nyquist plots at carried out at open-circuit conditions for different metal carbides and electrolytes, where R_u is estimated as the intersection with the Zreal axes. (a) 0.1 M KOH with R_u for Mo$_2$C NS = 30.1 Ω, Mo$_2$C NP = 28.4 Ω, Fe$_3$C = 30.8 Ω, Fe$_5$C$_2$ = 29.8 Ω; (b) 1 M KOH with R_u for Mo$_2$C NS = 3.6 Ω, Mo$_2$C NP = 3.4 Ω, Fe$_3$C = 3.6 Ω, Fe$_5$C$_2$ = 3.7 Ω; (c) 0.5 M Li$_2$SO$_4$ with R_u for Mo$_2$C NS = 12.8 Ω, Mo$_2$C NP = 12.6 Ω,; 0.05 M H$_2$SO$_4$ with R_u for Mo$_2$C NP = 25.0 Ω.
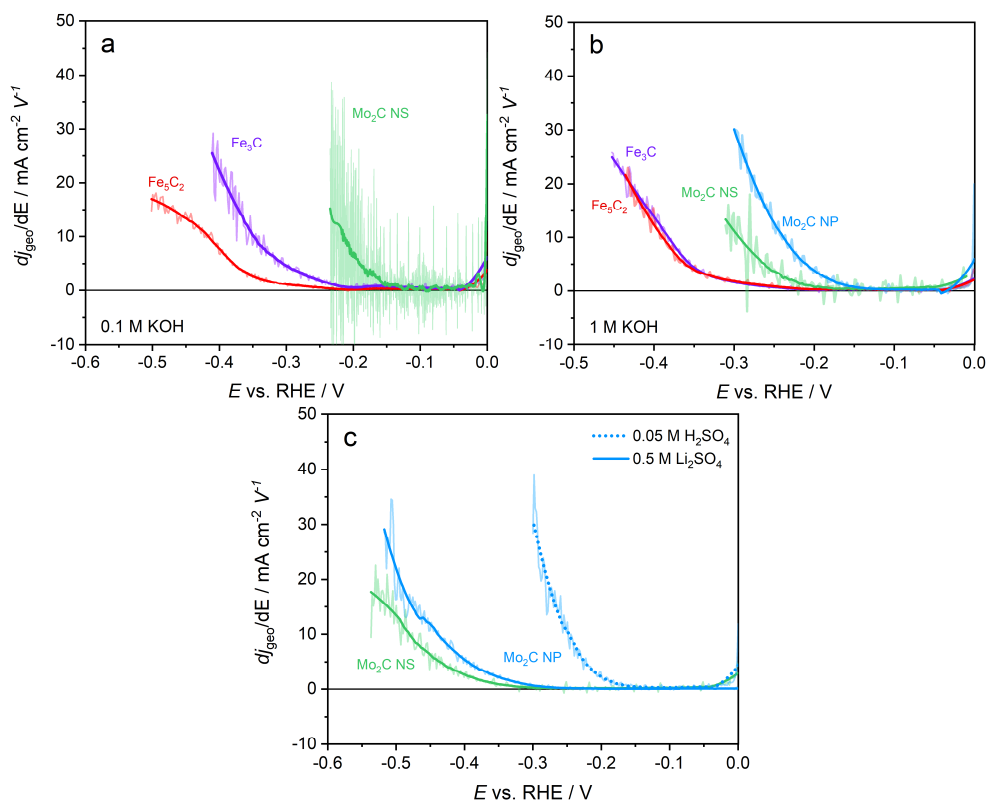
Figure A20. First derivative plot (dj/dE) vs. E of the cyclic voltammograms in **Figure 5**. The derivative was calculated with a build-in function in OriginPro. The derivative curves are plotted close to the onset potential (E_{onset}) region and show a significant level of noise, where we fitted an additional line for accurate determination. E_{onset} is defined in this work as the lift-off point of the fitted dj/dE curve from zero. (a) For 0.1M KOH, the derivative curve of Mo_2C NP is not plotted because the noise level was too high. The main issue was the very small time steps used during the recording of the CV, created a lot of data points that introduced a significant amount of noise. This was also observed for Mo_2C NS, but E_{onset} could still be estimated using data fitting. All E_{onset} below were converted to RHE scale. The following E_{onset} were obtained from the graph; Mo_2C NS = -0.13 V, Fe_3C = -0.22 V and Fe_5C_2 = -0.23 V. (b) For 1 M KOH; Mo_2C NS = -0.17 V, Mo_2C NP = -0.11 V, Fe_3C = -0.22 V and Fe_5C_2 = -0.22 V. (c) E_{onset} in 0.5 M Li_2SO_4 is Mo_2C NS = -0.32 V and Mo_2C NP = -0.28 V. E_{onset} for Mo_2C NP in 0.05 M H_2SO_4 is -0.17 V.
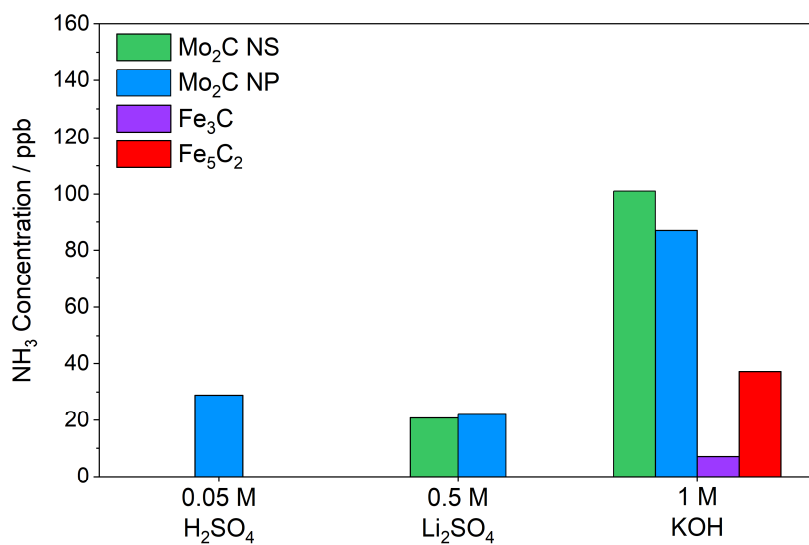
Figure A21. Qualitative analysis of the NRR activity of metal carbides at different pH. NH_3 concentrations were quantified after 40 cyclic voltammetry scans in a potential window where NRR is expected.
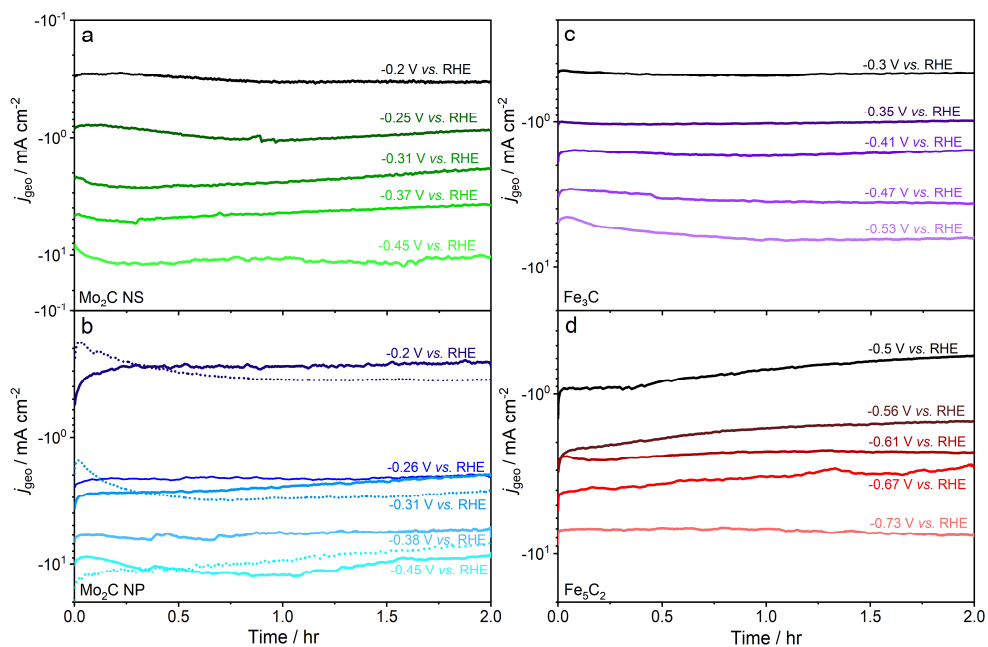
Figure A22. Chronoamperometry measurements at five different potentials (100% R_u compensated) in 0.1 M KOH with 0.06 mg cm^{-2} catalyst loading of (a) Mo$_2$C NS, (b) Mo$_2$C NP, including three measurements with saturated Ar (dotted line), (c) Fe$_3$C and (d) Fe$_5$C$_2$ in 0.1 M KOH.
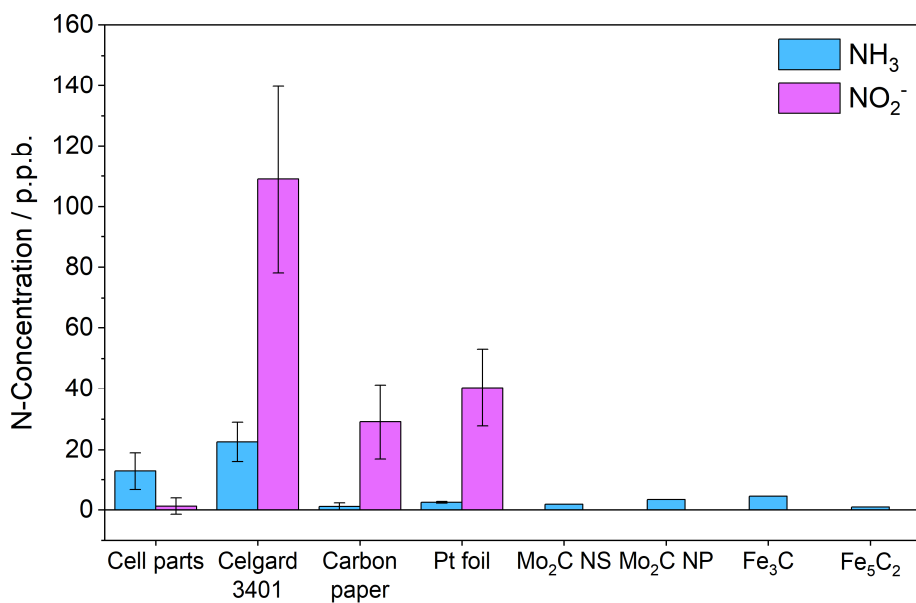
Figure A23. Quantification of several N-containing impurities after the cleaning procedure from several used cell components. After washing the PEEK cell body parts excessively with H_2O, the cell was assembled and filled with 10 ml 0.1 M KOH, then sealed off. The assembled cell was mounted for a duration of 15 min on a vortex shaker to trap the remaining impurities in the electrolyte. A 2.5 cm x 2.5 cm piece of Celgard 3401, 1.12 cm^2 carbon paper disk and 2.5x2.5cm^2 Pt foil were washed several times with H_2O and transferred to a separate test tube filled with 5 ml 0.1 M KOH. Subsequently, the test tubes were sonicated for 15 min. Afterwards, the impurities were directly quantified. The obtained results were extrapolated to the actual geometries of the used components in the electrochemical experiments in order to make a sound estimation of the level of background impurities after the cleaning procedure. Bar charts with error bars indicate the standard deviation of triplicates.
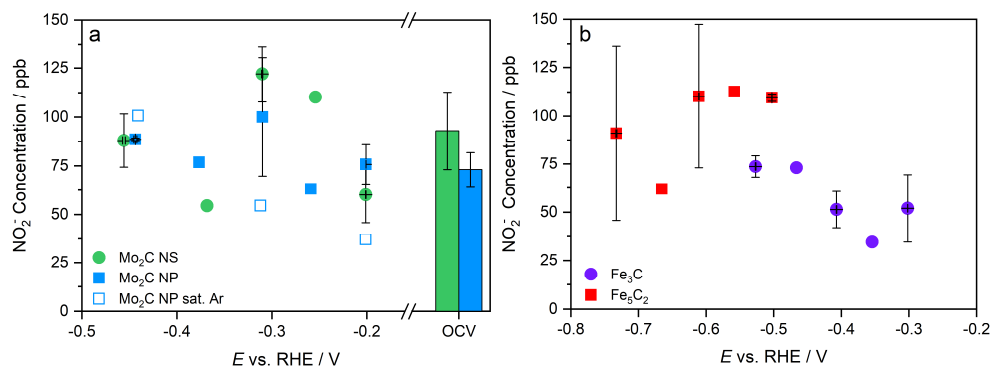
Figure A24. Quantified NO_2^- concentration after two hour chronoamperometry measurements in 0.1 M KOH corresponding to Figure 6. (a) Mo_2C NS (green, spherical) and Mo_2C NP in N_2 (blue, rectangular) and Ar (blue, open rectangular). (b) Fe_3C (purple, spherical) and Fe_5C_2 (red, rectangular). Data points with the error bars were done in duplicates.
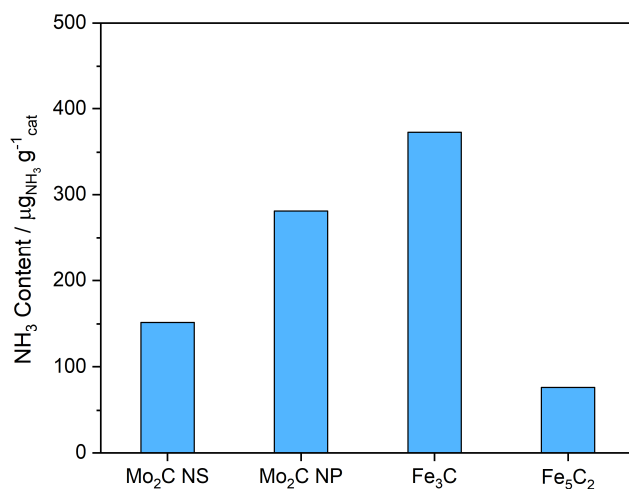
Figure A25. NH_3 impurities in the catalyst powders. For each material, 10 mg was dispersed in a sample tube filled with 5 ml 0.1 M KOH and sonicated for 15 min. Afterwards, the suspension was centrifuged for 15 min at 9000 rpm to separate the powder from the electrolyte in order to avoid major interference during the quantification process. Non-visible colloidal particles interfered most likely with the NO_2^- Griess test, therefore only NH_3 was quantified. An alternative method for the quantification of NO_2^- within various commercial metal powders has been implemented by Chen et al. but was not adopted in this work.[4]
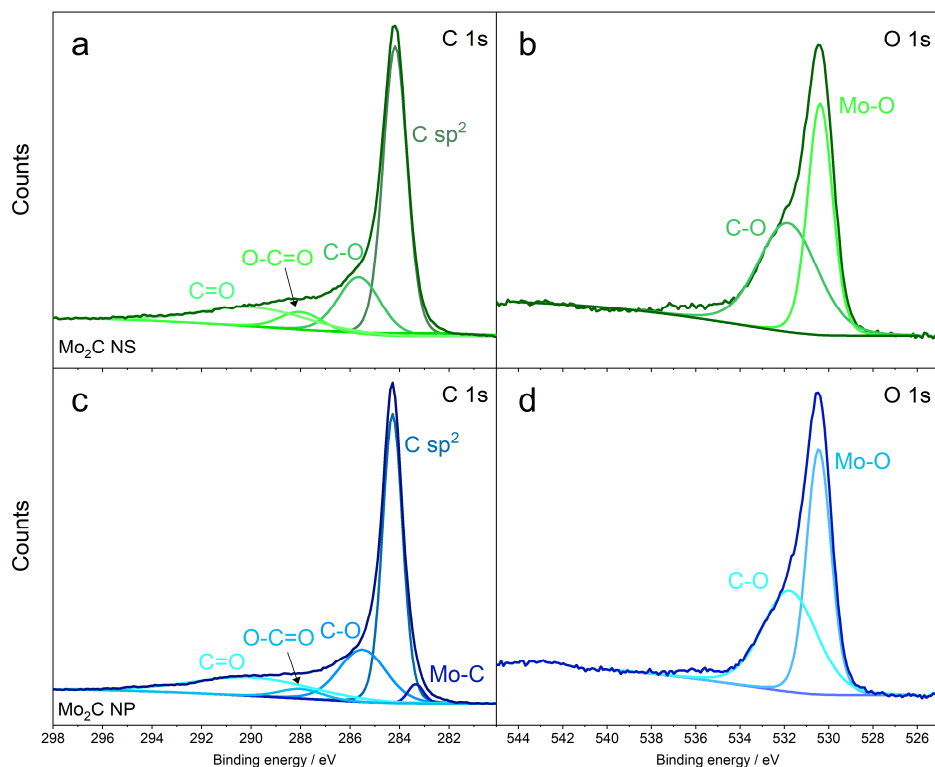
Figure A26. (a, c) C 1s and (b, d) O 1s spectra of Mo_2C NS (green) and Mo_2C NP (blue), respectively. The carbide phase (Mo-C) with a slightly lower binding energy as the C sp^2 bond could not be identified with great certainty. The role of adventitious hydrocarbon moieties might play a role due to exposure to air, which does also explain the relatively large Mo-oxide phase in the O 1s spectra. Another reason is the possible shielding effect by the excessive amount of carbon present in the support. The N 1s peak could not be deconvoluted because it overlaps with the Mo 3p peak.
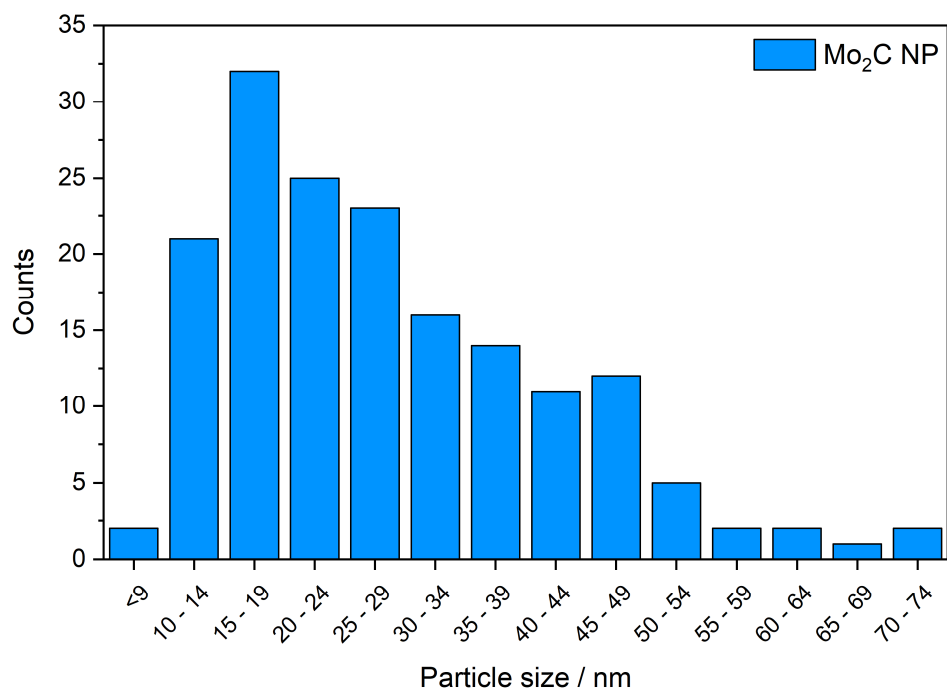
Figure A27. Mo₂C NP size distribution composed of 168 particles from four different TEM grid locations.
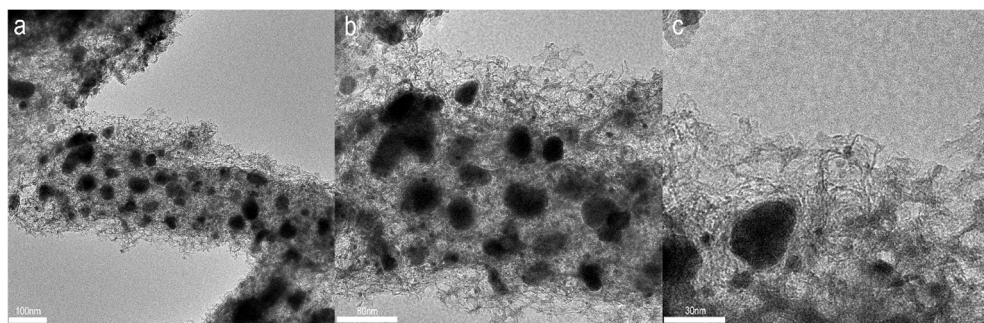
Figure A28. Transmission electron micrographs of the Fe₃C structure. The hollow features in the carbon support structure represent dissolved SiO₂ nanospheres (~20 nm) by alkaline treatment.
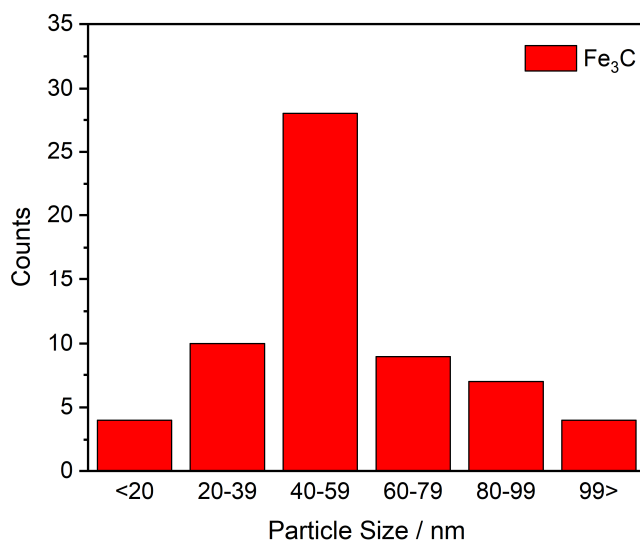
Figure A29. Fe$_3$C particle size distribution estimated by 62 particles at three different TEM grid locations.
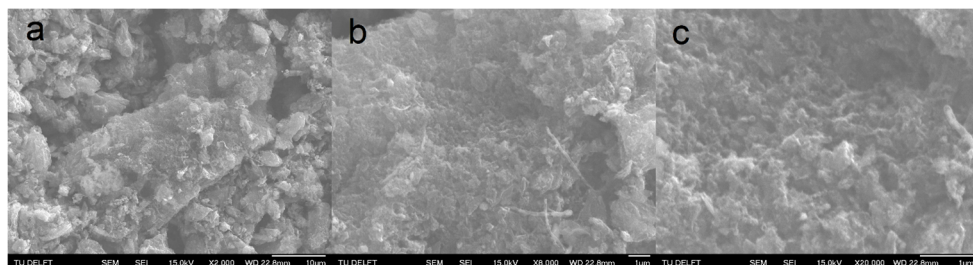
Figure A30. Scanning electron micrographs of the Fe$_3$C mesoporous surface structure, which agrees well with Giordano and coworkers.[5]
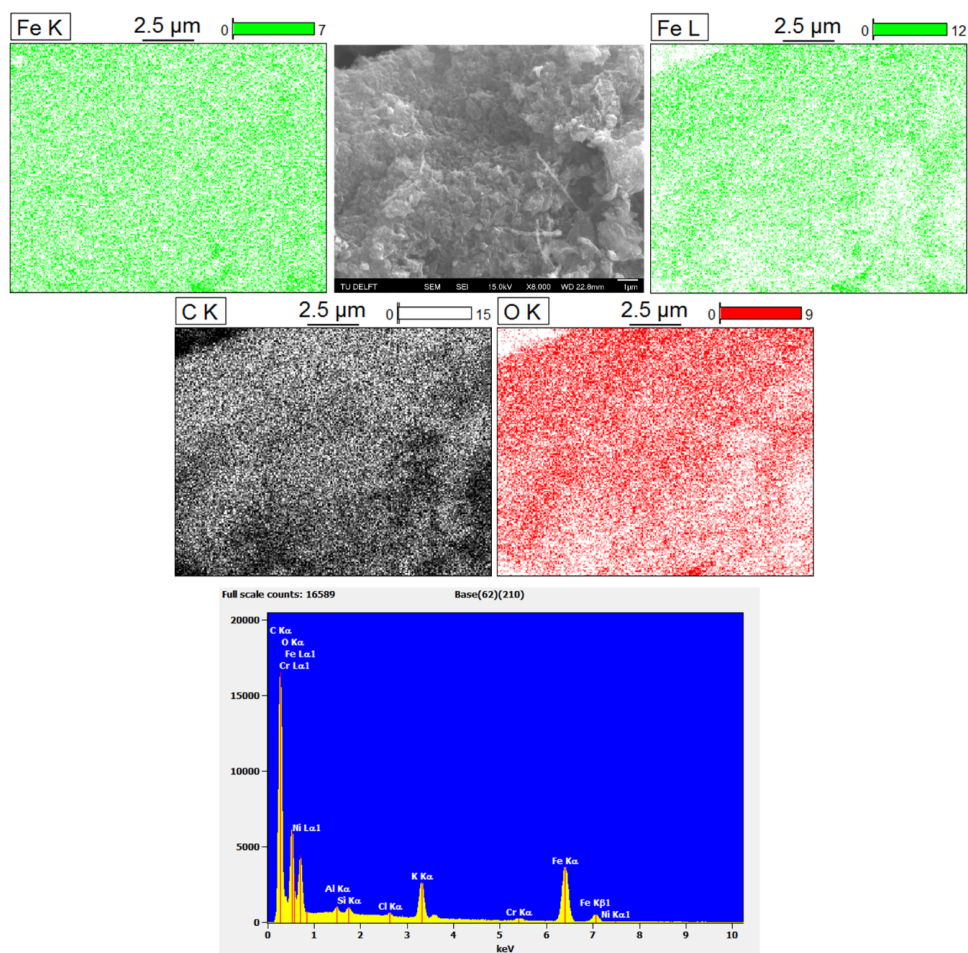
Figure A31. Energy-dispersive X-ray element mapping and spectra of the mesoporous Fe_3C. The EDX peaks at 0.28, 0.53 and 0.71 keV are assigned to C, O and Fe. Although small quantities of Cr and Ni were identified, it is unlikely that these species are present in the sample. The peak at 3.31 keV is the remaining K from the alkaline wash during the removal of SiO_2 particles, which appears to be effective due to the low intensity of the Si peak at 1.74 keV.
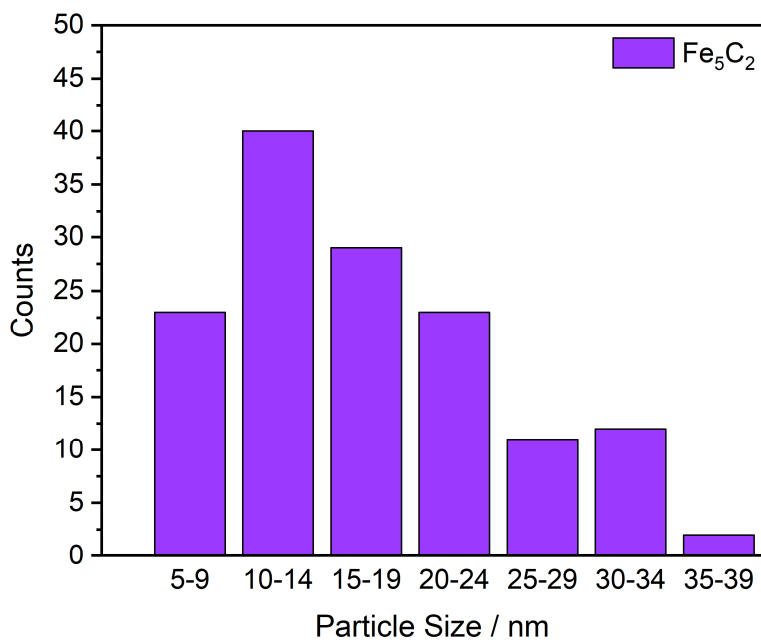
Figure A32. Fe_5C_2 particle size distribution of 161 particles collected from three different TEM grid locations. Particles lower than 5 nm could not be quantified due to the resolution limitations of the instrument.
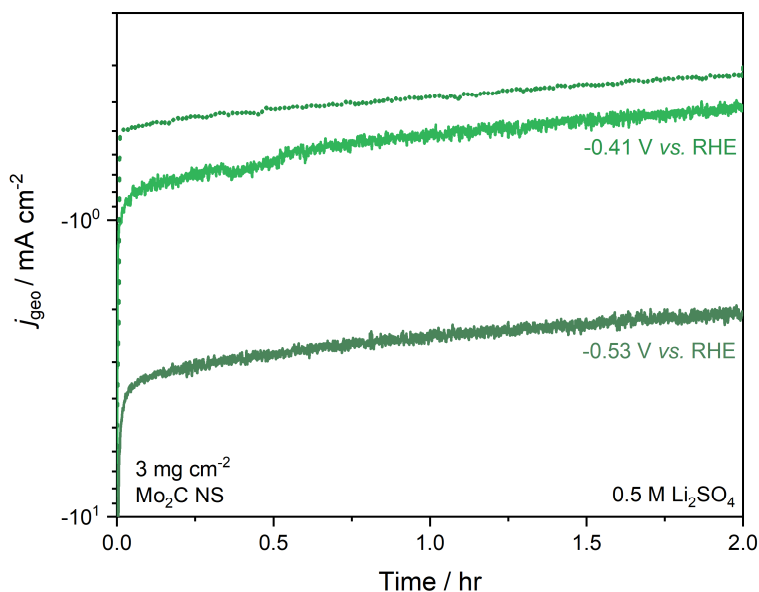
Figure A33. Chronoamperometry measurements of Mo_2C NS at -0.41 V and -0.53 V vs. RHE (100% R_u compensated) in 0.5 M Li_2SO_4 with 3 mg·cm^{-2} catalyst loading. The dotted line represents an Ar control experiment at -0.4 V vs. RHE.
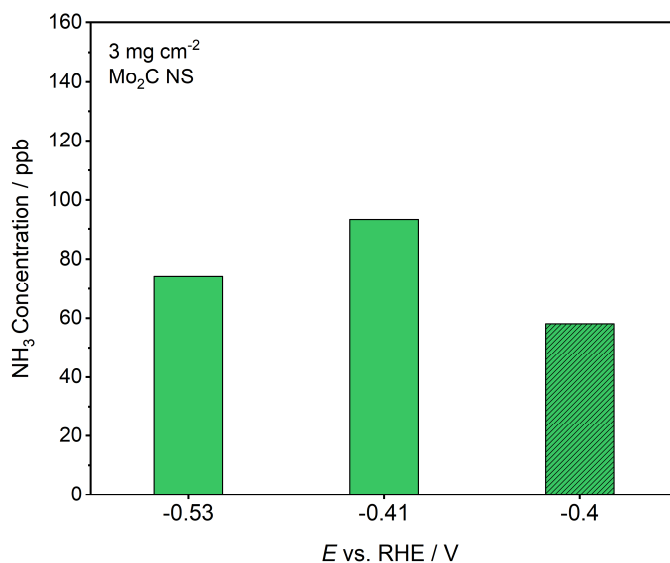
Figure A34. Quantified NH_3 concentrations after two hour chronoamperometry measurements with Mo_2C NS in 0.5 M Li_2SO_4 corresponding to **Figure A33**. The hatched histogram represents the NH_3 concentration after the Ar blank test.

Appendix Tables

Table A1. The average crystallite size estimated by the Scherrer equation.

	Peak (2θ)	FWHM (2θ)	$D_{Scherrer}$ (nm)
Mo_2C NS	40.35	0.16	35
	73.16	0.26	
	103.35	0.43	
Mo_2C NP	44.51	0.31	21
	61.49	0.37	
	83.05	0.45	
	98.20	0.54	
Fe_3C	52.92	0.18	42
	57.86	0.19	
	68.68	0.21	
	84.70	0.24	
Fe_5C_2	46.19	0.68	11
	52.70	0.78	
	67.43	0.88	
	69.16	0.88	

Table A2. The Mössbauer fitted parameters of the sample, obtained at 300 K. Experimental uncertainties: Isomer shift: I.S. ± 0.02 mm s⁻¹; Quadrupole splitting: Q.S. ± 0.02 mm s⁻¹; Line width: Γ ± 0.03 mm s⁻¹; Hyperfine field: ± 0.1 T; Spectral contribution: ± 3%.

Sample	IS (mm·s⁻¹)	QS (mm·s⁻¹)	Hyperfine field (T)	Γ (mm·s⁻¹)	Phase	Spectral contribution (%)
Fe_3C	0.00	-	33.0	0.29	Fe^0	11
	0.19	-	20.8	0.38	θ-Fe_3C	67
	0.31	-0.01	49.3	0.63	γ-Fe_2O_3	7
	0.31	0.72	-	0.60	Fe^{3+}	15
Fe_5C_2	0.00	-	33.2	0.32	Fe^0	4
	0.27	-	21.7	0.51	χ-Fe_5C_2 (I)	32
	0.21	-	18.1	0.51	χ-Fe_5C_2 (II)	26
	0.16	-	10.3	0.51	χ-Fe_5C_2 (III)	20
	0.28	0.00	49.1	0.25	Fe_3O_4 (I)	2
	0.71	-0.07	46.0	0.37	Fe_3O_4 (II)	5
	0.27	0.88	-	0.64	Fe^{3+}	11

Table A3. Elemental Mo and Fe analysis by ICP-OES.

	Mo (wt%)	Fe (wt%)
Mo_2C NS	41.5	
Mo_2C NP	59.2	
Fe_3C		15.1
Fe_5C_2		12.9

Ref	Catalyst	Electrolyte	j_{NH_3} (mA cm^{-2})	E_w (V vs. RHE)	Yield rate (nmol s^{-1} cm^{-2})	Yield rate (nmol s^{-1} mg$_{cat}^{-1}$)	FE (%)	Loading (mg)	N$^-$ in cat. or sup.	Dupl./ tripl.	Ar	OCV	$^{15}N_2$
8	Mo₃Fe₃C	0.1 M Li2SO4	-0.003	-0.05	0.016	0.020	27	0.8	Y	Y	Y	N	N
9	Mo₂C/C	0.5 M Li2SO4	-1.04	-0.3	0.930	0.093	7.8	3	N	N	N	N	Q
10	Fe₃Mo₃C/C	1 M KOH	-0.063	-0.5	0.214	0.021	0.05	3	N	N	Y	N	Q
11	Mo₂C/N-C	0.1 M Na2SO4	-0.002	-0.2	0.016	0.020	12.3	0.8	Y	Y	Y	N	N
12	Mo₂C film/Mo foil	0.1 M Na2SO4	-0.060	-0.55	0.055	-	40.2	-	Y	N	Y	Y	N
13	Mo/MoₓC NP	0.1 M Na2SO4	-0.009	-0.3	0.166*	0.33	13	0.13	N	Y	Y	N	N
6	Fe-doped Mo₂C	0.5 M Na2SO4	-0.101	-0.45	0.006	0.61	20.1	0.01	Y	Y	Y	Y	N
14	Mo-Mo₂C@N-CNT	0.005 M H2SO4 + 0.1 M K2SO4	-0.047	-0.25	0.263	-	5.9	-	Y	N	N	N	Q
15	SA Mo@N-C	0.1 M KOH	-0.175	-0.3	0.213*	0.56	14.6	0.38	Y	Y	Y	N	Y
16	Mo₂C nanoflakes	Nafion	-0.011	-0.5	0.022	-	1.8	0.5	N	N	Y	Y	N
17	O-MoC@N-C	0.1 mM HCl + 0.5 M LiSO4	-0.038	-0.35	0.13	0.37	25.1	0.14	Y	Y	Y	Y	N
18	Fe₃C/C	0.05 H2SO4	-0.092	-0.2	0.209	0.14	9.15	0.15	N	N	Y	Y	N
19	Fe₃C NP@N-C	0.1 M KOH	-0.064	-0.4	0.098	0.26	2.72	0.38	Y	Y	Y	Y	Q
7	Fe₃C/Fe₂O₃/Fe/C	6 M KOH	0.004	0.1	0.0049	0.005	0.38	1	Y	Y	Y	Y	Y
	Mo₂C NS (This work)	0.1 M KOH	-0.001	-0.2	0.004	0.065	0.41	0.06	N	Y	Y	Y	N
		0.5 M Li₂SO₄	-0.001	-0.41	0.003	0.001	0.18	3	N	N	Y	N	N
	Mo₂C NP (This work)	0.1 M KOH	-0.001	-0.2	0.004	0.065	0.42	0.06	Y	Y	N	Y	N
	Fe₃C/Fe-oxide/Fe (This work)	0.1 M KOH	-0.0005	-0.3	0.0017	0.028	0.11	0.06	Y	Y	N	N	N
	Fe₅C₂/Fe-oxide/Fe (This work)	0.1 M KOH	-0.0005	-0.5	0.0016	0.026	0.077	0.06	Y	Y	N	N	N

Table A5. XPS peak deconvolution details of molybdenum carbide. The line shape of the curves were approximated as a Lorentzian with LA(1.53,243) with a U2 Tougaard background type.

Material	Orbital	Peak	Binding Energy (eV)	FWHM (eV)	Relative area (%)	at %	wt %
Mo$_2$C NS	Mo 3d	Mo$^{0-3+}_{5/2}$	229.29	1.29	5.87	5.6	31.0
		Mo$^{0-3+}_{3/2}$	232.44	1.29	3.91		
		Mo$^{4+}_{5/2}$	230.88	1	3.36		
		Mo$^{4+}_{3/2}$	234.03	1	2.24		
		Mo$^{6+}_{5/2}$	232.45	1.56	48.31		
		Mo$^{6+}_{3/2}$	235.60	1.56	32.21		
	C 1s	C sp^2	284.17	1.06	46.56	78.6	54.4
		C-O	285.12	2.83	32.16		
		O-C=O	288	2.41	6.15		
		C=O	290	5.00	15.42		
	O 1s	O-Mo	530.39	1.32	26.40	15.8	14.6
		O-C	531.84	3.15	63.00		
Mo2C NP	Mo 3d	Mo$^{0-3+}_{5/2}$	228.22	1.01	4.13	4.8	27.9
		Mo$^{0-3+}_{3/2}$	231.37	1.01	2.75		
		Mo$^{4+}_{5/2}$	229.40	0.94	2.46		
		Mo$^{4+}_{3/2}$	232.55	0.94	1.64		
		Mo$^{6+}_{5/2}$	232.44	2.03	52.15		
		Mo$^{6+}_{3/2}$	235.57	2.03	34.77		
	C 1s	C-Mo	283.35	0.74	2.67	83.2	60.5
		C sp^2	284.28	0.96	52.49		
		C-O	285.5	2.25	21.94		
		O-C=O	288	2.05	3.66		
		C=O	289.95	5.75	19.43		
	O 1s	O-Mo	530.45	1.30	51.82	12.0	11.6
		O-C	531.77	2.88	47.20		

Table A6. XPS peak deconvolution details of iron carbide. The line shape of the curves were approximated as a Lorentzian with LA(1.53,243) with a Shirley background type.

Material	Orbital	Peak	Binding Energy (eV)	FWHM (eV)	Relative area (%)	at%	wt%
Fe_3C	Fe 2p	Fe_3C	708.37	2.00	6.75	2.9	11.4
		$Fe_2O_3{}^1$	709.80	1.20	26.63		
		$Fe_2O_3{}^2$	710.75	1.20	24.50		
		$Fe_2O_3{}^3$	711.67	1.31	18.77		
		$Fe_2O_3{}^4$	712.65	1.40	10.04		
		$Fe_2O_3{}^5$	713.71	2.20	9.93		
	C 1s	Fe-C	283.50	0.93	2.27	68.6	58.2
		$C\ sp^2$	284.30	0.91	19.42		
		$C\ sp^3$	284.96	1.50	43.63		
		C-O/C-N	286.20	1.50	16.89		
		C=O	288.00	2.47	18.24		
	O 1s	Fe-O	529.88	1.49	30.52	16	18.0
		C-O	531.15	1.91	54.02		
		C-O	532.92	2.00	16.11		
	N 1s	$C\text{-}N\text{-}6\ /\ \text{-}NH_3$	398.29	1.46	48.96	12.6	12.4
		$C\text{-}N\text{-}5\ /\ \text{-}NH_2$	399.89	2.24	52.04		
Fe_5C_2	Fe 2p	Fe^0	707.24	1.30	28.41	0.3	1.2
		Fe_3C	708.61	0.97	9.63		
		$Fe_2O_3{}^1$	709.80	1.20	17.11		
		$Fe_2O_3{}^2$	710.73	1.20	15.74		
		$Fe_2O_3{}^3$	711.78	1.40	12.06		
		$Fe_2O_3{}^4$	712.89	1.40	6.45		
		$Fe_2O_3{}^5$	713.97	2.29	6.38		
	C 1s	C-Fe	283.50	1.22	1.56	77.6	72.7
		$C\ sp^2$	284.30	1.36	10.42		
		$C\ sp^3$	285.00	1.87	45.24		
		C-O/C=N/C-OH	286.12	2.04	33.74		
		C=O	288.00	1.58	9.18		

			Binding Energy (eV)	FWHM (eV)	Relative area (%)	at%	wt%
O 1s	Fe-O	529.99	1.17	10.14	12.2	15.2
	C-O	531.23	2.39	90.38		
N 1s	C-N-6/ -NH_3	398.92	1.60	35.40	10.0	10.9
	C-N-5/ -NH_2	400.10	1.59	62.15		

Table A7. XPS peak deconvolution details of iron carbide. The line shape of the curves were approximated as a Lorentzian with LA(1.53,243) with a Shirley background type.

Material	Orbital	Peak	Binding Energy (eV)	FWHM (eV)	Relative area (%)	at%	wt%
Fe_3C	Fe 2p	Fe_3C	708.37	2.00	6.75	2.9	11.4
		$Fe_2O_3{}^1$	709.80	1.20	26.63		
		$Fe_2O_3{}^2$	710.75	1.20	24.50		
		$Fe_2O_3{}^3$	711.67	1.31	18.77		
		$Fe_2O_3{}^4$	712.65	1.40	10.04		
		$Fe_2O_3{}^5$	713.71	2.20	9.93		
	C 1s	Fe-C	283.50	0.93	2.27	68.6	58.2
		C sp^2	284.30	0.91	19.42		
		C sp^3	284.96	1.50	43.63		
		C-O/C-N	286.20	1.50	16.89		
		C=O	288.00	2.47	18.24		
	O 1s	Fe-O	529.88	1.49	30.52	16	18.0
		C-O	531.15	1.91	54.02		
		C-O	532.92	2.00	16.11		
	N 1s	C-N-6 / -NH_3	398.29	1.46	48.96	12.6	12.4
		C-N-5 / -NH_2	399.89	2.24	52.04		
Fe_5C_2	Fe 2p	Fe^0	707.24	1.30	28.41	0.3	1.2
		Fe_3C	708.61	0.97	9.63		
		$Fe_2O_3{}^1$	709.80	1.20	17.11		
		$Fe_2O_3{}^2$	710.73	1.20	15.74		

	Fe$_2$O$_3$[3]	711.78	1.40	12.06		
	Fe$_2$O$_3$[4]	712.89	1.40	6.45		
	Fe$_2$O$_3$[5]	713.97	2.29	6.38		
C 1s	C-Fe	283.50	1.22	1.56	77.6	72.7
	C sp^2	284.30	1.36	10.42		
	C sp^3	285.00	1.87	45.24		
	C-O/C=N/C-OH	286.12	2.04	33.74		
	C=O	288.00	1.58	9.18		
O 1s	Fe-O	529.99	1.17	10.14	12.2	15.2
	C-O	531.23	2.39	90.38		
N 1s	C-N-6/ -NH$_3$	398.92	1.60	35.40	10.0	10.9
	C-N-5/ -NH$_2$	400.10	1.59	62.15		

Appendix References

1   Kuhl, K. P.; Cave, E. R.; Abram, D. N.; Jaramillo, T. F. New insights into the electrochemical reduction of carbon dioxide on metallic copper surfaces. *Energy & Environmental Science* **2012**, *5* (5), 7050-7059.

2   Chastain, J.; King Jr, R. C. Handbook of X-ray photoelectron spectroscopy. *Perkin-Elmer Corporation* **1992**, *40*, 221.

3   Mayerhöfer, T. G.; Shen, Z.; Leonova, E.; Edén, M.; Kriltz, A.; Popp, J. Consolidated silica glass from nanoparticles. *Journal of Solid State Chemistry* **2008**, *181* (9), 2442-2447.

4   Chen, Y.; Liu, H.; Ha, N.; Licht, S.; Gu, S.; Li, W. Revealing nitrogen-containing species in commercial catalysts used for ammonia electrosynthesis. *Nature Catalysis* **2020**, 1-7.

5   Kraupner, A.; Markus, A.; Palkovits, R.; Schlicht, K.; Giordano, C. Mesoporous Fe3C sponges as magnetic supports and as heterogeneous catalyst. *Journal of Materials Chemistry* **2010**, *20* (29), 6019-6022.

6   Wang, T.; Kou, Z.; Zhang, J.; Wang, H.; Zeng, Y. J.; Wei, S.; Zhang, H. Boosting Faradic efficiency of dinitrogen reduction on the negatively charged Mo sites modulated via interstitial Fe doping into a Mo2C nanowall catalyst. *Chemical Engineering Journal* **2021**, *417*, 127924-127924.

7   Kim, J. H.; Ju, H.; An, B.-S.; An, Y.; Cho, K.; Kim, S. H.; Bae, Y.-S.; Yoon, H. C. Comparison between Fe2O3/C and Fe3C/Fe2O3/Fe/C Electrocatalysts for N2 Reduction in an Alkaline Electrolyte. *ACS Applied Materials & Interfaces* **2021**, acsami.1c20807-acsami.20801c20807.

8   Qin, B.; Li, Y.; Zhang, Q.; Yang, G.; Liang, H.; Peng, F. Understanding of nitrogen fixation electro catalyzed by molybdenum–iron carbide through the experiment and theory. *Nano Energy* **2020**, *68*, 104374.

9   Cheng, H.; Ding, L. X.; Chen, G. F.; Zhang, L.; Xue, J.; Wang, H. Molybdenum Carbide Nanodots Enable Efficient Electrocatalytic Nitrogen Fixation under Ambient Conditions. *Advanced Materials* **2018**, *30* (46), 1-7.

10 Cheng, H.; Cui, P.; Wang, F.; Ding, L. X.; Wang, H. High Efficiency Electrochemical Nitrogen Fixation Achieved with a Lower Pressure Reaction System by Changing the Chemical Equilibrium. *Angewandte Chemie - International Edition* **2019**, *58* (43), 15541-15547.

11 Zhang, Y.; Hu, J.; Zhang, C.; Cheung, A. T. F.; Zhang, Y.; Liu, L.; Leung, M. K. H. Mo2C embedded on nitrogen-doped carbon toward electrocatalytic nitrogen reduction to ammonia under ambient conditions. *International Journal of Hydrogen Energy* **2021**, *46* (24), 13011-13019.

12 Ba, K.; Wang, G.; Ye, T.; Wang, X.; Sun, Y.; Liu, H.; Hu, A.; Li, Z.; Sun, Z. Single Faceted Two-Dimensional Mo 2 C Electrocatalyst for Highly Efficient Nitrogen Fixation. **2020**.

13 Liu, Y.; Zhu, X.; Zhang, Q.; Tang, T.; Zhang, Y.; Gu, L.; Li, Y.; Bao, J.; Dai, Z.; Hu, J. S. Engineering Mo/Mo2C/MoC hetero-interfaces for enhanced electrocatalytic nitrogen reduction. *Journal of Materials Chemistry A* **2020**, *8* (18), 8920-8926.

14 Ma, Y.; Yang, T.; Zou, H.; Zang, W.; Kou, Z.; Mao, L.; Feng, Y.; Shen, L.; Pennycook, S. J.; Duan, L.; et al. Synergizing Mo Single Atoms and Mo2C Nanoparticles on CNTs

Synchronizes Selectivity and Activity of Electrocatalytic N2 Reduction to Ammonia. *Advanced Materials* **2020**, *32* (33), 1-8.

15 Han, L.; Liu, X.; Chen, J.; Lin, R.; Liu, H.; Fang, L. U.; Bak, S.; Liang, Z.; Zhao, S.; Stavitski, E.; et al. Atomically Dispersed Molybdenum Catalysts for Efficient Ambient Nitrogen Fixation. *Angewandte Chemie - International Edition* **2019**, *58* (8), 2321-2325.

16 Ramaiyan, K. P.; Ozden, S.; Maurya, S.; Kelly, D.; Babu, S. K.; Benavidez, A.; Garzon, F. G.; Kim, Y. S.; Kreller, C. R.; Mukundan, R. Molybdenum Carbide Electrocatalysts for Electrochemical Synthesis of Ammonia from Nitrogen: Activity and Stability. *Journal of The Electrochemical Society* **2020**, *167* (4), 044506-044506.

17 Qu, X.; Shen, L.; Mao, Y.; Lin, J.; Li, Y.; Li, G.; Zhang, Y.; Jiang, Y.; Sun, S. Facile Preparation of Carbon Shells-Coated O-Doped Molybdenum Carbide Nanoparticles as High Selective Electrocatalysts for Nitrogen Reduction Reaction under Ambient Conditions. *ACS Applied Materials & Interfaces* **2019**, *11* (35), 31869-31877.

18 Peng, M.; Qiao, Y.; Luo, M.; Wang, M.; Chu, S.; Zhao, Y.; Liu, P.; Liu, J.; Tan, Y. Bioinspired Fe3C@C as Highly Efficient Electrocatalyst for Nitrogen Reduction Reaction under Ambient Conditions. *ACS Applied Materials and Interfaces* **2019**, *11* (43), 40062-40068.

19 Cong, L.; Yu, Z.; Liu, F.; Huang, W. Electrochemical synthesis of ammonia from N 2 and H 2 O using a typical non-noble metal carbon-based catalyst under ambient conditions †. *Cite this: Catal. Sci. Technol* **2019**, *9*, 1208-1208.

2

2

3

Identification, Quantification, and Elimination of NO$_x$ and NH$_3$ Impurities for Aqueous and Li-Mediated Nitrogen Reduction Experiments

Abstract

Ammonia production via the electrochemical dinitrogen reduction reaction (NRR) enables a carbon free alternative to the fossil-based Haber-Bosch process. Current observed NH_3 yields remain low and challenge reliable NH_3 quantification. Various sources of extraneous N-species, including NH_3 and NO_x were recently identified, questioning earlier published results. In this work, we carry out a systematic investigation on the N-contaminations derived from several sources and on the efficacy of multiple removal strategies. $^{15}N_2$ gas is contaminated and can only be purified with certified gas filters because commonly adopted liquid scrubbers fail to eliminate impurities. The accumulation of atmospheric NO_x on ambient exposed lab materials is unavoidable and can be prevented by storing materials in gloveboxes or desiccators. To remove impurities that are already present, treatments with water, alkaline solutions, or heat can be considered. Our examined methods equip the experimentalist with specific guidelines and tools to perform reliable NRR studies.

3

3.1 Introduction

Ammonia (NH_3) ranks among the largest bulk chemical products in the world, with an annual production of 178 million tons and an estimated annual market growth of 3–5% to meet the global demand for fertilizer in the agricultural sector due to an increasing world population.[1,2] The majority of NH_3 is produced by the Haber–Bosch process, wherein elevated temperatures (300–500 °C) and pressures (200–300 bar) are required.[3] In addition, the current process has a major environmental impact (~1% of the global greenhouse emissions), mostly due to the production of hydrogen by steam-methane reforming.[4] To meet the net-zero emissions goal by 2050, as established in the latest IPCC report,[5] ammonia must be produced via a sustainable pathway.[6] Direct electrocatalytic synthesis of ammonia from dinitrogen and water at mild conditions could potentially offer a carbon-free alternative, resilient to intermittent renewable energy generation.[7]

Despite the large research efforts on nitrogen electroreduction in aqueous electrolytes, current NH_3 synthesis rates remain extremely low (0.003–14 nmol cm^{-2} s^{-1}).[8] This is mainly due to the lack of a suitable electrocatalyst and competition with the hydrogen evolution reaction (HER). Besides, the reliable quantification of these low ammonia yields has raised several concerns in the scientific community. The presence of trace amounts of extraneous N species (such as, NH_3, NO_x, N_2O, NO_x^-, and other, more labile forms of N) has led to an increasing number of reported false positives and non-reproducible results.[9–13] Overall, the electrochemical reduction of nitrogen oxide species into ammonia is more facile than the nitrogen reduction reaction (NRR) on many transition metals.[14–16] An exception is N_2O, which has been proven to only electroreduce into N_2 on several transition metals.[15,17] This implies that N_2O is not a concerning impurity source for the NRR. Numerous rigorous experimental protocols have been proposed to perform reliable quantification of NH_3 produced by electrochemical N_2 reduction.[18,19] Ultimately, purified $^{15}N_2$-labeled gas is used to reliably confirm the electroreduction of $^{15}N_2$ into the unambiguously traceable $^{15}NH_3$.[20] However, over recent years, a significant amount of publications, that implemented all recommended control experiments (including $^{15}N_2$ gas), could not be duplicated.[21,22] A common issue is that the efficacy of the implemented purification methods, such as gas purification or N removal from lab materials, is often poorly assessed. Additionally, it remains challenging to identify the main sources of extraneous N and to what extent it contributes to elevated NH_3 background levels.

In this chapter, we present a systematic impurity screening of the most common used lab materials and gases in the aqueous NRR and non-aqueous lithium-mediated NRR field. Not only does this give new insights into the origin of an impurity, but it also highlights the severity of specific sources for an impurity. More importantly, the effectiveness of earlier proposed cleaning strategies for gases, cell components, materials, and lab consumables are re-evaluated and further optimized.

We discover by using sensitive in-line gas detection methods that $^{14}N_2$ and Ar feed gases are free of NH_3 and NO_x impurities and do not require excessive N purification. Only $^{15}N_2$ is contaminated and must be purified with a certified or pre-assessed gas filter. Often-used in-house-made scrubbers or liquid traps have a much lower N trapping efficiency and should not be implemented. The accumulation of atmospheric N species on ambient exposed cell components, chemicals, lab consumables, and other labware is inevitable and is most likely the main source of elevated NH_3 background levels. This can be significantly reduced by our recommended pre-treatment procedures. For Li-NRR systems, trace amounts of nitrate might be present in Li-salts and can interfere with the genuine NH_3 quantification, especially at low concentrations. Therefore, we recommend to determine a nitrate background concentration since it cannot be removed from the salt. Ultimately, this work will equip the experimentalist with specific guidelines and tools to perform more reliable NRR measurements.

3.2 Experimental Section

3.2.1 Materials

Only ultrapure water (Millipore Milli-Q IQ 7000) was used for cleaning and solution preparation throughout this work. All materials were supplied by Sigma Aldrich unless stated otherwise: $Cu(NO_3)_2 \cdot 2.5H_2O$ (98%, Alfa Aesar), KOH (85% and 99.99%), NH_4Cl (99.99%), KNO_2 (97%), KNO_3 (99%), $NaClO_2$ (25wt% in H_2O), Sulfamic acid (99.3%), HCl (37%), $LiClO_4$ (99.99%), $LiBF_4$ (98% and 99.99%), $LiPF_6$ (98%, Honeywell), LiTFSI (98%), ethanol (anhydrous, VWR), isopropanol (98%, VWR), tetrahydrofuran (99.5%, anhydrous), 1,2-dimethoxyethane (99.5%, anhydrous), 2-methoxyethyl ether (99.5%, anhydrous), 1/8'' HDPE spheres (McMaster), Hydrophobic frit (19.6 mm x 3.2 mm, Biocomma), glass wool – silane treated, anion exchange membrane (Selemion), microporous membrane (Celgard 3401), carbon paper (Alfa Aesar), Pt foil (2.5 cm x 2.5 cm x 0.025 cm, Mateck), pipet tips (Thermo Fischer Scientific), polypropylene sample tubes (1.5 ml Eppendorf, 12 ml Kartell), Latex and Nitrile gloves (Ansell, size M).

3.2.2 Ammonia Quantification by GC/GC-MS

Gaseous ammonia quantification was carried out with gas chromatographic (GC)[1] and gas chromatography-mass spectrometry (GC-MS)[2] methods with a lower detection limit of about 0.15 and 1 ppm, respectively. A TRACE™ 1300 Gas Chromatograph (from Interscience BV - Thermo Fisher Scientific) was equipped with Agilent Select Low Ammonia column located in the GC oven chamber. Once eluted from the chromatography column, the analyte is partitioned between a pulse discharge detector (PDD) and a single quadrupole mass spectrometer (ISQ™ from Thermo Fisher Scientific), which simultaneously analyse the sample with matching retention times. Calibration standards were prepared diluting certified calibration gas mixtures of 13.8 ppm and 2.2 ppm of NH_3 in N_2 with purified N_2. Details of the detection method and calibration curves are available elsewhere.[1, 2]

3.2.3 Gaseous NO_x Quantification by the Chemiluminescence Analyser

A chemiluminescence 200E Nitric Oxides Analyser (API Teledyne) was used to measure gaseous NO and NO_2. The amount of nitric oxide (NO) present in the sample gas is directly determined from the infrared light ($hv_{[1200\,nm]}$) emitted by the reaction between NO and ozone (O_3), as shown in Equations 1-2.

$$NO + O_3 \rightarrow NO_2^* + O_2 \qquad (1)$$
$$NO_2^* \rightarrow NO_2 + hv_{[1200\,nm]} \qquad (2)$$
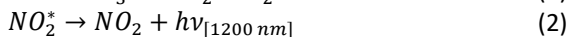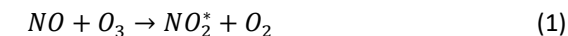
The emitted light of wavelength 1200 nm is then detected by the photo-multiplier tube light. In addition, NO_2 can be measured as sum of NO and NO_2 present in the gas sample. In this case, the gas sample passes through a molybdenum catalyst held at about 315 °C, where the NO_2 reacts to produce NO gas. Thus, the formed NO (together with the NO already present in the sample) is detected by reaction with ozone and generation of infrared light, following the Equations 1-2. The total inlet gas flow rate of the gas chemiluminescence nitric oxide analyser was 700 mL min^{-1}, as the instrument requires a relatively high gas flow. The gas purification scrubbers and filters were tested on a flow rate ranging between 1 and 50 mL min^{-1}, and feeding the remaining flow aliquot as He by mean of dedicated mass flow controllers, as illustrated in Figure B1. The detection limit of the NO analyser is 1 ppb.

Quantification of NO_x in $^{15}N_2$ was not performed due to the high cost of $^{15}N_2$ and because the NO_x chemiluminescence analyzer requires high flow rates (1 L min^{-1}) in combination with a long equilibration time (> 30 min).

3.2.4 N Impurity Assessment and Removal

All sample tubes, pipet tips, bottles, glassware (including the commercial and in-house made scrubber), and other involved materials in the sample handling and storage were always excessive prewashed with water. During a typical impurity assessment before and after an applied cleaning procedure, an experimental component with a predefined area (if applicable) was submerged in freshly prepared 0.1 M KOH (often 5 mL) in a sample tube and sonicated for 15 min. Aliquots were withdrawn from the sample tube for NH_3, NO_2^- and NO_3^- quantification. Four cleaning procedures were evaluated and consisted of; rinsing excessively with water; alkaline wash by submerging the material in 0.1 M KOH followed by 15 min of sonication; thermal decomposition in a tubular furnace (Lenton Blue) at 200 °C (10 °C min^{-1}, 12 hour) under Ar atmosphere; electrochemical NO_x^- reduction by performing 10 cyclic voltammetry scans in between -0.2 V to -0.7 V vs. RHE, where the sample was first rinsed with isopropanol and water as elaborately described in ref [3].

3.2.5 $NH_{3(aq)}$, NO_2^- and NO_3^- Spectrophotometric Quantification

The quantification of ammonia was performed by the Berthelot method.[4] A volume of 1.33 mL aliquot (typically 0.1 M KOH) was neutralized by adding 112 μL of 0.5 M H_2SO_4. Both 360 μL of phenol nitroprusside and alkaline hypochlorite (0.2% sodium hypochlorite) were added directly afterwards and stirred on a vortex shaker. An observable colour change ranging from light green to dark blue appeared after 30 min of incubation time. The coloured solutions were transferred to PMMA cuvettes (10 mm x 10 mm x 30 mm) and were inserted in the UV-Vis spectrophotometer (Hach DR6000) for analysis. Six different NH_4Cl concentrations of 0.01, 0.05, 0.1, 0.5, 1 and 2 ppm NH_3 in 0.1 M KOH were prepared to construct the calibration line with the maximum absorbance at 633 nm. The fitted linear curve with $A = 0.7279C_{NH3} - 0.001$ and $R^2 = 0.9999$ showed decent reproducibility (Figure B2).

Aliquots that interfered with the NO_2^- peak in the ion chromatogram were quantified with the spectrophotometric Griess test. A commercially available Griess reagent mixture with a detection range between 0.007-3.28 ppm NO_2^- (Spectroquant, Merck) was used. 2 ml Aliquots of 0.1 M KOH solutions were neutralized with 0.5 M H_2SO_4. Approximately, 30 mg of the Griess reagent mixture was added to the neutralized aliquots and mixed thoroughly. After 10 min of incubation time the solution appears between light pink and dark magenta ranging from low to high concentration. Five different concentrations from KNO_2^- of 0.02, 0.05, 0.1, 0.5, 1 ppm NO_2^- were used to construct the calibration line by taking the maximum absorbance at 542 nm. The calibration line was perfectly linear with $A = 0.8071C_{NO2-} - 0.0001$ and $R^2 = 1$ (Figure B3). The spectrophotometric samples were always compared versus a fresh 0.1 M KOH solution as blank.

Li-salts commonly used in Li-NRR were screened by dual-wavelength UV spectroscopy for NO_3^- detection. UV absorbance of NO_3^- in water can be detected at 210 nm, which is the same wavelength as for other organic compounds, such as carbonates. To compensate for this, the UV absorbance at 270 nm (common wavelength for most organics) was substracted by $A_{NO3-} = A_{210} - 2A_{270}$. Additionally, small quantities of HCl and sulfamic acid were added to reduce carbonate and nitrite interference, respectively. For the sample preparation, 2.5 mL aliquots were mixed with 50 µL 1 M HCl and 50 µL 10.5 mM sulfamic acid. Subsequently, the mixture was transferred to 10 mm Quartz glass cuvettes (Hellma). Five different KNO_3^- concentrations of 0.05, 0.1, 0.25, 1, 2 ppm NO_3^- were prepared in water to construct a linear calibration line (Figure B4) with $A_{NO3-} = 0.1126\ C_{NO3-} - 0.0006$ and $R^2 = 0.9998$.

3.2.6 NO_2^- and NO_3^- Quantification by Ion Chromatography.

Nitrite and nitrate were determined through ion chromatography (IC). The IC tests were performed by an Thermo Fischer Scientific, Dionex, Integrion HPIC System, equipped with a conductivity detector and AS18-Fast anion column. Additionally, according to application note 72481 from Thermo Fischer Scientific,[5] AutoNeutralization was installed to remove the KOH background. This removes the need for dilution of samples before injection and thus increases accuracy. With the used setup, a sample is manually injected, filling the sample loop (25 µL). Milli-Q water delivered from the external AXP pump and trap column (Dionex IonPac ATC-HC 500 trap column) is used to transfer the sample from the sample loop at 0.5 mL min^{-1} to the neutralizing suppressor and collected on the concentrator column. As the sample passes through the suppressor (4 mm high capacity Dionex AERS 500 Anion Electrolytically Regenerated Suppressor), the cation (K^+ in our case) is exchanged with hydronium thereby neutralising the alkaline sample. The anions of interest are retained on the concentrator column while the water flows to waste, thereby also concentrating the trace anions of the sample. The anions of interest elute from the concentrator column to the guard column and separation column. Here the anions are separated using an eluent consisting of 21.8 mM KOH in milli-Q water at 0.25 mL min^{-1} on the Dionex AS18-Fast anion column. As the analyte peaks elute from the column, they are detected by suppressed conductivity detection using a 2 mm Dionex AERS 500 Anion Electrolytically Regenerated Suppressor and conductivity detector. Two calibration lines were constructed by preparing five different concentrations of 0.01, 0.05, 0.25, 0.5 and 1 ppm NO_2^- and NO_3^- in H_2O from KNO_2 and KNO_3, respectively. Figure B5 indicates a clear peak separation between different anion species, which allows accurate integration of the respective peaks. The integrated conductance vs. NO_2^- and NO_3^- concentration were plotted in Figure B6, which show a linear relationship with $I = 0.7476*C_{NO_2^-} - 0.0082$ ($R^2 = 0.998$) and $I = 0.5821*C_{NO_3^-} - 0.0067$ ($R^2 = 0.997$).

Low concentrations of Li-salts (0.1 M) were injected into the IC only for NO_2^- screening because anions such as ClO_4^- and BF_4^- interferes with the NO_3^- peak (Figure B7). In case of LiBF$_4$ (98%), an unknown compound also interfered with the NO_2^- peak, which made it difficult to accurately determine the concentration. Higher salt concentrations (> 0.1 M) were not considered because it inflates the interference effects.

3.3 Results and Discussion

3.3.1 Impact of Atmospheric NO_x and NH_3 Species

One potential source of the extraneous N species can stem from the accumulation of atmospheric NH_3 or NO_x on exposed materials. The presence of NH_3 in the atmosphere is primarily caused by emissions from the agricultural sector, where NH_3 volatilization occurs due to intensified herbivore production and field-applied manure.[23] These emissions vary regionally and depend on multiple factors, such as wind direction and speed, humidity, and usage of N fertilizers. The monthly average atmospheric NH_3 concentration in The Netherlands varies between 2 and 44 ppb,[24] which might seem negligible. However, it is expected that long-term atmospheric exposure of chemicals, consumables, and glassware employed in NRR experiments will lead to an unavoidable introduction of contaminants due to the release of adsorbed NH_3. The majority of atmospheric NO_x emissions are derived from industrial and automotive combustion of fossil fuels.[25] Atmospheric NO_x concentrations in our laboratory were measured with a chemiluminescent NO_x analyzer (details available in Appendix B). Our results show that the concentrations fluctuated over the course of five consecutive days, with a maximum atmospheric concentration of 27 ppb (Figure 1a). However, the uptake rates during 24 h of both atmospheric NO_x and NH_3 in water and freshly prepared 0.1 and 1 M KOH solutions were negligible (Figure B8). This indicates that short-term atmospheric exposure is not an issue. Long-term accumulation of NO_x impurities was monitored for both low- and high-purity grade KOH (85% and 99.99%), and it was found to depend solely on the storage conditions (Figure B9). KOH bottles stored in a chemical safety cabinet, hence exposed to the laboratory environment for a considerable time period (10 months), contained 4.4 μmol NO_3^- L^{-1} in a freshly prepared 1 M KOH solution, while NO_2^- concentrations were negligible (<0.2 μmol NO_2^- L^{-1}). Remarkably, storing the KOH pellets in a vacuum desiccator for approximately 9 months reduced the NO_x impurities to negligible levels (<0.3 μmol NO_3^- L^{-1}). Therefore, it is strongly advised to store chemicals in controlled environments such as desiccators or Ar gloveboxes.
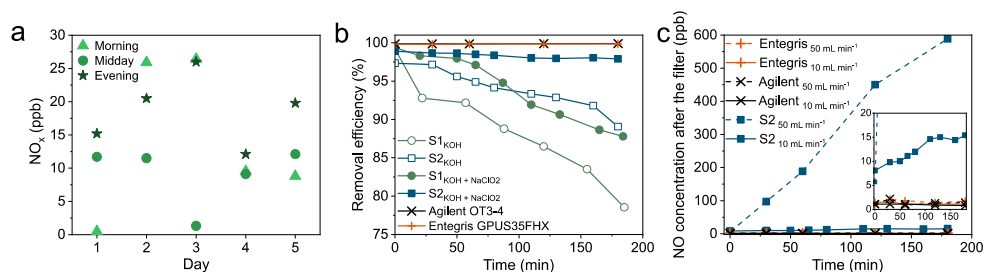
Figure 1. (a) Morning, midday, and evening measurements of atmospheric NO_x concentrations, recorded daily around 9.00, 12.30, and 18.00. Each data point is the average of the measured NO_x concentration over 5 min. (b) NO_x removal efficiency over time, measured for an inlet gas mixture of 50 ppm of NO in He at 10 mL min^{-1} for different scrubbers and liquid traps. S1 and S2 indicate two standard scrubbers connected in series and the in-house-made scrubber, respectively. (c) NO

concentrations measured over time at the outlet of each gas filter with an inlet gas mixture of 50 ppm of NO in He at 50 (dashed line) and 10 (solid line) mL min^{-1}. The in-house-made scrubber (S2) is filled with a 0.1 M KOH and 0.1 M NaClO$_2$ trapping solution. The complete data set with flow rates from 1 to 50 mL min^{-1} is given in Figure B15.

3.3.2 Impurity Assessment of the Feed Gases

Feed gases are suspected to contain ppm levels of NO$_x$ that can be continuously introduced in the electrolyte during reactant gas saturation. We used a commercially available NO$_x$ analyzer to assess our high-purity (99.999%) He, ^{14}N$_2$, and Ar gases (see Appendix B, Figure B1). Additional effort was made to screen the gases for trace levels of NH$_3$ with our recently developed gas chromatograph (GC).[26] Our analysis reveals that the NH$_3$ and NO$_x$ impurities in all the gases are extremely low. NH$_3$ concentrations do not exceed the lower detection limit (LOD$_{NH_3}$ < 150 ppb) of the GC, and the NO$_x$ content falls in the instrument's LOD (1 ppb). High-purity ^{14}N$_2$ and Ar gases are manufactured by cryogenic distillation of air. Low concentrations (ppb level) of atmospheric NH$_3$ and NO$_x$ can end up in the process but will be separated because of their significantly higher boiling point. This justifies our observation, while it is in contradiction with earlier claims. If in-line gas detection methods are not available or used, it remains challenging to adequately quantify impurities in the gas stream due to interference from other sources.

Conversely, a ^{15}N$_2$ isotopologue is commercially available at a lower purity level than the conventional ^{14}N$_2$; thus it might contain a higher concentration of contaminants. As such, we measured up to 9.8 ppm of ammonia contained in a ^{15}N$_2$ gas bottle (99% purity, Sigma-Aldrich), as reported in Figure B4a. By using isotope-sensitive GC-MS,[27] we found that the totality of the measured ammonia is in the form of ^{15}NH$_3$ (Figure B4b). The presence of ^{15}NH$_3$ presumably derives from traces of unreacted ^{15}NH$_3$ used during the catalytic oxidation process for the production of ^{15}N$_2$ gas from isotopically enriched ^{15}NH$_3$.[28] Although not measured by us, different ^{15}NO$_x$ species were previously detected in various ^{15}N$_2$ gas bottles and can be derivatives from the production process (Table B1). It should be noted that measuring gaseous NH$_3$ can be subject to underestimation, due to ammonia physisorption. To avoid this, it is recommended to use a direct gas analysis method in combination with inert materials for all the surfaces that are in contact with the gaseous sample. In fact, Figure B4a shows that no ammonia was detected when the same ^{15}N$_2$ gas was dosed via a non-passivated mass flow controller. Prolonged ^{15}N$_2$ bubbling into the electrolyte is often necessary to reach saturation, which means that the use of cumulative quantification methods requires several hours of reaction time to collect significant amounts of ^{15}NH$_3$.[27] This issue can be partly circumvented by adopting a gas recirculation setup in combination with a suitable gas filter to save costs and minimize accumulation of impurities.[29] From our analysis, it seems that, especially for the execution of ^{15}N$_2$ control experiments, the implementation of a gas purifier is strictly necessary.

3.3.3 Feed Gas Purification Methods

Strategies to purify the feed gases are based on catalytic reduction or scrubbing using commercially available certified gas filters (<1 ppb),[21,30] in-house-made catalytic filters (e.g., based on a Cu-Zn-Al oxide),[31] or scrubbers containing a liquid trap.[32–34] The latter are, to some extent, more economic and are therefore more common. However, it is especially important for uncertified filter systems, such as in-house-developed scrubbers or catalytic filters, to assess their N removal functionalities.

Here, the NO_x and NH_3 removal efficiency is examined for a set of commonly used filters by purging them with 50 ppm of NO in He or 13.8 ppm of NH_3 in $^{14}N_2$ for 3 h at experimentally relevant flow rates. We first tested two standard 20 mL scrubbers with a glass frit (Supelco Analytical, 6-4835) connected in series (Figure B5). The poor solubility of NO in aqueous media results in less than 25% NO removal efficiency when using Milli-Q water (Figure B6). Alkaline solutions are a common choice because gaseous NO_x can be trapped in the form of NO_x^-.[35,36] Substituting water with 0.1 M KOH already enhances the NO removal efficiency up to 78%.

Previous studies recommended the use of strong oxidizing agents, such as $KMnO_4$ or $NaClO_2$, to convert NO directly into soluble NO_2^- or NO_3^- and improve the overall filter performance.[8] $NaClO_2$ was mentioned as one of the most effective oxidants and is evaluated in the present work.[37] A solution of 0.1 M $NaClO_2$ in 0.1 M KOH removed 88% of NO after 3 h purging time (Figure 1b). Additionally, the scrubbing efficiency can be increased by optimizing the gas residence time and the bubble contact area between the gas–liquid interface. As such, inert polytetrafluoroethylene (PTFE) beads were inserted into a 30 cm long, 25 mL in-house-made scrubber (see Figure B7). This results in a further improvement in the removal efficiency, up to 98% over the course of 3 h at 10 mL min^{-1} (Figure 1b). However, the trapping efficiency drops drastically at higher flow rates (>10 mL min^{-1}), as is illustrated in Figure 1c, which limits this purification strategy only to lower flow rates. Remarkably, the commercially certified gas filters (Agilent OT3-4 and Entegris GPUS35FHX) show a consistent unity removal efficiency, within the 1–50 mL min^{-1} range (Figure 1c and Figure B8). NH_3 was completely eliminated by both commercial filters and our scrubber containing a 0.1 M $NaClO_2$ and 0.1 M KOH solution (Figure B9), which was expected due to the high ammonia solubility in water ($\sim$500 g L^{-1}). This analysis shows that certified commercial filters are the most efficient and durable solution for feed gas purification. Furthermore, both filters have been extensively used in our laboratories for over 1 year without showing any sign of decay in performance. Moreover, they do not require extensive cleaning and preparation procedures. Lastly, commercial filters are widely accessible and affordable, often with the possibility of being conveniently regenerated via thermal H_2 treatments.

3.3.4 Screening of Lab Consumables

Besides the impurity contributions from atmospheric N species and $^{15}N_2$ gas, there are additional concerns regarding lab consumables because significant NO_3^- concentrations have been observed earlier.[38,39] Therefore, we screened various consumables from our laboratory supply cabinets, including polypropylene 0.1–1 mL pipet tips, 1.5–12 mL sample tubes, and latex and nitrile chemically resistant gloves. For the analysis of the polypropylene consumables, the pipet tips and tubes were submerged and sonicated in 0.1 M KOH for 15 min. This procedure was repeated five times while reusing the same alkaline solution (more details in the Supporting Information). Remarkably, the N content per item is negligible (3–7 nmol), which was unexpected due to continuous ambient exposure. Nevertheless, several 1.5 mL sample tubes that were directly analyzed after arrival were completely free of any N impurities (Figure B10). This demonstrates that accumulation of adsorbed atmospheric N is inevitable, as was earlier observed for our KOH salts, but is to some extent less severe, and the N species can simply be removed with water.

Patches of latex and nitrile gloves (6 cm × 6 cm) were screened by cutting the patches in little chunks and sonicating them collectively in 0.1 M KOH for 15 min. The latex gloves released reproducible quantities of 5.1 ± 0.7 nmol NH_3 cm^{-2} and 31.7 ± 2.2 nmol NO_3^- cm^{-2}, while the nitrile gloves released 3.7 ± 0.5 nmol NH_3 cm^{-2} and 90.8 ± 1.3 nmol NO_3^- cm^{-2}. These significant NO_3^- concentrations are most likely remaining trace impurities from the calcium nitrate used as coagulant material to harden the gloves during the manufacturing process. Not all manufacturers use calcium nitrate as a coagulant, which can explain the NO_x^- variations reported in the literature.[19] Regardless, direct contact with electrolyte-exposed surfaces, such as membranes, electrodes, glassware, etc., should be avoided as much as possible. To demonstrate the impact, we performed a qualitative assessment (see the Appendix B) by rubbing a nitrile glove over the Celgard membrane and observed that reproducible amounts of N species (0.6 ± 0.1 nmol NH_3 cm^{-2}, 0.6 ± 0.2 nmol NO_2^- cm^{-2}, 12.2 ± 2.1 nmol NO_3^- cm^{-2}) were released (Figure 2a). This shows that especially NO_3^- can be unintentionally introduced during cell assembly.
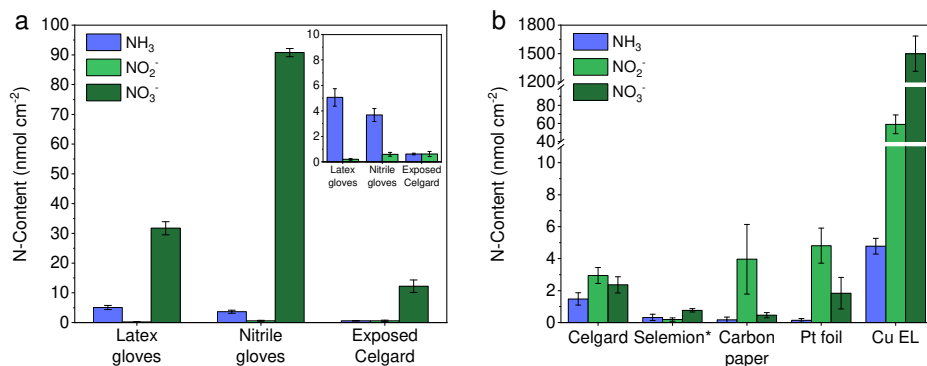
Figure 2. (a) NH_3, NO_2^-, and NO_3^- content of patches (6.0 cm × 6.0 cm) of latex and nitrile gloves cut from the center of the each glove. The N content was determined by cutting the patches into smaller chunks and sonicating them in 30 mL of 0.1 M KOH solution for 15 min. A Celgard membrane (2.5 cm × 2.5 cm) was exposed by rubbing the top and bottom surfaces with a nitrile glove. (b) The NH_3, NO_2^-, and NO_3^- content of cell materials was determined by sonicating 2.5 cm × 2.5 cm samples, except for the carbon paper and Cu electrodeposited on carbon paper (Cu EL), which were 1.2 cm diameter discs, in a 0.1 M KOH solution for 15 min. NH_3 detection was done by the spectrophotometric indophenol blue method. Both NO_2^- and NO_3^- were quantified by ion chromatography.* NO_2^- assay was performed with the spectrophotometric Griess test due to Cl^- overlap in the ion chromatogram. The error bars indicate the standard deviation of three individual experiments.

3.3.5 Encountered Impurities in Commonly Used Cell Materials

Nafion membranes are notorious for their initial NH_4^+ uptake and release during NRR experiments. Here, the buildup of atmospheric NH_4^+ appears to be the main issue,[40] and it remains difficult to remove because of its ion-selective and porous properties. Impurity effects in other commonly used membranes and electrode materials are, to some extent, unexplored. This motivated us to review other types of membranes, carbon paper (often used as a support), Pt foil, and a Cu electrode prepared by electrodeposition (Cu EL). A pre-defined geometrical area (indicated below) of each particular component was sonicated in 0.1 M KOH for 15 min either as received or after a treatment step for the quantification of trapped N impurities.

Celgard (3401) microporous membranes are considered cleaner alternatives to ion-exchange membranes.[20] From our analysis, we confirm that NH_3 levels for a 2.5 cm × 2.5 cm Celgard membrane are negligible (<1.5 nmol cm^{-2}), as shown in Figure 2b. However, we found a relatively high amount of NO_x^- species of around 7.5 nmol cm−2. According to the manufacturer, no sources of NO_x reactants were used during the production process, hence it is likely that physisorption of atmospheric NO_x occurred and accumulated over time. Yet, simply rinsing with water reduces impurity levels to <1 nmol cm^{-2}. Anion-exchange membranes (AEMs), also commonly used in the NRR field, are mostly used with alkaline electrolytes and have the lowest ammonia crossover rates. AEM ionomers consist of positively charged quaternary ammonium functional groups that give the membrane its

anion-selective properties. One could expect that, due to degradation and protonation of the N-functional groups, spontaneous ammonia formation occurs.[9,10,41] However, we did not observe any sign of ammonia leaching from a 2.5 cm × 2.5 cm AEM (Figure 2b), even after 1 h of sonication (Figure B11). Additionally, the amount of NO_x^- species was negligible, which is most likely related to the wetted and sealed storage of the membrane.

Catalyst and electrode materials can also be a potential source of N contaminants. Electrocatalysts prepared by using concentrated ammonia solvents or nitrate compounds should ideally be avoided. If usage is necessary, then additional pretreatment steps and careful examination of the removal effectiveness are advised. Herein, an example is discussed where a 1.13 cm^2 copper electrode (Cu EL) was prepared by electrodeposition using 0.5 M $Cu(NO_3)_2$ on carbon paper.[42] From Figure 2b, it becomes clear that a freshly prepared Cu EL released enormous amounts of NO_3^- (1499 ± 186 nmol cm^{-2}). Left-over NO_x^- can ideally be electroreduced with cyclic voltammetry by scanning the Cu EL between −0.2 and −0.7 V vs. RHE in 0.1 M KOH (see the Appendix B). More than 98% of the initial N-content was removed by this strategy, although the remaining ~30 nmol is still significant (Figure B12). Alternatively, metal nitrate hydrates can be thermally decomposed into metal oxides, water, and gaseous NO_x. The Cu EL was kept at 200 °C overnight because supported $Cu(NO_3)_2$ hydrate decomposition starts at 175 °C.[43] The thermal decomposition strategy was able to remove 99.3% of the initial N-content, indicating that it is more efficient than cyclic voltammetry. Moreover, this method was applied earlier to remove NO_x^- species from commercial metal oxide powders, and similar removal rates were reported.[12] Platinum foil is commonly used as an anode material due to its high stability. After excessively rinsing a 2.5 cm × 2.5 cm Pt foil with H_2O, approximately 6 nmol cm^{-2} of NO_x^- was released. This quantity is comparable with that found with the untreated Celgard membrane, which suggests that atmospheric adsorbed NO_x species on the Pt are more stable, forming most likely Pt mononitrosyls.[44] Flame annealing is an often used technique to remove organic impurities and to pre-oxidize the Pt surface. Interestingly, the flame annealing step provokes an increase in the N impurities (Figure B12). Sonicating the Pt foil in 0.1 M KOH or applying the thermal decomposition method was sufficient to reduce impurities to a bare minimum.

3.3.6 NO_3^- Assay of Common Used Lithium Salts in Li-NRR

NRR with electroplated lithium as a N_2 activator (Li-NRR) has recently gained significant scientific interest. There are, however, various concerns about high NO_3^- concentrations in Li-salts,[45] which can easily be converted to NH_3 in these extremely reduced environments. Herein, $LiClO_4$, $LiBF_4$, $LiPF_6$, and lithium bis(trifluoromethanesulfonyl)imide (LiTFSI, also abbreviated as $LiNTf_2$) are screened with dual-wavelength ultraviolet (UV) spectroscopy for NO_3^- quantification.[46] Figure 3 shows that $LiClO_4$ and $LiPF_6$ are free of NO_3^-. Clear UV absorbance at 210 nm (associated with NO_3^-) was measured for $LiBF_4$ and LiTFSI. Any organic interference at 210 nm was compensated by subtracting two times the absorbance at 270 nm (elaborated in the Appendix B). After this correction, LiTFSI has no noteworthy NO_3^-

absorbance, while LiBF$_4$ in Figure 3f shows a clear upward trend in NO$_3^-$ levels as a function of the salt concentration. It is important to note that NO$_3^-$ quantities can vary with different purities, suppliers, and batches.[45] Therefore, it is recommended to analyze Li-salts with this spectrophotometry method. NO$_2^-$ concentrations in all Li-salts were quantified by ion chromatography (IC) and remained negligible (<1 μmol L^{-1}). Ethereal solvents that are stable during Li-NRR, such as tetrahydrofuran, 1,2-dimethoxyethane, and 2-methoxyethyl ether, were screened by IC. Ethanol was also evaluated, since it is often used as a proton source for Li-NRR. None of the organic solvents showed any NO$_x^-$-related peak (Figure B13).
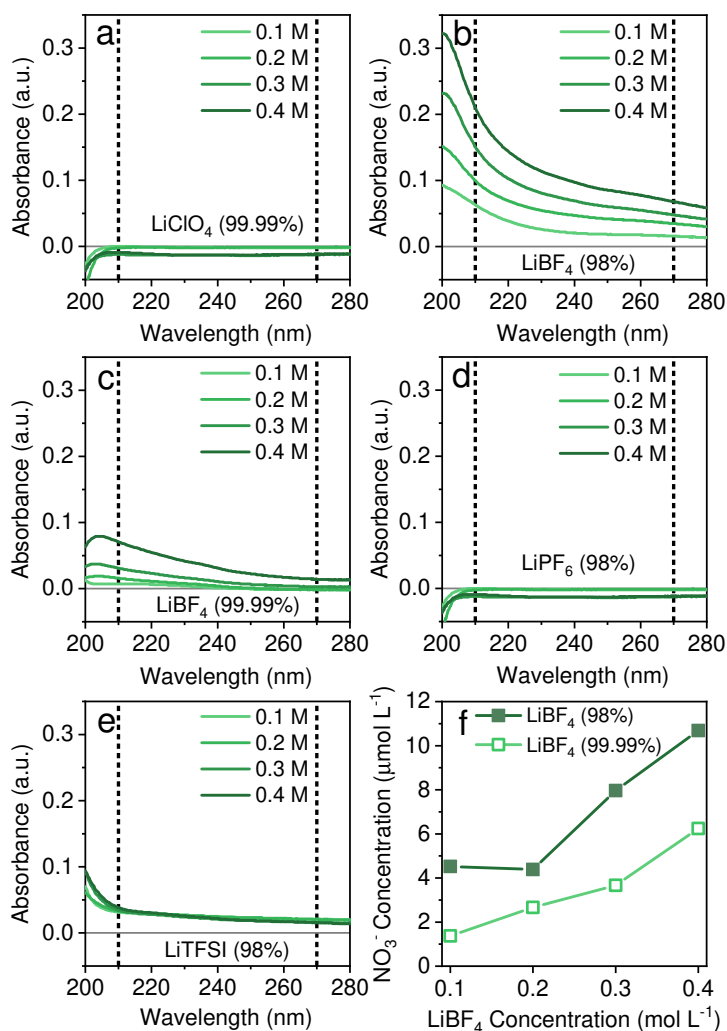
Figure 3. NO$_3^-$ assay showing UV spectra at different salt concentrations of (a) LiClO$_4$ (99.99%, Sigma), (b) LiBF$_4$ (98%, Sigma), (c) LiBF$_4$ (99.99%, Sigma), (d) LiPF$_6$ (98%, Honeywell), and (e) LiTFSI (98%, Sigma). (f) NO$_3^-$ concentrations as a function of the LiBF$_4$ concentration.

3.3.7 Implications of NO$_x$ Impurities for the Li-NRR experimentalists

Other extraneous N sources from atmospheric exposure are limited in Li-NRR systems because most handling and storage of solvents, salts, and cell materials are conventionally done in a glovebox, with the main motivation to control moisture content. The content of N contaminations in our feed gases and lab consumables is negligible (except $^{15}N_2$), thus only NO$_3^-$ impurities in the Li-salt seem to be relevant for Li-NRR. It is important to note that NO$_3^-$ (most likely present as LiNO$_3$) cannot simply be removed by a heat treatment,[45] since the decomposition temperature of LiNO$_3$ ($\geqslant 500$ °C) is much higher than those of LiBF$_4$, LiPF$_6$, and LiTFSI.[47] With the hypothetical experimental conditions stated in Figure 4, roughly 107 nmol of NO$_3^-$ can potentially be reduced into NH$_3$ during cell operation, leading to a yield of 0.12 nmol s^{-1} cm^{-2}. Our estimated NO$_3^-$ content can differ significantly if higher salt concentrations are used or with different Li-salt batches that contain more NO$_3^-$. Nevertheless, it is not realistic to expect that NH$_3$ yields obtained by the electroreduction of NO$_3^-$ will approach the recently obtained 2500 nmol s^{-1} cm^{-2} at 1 A cm^{-2},[48] and 150 nmol s^{-1} cm^{-2} at a current efficiency near unity (at 15–20 bar).[49] This, however, might not be true when the Li-NRR reports lower NH$_3$ yield (e.g., when operating at ~1 bar). Overall, we find that N impurities are less relevant for the Li-NRR field, although it remains good practice to assess the NO$_3^-$ content in the Li-salts to be certain of the origin of NH$_3$.

3.3.8 Estimating the Minimum Background Level for Aqueous NRR Measurements

In the NRR, the atmospheric N contributions are more severe, as experiments are generally not performed in a controlled environment, including storage of chemicals and cell materials in ambient air. By combining the most important findings from this study, as illustrated in Figure 4, a background level of ~140 nmol was estimated. By assuming that most NO$_x^-$ species electroreduce into NH$_3$, an obtained yield of 0.16 nmol s^{-1} cm^{-2} is already enough for a NRR catalyst to be labeled as plausible.[8] Approximately 84% of these impurities can be avoided by applying the most effective cleaning procedures. These are material dependent and include alkaline washing for membranes and electrodes, heat treatment for the Pt foil, desiccator storage for salts, and rinsing lab consumables with ultrapure water. Important factors such as catalyst impurities and the influence of gloves are excluded from this analysis because they may vary between studies. Extra care must be taken when validating electrocatalytic NRR activity with $^{15}N_2$ gas, since ppm levels of $^{15}NH_3$ were detected by our GC-MS and $^{15}NO_x$ by others. Cleaning the feed gases is not straightforward, since our analysis shows that commonly adopted liquid scrubbers do not properly eliminate the NO$_x$ contaminations, due to limited mass transport and reactivity. More importantly, the trapping efficiency should be evaluated at conditions close to experimental conditions, as we show that factors such as flow rate and duration of the experiment highly affect the removal efficiency. For these reasons we strongly recommend the application of commercial gas purifiers that exhibit the best performance at all relevant conditions. An absolute minimum background level is rather difficult to assess because of the large variety of

experimental approaches within the research community. Nevertheless, we provide experimentalists with recommendations and various cleaning procedures in order to reduce the effect of impurities to an acceptable minimum.
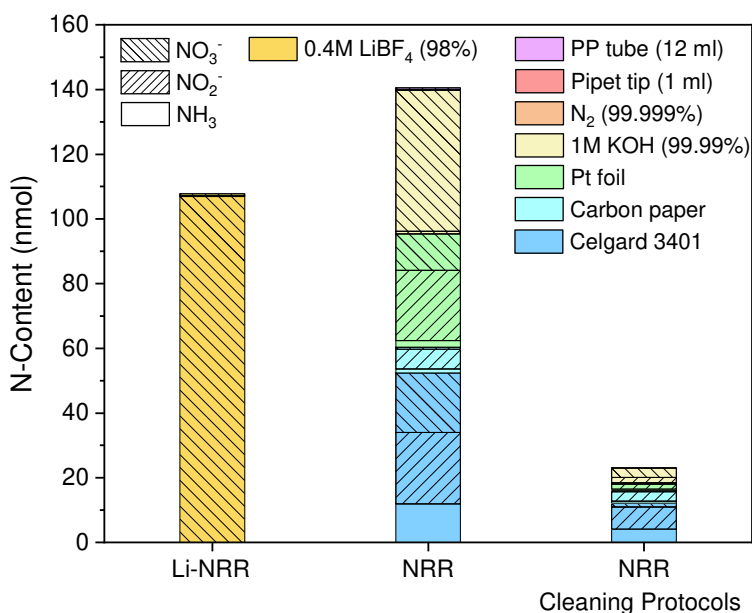
Figure 4. Estimation of the minimum background level of NH_3, NO_2^-, and NO_3^- with and without the most effective cleaning procedures. Values were obtained from Figure B12 and Tables B1–B4, assuming the N_2 flow (20 mL min^{-1}, 99.999%), membrane area (Celgard, 10 cm^2), working electrode (carbon paper, 1 cm^2), counter electrode (Pt foil, 4 cm^2), electrolyte (1 M KOH, 10 mL), 1 pipet tip, and 1 tube with a total experiment time of 15 min. For Li-NRR, only $^{14}N_2$ and electrolyte impurities were considered. The applied cleaning procedures for NRR were as follows: alkaline wash for Celgard 3401 membrane and carbon paper, heat treatment for Pt foil, KOH desiccator storage, and rinsing lab consumables with water.

3.4 Conclusions

In this work, we carried out a systematic investigation on the N contaminations derived from several sources and on the efficacy of multiple removal strategies. The aim of the study is to provide a benchmark to perform reliable electrochemical NRR studies. Notably, all the 99.999 % pure gases tested (N_2, He, Ar) were adequately clean as both NH_3 and NO/NO_2 were not detected (LOD_{NH3}: 150 ppb, LOD_{NOx}: 1 ppb). On the other hand, $^{15}N_2$ gas contains relatively large amounts of $^{15}NH_3$ and therefore a more rigorous purification is required. Our analysis shows that commonly adopted liquid scrubbers do not properly eliminate the NO_x contaminations from the feed gases, due to limited mass transport and reactivity. Importantly, the trapping efficiency should be evaluated at conditions close to experimental, as we show that factors such as flow rate and duration of the experiment highly affect the removal efficiency. For these reasons we strongly recommend the application of commercial gas purifiers that exhibit the best performance at all relevant conditions. The use of NH_3 and NO_x as precursors in synthesis procedures should be avoided, as it was not possible to sufficiently remove the remaining NO_x^- from a Cu electrodeposited electrode prepared with $Cu(NO_3^-)_2$. Another unresolvable observed issue is the NO_3^- content present in the chemical safety gloves. Even though its effect is difficult to assess in a quantitative manner, we consistently measured almost 1 ppm of NO_3^- after short contact with a membrane. The level of atmospheric NO_x in our laboratory was monitored, showing significant variations over time (1.5-27 ppb). These atmospheric NO_x species had a large impact on several materials commonly used during NRR experiments. As environmental exposure is inevitable, long term storage should be done in Ar gloveboxes or desiccators, which worked well for the electrolyte salts. To remove the already present N-species, the most effective treatments, depending on the material, include alkaline washing, heat treatment, and ultrapure water rinsing. Based on our conditions, we estimated that a typical NRR experiment would have a minimum background level of about 140 nmol, which can be reduced by 84% to 23 nmol following our cleaning procedures. An absolute minimum background level is rather difficult to assess because of the large variety of experimental approaches within the research community. Nevertheless, we provided experimentalists with recommendations and various tested cleaning procedures in order to reduce the effect of impurities to a bare minimum.

3.5 References

1   World fertilizer trends and outlook to 2022. *Food and Agriculture Organization of the United Nations* **2019**, 1-9. DOI: ISBN 978-92-5-131894-2.

2   Intelligence, M. *Ammonia Market - Growth, Trends, COVID-19 Impact, and Forecasts (2022 - 2027)*; 2021. https://www.researchandmarkets.com/reports/5682117/ammonia-market-forecasts-from-2022-to-2027?gclid=Cj0KCQjwtamlBhD3ARIsAARoaEzByEV7nMgHbYMoOj4ZzMgQEwAnJtHG1-v7ABXhVxX6V9DIzRlPvh0aAm5LEALw_wcB (accessed 2022-10-09).

3   Van Der Ham, C. J. M.; Koper, M. T. M.; Hettelscheid, D. G. H. Challenges in reduction of dinitrogen by proton and electron transfer. *Chemical Society Reviews* **2014**, *43* (15), 5183-5191. DOI: 10.1039/c4cs00085d.

4   MacFarlane, D. R.; Cherepanov, P. V.; Choi, J.; Suryanto, B. H. R.; Hodgetts, R. Y.; Bakker, J. M.; Ferrero Vallana, F. M.; Simonov, A. N. A Roadmap to the Ammonia Economy. *Joule* **2020**, *4*, 1186-1205. DOI: 10.1016/j.joule.2020.04.004.

5   Arias, P. A., N. Bellouin, E. Coppola, R.G. Jones, G. Krinner, J. Marotzke, V. Naik, M.D. Palmer, G.-K. Plattner, J. Rogelj,; M. Rojas, J. S., T. Storelvmo, P.W. Thorne, B. Trewin et al. *Technical Summary. In Climate Change 2021: The Physical Science Basis. Contribution of Working Group I to the Sixth Assessment Report of the Intergovernmental Panel on Climate Change* 2021. DOI: 10.1017/9781009157896.002 (accessed 2022-11-09).

6   Lim, J.; Fernández, C. A.; Lee, S. W.; Hatzell, M. C. Ammonia and Nitric Acid Demands for Fertilizer Use in 2050. *ACS Energy Letters* **2021**, *6* (10), 3676-3685. DOI: 10.1021/acsenergylett.1c01614.

7   Smith, C.; Hill, A. K.; Torrente-Murciano, L. Current and future role of Haber–Bosch ammonia in a carbon-free energy landscape. *Energy & Environmental Science* **2020**, *13* (2), 331-344, 10.1039/C9EE02873K. DOI: 10.1039/C9EE02873K.

8   Choi, J.; Suryanto, B. H. R.; Wang, D.; Du, H. L.; Hodgetts, R. Y.; Ferrero Vallana, F. M.; MacFarlane, D. R.; Simonov, A. N. Identification and elimination of false positives in electrochemical nitrogen reduction studies. *Nature Communications* **2020**, *11* (1), 1-10. DOI: 10.1038/s41467-020-19130-z.

9   Du, H. L.; Gengenbach, T. R.; Hodgetts, R.; Macfarlane, D. R.; Simonov, A. N. Critical Assessment of the Electrocatalytic Activity of Vanadium and Niobium Nitrides toward Dinitrogen Reduction to Ammonia. *ACS Sustainable Chemistry and Engineering* **2019**, *7* (7), 6839-6850. DOI: 10.1021/acssuschemeng.8b06163.

10   Hu, B.; Hu, M.; Seefeldt, L.; Liu, T. L. Electrochemical dinitrogen reduction to ammonia by Mo2N: catalysis or decomposition? *ACS Energy Letters* **2019**, *4* (5), 1053-1054.

11   Yu, W.; Buabthong, P.; Read, C. G.; Dalleska, N. F.; Lewis, N. S.; Lewerenz, H.-J.; Gray, H. B.; Brinkert, K. Cathodic NH 4 + leaching of nitrogen impurities in CoMo thin-film electrodes in aqueous acidic solutions †. *Sustainable energy & fuels* **2020**, *4*, 5080-5087. DOI: 10.1039/d0se00674b.

12   Chen, Y.; Liu, H.; Ha, N.; Licht, S.; Gu, S.; Li, W. Revealing nitrogen-containing species in commercial catalysts used for ammonia electrosynthesis. *Nature Catalysis* **2020**, *3*, 1055-1061. DOI: 10.1038/s41929-020-00527-4.

13   Kolen, M.; Ripepi, D.; Smith, W. A.; Burdyny, T.; Mulder, F. M. Overcoming nitrogen reduction to ammonia detection challenges: the case for leapfrogging to gas diffusion electrode platforms. *ACS catalysis* **2022**, *12* (10), 5726-5735.

14   Choi, J.; Du, H. L.; Nguyen, C. K.; Suryanto, B. H. R.; Simonov, A. N.; MacFarlane, D. R. Electroreduction of Nitrates, Nitrites, and Gaseous Nitrogen Oxides: A Potential Source of Ammonia in Dinitrogen Reduction Studies. *ACS Energy Letters* **2020**, *5* (6), 2095-2097. DOI: 10.1021/acsenergylett.0c00924.

15   Ko, B. H.; Hasa, B.; Shin, H.; Zhao, Y.; Jiao, F. Electrochemical Reduction of Gaseous Nitrogen Oxides on Transition Metals at Ambient Conditions. *Journal of the American Chemical Society* **2022**, *144* (3), 1258-1266. DOI: 10.1021/jacs.1c10535.

16   Dima, G. E.; De Vooys, A. C. A.; Koper, M. T. M. Electrocatalytic reduction of nitrate at low concentration on coinage and transition-metal electrodes in acid solutions. *Journal of Electroanalytical Chemistry* **2003**, *554-555* (1), 15-23. DOI: 10.1016/S0022-0728(02)01443-2.

17   Shibata, M.; Murase, K.; Furuya, N. Electroreduction of Nitrous Oxide to Nitrogen at Gas Diffusion Electrodes with Various Metal Catalysts. *Denki Kagaku oyobi Kogyo Butsuri Kagaku* **1997**, *65* (12), 1039-1043. DOI: 10.5796/kogyobutsurikagaku.65.1039.

18   Suryanto, B. H. R.; Du, H. L.; Wang, D.; Chen, J.; Simonov, A. N.; MacFarlane, D. R. Challenges and prospects in the catalysis of electroreduction of nitrogen to ammonia. *Nature Catalysis* **2019**, *2* (4), 290-296. DOI: 10.1038/s41929-019-0252-4.

19   Greenlee, L. F.; Renner, J. N.; Foster, S. L. The Use of Controls for Consistent and Accurate Measurements of Electrocatalytic Ammonia Synthesis from Dinitrogen. *ACS Catalysis* **2018**, *8* (9), 7820-7827. DOI: 10.1021/acscatal.8b02120.

20   Andersen, S. Z.; Čolić, V.; Yang, S.; Schwalbe, J. A.; Nielander, A. C.; McEnaney, J. M.; Enemark-Rasmussen, K.; Baker, J. G.; Singh, A. R.; Rohr, B. A.; et al. A rigorous electrochemical ammonia synthesis protocol with quantitative isotope measurements. *Nature* **2019**, *570* (7762), 504-508. DOI: 10.1038/s41586-019-1260-x.

21   Izelaar, B.; Ripepi, D.; Asperti, S.; Dugulan, A. I.; Hendrikx, R. W.; Böttger, A. J.; Mulder, F. M.; Kortlever, R. Revisiting the Electrochemical Nitrogen Reduction on Molybdenum and Iron Carbides: Promising Catalysts or False Positives? *ACS Catalysis* **2023**, *13*, 1649-1661.

22   Choi, J.; Du, H.-L.; Chatti, M.; Suryanto, B. H.; Simonov, A. N.; MacFarlane, D. R. Reassessment of the catalytic activity of bismuth for aqueous nitrogen electroreduction. *Nature Catalysis* **2022**, *5* (5), 382-384.

23   Huijsmans, J. F.; Schils, R. L. Ammonia and nitrous oxide emissions following field-application of manure: state of the art measurements in the Netherlands. 2009; International Fertiliser Society.

24   RIVM. *luchtmeetnet - NH3 and NO2*. 2014. https://www.luchtmeetnet.nl/componenten (accessed 2022-06-07).

3

25   Dentener, F.; Stevenson, D.; Ellingsen, K. v.; Van Noije, T.; Schultz, M.; Amann, M.; Atherton, C.; Bell, N.; Bergmann, D.; Bey, I. The global atmospheric environment for the next generation. *Environmental Science & Technology* **2006**, *40* (11), 3586-3594.

26   Zaffaroni, R.; Ripepi, D.; Middelkoop, J.; Mulder, F. M. Gas Chromatographic Method for In Situ Ammonia Quantification at Parts per Billion Levels. *ACS Energy Letters* **2020**, *5* (12), 3773-3777. DOI: 10.1021/acsenergylett.0c02219.

27   Ripepi, D.; Zaffaroni, R.; Kolen, M.; Middelkoop, J.; Mulder, F. M. Operando isotope selective ammonia quantification in nitrogen reduction studies via gas chromatography-mass spectrometry. *Sustainable Energy & Fuels* **2022**, *6* (8), 1945-1949, 10.1039/D2SE00123C. DOI: 10.1039/D2SE00123C.

28   Joe Eugene, L. S. M., Ferrenbach. Measurements of nitrogen fixation by direct means. In *Symbiotic Nitrogen Fixation Technology*, Taylor & Francis, 1987; pp 221-255.

29   Nielander, A. C.; Blair, S. J.; McEnaney, J. M.; Schwalbe, J. A.; Adams, T.; Taheri, S.; Wang, L.; Yang, S.; Cargnello, M.; Jaramillo, T. F. Readily Constructed Glass Piston Pump for Gas Recirculation. *ACS Omega* **2020**, *5* (27), 16455-16459. DOI: 10.1021/acsomega.0c00742.

30   Ripepi, D.; Zaffaroni, R.; Schreuders, H.; Boshuizen, B.; Mulder, F. M. Ammonia synthesis at ambient conditions via electrochemical atomic hydrogen permeation. *ACS Energy Letters* **2021**, *6* (11), 3817-3823.

31   Iriawan, H.; Andersen, S. Z.; Zhang, X.; Comer, B. M.; Barrio, J.; Chen, P.; Medford, A. J.; Stephens, I. E.; Chorkendorff, I.; Shao-Horn, Y. Methods for nitrogen activation by reduction and oxidation. *Nature Reviews Methods Primers* **2021**, *1* (1), 1-26.

32   Han, L.; Liu, X.; Chen, J.; Lin, R.; Liu, H.; Lü, F.; Bak, S.; Liang, Z.; Zhao, S.; Stavitski, E.; et al. Atomically Dispersed Molybdenum Catalysts for Efficient Ambient Nitrogen Fixation. *Angewandte Chemie* **2019**, *131* (8), 2343-2347. DOI: 10.1002/ANGE.201811728.

33   Wang, T.; Kou, Z.; Zhang, J.; Wang, H.; Zeng, Y. J.; Wei, S.; Zhang, H. Boosting Faradic efficiency of dinitrogen reduction on the negatively charged Mo sites modulated via interstitial Fe doping into a Mo2C nanowall catalyst. *Chemical Engineering Journal* **2021**, *417*, 127924-127924. DOI: 10.1016/J.CEJ.2020.127924.

34   Qin, B.; Li, Y.; Zhang, Q.; Yang, G.; Liang, H.; Peng, F. Understanding of nitrogen fixation electro catalyzed by molybdenum–iron carbide through the experiment and theory. *Nano Energy* **2020**, *68* (104374). DOI: 10.1016/j.nanoen.2019.104374.

35   Patwardhan, J. A.; Joshi, J. B. Unified Model for NOX Absorption in Aqueous Alkaline and Dilute Acidic Solutions. *AIChE Journal* **2003**, *49* (11), 2728-2748. DOI: 10.1002/aic.690491106.

36   Joshi, J. B.; Mahajani, V. V.; Juvekar, V. A. Absorption of nox gases. *Chemical Engineering Communications* **1985**, *33* (1-4), 1-92. DOI: 10.1080/00986448508911161.

37   Guo, R. T.; Hao, J. K.; Pan, W. G.; Yu, Y. L. Liquid Phase Oxidation and Absorption of NO from Flue Gas: A Review. *Separation Science and Technology (Philadelphia)* **2015**, *50* (2), 310-321. DOI: 10.1080/01496395.2014.956761.

38   Ishibashi, T.; Himeno, M.; Imaizumi, N.; Maejima, K.; Nakano, S.; Uchida, K.; Yoshida, J.; Nishio, M. NOx Contamination in Laboratory Ware and Effect of Countermeasures. *Nitric Oxide* **2000**, *4* (5), 516-525. DOI: 10.1006/NIOX.2000.0302.

39   Makela, S.; Yazdanpanah, M.; Adatia, I.; Ellis, G. Disposable Surgical Gloves and Pasteur (Transfer) Pipettes as Potential Sources of Contamination in Nitrite and Nitrate Assays. *Clinical Chemistry* **1997**, *43* (12), 2418-2420. DOI: 10.1093/CLINCHEM/43.12.2418.

40   Hanifpour, F.; Sveinbjörnsson, A.; Canales, C. P.; Skúlason, E.; Flosadóttir, H. D. Preparation of Nafion Membranes for Reproducible Ammonia Quantification in Nitrogen Reduction Reaction Experiments. *Angewandte Chemie International Edition* **2020**, *59* (51), 22938-22942. DOI: 10.1002/anie.202007998.

41   Shipman, M. A.; Symes, M. D. A re-evaluation of Sn (II) phthalocyanine as a catalyst for the electrosynthesis of ammonia. *Electrochimica Acta* **2017**, *258*, 618-622.

42   Kani, N. C.; Prajapati, A.; Collins, B. A.; Goodpaster, J. D.; Singh, M. R. Competing Effects of pH, Cation Identity, H 2 O Saturation, and N 2 Concentration on the Activity and Selectivity of Electrochemical Reduction of N 2 to NH 3 on Electrodeposited Cu at Ambient Conditions. *ACS Catalysis* **2020**, *10*, 14592-14603. DOI: 10.1021/acscatal.0c04864.

43   Małecka, B.; Łącz, A.; Drożdż, E.; Małecki, A. Thermal decomposition of d-metal nitrates supported on alumina. *Journal of Thermal Analysis and Calorimetry* **2015**, *119*, 1053-1061.

44   Prinetto, F.; Ghiotti, G.; Nova, I.; Lietti, L.; Tronconi, E.; Forzatti, P. FT-IR and TPD Investigation of the NO x Storage Properties of BaO / Al 2 O 3 and Pt - BaO. **2001**, *105* (51), 12732-12745.

45   Li, L.; Tang, C.; Yao, D.; Zheng, Y.; Qiao, S.-Z. Electrochemical Nitrogen Reduction: Identification and Elimination of Contamination in Electrolyte. *ACS Energy Letters* **2019**, *4* (9), 2111-2116. DOI: 10.1021/acsenergylett.9b01573.

46   Norman, R. J.; Edberg, J. C.; Stucki, J. W. Determination of nitrate in soil extracts by dual-wavelength ultraviolet spectrophotometry. *Soil Science Society of America Journal* **1985**, *49* (5), 1182-1185.

47   Lu, Z.; Yang, L.; Guo, Y. Thermal behavior and decomposition kinetics of six electrolyte salts by thermal analysis. *Journal of power sources* **2006**, *156* (2), 555-559.

48   Li, S.; Zhou, Y.; Li, K.; Vesborg, P. C. K.; Nørskov, J. K.; Li, S.; Zhou, Y.; Li, K.; Saccoccio, M.; Sa, R. Electrosynthesis of ammonia with high selectivity and high rates via engineering of the solid-electrolyte interphase Electrosynthesis of ammonia with high selectivity and high rates via engineering. *Joule* **2022**, *6* (9), 2083-2101. DOI: 10.1016/j.joule.2022.07.009.

49   Du, H.-L.; Chatti, M.; Hodgetts, R. Y.; Cherepanov, P. V.; Nguyen, C. K.; Matuszek, K.; MacFarlane, D. R.; Simonov, A. N. Electroreduction of nitrogen at almost 100% current-to-ammonia efficiency. *Nature* **2022**, *609* (7928), 722-727. DOI: 10.1038/s41586-022-05108-y.

Appendix B

Appendix Figures

3
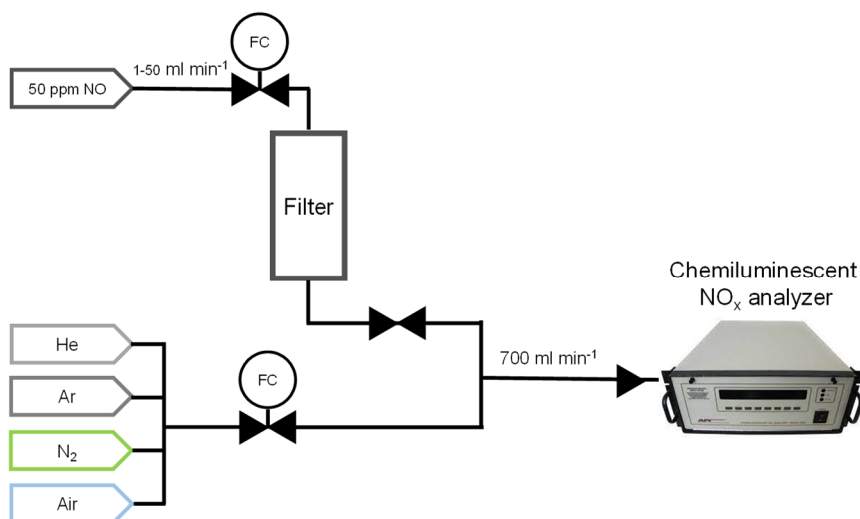
Figure B1. Schematic of the NO_x quantification measurements.
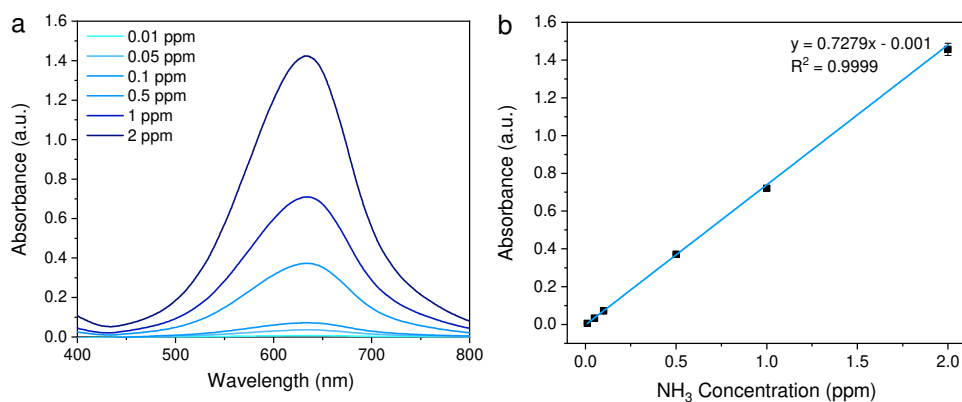
Figure B2. (a) UV-Vis spectra of different NH_3 concentrations in 0.1 M KOH. (b) Fitted calibration curve (blue) from the absorbance at 633 nm versus different NH_3 concentrations.
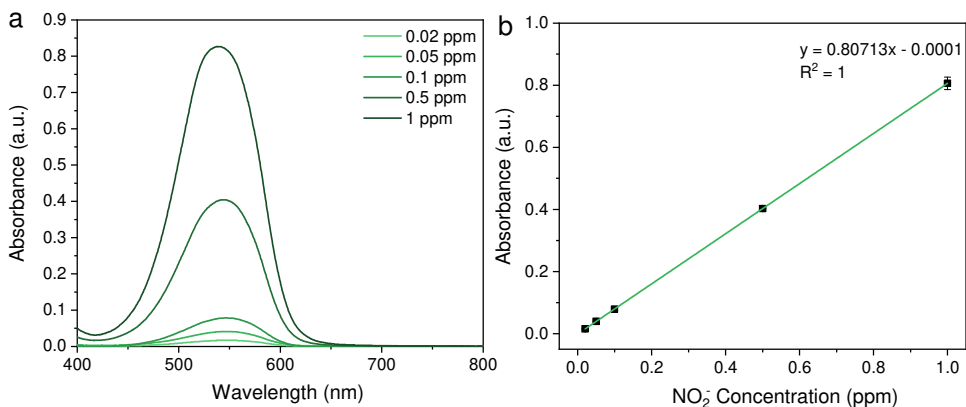
Figure B3. (a) UV-Vis spectra of different NO_2^- concentrations in 0.1 M KOH. (b) Fitted calibration curve (light green) from the absorbance at 542 nm versus different NO_2^- concentrations.
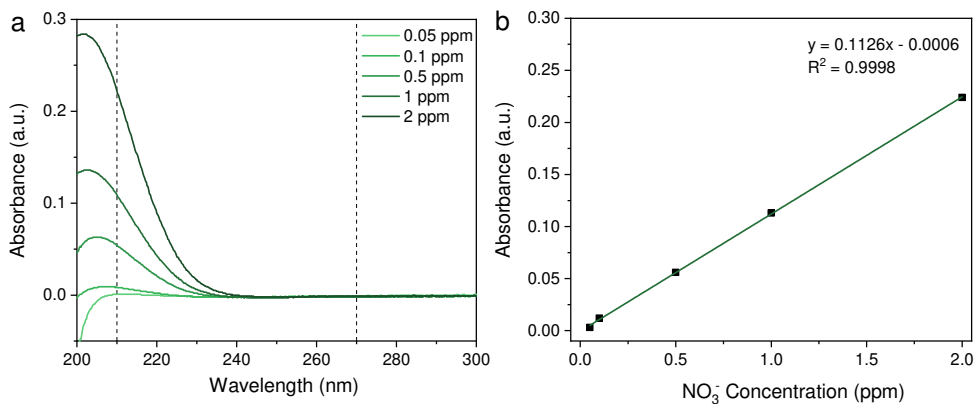
Figure B4. (a) UV spectra of different NO_3^- concentrations in H_2O. (b) Fitted calibration curve (dark green) from the absorbance at 210 nm versus different NO_3^- concentrations.
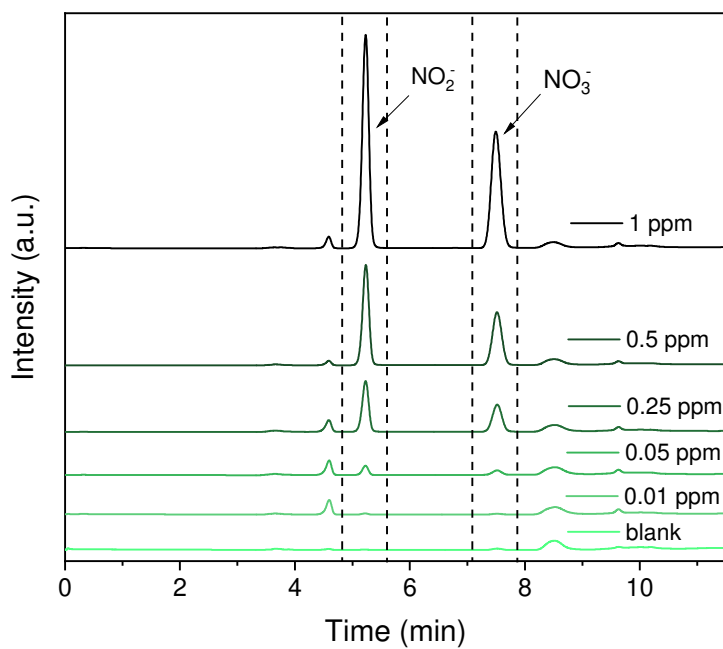
Figure B5. Ion chromatograms recorded at different NO_2^- and NO_3^- concentrations in H_2O.
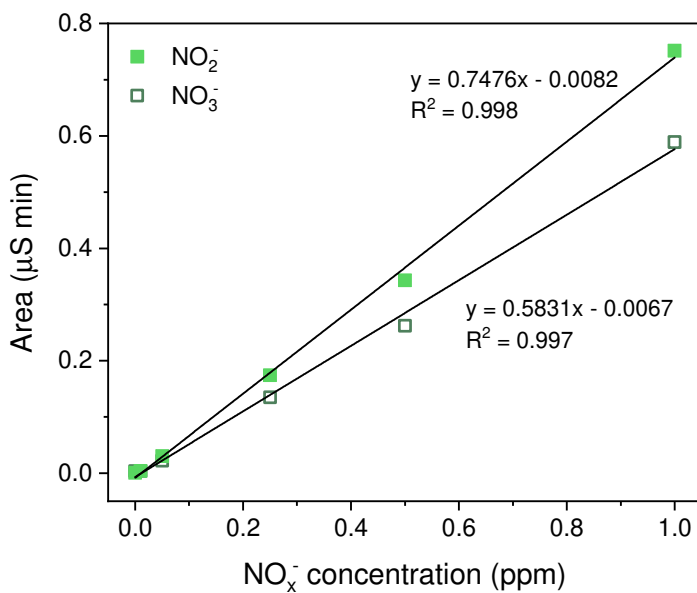
Figure B6. Ion chromatography calibration curves for NO_2^- and NO_3^- in H_2O.
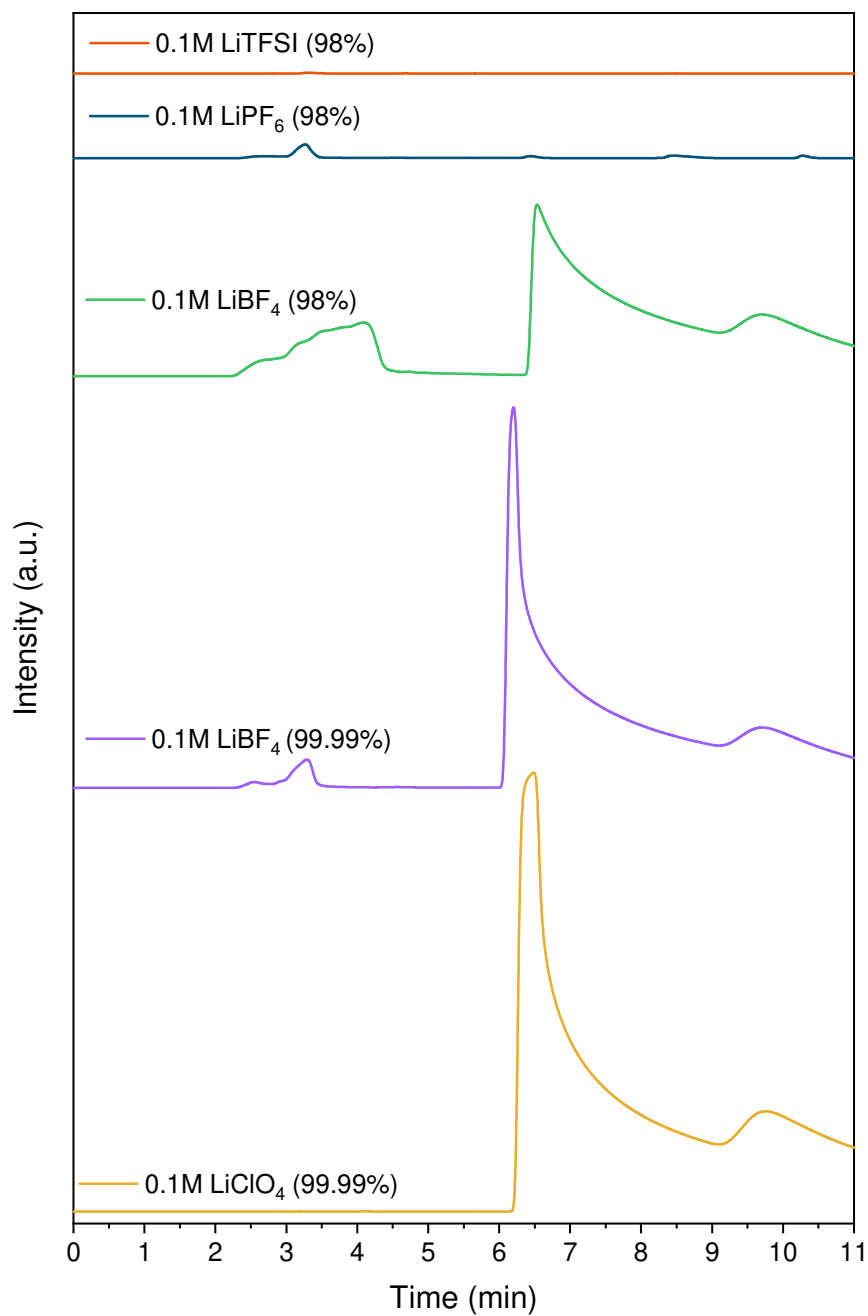
Figure B7. Ion chromatograms of diluted Li-salts concentrations in water.
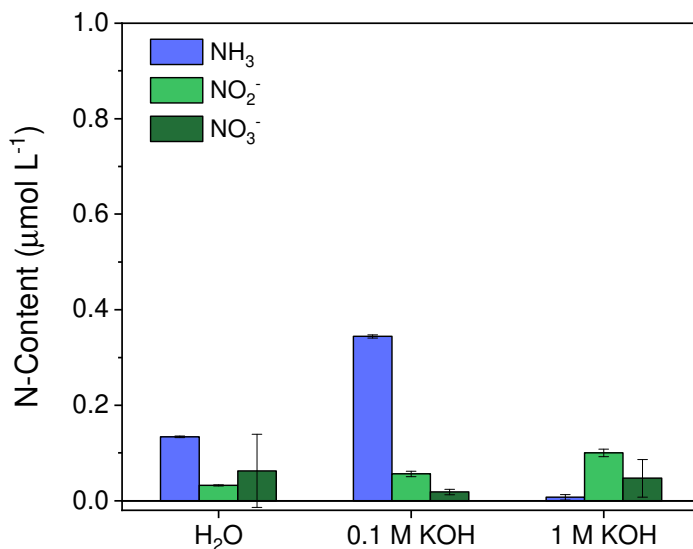
Figure B8. 24 hour open-to-air exposure of 2 ml H_2O, 0.1 M KOH and 1 M KOH in a 12 ml sample tube. The presented values are corrected with blank samples measured at t = 0. Error bar indicates the standard deviation of triplicates.
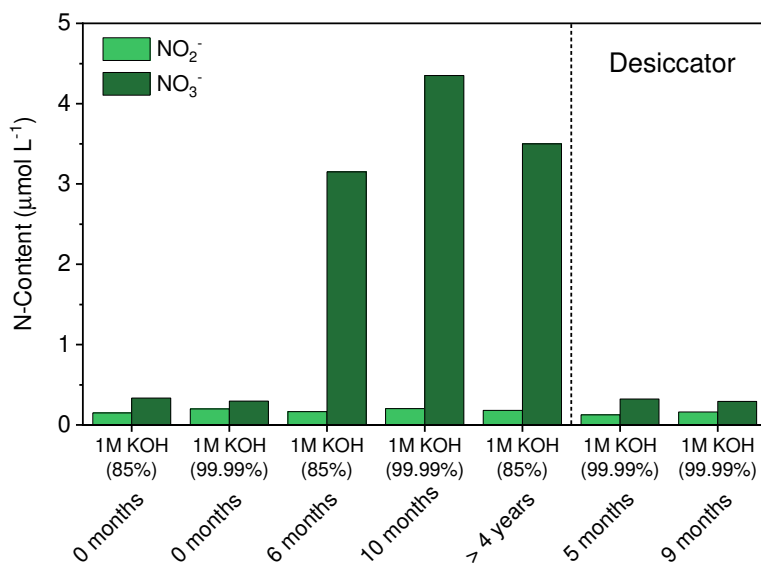
Figure B9. Comparison between KOH salt storage conditions in a chemical safety cabinet and vacuum desiccator. The projected impurity concentrations were quantified by IC using freshly prepared 1 M KOH solutions.
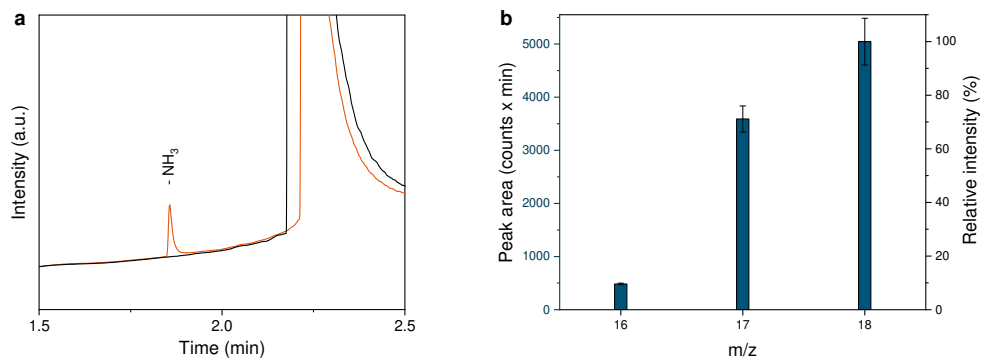
Figure B10. (a) Close up of the chromatograph around the ammonia elution time of the GC from the analysis of $^{15}N_2$ gas. Ammonia contaminations (9.8 ppm) are detected in the $^{15}N_2$ gas directly connected to the GC inlet (orange line). Interestingly, when the $^{15}N_2$ gas was dosed via a mass flow controller (not passivated against ammonia adsorption), no ammonia was detected (black line). (b) Integrated peak areas of the mass-to-charge ratio (m/z) of the ions detected with GC-MS at 1.84 min retention time (i.e. ammonia retention time). The relative intensity of the m/z corresponds to the $^{15}NH_3$ ionization fragments. Error bars correspond to the standard deviation of three independent measurements.
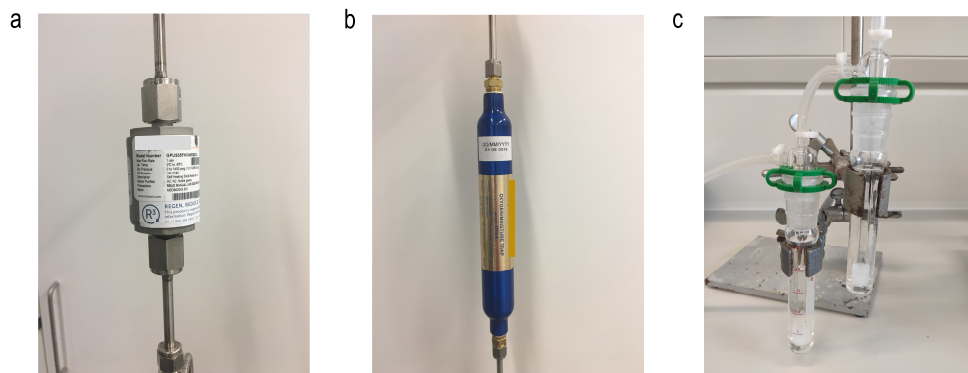
Figure B11. Photographs of the tested gas filters. (a) Entegris GPUS35FHX and (b) Agilent OT3-4 commercial packed gas filters. (c) Two 20 mL scrubbers (Supelco Analytical, 6-4835) with liquid trap solution connected in series.
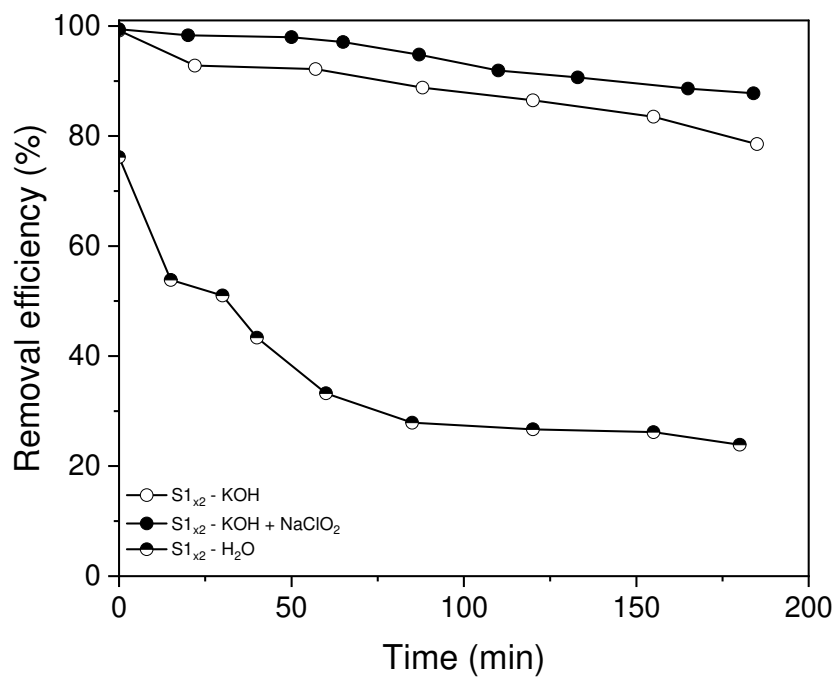
Figure B12. NOx removal efficiency over time, measured at 10 mL min^{-1} of 50 ppm NO in He for two 20 mL scrubbers (Supelco Analytical, 6-4835) connected in series containing MilliQ water (half-filled symbols), 0.1 M KOH (open symbols) and 0.1 M KOH + 0.1 M NaClO$_2$ (solid symbols) as with liquid trap solution.
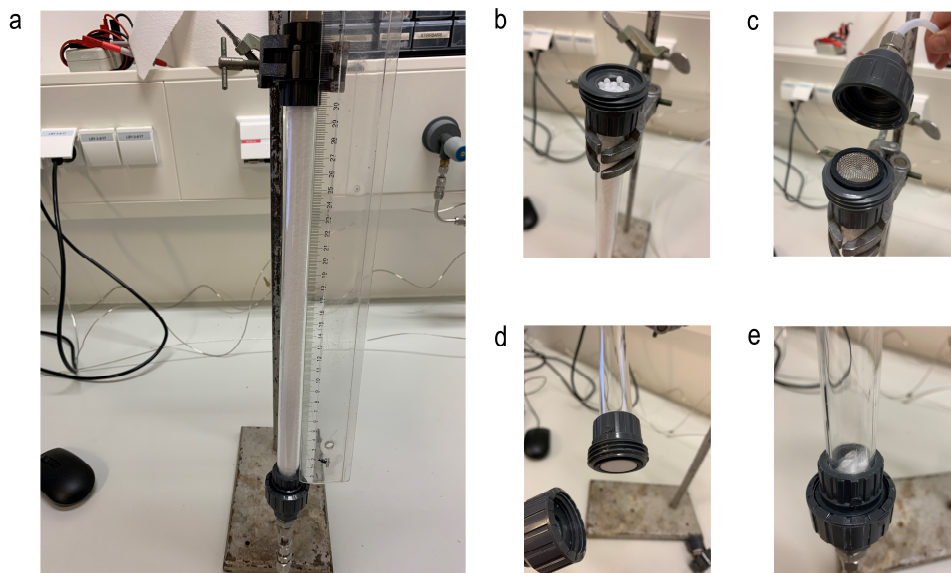
Figure B13. Photographs of the in-house made scrubber. (a) Assembled scrubber with 30 cm length and 1.5 cm diameter made of polymethyl-methacrylate. (b) Visible inert 1/8'' HDPE beads as packing material to improve the tortuosity were filled from the top part prior to each experiment, (c) and closed off with a stainless steel mesh to keep the beads in place during operation. (d) A hydrophobic frit (19.6 x 3.2 mm) was inserted at the bottom of the column (e) with an additional layer of glass wool.
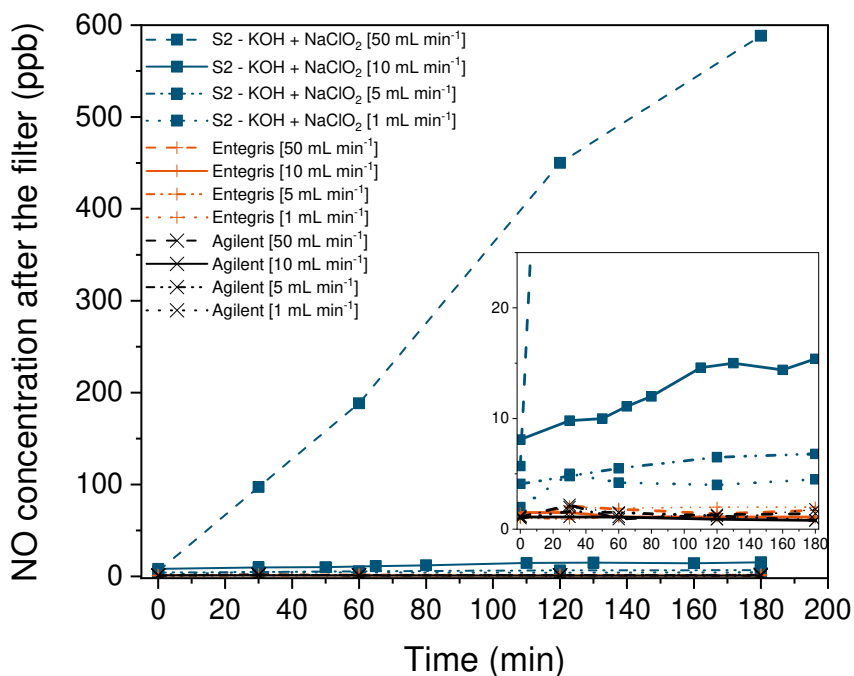
Figure B14. NO concentration measured over time at the outlet of each gas filter tested with an inlet gas mixture of 50 ppm NO in He at different flow rates (50 mL min^{-1} dashed line, 10 mL min^{-1} solid line, 5 mL min^{-1} dash-dot line, and 1 mL min^{-1} dotted line). In-house made scrubber (S2) filled with a 0.1 M KOH and 0.1 M NaClO$_2$ trapping solution is shown in blue, while the commercial Entegris and Agilent packed filters are shown in orange and black, respectively.
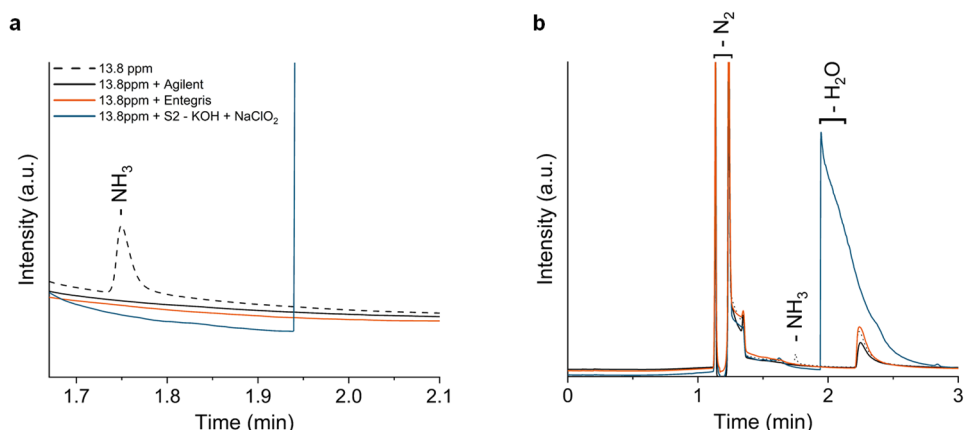
Figure B15. (a) Close up of the chromatograph around the ammonia elution time obtained from the analysis of a 13.8 ppm NH_3 in N_2 calibration gas flowing at 10 mL min^{-1} connected directly to the GC (dashed black line) and purified with the Agilent OT3-4 filter (solid black line), Entegris GPUS35FHX filter (solid orange line) and in-house made scrubber (S2) filled with a 0.1 M KOH and 0.1 M $NaClO_2$ trapping solution (solid blue line) prior entering the GC. All the ammonia contained in the gaseous analyte is captured by the filters. (b) Full chromatograph highlighting that the purification with the in-house made scrubber introduces a significant amount of water into the feed gas.
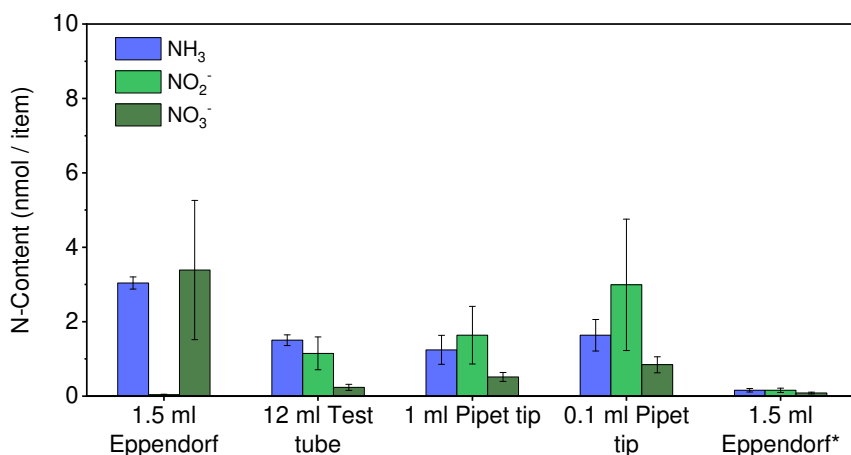
Figure B16. Screening of various lab consumables stocked in our laboratory. 1.5 ml and 12 ml polypropylene sample tubes were completely filled with 0.1 M KOH. The 0.1 ml and 1 ml polypropylene pipet tips were transferred into a pre-cleaned sample tube filled with 12 ml and 6 ml of 0.1 M KOH, respectively. All consumables were sonicated for 15 min. This procedure was repeated 5 times using the same solution. *Directly analysed after arrival.
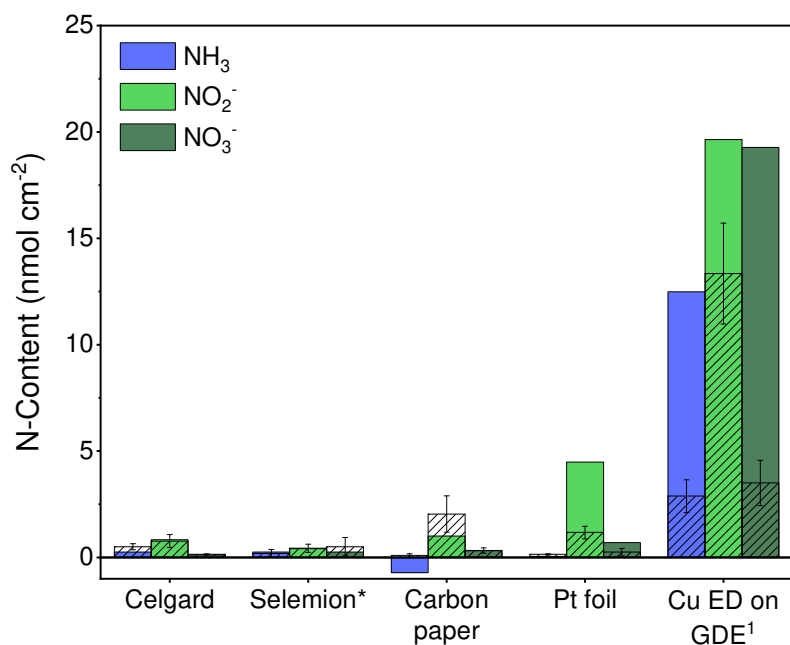
Figure B16. Release of N impurities after 1 hour sonication in 0.1 M KOH after the following pre-treatment steps; 15 min of ultra-sonication in 0.1 M KOH; [1] rinsed with H_2O and isopropanol, than electrochemically reduced by performing 10 cyclic voltammetry scans with in a reduction regime (-0.2 V to -0.7 V vs. RHE) and rinsed with H_2O afterwards as elaborately described in ref [3].* NO_2^- was quantified with the spectrophotometric Griess test due to identified Cl^- overlap in the ion chromatogram.
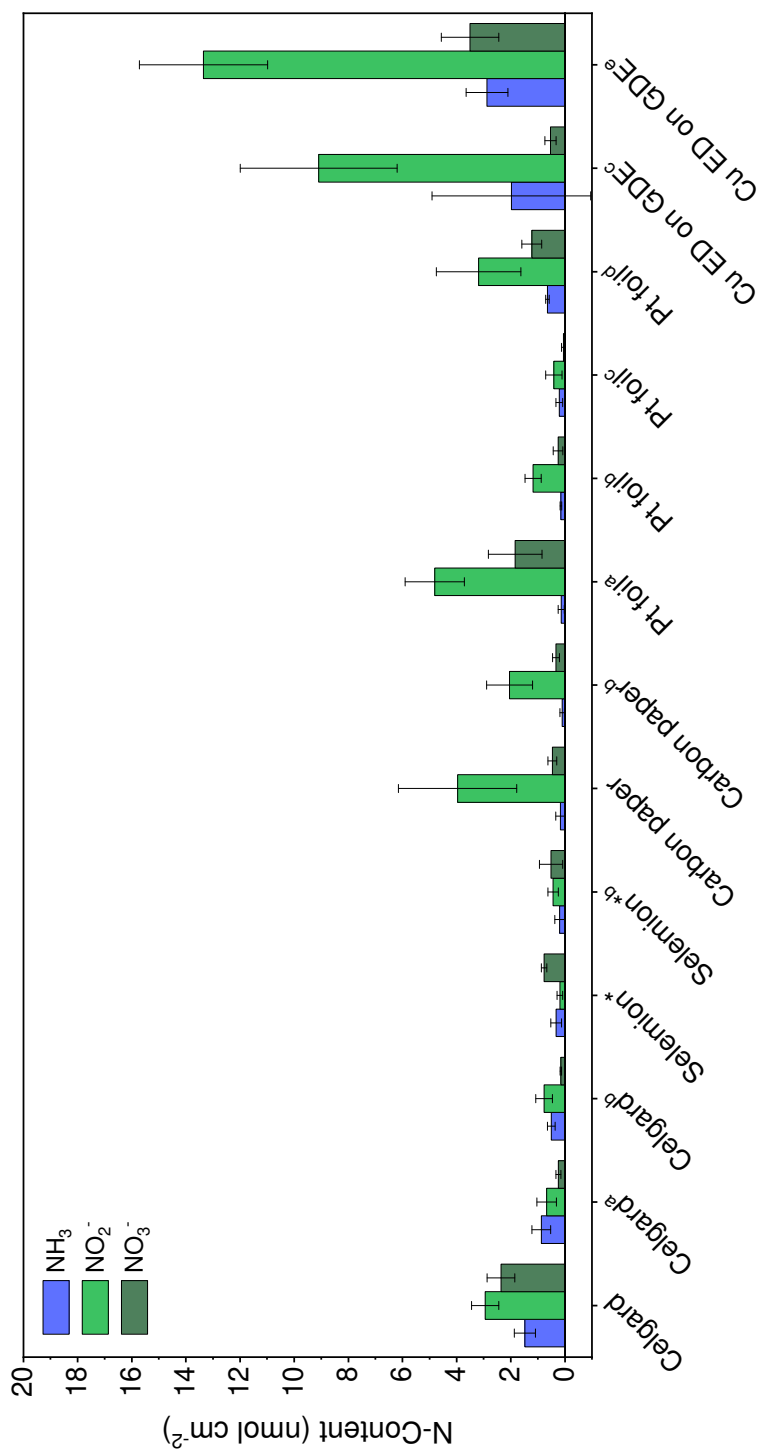
Figure B17. Screening of typical electrochemical cell components and the effectiveness of various cleaning procedures. Obtained concentrations of NH_3, NO_2^- and NO_3^- were converted to nmol and normalized by the geometric area. All components, except the carbon paper had a 2.5 cm x 2.5 cm dimension. The carbon paper and Cu GDE were finely cutted discs with a diameter of 1.2 cm. The cell materials were ultra-sonicated in 5 ml of 0.1 M KOH for 15 min with different pre-treatment steps. Indicated as unlabelled is untreated and fetched from the as received package. (a) rinsed excessively with H_2O, (b) sonicated for 15 min in 0.1 M KOH, (c) thermal decomposition in Ar at 200 °C overnight (12 hours), (d) sonicated for 15 min in 0.1 M KOH plus flame annealing with butane flame torch, (e) rinsed with H_2O and isopropanol, than electrochemically reduced by performing 10 cyclic voltammetry scans with only reductive currents (-0.2 V to -0.7 V vs. RHE) and rinsed with H_2O afterwards as elaborately described in ref [3]. * NO_2^- assay performed with the spectrophotometric Griess test due to identified Cl^- overlap with NO_2^- in the ion chromatogram. Every component is measured in triplicates.
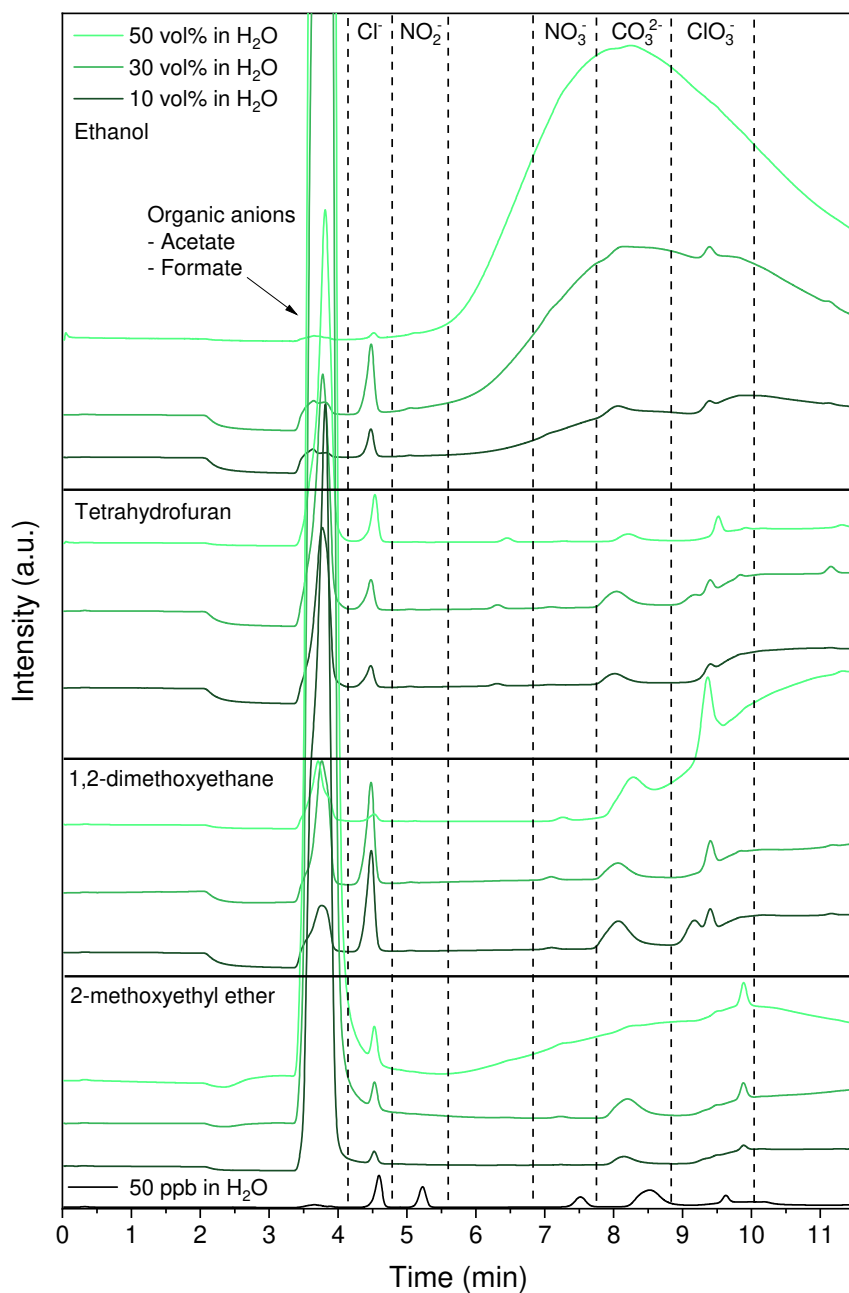
Figure B18. Ion chromatograms of 10, 30 and 50 vol% of ethanol, tetrahydrofuran, 1,2-dimethoxyethane, 2-methoxyethane in H_2O. An extra ion chromatogram of 50 ppb NO_2^- and NO_3^- in H_2O is plotted as reference. Organic anions, chloride, carbonate and chlorate were also identified by using reference data.[6]
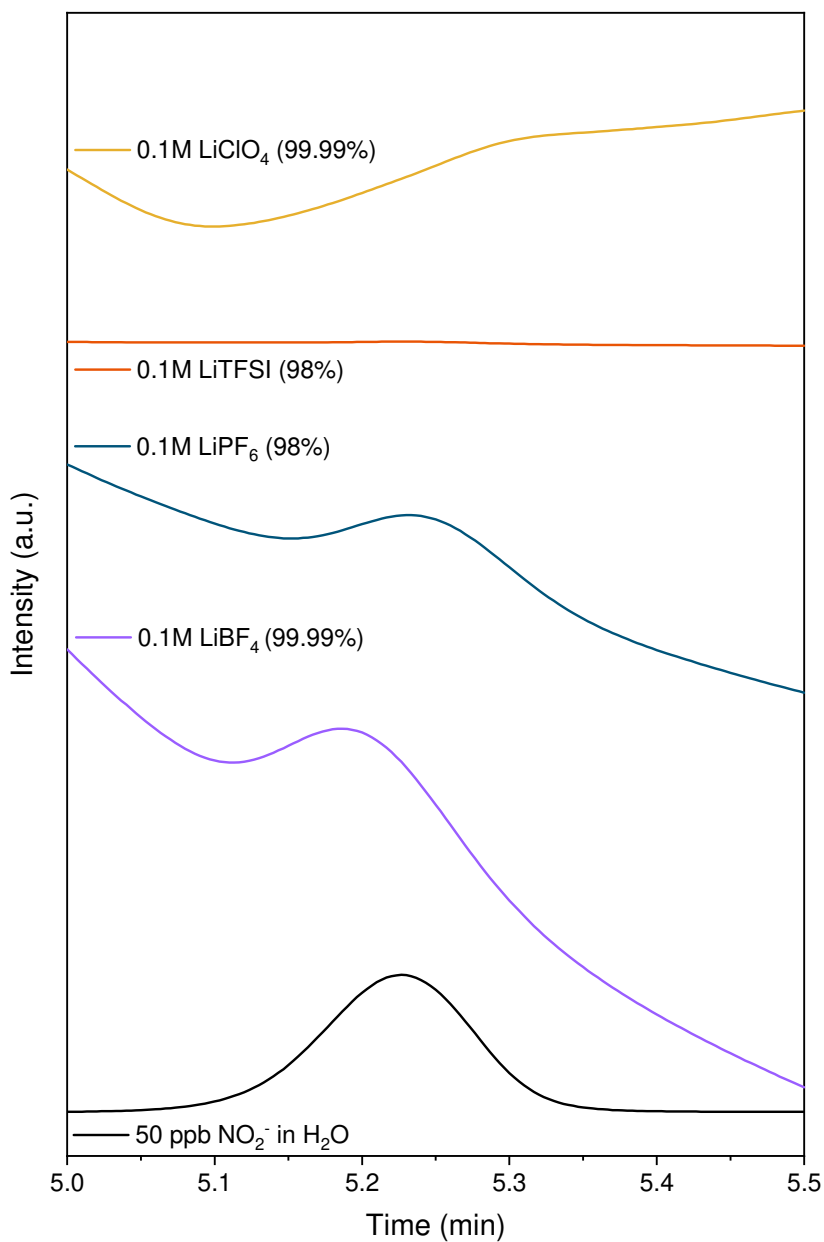
Figure B19. NO_2^- peaks in the ion chromatograms of various diluted Li-salts in H_2O and 50 ppb NO_2^- in H_2O.
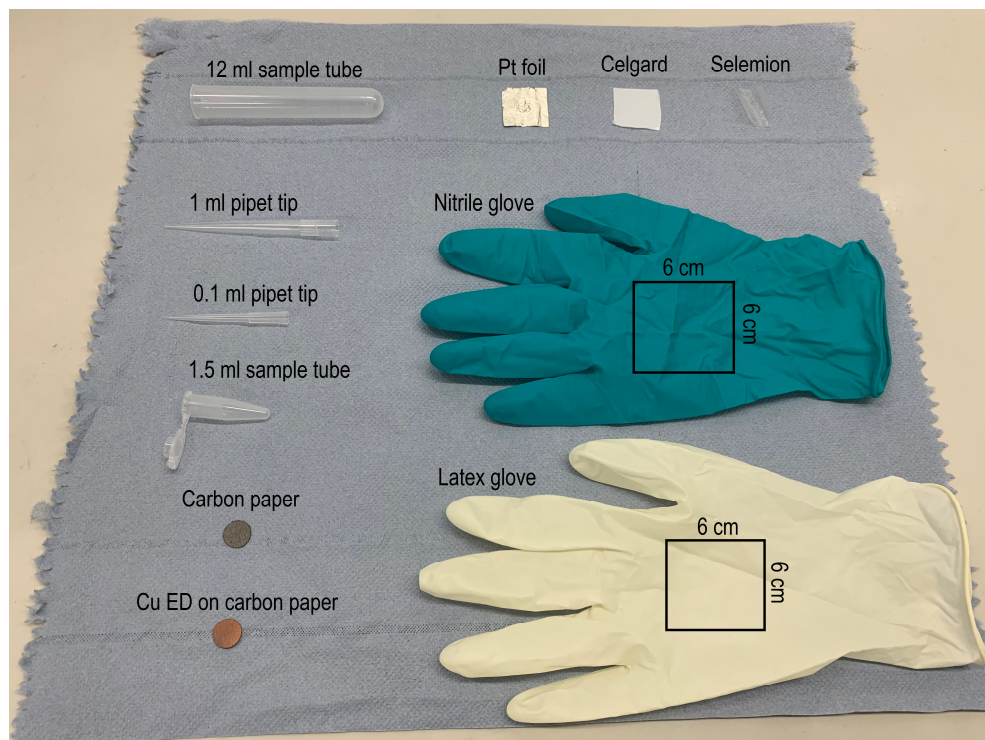
Figure B20. Photographic overview of the lab consumables and components used for screening.

Appendix Tables

Table B1. Data summary of feed gas and ambient impurities measured in the present study and complemented by literature values.

Compounds	NH$_3$ (ppm)	NO$_x$ (ppm)	Ref
Ambient air	0.003-0.022	0.015-0.04	[7]
		0-0.0048	[8]
		0.0015-0.027	This work
Human breath	0.03-3		[9]
	0.28-1.4		[10]
He (99.999%)	<0.15	0.0011	This work
^{14}N$_2$ (99.999%)	<0.15	0.0019	This work
		0.0031	[8]
^{15}N$_2$ (99%)	9.8 (^{15}NH$_3$)		This work
	0–1.61	0–1.03	[11]
Ar (99.999%)	<0.15	0.0018	This work
		0.0013	[8]

Table B2. Data summary of impurities in lab consumables measured in the present study and complemented by literature values.

Lab consumables	NH_3^+ (nmol / item)	NO_2^- (nmol / item)	NO_3^- (nmol / item)	Ref
15 ml tube (borosilicate)		0.007	0.66	[12]
15 ml tube (soda lime)		0.003	1.42	[12]
15 ml tube (polypropylene)		0.002	0.56	[12]
12 ml tube (polypropylene)	1.5	1.15	0.23	This work
1.5 ml tube (polypropylene)	0.16 - 3.04	0.035 - 0.16	0.08 - 3.39	This work
1 ml pipet tip (polypropylene)		0 - 0.003	0.011 - 0.11	[12]
	1.24	1.64	0.52	This work
0.2 ml pipet tip (polypropylene)		0.0008	0.005	[12]
0.1 ml pipet tip (polypropylene)	1.65	2.99	0.84	This work
Latex gloves		0-1500	0-152000	[13]
	569.4	10.7	(full glove)	This work
	182.5	3.35	10168 (finger tips)	This work
			297 (patch 6x6 cm)	
Nitrile gloves	276.2	20.3	9141 (finger tips)	This work
	132.5	10.2	850 (patch 6x6 cm)	
	1644 (patch 5 cm^2)			[9]

3

Table B3. Data summary of impurities in various cell components and materials measured in the present study and complemented by literature values.

Materials	NH_3 (nmol cm^{-2})	NO_2^- (nmol cm^{-2})	NO_3^- (nmol cm^{-2})	Ref
Nafion	1 - 25			9, 14, 15
Selemion	0.3	0.2	0.8	
Celgard 3401	1.5	2.9	2.3	This work
				This work
Carbon paper	0.2	4	0.5	This work
Pt foil	0.14	4.8	1.8	This work
Cu electrodeposited on carbon paper (Prepared with $CuNO_3$)	4.8	59	1499	This work
Fe_2O_3		0	41.7 nmol mg^{-1}	16
Bi_2O_3		23.5 nmol mg^{-1}	92.3 nmol mg^{-1}	
Al_2O_3		1.98 nmol mg^{-1}	47.6 nmol mg^{-1}	

Table B4. Data summary of impurities in electrolytes and organic solvents measured in the present study and complemented by literature values.

Electrolytes and solvents	NO_2^- (µmol L^{-1})	NO_3^- (µmol L^{-1})	Ref
1 M KOH (85%, Sigma)	0.147	0.333	This work
1 M KOH (99.99%, Sigma)	0.198	0.297	
0.5 M Li$_2$SO$_4$	0.713	0 – 180.5	[17]
0.5 M LiClO$_4$		22.4 – 38.4	
0.1 M LiClO$_4$ (99.99%, Sigma)	0.485	0*	This work
0.4 M LiClO$_4$		0*	
0.1 M LiBF$_4$ (98%, Sigma)		4.53	
0.4 M LiBF$_4$		10.69	
0.1 M LiBF$_4$ (99.99%, Sigma)	0.776	1.385	
0.4 M LiBF$_4$		6.25	
0.1 M LiPF$_6$ (98%, Honeywell)	0.385	0*	
0.4 M LiPF$_6$		0*	
0.1 M LiTFSI (98%, Sigma)	0*	0*	
0.4 M LiTFSI		1.23	
10vol% ethanol (anhydrous, VWR)	0.016	0.043	This work
50vol% ethanol	0.009		
10vol% Tetrahydrofuran (anhydrous, 99.5%, Sigma)	0.012	0.172	
50vol% Tetrahydrofuran	0*	0.024	
10vol% 1,2-dimethoxyethane (anhydrous, 99.5%, Sigma)	0.009	0.091	
50vol% 1,2-dimethoxyethane	0	0.177	
10vol% 2-methoxyethyl ether (anhydrous, 99.5%, Sigma)	0*	0.204	
50vol% 2-methoxyethyl ether	0*	0.266	

*Lower than the background, therefore assumed to be 0.

Appendix References

1   Zaffaroni, R.; Ripepi, D.; Middelkoop, J.; Mulder, F. M. Gas Chromatographic Method for In Situ Ammonia Quantification at Parts per Billion Levels. *ACS Energy Letters* **2020**, *5* (12), 3773-3777. DOI: 10.1021/acsenergylett.0c02219.

2   Ripepi, D.; Zaffaroni, R.; Kolen, M.; Middelkoop, J.; Mulder, F. M. Operando isotope selective ammonia quantification in nitrogen reduction studies via gas chromatography-mass spectrometry. *Sustainable Energy & Fuels* **2022**, *6* (8), 1945-1949, 10.1039/D2SE00123C. DOI: 10.1039/D2SE00123C.

3   Kani, N. C.; Prajapati, A.; Collins, B. A.; Goodpaster, J. D.; Singh, M. R. Competing Effects of pH, Cation Identity, H 2 O Saturation, and N 2 Concentration on the Activity and Selectivity of Electrochemical Reduction of N 2 to NH 3 on Electrodeposited Cu at Ambient Conditions. *ACS Catalysis* **2020**, *10*, 14592-14603. DOI: 10.1021/acscatal.0c04864.

4   Weatherburn, M. W. Phenol-Hypochlorite Reaction for Determination of Ammonia. *Analytical Chemistry* **1967**, *39* (8), 971-974. DOI: 10.1021/ac60252a045.

5   ThermoFisher. *Application Notes: 72481 IC trace anions concentrated bases*. https://assets.thermofisher.com/TFS-Assets/CMD/Application-Notes/an-72481-ic-trace-anions-concentrated-bases-an72481-en.pdf (accessed 2022-20-8).

6   ThermoScientific. Errata - Product Manual for Dionex IonPac AS18 and AG18 Columns. 2012.

7   RIVM. *luchtmeetnet - NH3 and NO2*. 2014. https://www.luchtmeetnet.nl/componenten (accessed 2022-06-07).

8   Yu, W.; Buabthong, P.; Read, C. G.; Dalleska, N. F.; Lewis, N. S.; Lewerenz, H.-J.; Gray, H. B.; Brinkert, K. Cathodic NH 4 + leaching of nitrogen impurities in CoMo thin-film electrodes in aqueous acidic solutions †. *Sustainable energy & fuels* **2020**, *4*, 5080-5087. DOI: 10.1039/d0se00674b.

9   Andersen, S. Z.; Čolić, V.; Yang, S.; Schwalbe, J. A.; Nielander, A. C.; McEnaney, J. M.; Enemark-Rasmussen, K.; Baker, J. G.; Singh, A. R.; Rohr, B. A.; et al. A rigorous electrochemical ammonia synthesis protocol with quantitative isotope measurements. *Nature* **2019**, *570* (7762), 504-508. DOI: 10.1038/s41586-019-1260-x.

10   Larson, T. V.; Covert, D. S.; Frank, R.; Charlson, R. J. Ammonia in the human airways: neutralization of inspired acid sulfate aerosols. *Science* **1977**, *197* (4299), 161-163.

11   Dabundo, R.; Lehmann, M. F.; Treibergs, L.; Tobias, C. R.; Altabet, M. A.; Moisander, P. H.; Granger, J. The Contamination of Commercial 15N2 Gas Stocks with 15N–Labeled Nitrate and Ammonium and Consequences for Nitrogen Fixation Measurements. *PLOS ONE* **2014**, *9* (10), e110335-e110335. DOI: 10.1371/JOURNAL.PONE.0110335.

12   Ishibashi, T.; Himeno, M.; Imaizumi, N.; Maejima, K.; Nakano, S.; Uchida, K.; Yoshida, J.; Nishio, M. NOx Contamination in Laboratory Ware and Effect of Countermeasures. *Nitric Oxide* **2000**, *4* (5), 516-525. DOI: 10.1006/NIOX.2000.0302.

13   Makela, S.; Yazdanpanah, M.; Adatia, I.; Ellis, G. Disposable Surgical Gloves and Pasteur (Transfer) Pipettes as Potential Sources of Contamination in Nitrite and

Nitrate Assays. *Clinical Chemistry* **1997**, *43* (12), 2418-2420. DOI: 10.1093/CLINCHEM/43.12.2418.

14   Hanifpour, F.; Sveinbjörnsson, A.; Canales, C. P.; Skúlason, E.; Flosadóttir, H. D. Preparation of Nafion Membranes for Reproducible Ammonia Quantification in Nitrogen Reduction Reaction Experiments. *Angewandte Chemie International Edition* **2020**, *59* (51), 22938-22942. DOI: 10.1002/anie.202007998.

15   Liu, H.; Zhang, Y.; Luo, J. The removal of inevitable NOx species in catalysts and the selection of appropriate membrane for measuring electrocatalytic ammonia synthesis accurately. *Journal of Energy Chemistry* **2020**, *49* (x), 51-58. DOI: 10.1016/j.jechem.2020.01.029.

16   Chen, Y.; Liu, H.; Ha, N.; Licht, S.; Gu, S.; Li, W. Revealing nitrogen-containing species in commercial catalysts used for ammonia electrosynthesis. *Nature Catalysis* **2020**, *3* (12), 1055-1061. DOI: 10.1038/s41929-020-00527-4.

17   Li, L.; Tang, C.; Yao, D.; Zheng, Y.; Qiao, S.-Z. Electrochemical Nitrogen Reduction: Identification and Elimination of Contamination in Electrolyte. *ACS Energy Letters* **2019**, *4* (9), 2111-2116. DOI: 10.1021/acsenergylett.9b01573.

3

3

4

The Effect of Potential on the Li-mediated NRR Performance

Abstract

The current understanding of the Li-mediated NRR reaction mechanism and specifically its relationship with the applied potential remains limited. Herein, we investigated if there is a dependency between the applied potential and the Li-NRR performance indicators, such as the electrochemical stability, NH_3 production rate and the Faradaic efficiency (FE_{NH3}). To do this, a partially delithiated sheet of Li_xFePO_4 was implemented in a homemade three electrode autoclave cell as a reliable and stable reference electrode. The Li-NRR experiments were executed under 20 bar of N_2 pressure using LiTFSI and 0.1 M EtOH dissolved in THF as a high performance electrolyte. Cyclic voltammetry measurements did not show any peak besides Li plating and stripping, suggesting that both the N_2 activation and protonation steps are chemical by nature. With 2 M LiTFSI, the chronoamperometry measurements at >-3.23 V vs. SHE were stable, but the FE_{NH3} remained below 15% and increased to 50% at potentials <-3.43 V vs. SHE. This suggests that an overpotential of ~0.4 V is required to reach a desirable selectivity. At applied potentials <-3.74 V vs. SHE, the current response was very unstable and deteriorate over time. This negatively affected the R_{NH3}, but not the Faradaic efficiency, which remained at ~50%. XPS analysis reveals that the SEIs were mostly enriched with LiF. The ratio between inorganic and organic compounds in the layer varied with the applied potential but does not fully explain the potential effect on the Li-NRR. More fundamental work on the electrode interface needs to be done in order to get a better understanding of the relationship between the potential and the performance.

4.1 Introduction

The electrochemical nitrogen reduction reaction (NRR) in aqueous electrolytes is seen as a promising sustainable route towards green ammonia synthesis. However, most of the publications that incorporated all the necessary control experiments,[1-3] report impractical NH_3 production rates (<0.001 A cm^{-2}) and Faradaic efficiencies (<1%).[4-9] A potentially more successful approach for electrochemical ammonia synthesis is based on non-aqueous Li-mediated NRR (Li-NRR), which was initially studied in the 1990s by Tsuneto et al.,[10,11] but was only recently further explored. Measurements performed with isotope labelled $^{15}N_2$ gas by independent laboratories have irrevocably confirmed electrochemical ammonia synthesis by Li-NRR,[1,12] where evidence for N_2 activation in aqueous conditions remains absent. By now, it is commonly accepted that electroplated Li^0 from Li^+, spontaneously dissociates N_2 into Li_3N, and undergoes either several hydrolysis or proton-coupled electron transfer (PCET) steps using EtOH as proton source to form NH_3.[13-15]

In analogy to Li-metal batteries, electroplated Li^0 reacts instantaneously with elements in the surrounding electrolyte, forming a layer of insoluble and partially soluble reduction products. This layer forms an electronically insulating barrier of "solidified electrolyte" that shields Li^0 from the surrounding electrolyte, but is at the same time ionically conductive for Li^+.[16] The composition of this solid electrolyte interphase (SEI) depends on the species in the Li^+ ion solvation shell, which are preferentially reduced during the stage of initial charging.[17] The structure of an ideal SEI has both a compact inorganic layer at the Li/SEI interface, and a porous organic layer at the SEI/electrolyte side.[16] The inorganic layer prevents excessive growth of the SEI because it is mostly selective towards Li^+ diffusion. For Li-NRR, engineering towards a more inorganic SEI has led to a significant improvement in electrochemical stability.[12,17,18] This was accomplished by increasing the electrolyte concentration, or incorporating decomposable additives, such as dimethyl sulfide into the electrolyte.[19]

Theoretical work suggests that the Li-NRR elementary reaction steps are fast due to the very negative potentials applied for Li plating (<-3 V vs. SHE), meaning that the diffusion of reactant species (Li^+, N_2 and H^+) through the SEI is the rate limiting step.[14,18] Especially the Li^+ diffusion rate is influenced by the inorganic composition of the SEI. Experimental results point out that LiF enriched SEI's derived from 2 M $LiBF_4$ in 0.17 M EtOH/THF or 2 M Li bis(trifluoromethanesulfonyl)imide (LiTFSI) in 0.1 M EtOH/THF can sustain stable Li-NRR for longer periods of time and obtain a Faradaic efficiency (FE_{NH3}) above 95% under a specific set of reaction conditions. Simulations based on first-principles calculated the Li^+ conductivity through different Li salts and concluded that LiF is in the lower conductivity range with respect to other Li salts.[18] This means that the electrodeposition rate of Li^+ is much slower, and gives the negatively charged Li electrode more time to adsorb and dissociate N_2 before an electron is consumed by Li plating. This is in great contrast with $LiClO_4$/LiCl enriched SEIs, where significantly lower FE_{NH3}'s were obtained. It is important to

note that the N_2 and H^+ diffusion rates are less sensitive to the composition of the SEI,[18] but their respective concentrations in the bulk influences the reaction selectivity.[13,20,21]

Despite all the recent progress in the Li-NRR performance, the current understanding of the reaction mechanism and specifically its potential dependencies remain limited. The latter is inherently related to the commonly implemented quasi reference electrodes (QREs) such as a Ag or Pt wire, to either measure or control the potential during an experiment. These QREs have an ill-defined redox potential and are unstable under harsh non-aqueous environments, causing the potential to "drift" enormously during an electrochemical experiment.[22,23] Therefore, electrochemical measurements are typically in constant current mode using a QRE to monitor the cell's stability. This approach does not allow for the decoupling of Li-NRR overpotential contributions from the total cell voltage, which is crucial to estimate the energy efficiency, elucidate different processes in the cell, and to allocate specific potential losses in the cell. Recently, a partially delithiated sheet of Li_xFePO_4 (LFP) has been identified as a reliable reference electrode material for Li-NRR systems, since its potential is stable over a large range of lithiation states.[22,23] This motivated us to implement a LFP based RE in a three electrode autoclave cell at 20 bar N_2 pressure to investigate the effect of potential on the NH_3 production rate, Faradaic efficiency and stability using LiTFSI and 0.1 M EtOH dissolved in THF as a high performance electrolyte.

4.2 Experimental Section

4.2.1 Materials

Copper wire (Ø0.5 and Ø2 mm, 99.95%) and Platinum wire (Ø0.5 mm, 99.9%) were purchased from Mateck. A sheet of double coated $LiFePO_4$-on-aluminium sheet (241 mm × 200 mm x 0.1 mm) with a specific capacity of 127 mAh/g and coating areal density of 160 g/m^2 was obtained from MTI Corporation. Anhydrous tetrahydrofuran (99.9%, inhibitor) and ethanol (<30 ppm H_2O) were supplied by Sigma-Aldrich and VWR, respectively. Li bis(trifluoromethanesulfonyl)imide (<20 ppm H_2O, 99.9%) was purchased from Solvionic and did not require further drying. Molecular sieves (3A 4-8 mesh, Sigma) were purchased from Sigma-Aldrich. Their activation procedure was as follows: The molecular sieves were washed with acetone, pre-dried overnight in a vacuum oven (at 80 °C), transferred to the antechamber of the Ar glovebox (GS, <0.1 ppm H_2O, <0.1 ppm O_2) and dried a second time at 200 °C for 24 hours. Anhydrous EtOH and THF were dried over activated molecular sieves for 5 days with a 25% mass/volume ratio and stored over a new batch of activated molecular sieves inside the glovebox. Lower grade ethanol (denatured 96%) and acetone (≥99%) were used for various cleaning purposes and were supplied by Technisolv and VWR. Concentrated sulfuric acid (95–98 wt % H_2SO_4, trace metal purity) was bought from Sigma-Aldrich and used either directly for glassware acid cleaning or diluted for other purposes. Both potassium hydroxide (85%) and phosphoric acid (≥85%) were purchased from Sigma-Aldrich. Ultrapure water (Milllipore Milli-Q 7000) was used for solution preparation and cleaning. High purity N_2 and Ar gases (99.999%) were supplied by Linde.

4.2.2 Reference Electrode Preparation

A small piece (2.4 cm × 1.4 cm) was cut from a double coated LiFePO$_4$-on-aluminium sheet and mounted into a two electrode beaker cell filled with 0.5 M LiTFSI in pre-dried THF (<10 ppm) using a Cu wire (Ø2 mm) in a helix coil as anode (Figure C1). The electrode was partly delithiated at 0.1 C rate for 5 hours (charging current is ~0.6 mA) to obtain a separate LiFePO$_4$ and FePO$_4$ phase, which results in a well defined Fe^{2+}/Fe^{3+} redox potential of 0.4 V vs SHE.[22,23] The delithiation experiment and further storage of the delithiated sheet was done in the glovebox to prevent phase transitions during air exposure.

4.2.3 Electrochemical Measurements

All electrochemical ammonia synthesis experiments were performed in a polyether ether ketone (PEEK) three electrode autoclave cell at 20 bar N$_2$ pressure. The cell design and configuration was inspired by the work of MacFarlane, Simonov and coworkers.[12] The cell consists of a glass insulated Cu wire (Ø0.5 mm × 6 mm) as working electrode (WE), a Pt wire (Ø0.5 mm × 400 mm) as counter electrode (CE) coiled around the WE with a Ø14 mm, a small Li$_x$FePO$_4$ ribbon (approximately 2 mm x 11 mm x 0.1 mm) as reference electrode (RE) positioned near the WE (see Figure C1 for more details), and a glass magnetic stirrer (Ø5 mm × 12 mm, Fischerbrand). The insulated Cu wire was electropolished at 5 V versus the copper anode for 2 min in a two-electrode beaker cell containing H$_3$PO$_4$ and a Cu anode (Ø2 mm) coiled in helix shape. The smooth Cu wire (indicated by the scanning electron microscopy image in Figure C2) was sonicated in water for 5 min and blow dried with N$_2$. The Pt wire was flame annealed and reshaped into the Ø14 mm coil. The RE was soaked in a diluted LiTFSI/THF solution for about an hour inside the glovebox for cleaning purposes. The Pt wire, stirrer and the internal body of the cell were rinsed with acetone, ethanol, acid cleaned in 10 vol% H$_2$SO$_4$ (95-98%, Sigma) in water for an hour, and rinsed excessively with water and blow dried with N$_2$. If the cell parts were exposed to ambient air for > 1 day, an additional 15 min of sonication in 0.1 M KOH was added to the cleaning procedure to remove any surface accumulated NO$_x$ species.[24] Other items, such as the top part of the cell, o-rings (ERIKS), beakers, vials, caps and spatulas were all cleaned with ultrapure H$_2$O and blow dried with N$_2$. The cell parts, consumables and other labware required for assembling the cell in the glovebox were dried overnight in a vacuum oven (Vacuterm, Thermo Scientific) at 90 °C and ≤3 mbar. Afterwards, all items were transferred to a preheated antechamber at 80 °C and flushed 3 x 5 min before introducing into the glovebox. A fresh batch of 1 M or 2 M LiTFSI in 0.1 M EtOH/THF was prepared prior to each experiment. Moisture content of the electrolyte was measured by Karl Fischer titration (Metrohm, 756 KF Coulometer) and was typically < 30 ppm H$_2$O. The assembled cell was transferred out of the glovebox and connected to a gas purification skid (see Figure C3) on the bench. Residual moisture in the gas (≤3 ppm H$_2$O) was removed by a home-made stainless steel column (Ø12mm x 250mm, Swagelock) filled with activated molecular sieves. Any remaining impurities were removed (< 1 parts per trillion) via a certified commercial gas filter (Entegris GPUS35FHX). The cell was slowly pressurized until 20 bar N$_2$ and saturated for at least 30 min. The stirring rate was set to 300 rpm throughout the entire experiment.

All electrochemical measurements were performed using a SP-200 Biologic potentiostat in combination with EC-Lab software. A typical measurement sequence was as follows: (i) An initial potentiostatic electrochemical impedance spectroscopy (PEIS) measurement at open-circuit voltage (OCV) was carried out to determine the ohmic resistance (R_u) between the RE and the WE. (ii) Cyclic voltammetry was performed between -2.6 V and -3.2 V vs. SHE for 10 cycles to examine whether the Li/Li$^+$ equilibrium potential (E_{Li/Li^+}) is close to -3 V vs. SHE. (iii) Chronoamperometry (CA) was performed at the potential of interest for 4 hours. (iv) The RE potential was reassessed using cyclic voltammetry to detect possible potential drifts. (v) A final PEIS was performed to determine any changes in the R_u. The applied potential was corrected post-measurement if we noticed minor deviations in the LFP-RE potential by taking the average of (ii) and (iv). We decided not to correct the applied potentials of the CA measurements for the R_u. An elaborate discussion supporting this decision is given in the Results and Discussion section.

After the electrochemical ammonia synthesis experiment, the pressurized head space was slowly purged through an acid trap (Supelco Analytical, 6-4835) filled with 20 ml of 0.05 M H$_2$SO$_4$. Subsequently, the cell was flushed for 10 min with Ar to recover any left-over ammonia. The cell was disconnected and reintroduced into the glovebox to withdraw the electrolyte and remove the RE for cleaning. The rest of the cell was cleaned outside the glovebox following the procedure outlined earlier. We noticed that during depressurization, the fragile solid electrolyte interface layer breaks down and disperses into the electrolyte as was earlier observed by Chorkendorff and coworkers.[18] The reason for that is the escaping dissolved N$_2$ gas. Therefore, we added a small drain to one of the cell bodies (Figure C1) to remove the electrolyte before degassing. In order to sustain the SEI as much as possible, the electrolyte was directly removed after the CA measurement, meaning that the additional CV (iv) and PEIS (v) were not performed. After removing the electrolyte, the procedure was kept the same as before. The WE with the SEI was stored in the glovebox for further physical characterization.

4.2.4 Physical Characterization

Semi-quantitative information related to the phase composition of the delithiated LFP electrode was obtained by X-ray diffraction (XRD) with Rietveld refinement. XRD was performed on a Bruker D8 Advance diffractometer with a Bragg-Brentano geometry, a Lynxeye position sensitive detector, a divergence slit with a 12 mm opening, a scatter screen with 5 mm height, and a Cu Kα (λ = 1.5406 Å) radiation source at 45 kV 40 mA operation conditions. The measurement was done within the 5-135° 2θ range with a 1 s time per step and a 0.020° 2θ step size. Bruker DiffracSuite.EVA v6.1 was used to subtract the background, correct small displacements, strip the Kα2 contribution from the patterns, and identify present phases using the ICDD pdf4 database. The Rietveld refinement was performed in Profex.

The solid-electrolyte interface (SEI) was characterized post-mortem with X-ray photoelectron spectroscopy (XPS). The SEI was suspended in 2 mL of dried THF (< 10 ppm) for a few minutes to remove any salt precipitation on the surface. A mobile XPS sample stage

with a vacuum sealable lid (Figure C4) was used to avoid air exposure during transfer from the glovebox to the XPS chamber. During a typical procedure, the parts of the sample holder were shortly dried in the antechamber and introduced into the glovebox. Small parts of the SEI were carefully deposited onto the sample stage. The sample holder was assembled, vacuum sealed in the antechamber and transferred into the XPS chamber. XPS spectra were acquired with a Thermo Scientific K_α spectrometer with a monochromatic Al K_α excitation source. The analysis chamber has a base pressure of about 2×10^{-9} mbar. High resolution XPS spectra were recorded using a 400 µm spot size, 0.1 eV step size, and 50 eV pass energy (200 eV for survey). C 1s adventitious carbon (284.8 eV) was used to correct the charge of all spectra. A depth-profile of the sample was generated by Ar^+ ion etching (1000 eV, 2 mm × 2 mm) at different time intervals in between the XPS measurements. CasaXPS v2.3 was used to deconvolute the obtained spectra.

4.2.5 Ammonia Quantification

All electrolyte and acid trap samples were analyzed using ion chromatography (IC, Dionex Aquion from Thermo Scientific) with an autosampler (Dionex AS-AP). The autosampler injects 250 µL aliquots into the 25 µL sample loop, where it is diluted with 2.6 mM methanesulfonic acid (eluent) at a flow rate of 1 mL/min upon injection. The total acquisition time was 10 min. Tubing, connections and the injection needle are made from PEEK, thus being compatible with organic solvents. The IC column (Dionex IonPac CS12A, 4 × 250mm) is packed with ethylvinylbenzene/divinylbenzene. A guard column (Dionex IonPac CG12A, 4 × 50 mm) was installed upstream to extend the life-time of the main column. The IC is equipped with an additional electrolytic suppressor (Dionex CDRS 600, 4 mm) to remove conductive ions from the eluent for improving the sensitivity of the conductivity detector. As precaution, the electrolyte samples were diluted with ultrapure water (200 x for 1 M LiTFSI and 400 x for 2M LiTFSI) to protect the column, which is not compatible with alcohols. Aliquots taken from the acid trap were injected without dilution. To construct the calibration lines, seven concentrations of NH_4Cl (99.99%, Sigma-Aldrich) in water, 0.002 M LiTFSI (1 M LiTFSI 200 x diluted) and 0.005 M LiTFSI (2 M LiTFSI 400x diluted) were prepared with their respective concentrations of 5, 10, 50, 100, 200, 300, 500 µM. Additional calibration lines in diluted LiTFSI solutions were necessary to compensate for the overlapping Li^+ shoulder peak with NH_4^+ (Figure C5). All fitted calibration curves resulted in a nonlinear relationship (see Figure C6), which is not unusual for a broad range of concentrations.

4.3 Results and Discussion

4.3.1 Electrochemical Characterization

The XRD Rietveld refinement of our LFP reference electrode (LFP-RE) shown in Figure C7 indicates two clear crystalline phases of 67 mol% $LiFePO_4$ and 33 mol% $FePO_4$, respectively. Although this deviates to some extent from a 50/50 molar distribution, the Fe^{2+}/Fe^{3+} redox potential of ~0.4 V vs. SHE is stable over a broad range of lithiation states.[22] The LFP-RE was used to establish j-V relationships of the Li-NRR system with 2 M LiTFSI under Ar (Figure 1a), 20 bar N_2 pressure (Figure 1b), both with and without EtOH (Figure 1c,d). The main aim of these measurements is to perform a preliminary investigation of whether the overpotential of Li^+ reduction is influenced by different species in the electrolyte, and to identify the presence of other (electro)chemical reactions. To do this, we performed multiple CV experiments around -3 V vs. SHE and studied the reduction and oxidation peaks by shifting the reduction potentials to more negative values. At the start of each measurement, the WE was preconditioned by scanning for at least 20 cycles at 20 mV s^{-1} between -3.1 V and -2.6 V vs. SHE. Afterwards, the j-V behaviour was stable and reproducible. It is important to mention that we were able to apply ohmic drop correction (85% with the build-in function of the potentiostat) for the CVs without any issues because the potentials under investigation remain close to the equilibrium potential.

All voltammograms in Figure 1 indicate that the equilibrium potentials are between -3.03 V and -3.02 V vs. SHE, which slightly deviates from the standard equilibrium potential (E^0_{Li/Li^+}) in THF (-2.98 V vs. SHE).[25] As defined by the Nernst equation (Equation 1), the equilibrium potential of Li^+ reduction is a function of the activity coefficient of Li^+ ions (a_{Li^+}) in the solution.[25] This means that the E_{Li/Li^+} depends on the salt selection, salt concentration and solvent. Therefore, we associate this small discrepancy to differences of the a_{Li^+} among our examined Li-NRR systems and not to a malfunctioning LFP-RE.

$$E_{Li^+/Li} = E^0_{Li^+/Li} - \frac{RT}{F} ln\left(\frac{1}{a_{Li^+}}\right) \quad (1)$$

A minimum overpotential of 0.08 V was necessary to initiate Li nucleation on the Cu wire, irrespective of the addition of EtOH or N_2. However, we observe that the overall j-V relationship is influenced by species other than the Li-salt. The measured charge of the reduction (Q_{red}) and oxidation (Q_{ox}) peaks of the CVs are summarized in Figure C8 and reveals a striking degree of asymmetry between the peaks. Voltammograms with 2 M LiTFSI in an Ar atmosphere (Figure 1a) show a clear Li^+ reduction peak, while Li oxidation is mostly absent. We assign this to the SEI formation process, whereby the majority of "freshly" plated Li^0 reacts instantaneously and irreversibly in non-Faradaic reactions with nearby solvent molecules (TFSI$^-$ and THF). Therefore, an initial part of the electrons is lost due to SEI formation until the entire layer of metallic Li is insulated from the surrounding solvent molecules. Thus, the degree of reversibility between the Li plating and stripping process can

be used to evaluate whether the SEI structure is fully developed (steady-state). It is surprising that during continuous cycling, Li stripping remains mostly small, indicating that a stable SEI was not obtained while performing CV measurements.

The natural tendency to form dendritic shaped morphology during continuous Li deposition hinders the establishment of a mechanically rigid and homogeneously covering SEI. Strategies to suppress dendritic growth are extensively discussed in the Li-ion battery field and can generally be obtained when operating at low current densities and selecting electrolytes with a high surface tension, high Li^{+} transference number and high ionic conductivity.[26] LiTFSI and Li bis(fluorosulfonyl)imide (LiFSI) are commonly implemented because they have a relatively high ionic conductivity and form LiF-enriched SEIs. The latter promotes regulated Li^{+} ion transport in the SEI and increases the surface tension allowing the suppression of dendrite formation. In Li-NRR, it is however desirable to operate at higher current densities, which most likely induces dendritic growth as was earlier observed in Li-ion batteries.[27] The low amount of reversible Li[0] in Figure 1a may indicate that plating at high current densities initiate dendrite growth with a high specific area to volume ratio, wherein surface Li[0] is lost through salt and solvent passivation.

Figure 1b shows that the j-V behaviour of Li plating and stripping is influenced by N_2 due to the formation of additional Li_3N SEI species as was observed by Blair et al. using grazing-incidence X-ray scattering in the absence of EtOH.[28] The slope of the forward reduction scan under 20 bar N_2 is roughly 60 mA/V lower than under Ar atmosphere, meaning that the presence of more Li_3N in the SEI negatively correlates with the kinetics of Li plating. The overpotential of lithium plating (η_{Li}) can be approximated by the Doyle-Fuller-Newman model:[25,29]

$$\eta_{Li} = \varphi_s - \varphi_e - \rho_{SEI} L_{SEI} \frac{j_{int}}{a_-} \tag{3}$$

Where φ_s and φ_e are the solution and electrode potential, L_{SEI} the SEI thickness, ρ_{SEI} the resistivity of the SEI, a_- the specific interfacial area of the cathode and j_{int} the interfacial current density. Hence, the third term indicates that the SEI characteristics influences the η_{Li}. Due to the relatively high Li^{+} conductivity ($\sigma_{SEI} = \rho_{SEI}^{-1}$) of Li_3N SEI species ($\sigma_{Li_3N} \sim 10^{-4}$ S cm^{-1} versus $\sigma_{LiF} \sim 10^{-30}$ S cm^{-1}),[18,30] we expect that the heterogeneity of multiple inorganic SEI species may result in a geometric expansion of the layer thickness (L_{SEI}), which explains an increase in the η_{Li}.

Interestingly, the degree of reversibility of Li plating in the presence of N_2 is greatly enhanced with respect to Ar, and suggests that Li_3N accelerates the formation of a stable SEI layer, but also promotes relatively more homogeneous plating. Thus, less Li is consumed by irreversible Li-related surface passivation reactions. This is also the reason why Li_3N is generally considered as a desirable compound for high performance SEI's in Li-metal batteries (LMB).[26,31] It is suggested that induced homogeneous Li plating in Li_3N-containing SEI's is related to the high Li^{+} mobility because the Li^{+} migration energy barrier (0.007 eV for

α-Li$_3$N and 0.038 eV for β-Li$_3$N) is considered to be small with respect to other salt species such as Li$_2$CO$_3$ (0.3 eV).[30]
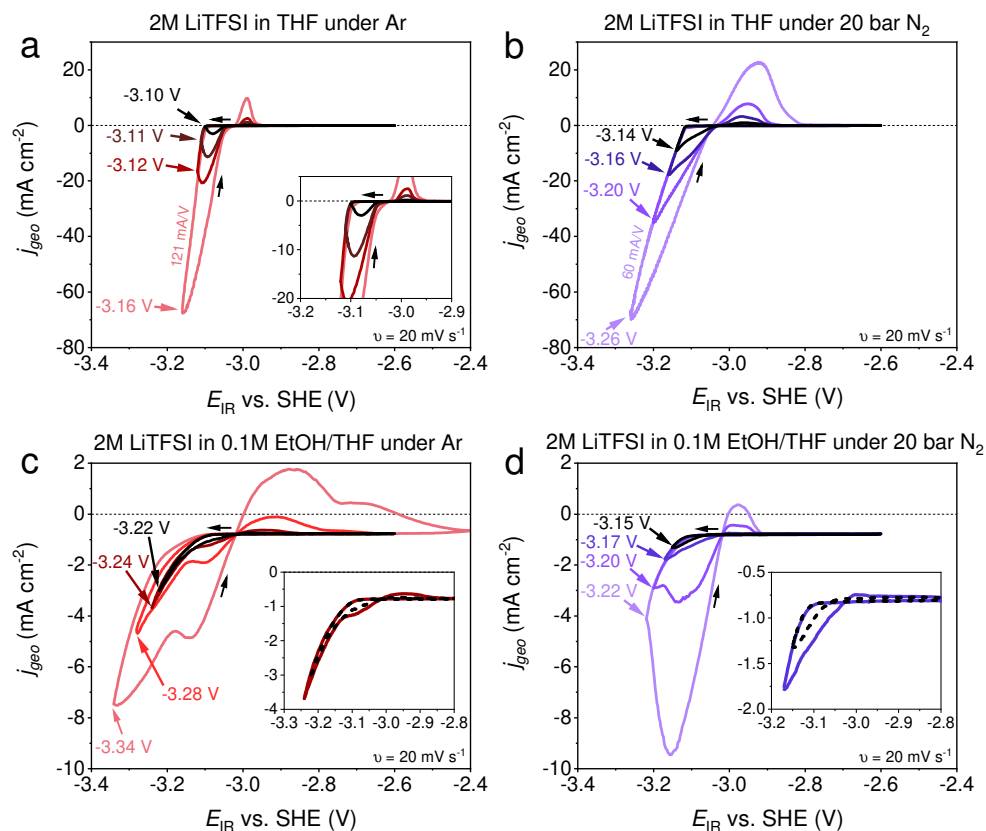
Figure 1. Cyclic voltammograms at different cathodic scan potentials with a scan rate of 20 mV s^{-1} with different species in the electrolyte. (a) 2M LiTFSI in THF under Ar. (b) 2M LiTFSI in THF under 20 bar N$_2$ pressure. (c) 2M LiTFSI in 0.1M EtOH in THF under Ar. (d) 2M LiTFSI in 0.1M EtOH/THF under 20 bar N$_2$ pressure.

After adding 0.1 M EtOH to the electrolyte, the voltammograms in Figure 1c show a distinct j-V behaviour, where the additional reactivity of EtOH in the cell increases the η_{Li} and decreases the overall Li$^+$ reduction current density. This can be explained by the recent cryogenic electron microscopy observations from Steinberg et al., wherein the SEI layer thickness increases upon adding EtOH to the Li-NRR system.[32] This phenomena was confirmed by McShane et al., who quantified the SEI thickness and also its composition via a NMR rinsate approach.[33] As discussed previously, a thicker SEI layer (L_{SEI}) increases the η_{Li} (Equation 3), thus it is evident that higher overpotentials for Li plating are necessary when

144

EtOH is present in the electrolyte. Cycling up to -3.22 V vs. SHE (inset of Figure 1c) reveals only a cathodic peak, which can be assigned entirely to irreversible Li plating. After -3.24 V vs. SHE, an additional Li$^+$ reduction (-3.1 V) and Li oxidation (-2.95 V) peak appear and further develop during the measurement. The establishment of the secondary Li plating peak is most likely related to surface preconditioning by the first Li plating peak enabling reversible Li plating and stripping at a lower energy barrier.[34]

Figure 1d represents the *j-V* relationship of the Li-NRR system containing 20 bar of N$_2$ pressure and 0.1 M EtOH. As mentioned earlier, the "apparent" E_{Li/Li^+} for Li-NRR is comparable with the Ar, N$_2$ and EtOH-in-Ar systems in Figure 1a,b and c. This indicates that the E_{Li/Li^+} is not influenced by the presence of EtOH and N$_2$ as was suggested previously.[12,25] Again, after adding EtOH to the N$_2$ system, the Li plating current density decreases with almost one order of magnitude. The cathodic part of the voltammogram shows a comparable behaviour with the EtOH-in-Ar system where additional peaks associated with Li plating appear between -3.13 V and -3.15 V vs. SHE during the backward scan. We do not assign these peaks to EtOH related PCET reactions involved in Li-NRR because the peak potentials are similar to the other Li plating peaks in the absence of EtOH and N$_2$ (Figure 1a and 1c). Thus, it is most likely that the protons originate from EtOH hydrolysis over Li^0 metal (Equation 1). This suggests that Li plating is the only electrochemical step in the Li-NRR reaction mechanism as was also mentioned in previous reports.[15,23,32,35]

4.3.2 Relationship Between Potential and the Li-mediated NRR Performance

Chronoamperometry measurements (CA) at different potentials were performed over the course of 4 hours to measure the Li-NRR stability, NH$_3$ production rate and Faradaic efficiency. The Nyquist plots in Figure 2a, 2c and 2e show the results from the PEIS measurements for a 2 M LiTFSI and 0.1 M EtOH in THF electrolyte before and after a CA at -3.20 V vs. SHE, -3.59 V vs. SHE and -3.92 V vs. SHE. The low frequency domain, typically associated with the SEI, could not be analysed due to irreproducible data. The resistance of the electrolyte (R$_u$), obtained by the high frequency domain, did not change significantly after the CA measurements and varied between 50-70 Ω. A depressed semi-circle was always noticeable in the initial PEIS measurements and is partly representing the charge transfer resistance (R$_{ct}$) coupled to the Li plating kinetics. Interestingly, the PEIS data after the CA only show a minor to no response of the R$_{ct}$ contribution. This indicates that the conditions at the electrode surface are highly favourable for Li plating, and suggests that the SEI and the metallic Li layer on the Cu wire remain intact after the CA. Cyclic voltammetry was performed before and after the CA to monitor any potential drift in the LFP-RE. The voltammograms in Figure 2b clearly illustrates that the E_{Li/Li^+} did not change noticeably, which proves that the LFP-RE remain stable throughout the entire set of electrochemical experiments. However, the CV measurements after the CA indicate a significant decrease in the current response after each cycle. We expect that this is related to the breakdown of

the SEI when cycling above 0 V vs. Li/Li$^+$. This phenomena has also been observed by Blair et al., who showed that the thickness of the SEI shrinks at the open-circuit potential.[28]

4
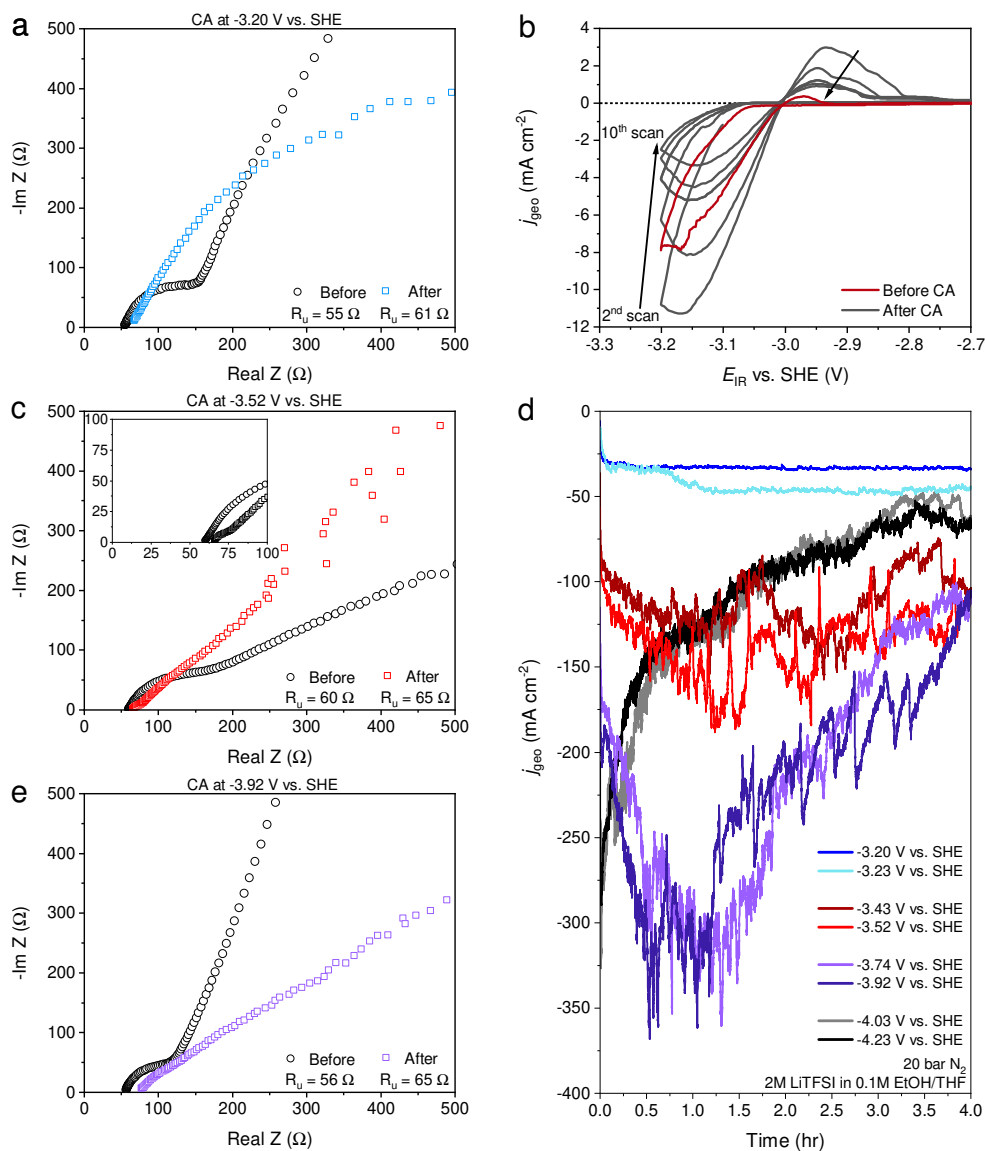
Figure 2. Electrochemical measurements before, during and after 4 hour chronoamperometry experiments with (a) PEIS before and after a CA at -3.20 V vs. SHE, (b) CV measurements before and after a CA, (c) PEIS before and after a CA at -3.52 V vs. SHE, (d) overview of CA measurements at different potentials, (e) PEIS before and after a CA at -3.92 V vs. SHE.

As mentioned in the experimental section, the applied potentials for the CA measurements in Figure 2d and C9 were not compensated for the R_u because of the following reasons; 1) Build-in IR_u compensation by positive feedback was not possible since it caused signal distortion and eventual breakdown of the electrochemical measurement; 2) PEIS measurements could only be performed close to the open-circuit potential, which means that R_u does not accurately represent the uncompensated resistance of the Li-NRR system during operation. Even if this would be possible, the electrode surface and its local environment are very dynamic, especially at a high overpotential. Thus, using a predetermined R_u will not reflect the actual R_u between the reference and the working electrode during a CA measurement. It is therefore expected that the herein reported potentials will slightly shift to more positive values.

Figure 2d presents an overview of potentiostatic measurements performed with 2 M LiTFSI. The current response is greatly affected by the applied potential. Up to -3.23 V vs. SHE, the current is relatively stable, while the NH_3 production rate (R_{NH3} <31 nmol s^{-1} cm^{-2}) and FE_{NH3} (<16%) remain low as illustrated in Figure 3a. It is important to mention that NH_3 in the acid trap is for most cases ~100 times lower than in the electrolyte. Therefore, we decided to use only the quantified NH_3 in the electrolyte to calculate the R_{NH3} and FE_{NH3}. At potentials ≤-3.43 V vs. SHE, the current density starts to show periodic oscillations but does not lose much of its electrochemical activity. At more negative potentials (≤-3.74 V vs. SHE), the current density increased to -300 mA cm^{-2} and remained relatively stable for 1 hour, but gradually deteriorated afterwards. We expect that operating at these potentials for longer periods of time (>4 hr) is not sustainable and will eventually lead to a significant decrease in current density. The complete breakdown of the Li-NRR system is observed at more negative potentials (<-4.03 V vs. SHE). Interestingly, the FE_{NH3} remained at roughly 50% at potentials below -3.43 V vs. SHE, while there is a clear upward trend at more positive potentials. This suggests that a minimum energy barrier of ~0.4 V is required for the build-up of a selective SEI. The oscillating current behaviour below -3.43 V vs. SHE may also be characteristic to achieve high FE_{NH3}'s. These patterns in the current density were also observed by Du et al. using a similar set of reaction conditions.[12] It remains unclear what causes these large periodic oscillations at the Li-NRR electrode, but it seems to be important for the NH_3 selectivity. These fluctuations were not observed with 1 M LiTFSI (Figure C9), where the current density response remained stable over a wide range of potentials (up to -3.83 V vs. SHE). Figure 3b summarizes the relationship between the potential and the Li-NRR performance with 1 M LiTFSI, showing a remarkably different dependency. There is a clear upward trend of both E, FE_{NH3} and R_{NH3} reaching an optimum of 39% and 194 nmol s^{-1} cm^{-2} at -4.23 V vs. SHE. Not only are both the FE_{NH3} and R_{NH3} lower in comparison with 2 M LiTFSI, the applied potentials are also more negative. To verify that NH_3 originates from the Li-NRR, an Ar blank test at -3.72 V vs. SHE was performed and did not result in any observable NH_3. This demonstrates that NH_3 production only occurs under N_2 atmosphere and that our earlier reported cleaning procedures are sufficient.[24] It is evident by now that the potential has a significant effect on the performance metrics. Differences in the structure and

composition of the SEI are presumably the underlying reason for our observations and will be further investigated in the next section.
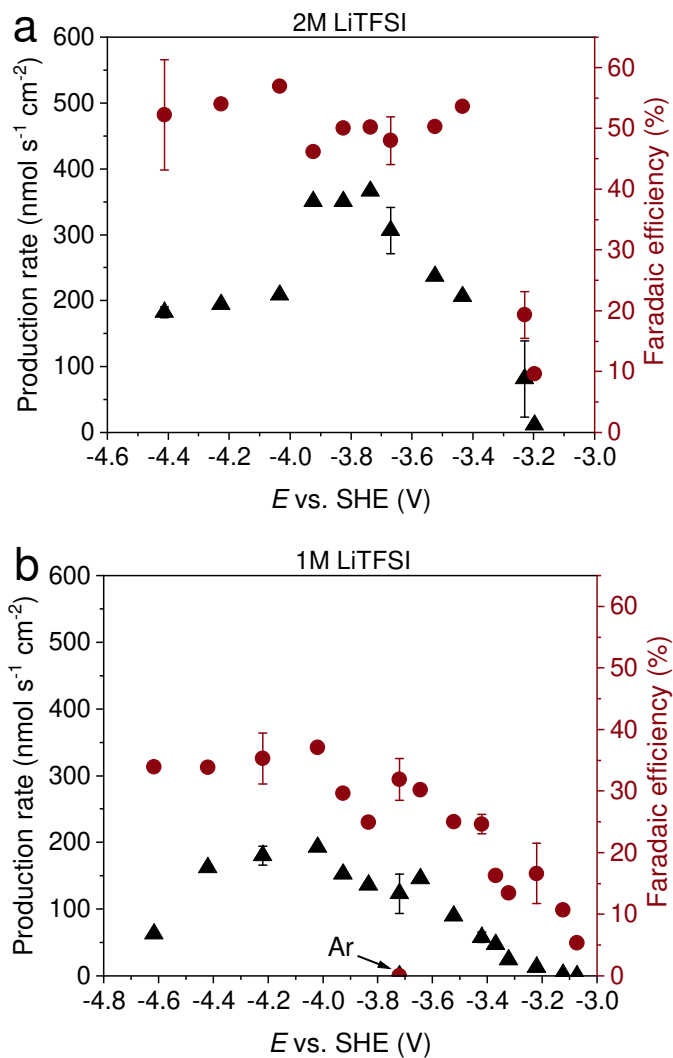
Figure 3. Potential dependency of the NH_3 production rate and Faradaic efficiency in (a) 2 M LiTFSI and (b) 1 M LiTFSI dissolved in 0.1 M EtOH/THF.

4.3.3 Physical Characterization of the SEI

Previous studies have identified the importance of a highly inorganic and F-enriched SEI in order to reach optimal Li-NRR performance.[12,18] Here, we investigate if the applied potential has an effect on the SEI composition. The Cu electrodes covered with the SEI layer were retrieved from the cell by removing the electrolyte before degassing as is elaborately described in the Experimental section. Figure C10 shows a photographic example of the Cu wire with the SEI for illustrative purposes. Although the exact SEI thickness was not quantified after each measurement, the layer was always visible with the eye. A small part of the SEI was collected and deposited onto the XPS sample holder inside the glovebox. Since the glovebox contains trace amounts of water (0.1 ppm) and O_2 (0.1 ppm) it is impossible to completely irradicate adventitious species interacting with the SEI. To work around this issue, we used XPS depth profiling and removed a large part of the surface layers by Ar^+ ion etching (up to 600 s). XPS was also measured at intermediate etching times.

Figure 4 shows the high resolution spectra of C 1s, F 1s, S 2p and Li 1s of the retrieved SEI with 2 M LiTFSI within the moderate potential window (-3.74 V vs. SHE). The F 1s spectra clearly illustrates two peaks at 684.5 eV and 687.5 eV, where the former is associated with LiF, and the latter with the CF_3 functional group of LiTFSI. We confirm this by comparing the signals with the XPS spectra of pristine LiTFSI salt (see Figure C11). LiTFSI is mostly present as salt residue on the SEI's surface, while LiF becomes more prominent in the deeper layers. The elemental composition in Figure C12b reveal that F or LiF, is the most dominant element (besides Li) in the SEI, which is in agreement with other studies employing a F-based salt.[12,18] The N 1s spectra (not shown) were masked by the organic N contribution of LiTFSI, which hindered Li_3N identification. The C 1s spectra show two prominent peaks at 284.8 eV (C-C) and 286 eV (C-O) that are assigned to derivative products of THF decomposition, representing Li butoxide or other Li alkoxide species. Additionally, the low intensity C 1s peaks at 287.6 eV (C=O) and 289 eV (O-C=O) indicate the presence of small Li_2CO_3 quantities in the SEI. The S 2p spectra in Figure 4c contains two S $2p_{3/2}$ peaks at 168.5 eV and 166.8 eV assigned to LiTFSI (sulfone groups) and Li_2SO_4. The other three S $2p_{3/2}$ peaks at 162.8 eV (Li_2S_6), 161.2 eV (Li_2S_4) and 159.8 eV (Li_2S) are observed as three different oxidation states of lithium sulfide (Li_xS_y).[36] At longer etching time, Li_2S_6 and Li_2S_4 become more prevalent, while Li_2S remain negligible. The Li_2SO_4 contribution in the S 2p spectra has generally the highest intensity. Deconvolution of the Li 1s peak is challenging because Li species are resembled in a singlet with overlapping binding energies. Nevertheless, based on the F 1s and S 2p spectra, we can confidently identify LiF (55.6 ± 0.2 eV),[37] a small amount of Li_2SO_4 (55.8 eV),[19] and LiOH (55 ± 0.3 eV) as Li species present in the SEI.[37] The right shoulder of the Li 1s spectra extends to smaller BEs beyond LiOH and could indicate the existence of electronically insulated "dead" Li^0 (54.7 ± 0.3 eV).[37] At longer etching times, the Li 1s peak shifts towards higher BEs, favoring LiF over the other species. This demonstrates that LiOH is mostly present in the surface layers due to inevitable air exposure by sample handling and storage. Therefore, it is beneficial to remove several layers before XPS characterization.

Complementary characterization with for instance solid-state NMR can give more clarification about the specific Li species in the SEI and will be discussed in a future work.

Post-mortem 2 M LiTFSI (E = -3.74 V vs. SHE)
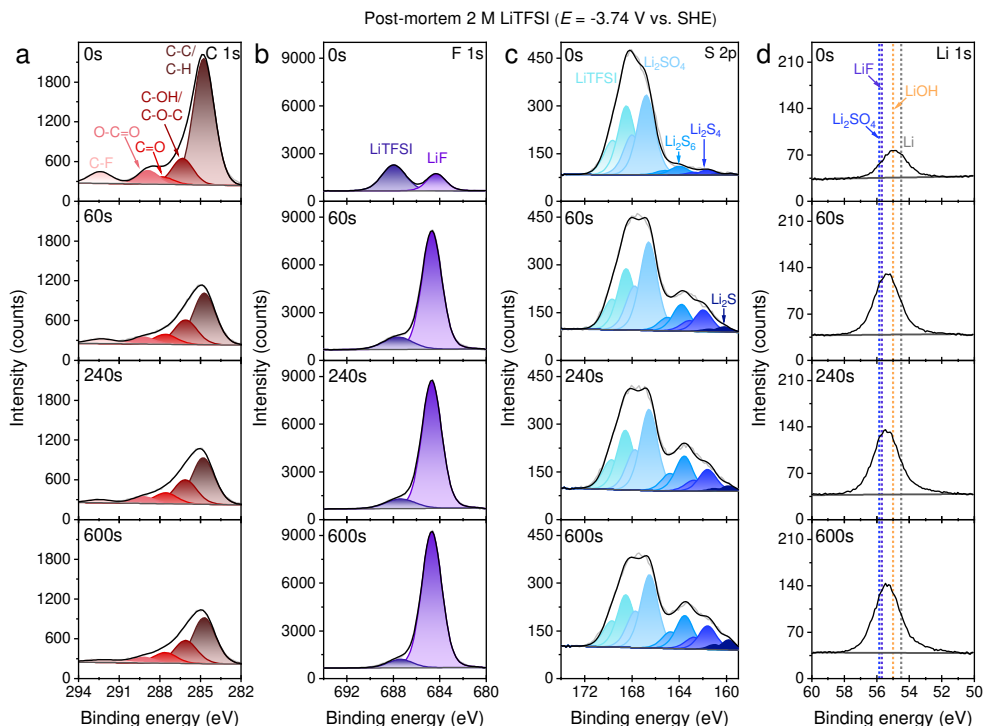
Figure 4. High resolution XPS spectra of (a) C 1s, (b) F 1s, (c) S 2p and (d) Li 1s at 0s, 60s, 240s and 600s of Ar$^+$ ion etching with the retrieved SEI from 2 M LiTFSI at -3.74 V vs. SHE. The S 2p orbital has a 2p$_{3/2}$ – 2p$_{1/2}$ doublet peak separation of 1.18 eV and 2:1 intensity ratio.

Previous reports showed that both LiTFSI and THF starts to decompose at -1.50 V and -2.54 V vs. SHE on a Pt and Au surface in the presence of Li$^+$.[38,39] Thus, the initiation and the decomposition rate of solvent and electrolyte species are potential dependent. SEIs obtained after electrochemical measurements at lower and higher applied potential were also characterized with XPS and were predominately enriched with LiF as shown in Figures C12, C13 and C14. Interestingly, Figure 5 indicates that the composition of inorganic species follows a similar potential relationship as the NH$_3$ production rate and therefore the electrochemical activity and stability of the system. By decreasing the potential from -3.23 V to -3.92 V vs. SHE, the F/C ratio increases from 1.9 to 2.66. Hence, the potential effect can be partly explained by altering the selectivity of the electrolyte and solvent passivation reactions in the SEI. At 1 M LiTFSI, the XPS results in Figure 5, C15 and C16 show a noticeable shift towards more organic species in the SEI, *i.e.* Li alkoxides and carbonates. This can be explained by a change in the Li$^+$ ion solvation environment, wherein the probability of having solvent molecules in the Li$^+$ solvation shell is higher in comparison with 2 M LiTFSI (F/C ratio

is 1).[17] Thus, the salt concentration clearly influences the SEI's composition, and in particular the LiF content. The latter has a significant effect on the selectivity, which is in agreement with previous studies.[12,17] However, the underlying phenomena that links the applied potential to the Li-NRR performance cannot solely be explained by the SEI composition.
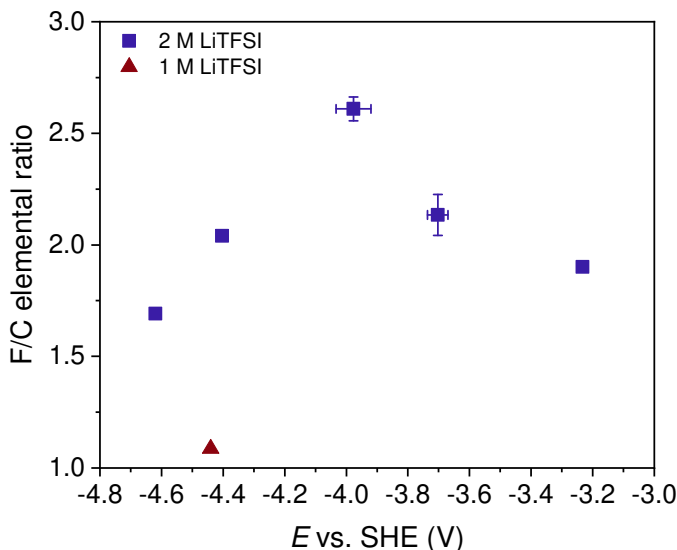
Figure 5. Elemental F to C ratio obtained by XPS after 600 s of Ar ion etching of the retrieved SEIs after different chronoamperometry measurements.

4.3.4 Overpotential and Surface Morphology

In Li-ion batteries, several studies correlate the overpotential of Li plating to changes in the surface morphologies of the Li deposits.[34,40] Pei et al. studied the fundamental Li nucleation and growth process on a copper substrate by recording the applied potential and analysing the surface structure with ex-situ SEM.[34] They found that the size of the Li nuclei is inversely proportional to the overpotential, and that the nuclei density has a cubic power dependency with the overpotential, which is in line with classical theory of homogeneous nucleation.[41] The critical radius of a hemispherical particle until it reaches a thermodynamically stable shape during nucleation is given by:

$$r_{crit} = \frac{2YV_M}{F\eta_{Li}} \qquad (4)$$

Where V_M is the molar volume, F the Faraday constant and Y the surface energy. The cubic relationship between the overpotential and the nuclei density ($N \sim \eta^3/Y^3$) follows immediately after using the critical volume of a spherical nuclei.[42] Thus, at high

overpotentials, Li nuclei are densely distributed over the surface and form a network of small micron sized particles, which generally promote two dimensional plating. At low overpotentials, large island-like agglomerates were randomly distributed over the substrate's surface.[34] This indicates that the applied potential can have a significant effect on the Li morphology and may explain the relationship between the Li-NRR performance and potential. This will be subject of a forthcoming study.

4.4 Conclusion

Li-NRR experiments under 20 bar N_2 pressure with LiTFSI as a high performance electrolyte were for the first time performed with a reliable reference electrode, based on a partially delithiated sheet of Li_xFePO_4. This allowed us to couple the potential dependency to important Li-NRR performance parameters, such as the Faradaic efficiency, NH_3 production rate and the stability at different electrolyte concentrations. Cyclic voltammetry measurements were also performed with 2 M LiTFSI under Ar or N_2 with or without EtOH and did not show any peaks besides Li plating and stripping, suggesting that both the N_2 activation and protonation steps are chemical by nature. With 2 M LiTFSI, the FE_{NH3} remained lower than 15% after chronoamperometry measurements at potentials >-3.23 V vs. SHE and increased to 50% at -3.43 V vs. SHE. The current was very unstable at potentials more negative than -4.03 V vs. SHE, and affected the production rate, but not the FE_{NH3}, which remained close to 50%. With 1 M LiTFSI, the current response of the system is generally more stable in comparison with 2 M LiTFSI, but at the cost of lower Faradaic efficiencies, NH_3 production rates and more negative potentials. XPS analysis reveals that the SEIs were mostly enriched with LiF. The ratio between inorganic and organic compounds in the layer varied with the applied potential but does not fully explain the potential dependency trend with the Li-NRR performance parameters. We believe that the potential also affects the surface morphology via the nucleation and growth process of Li deposits, which will be investigated in a future study. The composition of the SEIs obtained after measurements with 1 M LiTFSI indicates more organic species in the layer, which implies that more uncontrolled and unselective Li plating occurs at the electrode surface. The relation between salt concentration and the Li-NRR performance is already well documented, while the influence of potential remains poorly understood and requires more attention in future works.

4.5 References

1   Andersen, S. Z. *et al.* A rigorous electrochemical ammonia synthesis protocol with quantitative isotope measurements. *Nature* **570**, 504-508 (2019). https://doi.org:10.1038/s41586-019-1260-x

2   Choi, J. *et al.* Identification and elimination of false positives in electrochemical nitrogen reduction studies. *Nature Communications* **11**, 1-10 (2020). https://doi.org:10.1038/s41467-020-19130-z

3   Greenlee, L. F., Renner, J. N. & Foster, S. L. The Use of Controls for Consistent and Accurate Measurements of Electrocatalytic Ammonia Synthesis from Dinitrogen. *ACS Catalysis* **8**, 7820-7827 (2018). https://doi.org:10.1021/acscatal.8b02120

4   Du, H. L., Gengenbach, T. R., Hodgetts, R., Macfarlane, D. R. & Simonov, A. N. Critical Assessment of the Electrocatalytic Activity of Vanadium and Niobium Nitrides toward Dinitrogen Reduction to Ammonia. *ACS Sustainable Chemistry and Engineering* **7**, 6839-6850 (2019). https://doi.org:10.1021/acssuschemeng.8b06163

5   Hodgetts, R. Y., Du, H. L., MacFarlane, D. R. & Simonov, A. N. Electrochemically Induced Generation of Extraneous Nitrite and Ammonia in Organic Electrolyte Solutions During Nitrogen Reduction Experiments. *ChemElectroChem* **2**, 1-10 (2021). https://doi.org:10.1002/celc.202100251

6   Yu, W. *et al.* Cathodic NH 4 + leaching of nitrogen impurities in CoMo thin-film electrodes in aqueous acidic solutions †. *Sustainable energy & fuels* **4**, 5080-5087 (2020). https://doi.org:10.1039/d0se00674b

7   Shipman, M. A. & Symes, M. D. A re-evaluation of Sn (II) phthalocyanine as a catalyst for the electrosynthesis of ammonia. *Electrochimica Acta* **258**, 618-622 (2017).

8   Hu, B., Hu, M., Seefeldt, L. & Liu, T. L. Electrochemical dinitrogen reduction to ammonia by Mo2N: catalysis or decomposition? *ACS Energy Letters* **4**, 1053-1054 (2019).

9   Du, H.-L. *et al.* Is Molybdenum Disulfide Modified with Molybdenum Metal Catalytically Active for the Nitrogen Reduction Reaction? *Journal of The Electrochemical Society* **167**, 146507-146507 (2020). https://doi.org:10.1149/1945-7111/abc1a8

10   Tsuneto, A., Kudo, A. & Sakata, T. Vol. 22   851-854 (1993).

11   Tsuneto, A., Kudo, A. & Sakata, T. Lithium-mediated electrochemical reduction of high pressure N2 to NH3. *Journal of Electroanalytical Chemistry* **367**, 183-188 (1994). https://doi.org:10.1016/0022-0728(93)03025-K

12   Du, H.-L. *et al.* Electroreduction of nitrogen at almost 100% current-to-ammonia efficiency. *Nature* **609**, 722-727 (2022). https://doi.org:10.1038/s41586-022-05108-y

13   Lazouski, N., Schiffer, Z. J., Williams, K. & Manthiram, K. Understanding Continuous Lithium-Mediated Electrochemical Nitrogen Reduction. *Joule* **3**, 1127-1139 (2019). https://doi.org:10.1016/j.joule.2019.02.003

14   Andersen, S. Z. *et al.* Increasing stability, efficiency, and fundamental understanding of lithium-mediated electrochemical nitrogen reduction. *Energy & Environmental Science* **13**, 4291-4300 (2020). https://doi.org/10.1039/d0ee02246b

15   Cai, X. *et al.* Lithium-mediated electrochemical nitrogen reduction: Mechanistic insights to enhance performance. *Iscience* **24** (2021).

16   Peled, E. & Menkin, S. Review—SEI: Past, Present and Future. *Journal of The Electrochemical Society* **164**, A1703-A1719 (2017). https://doi.org/10.1149/2.1441707jes

17   Westhead, O. *et al.* The role of ion solvation in lithium mediated nitrogen reduction. *Journal of Materials Chemistry A* (2023).

18   Li, S. *et al.* Electrosynthesis of ammonia with high selectivity and high rates via engineering of the solid-electrolyte interphase Electrosynthesis of ammonia with high selectivity and high rates via engineering. *Joule* **6**, 2083-2101 (2022). https://doi.org/10.1016/j.joule.2022.07.009

19   Lim, C. *et al.* Effect of Sulfur-Derived Solid Electrolyte Interphase on Li-mediated Nitrogen Reduction. *ACS Energy Letters* **8**, 4875-4884 (2023).

20   Fu, X. *et al.* Continuous-flow electrosynthesis of ammonia by nitrogen reduction and hydrogen oxidation. *Science* **379**, 707-712 (2023).

21   Du, H.-L. *et al.* The chemistry of proton carriers in high-performance lithium-mediated ammonia electrosynthesis. *Energy & Environmental Science* **16**, 1082-1090 (2023).

22   McShane, E. J. *et al.* A Versatile Li0. 5FePO4 Reference Electrode for Nonaqueous Electrochemical Conversion Technologies. *ACS Energy Letters* **8**, 230-235 (2022).

23   Tort, R. *et al.* Nonaqueous Li-Mediated Nitrogen Reduction: Taking Control of Potentials. *ACS Energy Letters* **8**, 1003-1009 (2023).

24   Izelaar, B. *et al.* Identification, Quantification, and Elimination of NO x and NH3 Impurities for Aqueous and Li-Mediated Nitrogen Reduction Experiments. *ACS Energy Letters* **8**, 3614-3620 (2023).

25   Westhead, O. *et al.* The origin of overpotential in lithium-mediated nitrogen reduction. *Faraday Discussions* (2023).

26   Tikekar, M. D., Choudhury, S., Tu, Z. & Archer, L. A. Design principles for electrolytes and interfaces for stable lithium-metal batteries. *Nature Energy* **1**, 1-7 (2016). https://doi.org/10.1038/nenergy.2016.114

27   Bai, P., Li, J., Brushett, F. R. & Bazant, M. Z. Transition of lithium growth mechanisms in liquid electrolytes. *Energy & Environmental Science* **9**, 3221-3229 (2016).

28   Blair, S. J. *et al.* Combined, time-resolved, in situ neutron reflectometry and X-ray diffraction analysis of dynamic SEI formation during electrochemical N2 reduction. *Energy & Environmental Science* **16**, 3391-3406 (2023).

29   O'Kane, S. E. *et al.* Lithium-ion battery degradation: how to model it. *Physical Chemistry Chemical Physics* **24**, 7909-7922 (2022).

30   Li, W. *et al.* Li+ ion conductivity and diffusion mechanism in α-Li3N and β-Li3N. *Energy & environmental science* **3**, 1524-1530 (2010).

31   Kim, M. S. *et al.* Revealing the Multifunctions of Li3N in the Suspension Electrolyte for Lithium Metal Batteries. *ACS nano* **17**, 3168-3180 (2023).

4

32   Steinberg, K. *et al.* Imaging nitrogen fixation at lithium solid electrolyte interphases via cryo-electron microscopy. (2022).

33   McShane, E. J. *et al.* Quantifying Influence of the Solid-Electrolyte Interphase in Ammonia Electrosynthesis. *ACS Energy Letters* **8**, 4024-4032 (2023).

34   Pei, A., Zheng, G., Shi, F., Li, Y. & Cui, Y. Nanoscale nucleation and growth of electrodeposited lithium metal. *Nano letters* **17**, 1132-1139 (2017).

35   Bjarke Valbæk Mygind, J. *et al.* Is Ethanol Essential for the Lithium-Mediated Nitrogen Reduction Reaction? *ChemSusChem* **16**, e202301011 (2023).

36   Su, Y.-S., Fu, Y., Cochell, T. & Manthiram, A. A strategic approach to recharging lithium-sulphur batteries for long cycle life. *Nature communications* **4**, 2985 (2013).

37   Chastain, J. & King Jr, R. C. Handbook of X-ray photoelectron spectroscopy. *Perkin-Elmer Corporation* **40**, 221 (1992).

38   Aurbach, D., Chusid, O., Weissman, I. & Dan, P. LiC (SO2CF3) 3, a new salt for Li battery systems. A comparative study of Li and non-active metal electrodes in its ethereal solutions using in situ FTIR spectroscopy. *Electrochimica acta* **41**, 747-760 (1996).

39   Gofer, Y. *et al.* Underpotential deposition of lithium on polycrystalline gold from a LiClO4/poly (ethylene oxide) solid polymer electrolyte in ultrahigh vacuum. *The Journal of Physical Chemistry* **99**, 11739-11741 (1995).

40   Rehnlund, D., Ihrfors, C., Maibach, J. & Nyholm, L. Dendrite-free lithium electrode cycling via controlled nucleation in low LiPF6 concentration electrolytes. *Materials Today* **21**, 1010-1018 (2018).

41   Plieth, W. *Electrochemistry for materials science*. (Elsevier, 2008).

42   Horstmann, B. *et al.* Strategies towards enabling lithium metal in batteries: interphases and electrodes. *Energy & Environmental Science* **14**, 5289-5314 (2021).

4
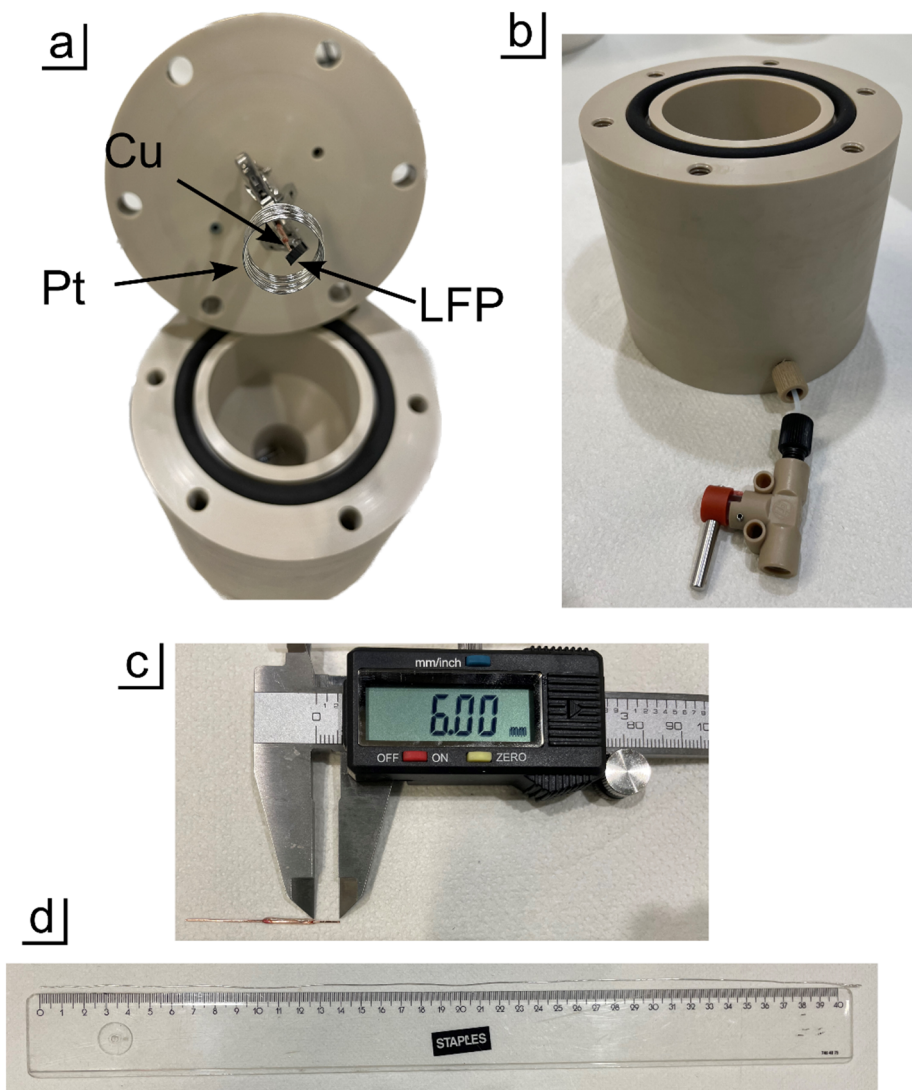
Figure C1. (a) Home-built autoclave three-electrode cell configuration. (b) Modified cell body with a drain to remove electrolyte before degassing. (c) Glass isolated Cu wire with Ø0.5mm and 6 mm length (A = 0.1 cm^2). (d) Pt wire has a Ø0.5mm and 40 cm length which is eventually reshaped into a Ø1.4 cm coil with A = 6.3 cm^2. Typically, half of the coiled Pt wire was submerged in the electrolyte.
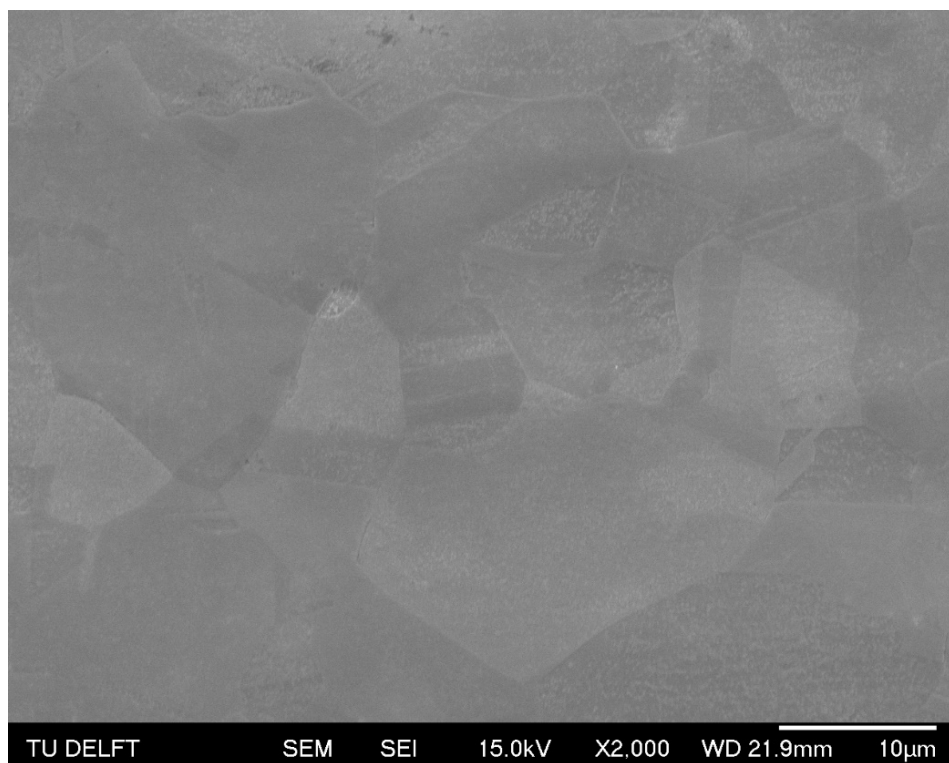
Figure C2. Scanning electron microscopy image of the Cu electrode after electropolishing.

1. Moisture trap
2. Gas filter
3. Pressure gauge
4. Autoclave Cell
5. Acid trap
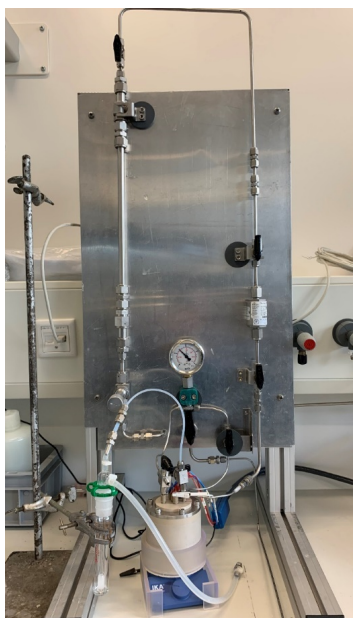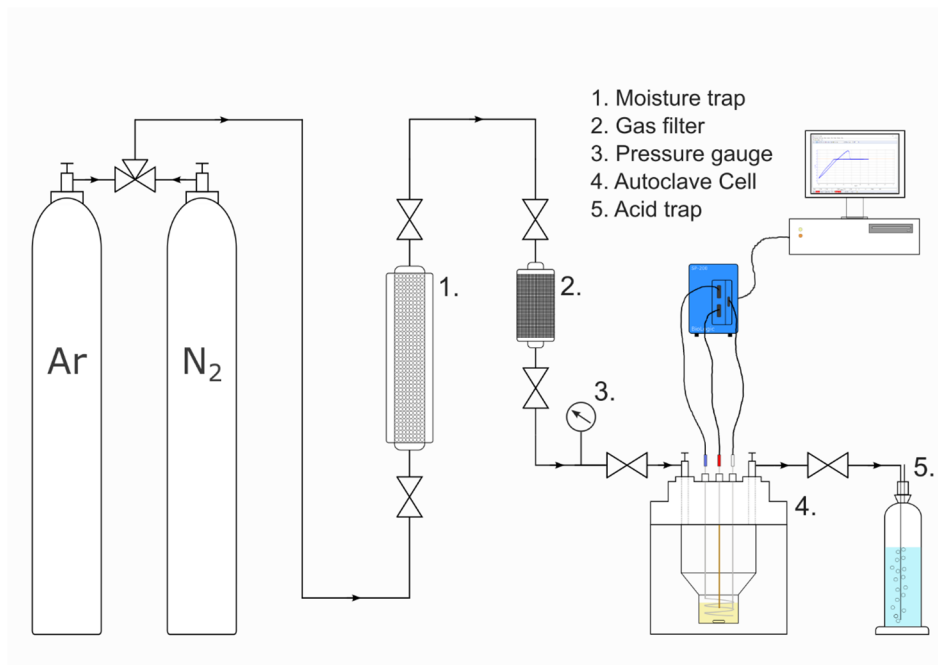
Figure C3. Schematic (top) and photograph (bottom) of the experimental setup configuration, including the gas cleaning skid, cell, stirrer and acid trap. A local suction point was always placed over the top of the cell and acid trap during operation but was omitted for the photograph.
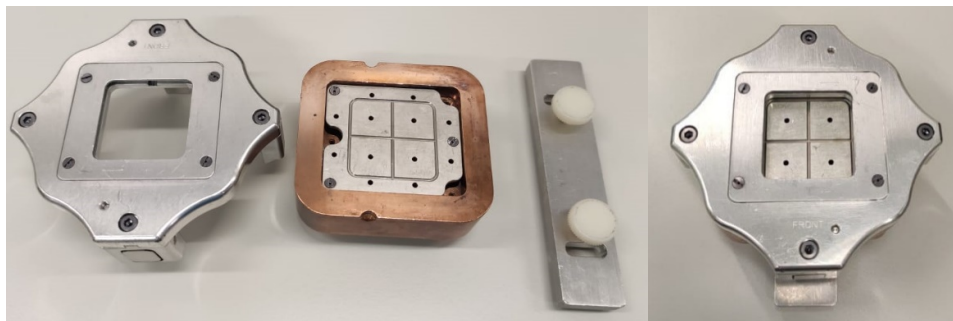
Figure C4. Photographs of the inert XPS sample holder for the Thermo Fischer K-Alpha XPS system.
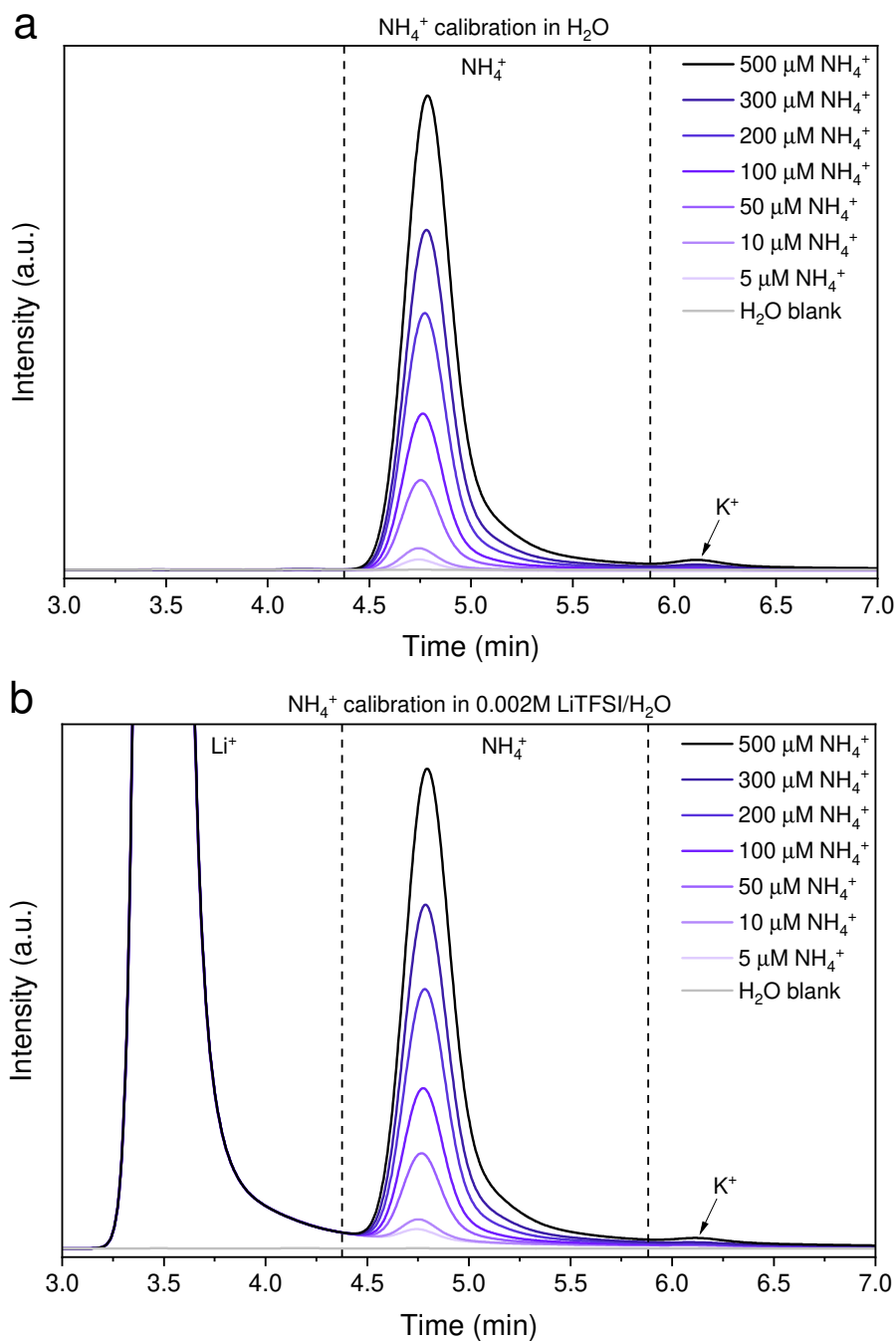
Figure C5. Ion chromatographs of different NH_4^+ concentrations in (a) ultrapure H_2O and (b) 0.002 M LiTFSI in H_2O.
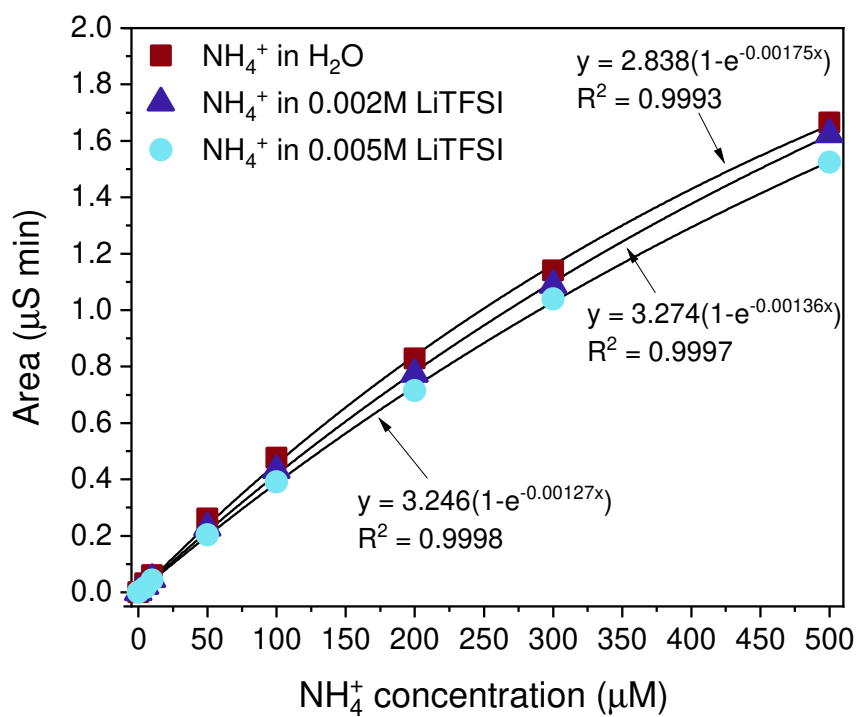
Figure C6. Ion chromatography calibration curves for NH_4^+ in H_2O, 0.002M LiTFSI and 0.005M LiTFSI in H_2O.
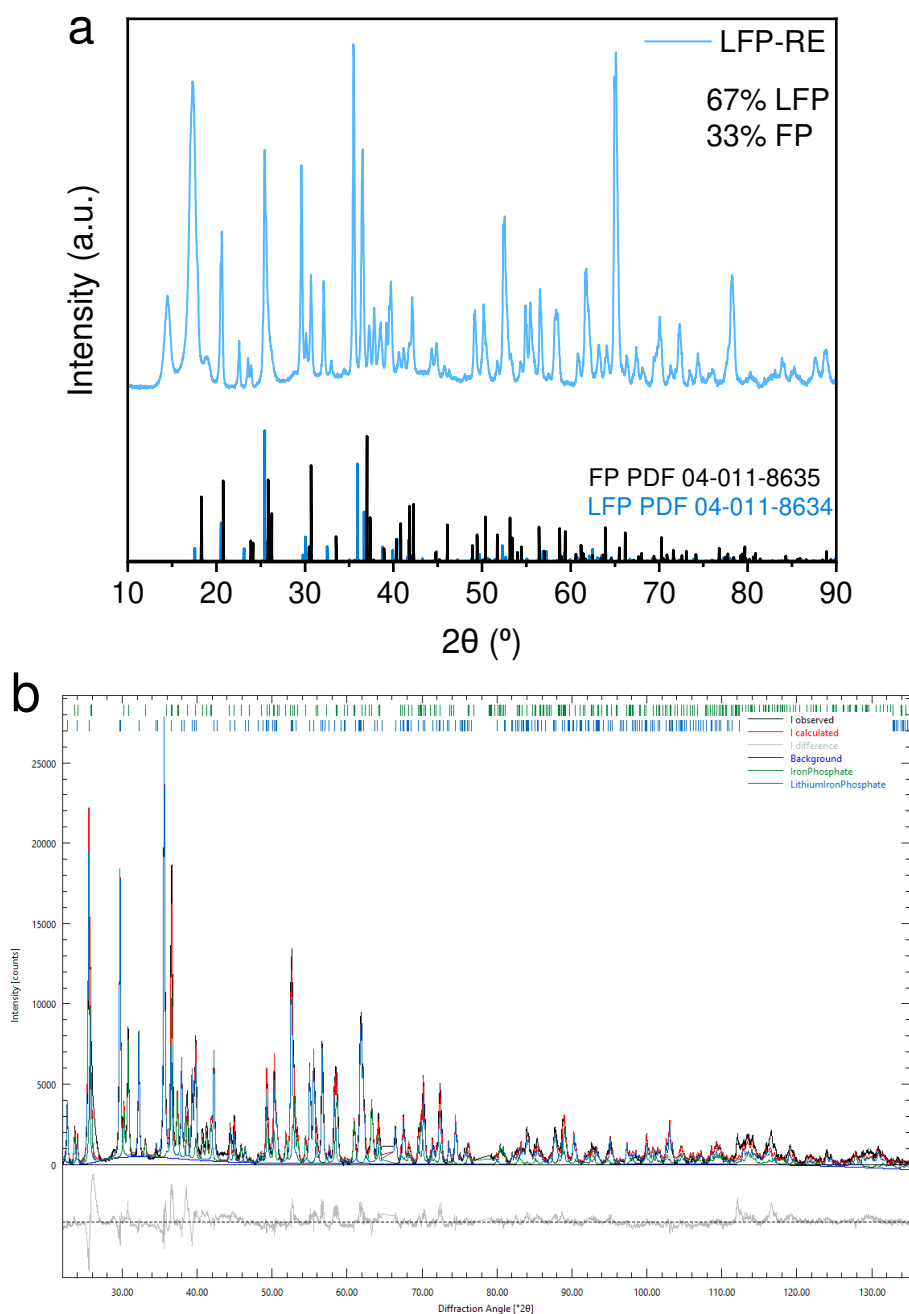
Figure C7. (a) XRD pattern of a partially delithiated LFP sheet with the respective LFP and FP phase composition obtained by Rietveld refinement. (b) Profex software environment with the XRD pattern fitting results.
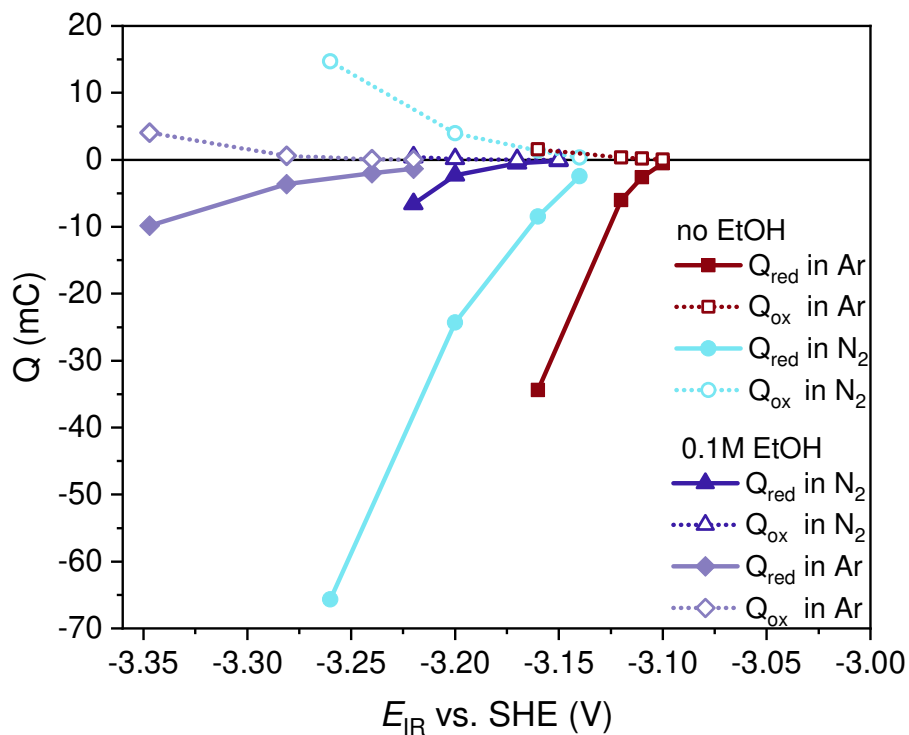
Figure C8. Total charge of the reduction and oxidation peaks of the CVs in Figure 1.
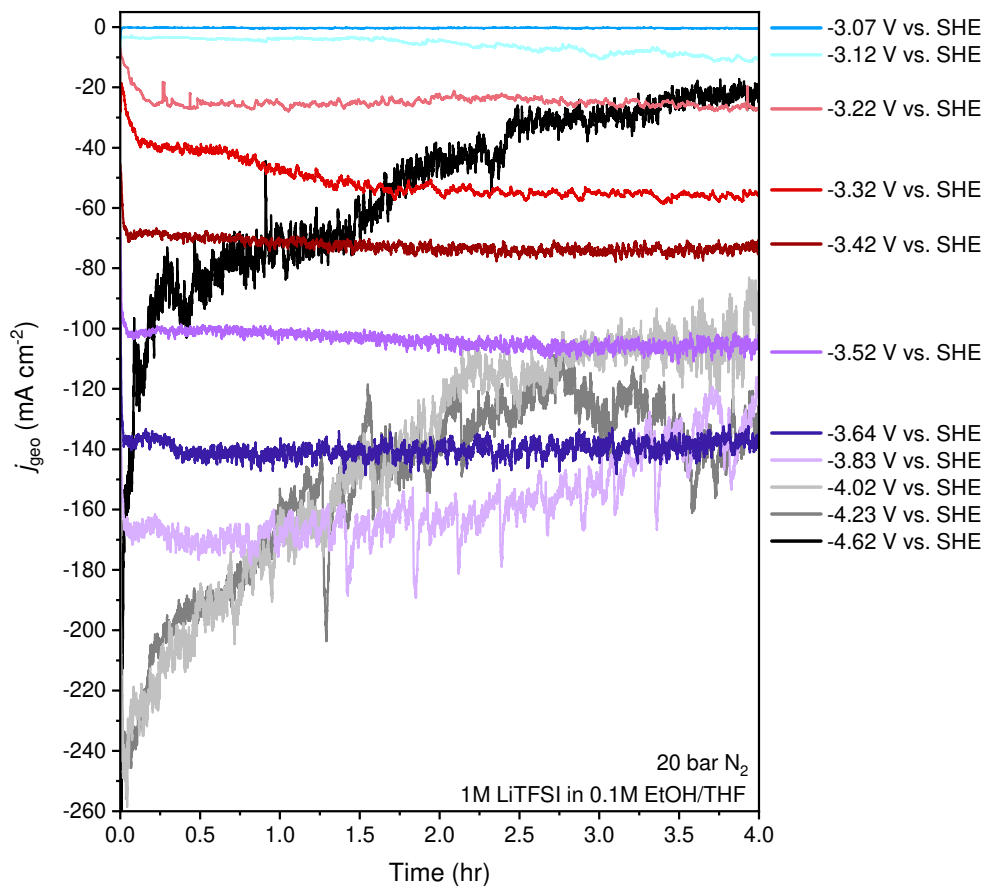
Figure C9. Chronoamperometry measurements at various potentials with 1 M LiTFSI in 0.1 M EtOH/THF.
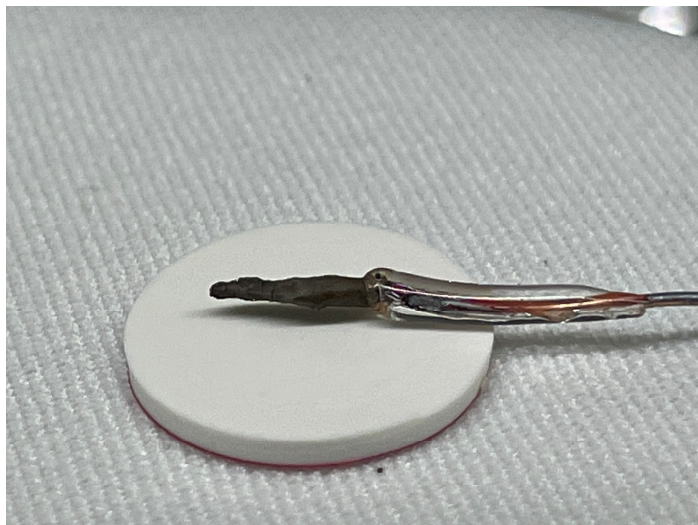
Figure C10. Photograph of the retrieved electrode with an intact SEI.
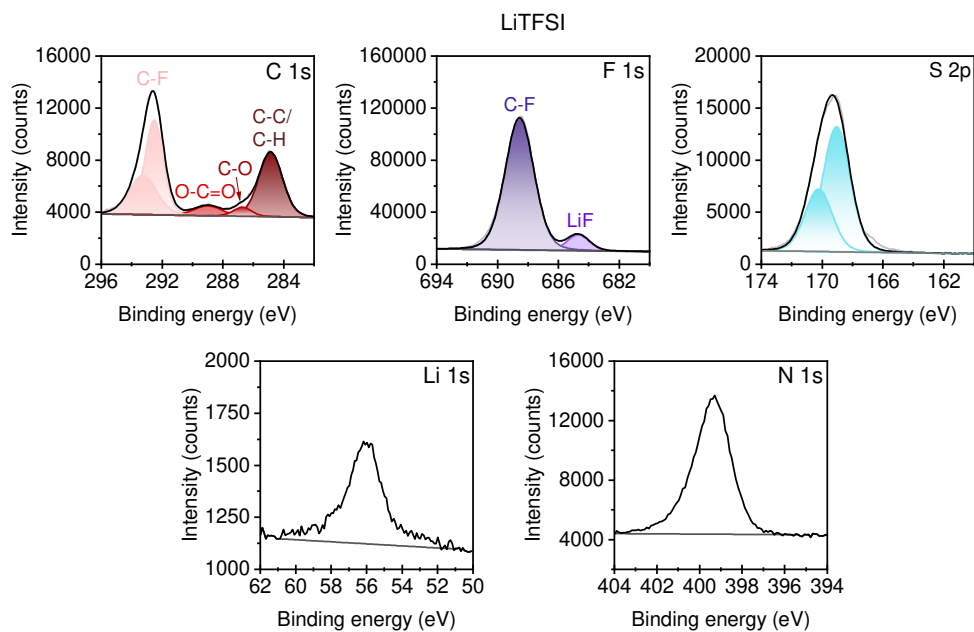
Figure C11. C 1s, F 1s, S 2p, Li 1s and N 1s high resolution XPS spectra of (as received) LiTFSI salt.
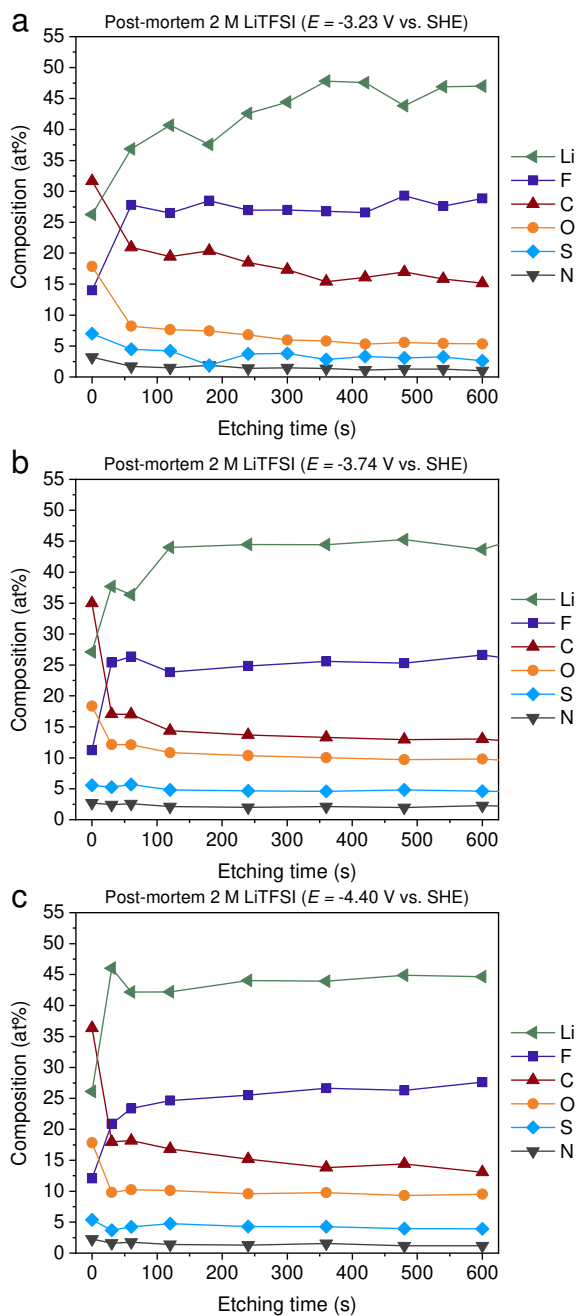
Figure C12. Elemental composition by XPS depth profiling of a SEI retrieved from 2 M LiTFSI at (a) -3.23 V vs. SHE, (b) -3.74 V vs. SHE and (c) -4.40 V vs. SHE.
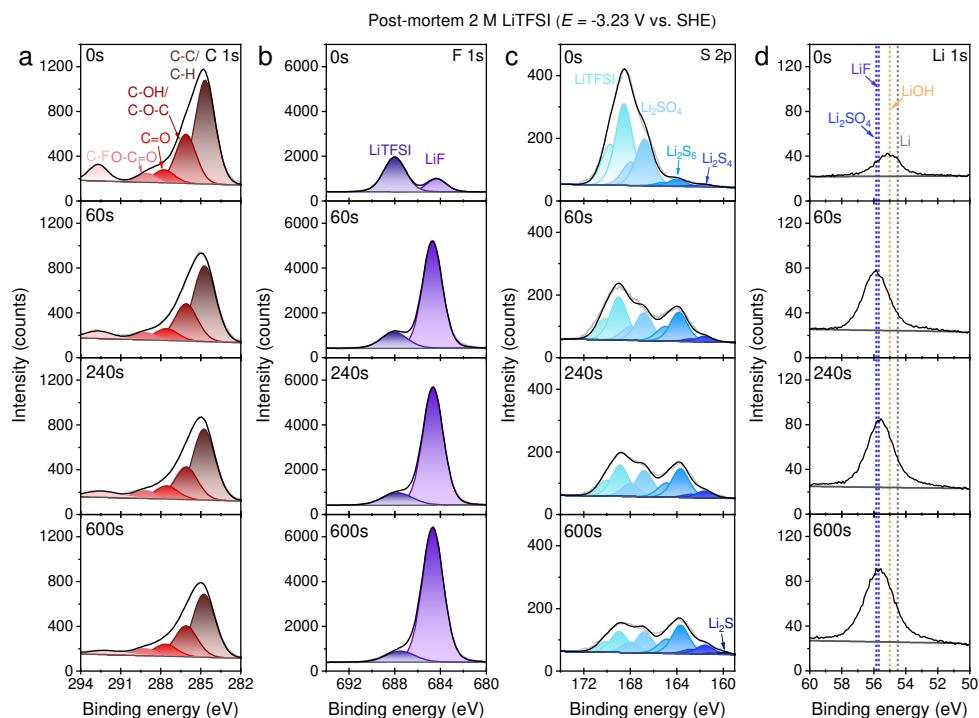
Figure C13. High resolution XPS spectra of (a) C 1s, (b) F 1s, (c) S 2p and (d) Li 1s at 0s, 60s, 240s and 600s of Ar⁺ ion etching with the retrieved SEI from 2 M LiTFSI at -3.23 V vs. SHE.
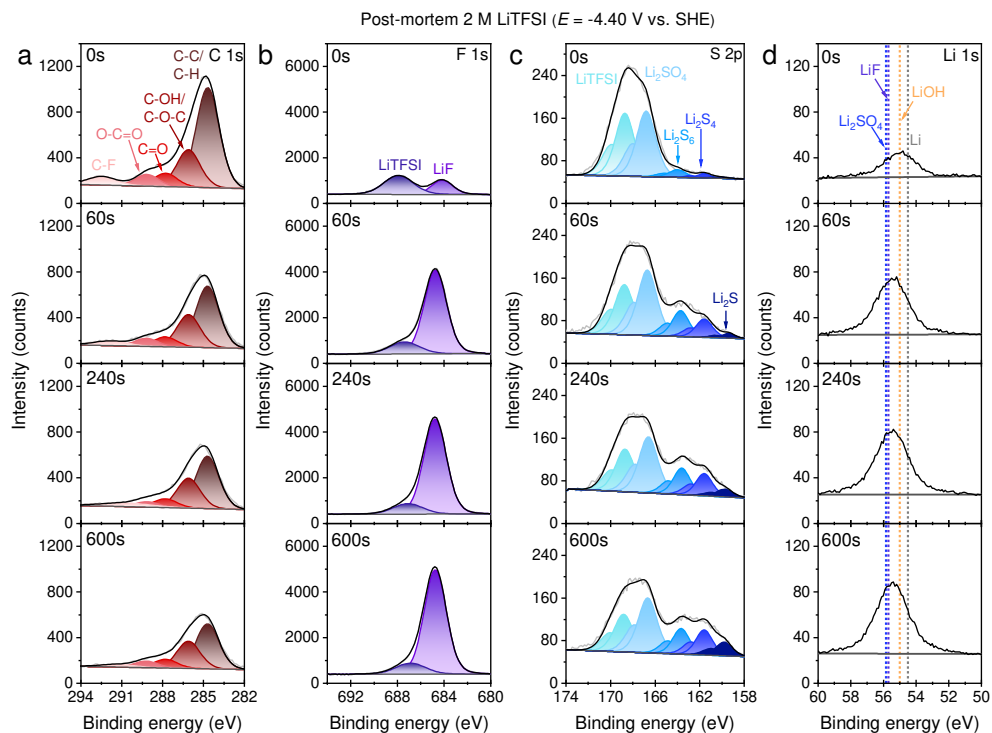
Figure C14. High resolution XPS spectra of (a) C 1s, (b) F 1s, (c) S 2p and (d) Li 1s at 0s, 60s, 240s and 600s of Ar$^+$ ion etching with the retrieved SEI from 2 M LiTFSI at -4.40 V vs. SHE.
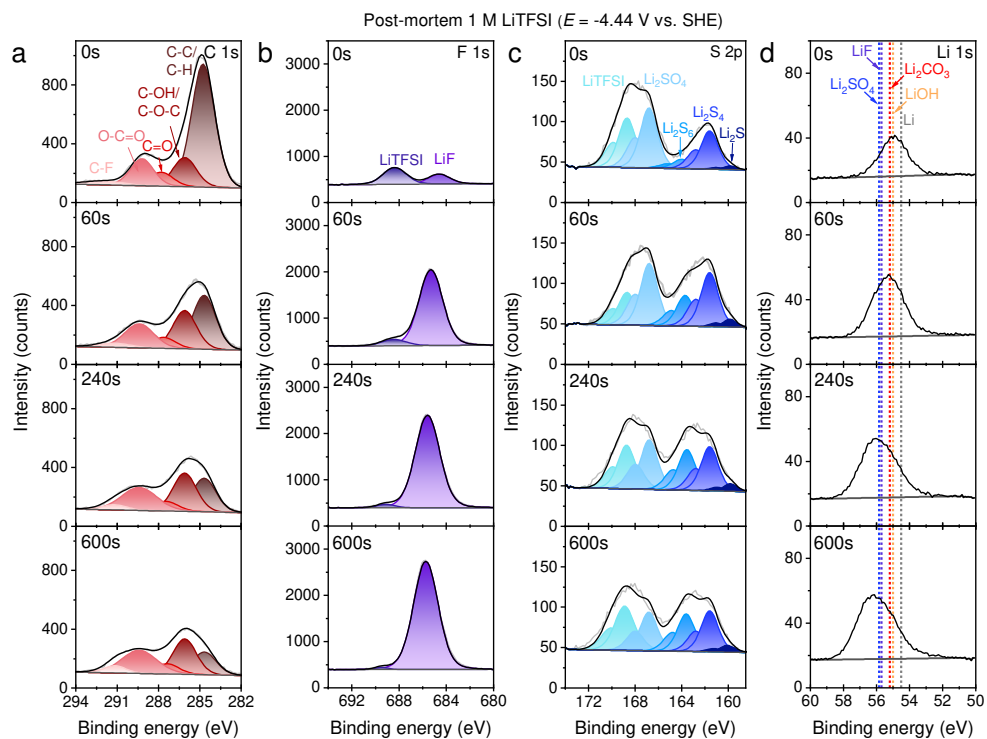
Figure C15. High resolution XPS spectra of (a) C 1s, (b) F 1s, (c) S 2p and (d) Li 1s at 0s, 60s, 240s and 600s of Ar+ ion etching with the retrieved SEI from 1 M LiTFSI at -4.44 V vs. SHE.
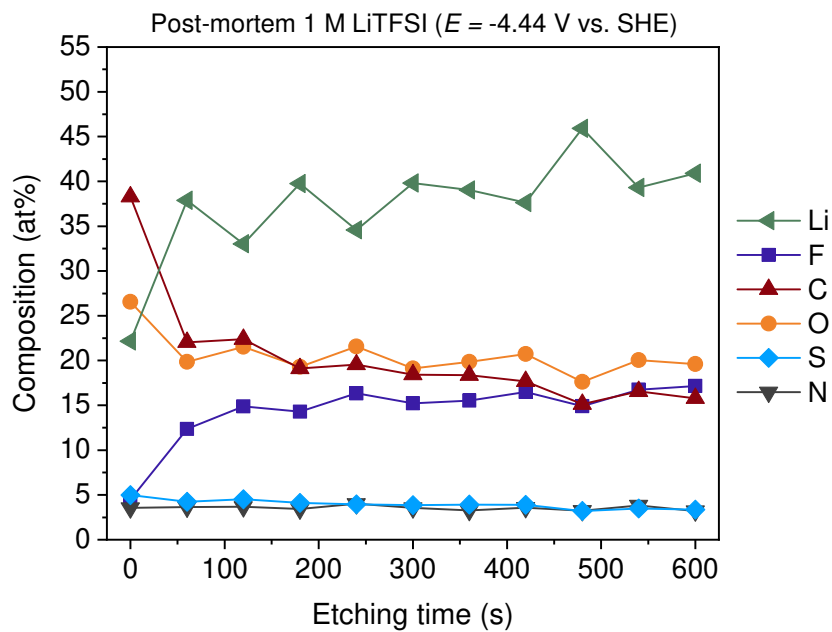
Figure C16. Elemental composition by XPS depth profiling of a SEI retrieved from 1 M LiTFSI at -4.44 V vs. SHE.

4

5

Techno-economic Assessment of Different Small-scale Electrochemical NH$_3$ Production Plants

Abstract

Electrochemical ammonia synthesis via the nitrogen reduction reaction (NRR) has been poised as one of the promising technologies for the sustainable production of green ammonia. In this work, we developed extensive process models of fully integrated electrochemical NH_3 production plants at small scale (91 tonnes per day), including their techno-economic assessments, on (Li-)mediated, direct and indirect NRR pathways at ambient and elevated temperatures, which were compared with electrified and steam-methane reforming (SMR) Haber-Bosch. The levelized cost of ammonia (LCOA) of aqueous NRR at ambient conditions may only become comparable with SMR Haber-Bosch at very optimistic electrolyzer performance parameters (FE > 80% at $j \geq 0.3$ A cm^{-2}) and electricity prices (< \$0.024 per kWh). Both high temperature NRR and Li-mediated NRR are not economically feasible within the tested variable ranges. High temperature NRR is very capital intensive due the requirement of a heat exchanger network, more auxiliary equipment and an additional water electrolyzer (considering the indirect route). For Li-mediated NRR, the high plating potentials, ohmic losses and the requirement for H_2, limits its commercial competitiveness with SMR Haber-Bosch. This incentivises the search for materials beyond lithium. Hitherto, electrified Haber-Bosch remains the only compelling electrochemical route towards green ammonia.

5.1 Introduction

Ammonia (NH$_3$) ranks among the largest produced synthetic chemicals in the world with an annual market size of ~180 Mt, total market capitalization of around $76 billion USD and an expected annual growth of 3-5%.[1,2] The majority of NH$_3$ (80%) is processed into N-based fertilizers such as urea and ammonium nitrate, where the latter is also used for the production of explosives (5%). Other applications are in the manufacturing of cleaning detergents, pharmaceuticals, rubber and other polymers (15%).[3,4] The vast majority of NH$_3$ is produced by the conventional thermochemical Haber-Bosch process, where high temperatures (300 – 500 °C) and pressures (200-300 atm) are required to reach sufficient NH$_3$ conversions from N$_2$ and H$_2$ over an iron catalyst.[5] Due to these intensive process conditions, this process requires substantial capital investments, with costs reaching billions of USD for plants producing >2000 tonnes ammonia per day to minimize costs by economy of scale.[6] The downside of these centralized plants are the increasing transportation costs, especially to remote areas. However, small scale plants (typically <100 tonnes per day) catering to local markets with regional price agreements have been reported.[7]

The most energy efficient method for H$_2$ feed production is steam methane reforming (SMR) based on natural gas, but this has significant environmental consequences as it releases 1.22 tCO$_2$ per tNH$_3$ alongside additional emissions related to burning fuel, natural gas extraction and other losses.[8] Approximately 1.2% of the anthropogenic CO$_2$ emissions are caused by the NH$_3$ sector, necessitating a transition to greener production alternatives to meet the net-zero emission goal in 2050.[9] A significant reduction in emissions can be accomplished if the SMR or coal gasification plant is substituted by greener alternatives, such as water electrolysis. This "electrified" version of the Haber-Bosch process, first implemented in 1928 (Rjukan, Norway), was discontinued in the 1960's when SMR became more competitive because of the cheap availability of natural gas; however, it is now poised for a comeback.[10] This is mainly due to the decreasing costs for renewable electricity from onshore wind and solar photovoltaics.[11] Moreover, the expected decline in manufacturing costs of alkaline and proton-exchange membrane electrolyzers (decreasing 3.0% and 4.8% each year),[12] for water electrolysis further enhances the competitiveness for the electrified Haber-Bosch in the near future.[8,13,14]

Alternative technologies for sustainable NH$_3$ production are based on the electrochemical nitrogen reduction reaction (NRR), where nitrogen gas in combination with a proton source can in theory be electrochemically reduced with electricity from renewable energy sources. The proton source can be "directly" used from water or "indirectly" from hydrogen. Both the direct and indirect NRR electrolyzer can in theory operate at ambient temperatures and pressures, thereby saving energy and capital expenditure on compressors and heat exchangers. Additionally, these technologies can be compatible with an intermittent renewable energy supply, which could be a major drawback for electrified Haber-Bosch.[15]

Another promising approach is NRR at elevated temperatures, harvesting waste heat from the chemical industry to produce NH_3 at higher rates and energy efficiencies.

Most of the current research in electrochemical NRR emphasizes the development of active, selective and stable electrocatalysts for the electrolyzers. Only a handful of publications have assessed the techno-economic feasibility of NRR technologies on a system level,[16] and focusing mostly on the electrolyzer costs.[17,18] Particularly, there is a lack of knowledge about the future design, energy consumption and techno-economic feasibility of a fully integrated electrochemical NH_3 process plant, including upstream and downstream separation units, heat integration and storage. To that end, we have developed comprehensive conceptual process models of direct and indirect NRR pathways at ambient and elevated temperatures, Li-mediated NRR and the electrified Haber-Bosch process as a sustainable benchmark. Moreover, we have used a consistent set of assumptions to perform a comparative analysis between these technologies, which gives key insights into the required electrolyzer performance metrics and the minimum ammonia production price necessary to enable carbon emission-free ammonia.

5.2 Methodology

5.2.1 Process Design Assumptions and Descriptions

It is expected that electrochemical ammonia plants operate in a decentralized manner. Therefore, a small capacity of 91 tNH_3 per day is considered, which is based on the smallest commercial SMR HB plant that supplies only to local markets.[7] The synthesis process is assumed to be continuous, which means that a variable availability of renewable energy is outside the scope of the current study and capacity factors of the process are high.

The majority of the mass balance and economic calculations were performed in conventional spreadsheet software. Aspen Plus™ was used to model distinct unit operations, such as distillation and adsorption columns, flash evaporation, pump and compressor duties and heat integration if necessary. All NRR electrolyzers are considered as stoichiometric black box models. The total cell voltage (E_{cell}) is defined as:

$$E_{cell} = E_{eq} + \eta_{cat} + \eta_{an} + \eta_{mem} + \eta_{ohmic} \qquad \text{(Equation 1)}$$

, which summates the equilibrium potential (E_{eq}), cathodic (η_{cat}) and anodic (η_{an}) half-reaction overpotentials, ionic transport resistance in the membrane (η_{mem}) and electrolyte (η_{ohmic}). The power consumption of the electrolyzer (P_{elect}) is a function of E_{cell} and the total current (I):

$$P_{elect} = E_{cell} \cdot I = E_{cell} \cdot \frac{n_{NRR} \cdot F \cdot R_{NH_3}}{FE} \qquad \text{(Equation 2)}$$

, wherein the latter can be expressed in the NH_3 mole-based production capacity (R_{NH_3}) and faradaic efficiency (FE) to include the losses from the hydrogen evolution reaction (HER).

Losses associated with power electronics, connections and cables are excluded. All assumptions and more detailed calculations related to the electrolyzer are provided in the "Supplemental Methods" in Appendix D. We defined the energy efficiency (EE) of the electrolyzer or the entire process as the ratio between the LHV of NH_3 (18.6 GJ per tNH_3) and the total energy input (e_{in}):

$$EE_{elect} = \frac{LHV_{NH_3}}{\sum e_{in}} = \frac{LHV_{NH_3}}{\dfrac{P_{elect}}{\dot{m}_{NH_3}}} \qquad \text{(Equation 3)}$$

, where $\dot{m}_{NH_3}$ is the production capacity in tonnes per seconds. Figure 1 shows basic representations of the envisioned process flow diagrams (PFDs). More detailed PFDs are illustrated in Figure D1-6, including stream data and equipment specifications, which can be found in Tables D1-14. The processes can be generalized into three segments; (1) feed pretreatment, (2) NH_3 synthesis and (3) NH_3 separation. The exact unit operations for each segment depend on the NH_3 synthesis configuration. In contrast to SMR-based Haber-Bosch, all electrolysis based NH_3 processes require a pure N_2 feed from an air separation unit (ASU) via either cryogenic distillation or pressure swing adsorption (PSA). The selection of a specific ASU technology depends on the N_2 capacity, where PSA is more economical below 500 tN_2 per day.[19] If a PSA is integrated in the process, the oxygen waste stream can not be sold as commodity because its purity is below market grade (< 99.9%), which is not the case for cryogenic distillation. Argon is also a by product of the ASU, but is excluded from the analysis.

For the electrified Haber-Bosch process (see Figure 1a), an alkaline electrolyzer (AEL) or proton exchange membrane electrolyzer (PEMEL) is integrated in the model for the production of H_2. The main advantage of PEMEL over AEL is its load flexibility, compact design, high pressure operation and a better energy efficiency, but is significantly more costly.[20] Therefore, it is valuable to understand the economic benefit of both scenarios. N_2 and H_2 are both pressurized to 155 bar in an intercooled multi-stage compressor before entering the Haber-Bosch reactor. The thermocatalytic NH_3 reaction is exothermic (-53.8 kJ mol^{-1} at 155 bar, 400 °C), which can be harnessed to pre-heat the reactor feed. Hence, no additional heat source is required. The $N_2/H_2/NH_3$ mixture is cooled down to -5 °C and separated by flash evaporation into a 99.5 mol% NH_3 product stream and 4 mol% $NH_3/N_2/H_2$ gaseous mixture. The latter is recycled back to the compressor and mixed with the other feed gases.
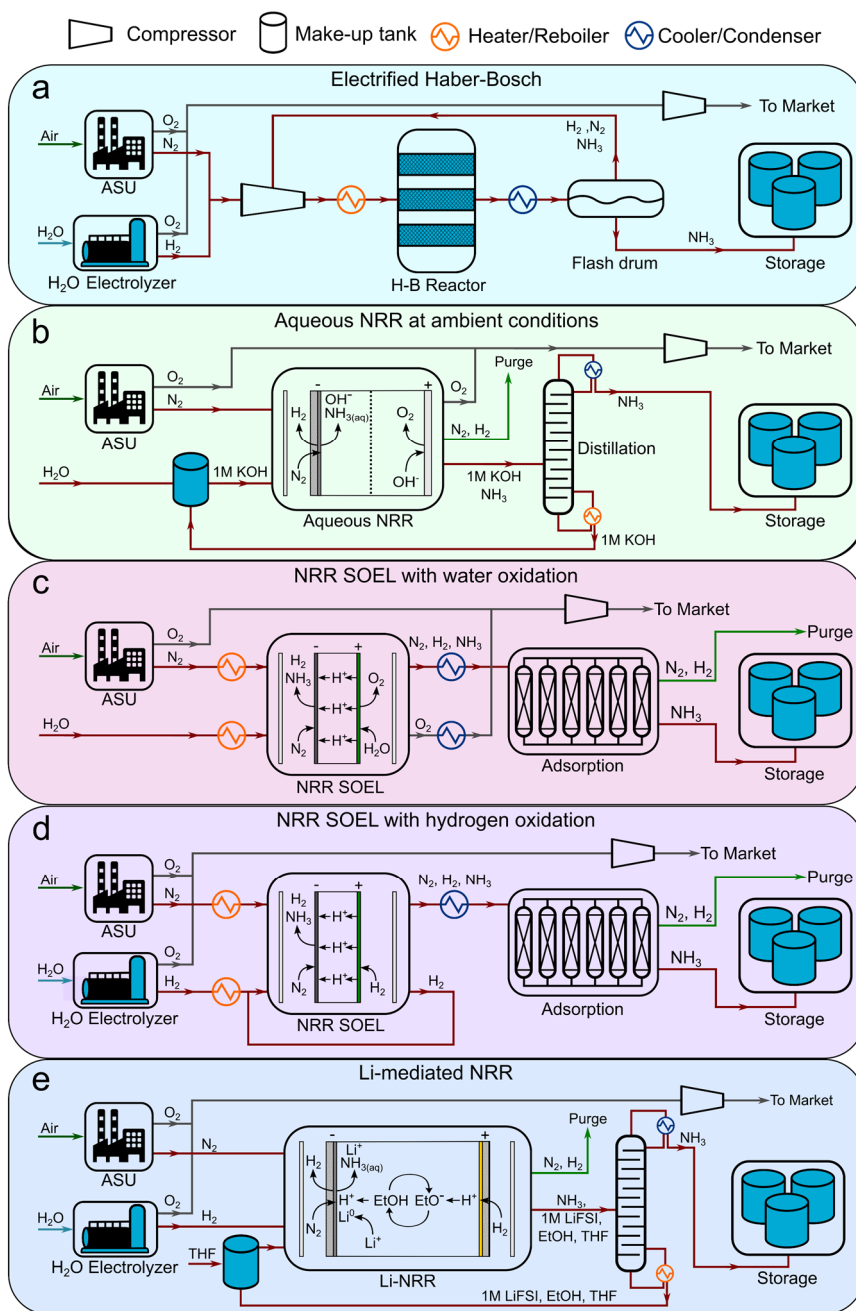
Figure 1. Schematic process diagrams of (a) electrified Haber-Bosch, (b) aqueous NRR at ambient conditions using a GDE electrolyzer configuration, (c) High temperature NRR with water oxidation in a SOEL, (d) high temperature NRR with hydrogen oxidation in a SOEL, (e) Li-mediated NRR with hydrogen oxidation in a GDE electrolyzer.

Figure 1b illustrates our proposed design for aqueous based electrochemical ammonia synthesis at ambient conditions (aqueous NRR). The aqueous NRR electrolyzer is modelled as a gas diffusion electrode cell (GDE). The NRR occurs at the triple phase boundary (TPB) at the liquid catholyte side of the GDE, where it is assumed that produced NH_3 will directly dissolve into the electrolyte due to its high solubility (540 g per L_{H_2O} at 20 °C).[21] H_2 is formed as a byproduct at the TPB and flows back through the GDE into the gas compartment. Two design alternatives for the utilization of the gaseous N_2/H_2 product stream were considered; The N_2/H_2 product stream can simply be purged (referred as "purge scenario") or is partly separated via a N_2/H_2 PSA to sell H_2 as a commodity ("PSA scenario"). However, N_2/H_2 separation is non-trivial and may require at least 60 mol% H_2 in the PSA feed to be technically feasible.[22] Therefore, we incorporated an accumulation loop in the PSA scenario that recycles a N_2/H_2 mixture back to the GDE to satisfy this requirement (see Figure D3). Another potential strategy is to harvest the energy of the N_2/H_2 mixture by the generation of heat via combustion. The latter is not desirable because N_2 forms NO_x-related greenhouse gases upon combustion,[23] which require additional $DeNO_x$ installations. Dissolved NH_3 in 1M KOH aqueous solution is separated by distillation with a distillate purity of 99.5 mol% and 99.9% NH_3 recovery. The energy consumption of the column depends mainly on the NH_3 composition in the feed (see Figure D7). From our analysis, a minimum of 10 mol% NH_3 is implemented to limit the distillation energy consumption.

High temperature NRR occurs in a solid oxide electrolyzer (SOEL) that operates at 550 °C and 1 atm. This pathway is divided into two similar process variations, wherein the SOEL reduces N_2 with water oxidation (NRR SOEL with water oxidation, Figure 1c) or hydrogen oxidation including an additional water electrolyzer for H_2 production (NRR SOEL with hydrogen oxidation, Figure 1d). The SOEL operates in thermoneutral mode, meaning that the heat balance within the cell is in equilibrium.[20] A heat exchanger network is designed to minimize the required heat input for the SOEL feed, by integrating inlet with outlet streams, as can be seen in the PFDs (Figure D4 and D5). The $NH_3/N_2/H_2$ product mixture cannot be separated by flash evaporation because the stream is at atmospheric pressure. NH_3 condensation is only techno-economically feasible when higher pressures (≥ 150 bar) are considered (as for the electrified Haber-Bosch process).[8] For low pressure systems, adsorption by zeolites or absorption in alkaline earth metal salts are poised as promising separation technologies.[24] In this process, NH_3 is separated by an adsorption step with an NH_3 product purity of 99.5 mol% and recovery of 90%. The other 10% cannot be recycled because NH_3 will decompose directly (> 400 °C). Due to the complexity of the heat integration system, it was not possible to further separate the N_2/H_2 stream in a similar fashion as the aqueous NRR process (PSA scenario). Combustion of the N_2/H_2 mixture for heat extraction is not desirable due to the formation and emission of NO_x-species.

The electrolyzer design in the Li-mediated NRR process (Figure 1e) is inspired on the continuous flow cell recently developed by Chorkendorff and coworkers.[25] The electrolyzer is modelled as a symmetric GDE cell for Li-NRR and hydrogen oxidation, separated by an

organic electrolyte that contains 1M lithium bis(fluorosulfonyl)imide (LiFSI) in 0.25 vol% EtOH/THF. We selected 1M LiFSI due to its high conductivity with respect to other Li salts, while we are aware that the highest FEs in a batch-type cell were obtained with 2M LiBF$_4$ and 2M LiTFSI.[26,27] Again, it is assumed that NH$_3$ will directly dissolve in the organic electrolyte and can be separated by distillation with a distillate purity of 99.5 mol% and 99.5% NH$_3$ recovery.

5.2.2 Assumptions for the Techno-Economic Analysis

The techno-economic analysis is based on small scale NH$_3$ plants with the same capacity (91 tNH$_3$ per day) that operate 333 days per year, with a life time of 20 years for electrolysis based ammonia processes and 40 years for SMR Haber-Bosch. It is assumed that the electrolyzer stacks do not have to be replaced during the life time of the plant. The investment cost for a 91 tNH$_3$ per day SMR Haber-Bosch plant is \$$_{2022}$ 936M taken from ref [7] (with inflation correction). The capital costs of the sustainable ammonia processes were estimated based on the equipment costs of all the the process units in the plant. Standard process equipment, such as compressors, heat exchangers, pumps and columns are designed based on industrial heuristics. The equipment costs (C$_E$) were calculated via different equipment capacity (S) correlation functions:

$$C_E = a + b \cdot S^N = C_B \cdot \left(\frac{S}{S_B}\right)^N = 10^{K_1 + K_2 \log(S) + K_3 \log(S)^2} \qquad \text{(Equation 4)}$$

Where the coefficients (a, b, N, K$_1$, K$_2$, K$_3$) are tabulated in chemical engineering handbooks and summarized in Table D15.[39-42] The costs for cryogenic distillation (ASU) and N$_2$/H$_2$ PSA were calculated based on the 6th tenth rule with base estimates from Morgan et al. and Mivechian et al.[43,44] For the ASU PSA, a modular cost estimation was applied (N = 1) with a base estimate from Banares-Alcantara et al.[45] The equipment cost of the electric steam boiler was assumed to be \$60 per kW.[46,47]

The electrolyzer costs, electricity and hydrogen prices for the base case scenario are inter- and extrapolated from 2022-2050 cost projections taken from numerous available sources (see Figure 2 and Table D16 for referencing).[11,48-51] Other base case parameters, such as the price of O$_2$ (\$0.14 per kg),[52] natural gas (\$3.78 per GJ),[53] H$_2$O (\$7.5 per m^3),[54] CO$_2$ tax (\$58 per tCO$_2$),[55] labor and O&M (3% of total capital costs) are kept constant.[20,32] These numbers are mostly based on North American price indexing if available. For each cost parameter, more conservative and optimistic price projections reported by other literature sources were also included in the analysis (see Table D16 for more details). This wide range of model input data allows us to predict under what conditions green NH$_3$ becomes feasible and in which timeframe.

It is important to note that there is no available capital cost data of NRR electrolyzers. Therefore, their capital costs were derived from commercial H$_2$O electrolyzers and compared with other cost data from the literature for validation.[56,57] Electrolyzer costs, often

expressed in $ per unit power, were converted with their respective power density (kW per m^2) to $ per unit area to include the effect of the current density on the economics. The power density is related to the *j-E* characteristics of the electrolyzer, hence the $ per m^2 is different for each particular system as can be seen in Figure 2c. Additional statements regarding the electrolyzer capital cost assumptions and an extended discussion on the calculations are available in Appendix D (Subsection "Techno-economic Assumption")

Figure 2. Price projections for; (a) renewable electricity for a conservative, base case and optimistic scenario; (b) base case water electolyzer costs of PEMEL, AEL and SOEL in $ per unit power; (c) base case electrolyzer costs of NRR electrolyzers in $ per unit area. Data used for these figures is listed in Table D16.

The inflation was corrected with the chemical engineering plant cost index (CEPCI). The total capital cost was estimated from the equipment cost with the Lang factorial method.[40] These factors include the installation costs, contingency and working capital (more details can be found in Table D17). It is important to note that the installation costs in the "inside battery

limit" (ISBL) are temperature, pressure and material dependent, therefore the ISBL was calculated for each piece of equipment independently. The electrolyzer installation costs were not estimated via the Lang factors, but were assumed to be 10% of the equipment costs.[20] General assumptions regarding the OPEX are mentioned in Table D18. The end-of-life net present value (NPV) was calculated using Equation 5 with 25% tax rate, 25% salvage value and a linear depreciation scheme by taking the cumulative sum of the cash flow (CF) discounted with 4.28% interest rate (median between 1954-2023 US interest rates):[58]

$$NPV = \sum_{t=1}^{n} \frac{CF_t}{(1 + \text{interest rate})^t}$$

(Equation 5)

The levelized cost of ammonia (LCOA) is used as an indicator to estimate and compare the economic feasibility of the different ammonia production plants. The LCOA is a function of the product revenue present value (Equation 6), which can be obtained by adjusting the NH_3 selling price until the NPV is equal to zero.[16,59] The total capital cost is incurred during the first construction year of the plant (t = 0), where it assumed that the plant is fully operational at $t \geq 1$.

$$NPV = 0 = \text{product revenue PV (LCOA) - operating cost PV - total capital costs}$$

(Equation 6)

5.3 Results and Discussion

5.3.1 Identification of Energy Losses in Different NRR Electrolyzers

The energetics of the electrolyzer often dominate the overall energy input of an electrochemical process. Here we used a simple model to estimate the current – voltage relationship (Figure 3) and identify the losses of the considered NRR electrolyzers (with Equations 1 and 2, respectively). This gives us a preliminary estimate of the energy efficiency of each process and how this relates to the energy efficiency of SMR Haber-Bosch.

An important advantage of the aqueous NRR compared to the electrified Haber-Bosch is the process intensification step, where NH_3 can potentially be synthesized in a single electrolyzer with a considerably lower $E_{eq,0}$ (1.17 V) versus 1.23 V for H_2O electrolysis, with a thermodynamic minimum of 19.9 GJ per tNH_3 with respect to 21.3 GJ per tNH_3 for H_2O electrolysis (based on the LHV of stoichiometric amount of H_2).[8] However, NRR involves six proton-coupled electron transfer steps, where the intermediates impose thermodynamic constraints. As a result, a minimum barrier in the form of an η_{NRR} (0.4-0.6 V) is required to activate the reaction.[5,28,29] The j-E curve in Figure 3a indicates that below 0.42 A cm^{-2}, the activation overpotentials (η_{NRR} and η_{OER}) dictate E_{cell}. At higher j, ohmic losses become more significant due to the relatively low conductivity of the 1M KOH electrolyte (0.215 S cm^{-1} at 25°C). At 0.3 A cm^{-2} and 90% FE, taken as electrolyzer aspirational values from the US Department of Energy ARPA-e REFUEL program,[30] the ohmic losses are so severe that the

electrolyzer's EE decreases to 39% (see Figure 4a). This can partly be circumvented by considering a 25 wt% KOH aqueous solution as a more conductive electrolyte, thereby increasing the EE with +9%.
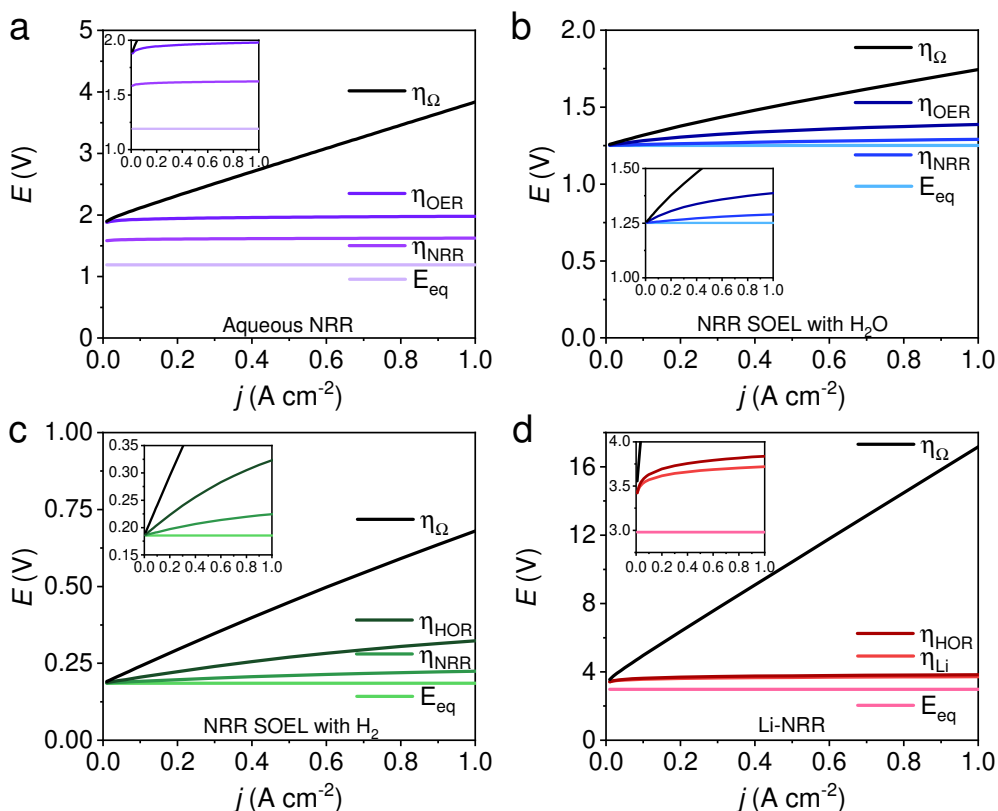
Figure 3. Build-up of the current – voltage relationship with the equilibrium potentials, overpotentials and ohmic losses for: a) aqueous NRR, (b) NRR SOEL with water, (c) NRR SOEL with hydrogen and (d) Li-NRR. Relevant input data is listed in Table D19 and assumptions are discussed in the "Supplemental Methods" in Appendix D.

An advantage of high temperature NRR is the lower activation barrier for both the NRR (0.04 V at 1 A cm^{-2}) and the H$_2$O oxidation reaction (0.1 V at 1 A cm^{-2}) as illustrated in Figure 3b. In contrast to a water SOEL, the $E_{eq,0}$ of NRR increases with temperature (1.17 V at 25°C to 1.21 V at 550°C) due to a negative change in reaction entropy (see Figure D8-10). The main reason why SOELs operate at such high temperatures is to increase the conductivity of the solid electrolytes. Ce$_{0.8}$Sm$_{0.2}$O$_2$ is commonly used as an electrolyte and it has a conductivity of 0.014 S cm^{-1} at 650°C, which is an order of magnitude lower than 1 M KOH (0.215 S cm^{-1}), but this is typically compensated by using a thin slab of 0.05 mm. At 0.3 A cm^{-2}, the voltage losses account for 13% of E_{cell}, thus the $E_{eq,0}$ dictates the energy efficiency. By substituting the water oxidation reaction (OER) for the hydrogen oxidation reaction (HOR), the $E_{eq,0}$

decreases to 0.19 V (see Figure 3c). Nevertheless, the net energy gain of the cell voltage is compensated by the additional requirement for H_2 (alkaline water electrolysis consumes 28.4 GJ per tNH_3 based on the Nel Hydrogen type "A485"). Figure 4b and 4c clearly demonstrates that the indirect approach is more energy intensive (without considering the up- and downstream units), where the EE of NRR SOEL with water is +14% higher than NRR SOEL with H_2 (including AEL).
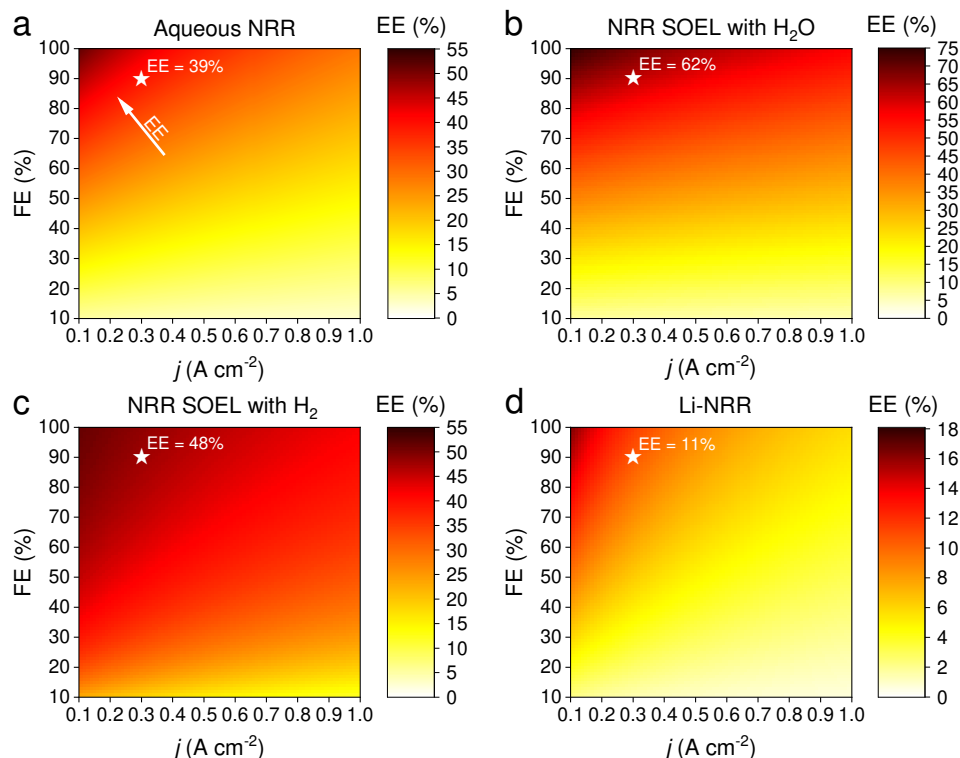
Figure 4. Contour plots of the electrolyzer's EE as a function of j and FE for: (a) aqueous NRR at ambient conditions, (b) high temperature NRR in a SOEL with water oxidation, (c) high temperature NRR in a SOEL with hydrogen oxidation and (d) Li-NRR with hydrogen oxidation. Both (c) and (d) include an additional energy input term for H_2 production with an alkaline H_2O electrolyzer (28.4 GJ per tNH_3 based on the commercial AEL type "A484" of Nel Hydrogen).[20] Star symbol indicates the calculated EE at the US DoE Arpa-e electrolyzer aspirational values (0.3 A cm^{-2} and 90% FE). It is important to note that the plots imply a low j (< 0.1 A cm^{-2}) seems appealing. However, there is an economic trade-off between the EE and j, where the former has an effect on the OPEX and the latter on the capital costs. The optimal electrolyzer operation parameters will be discussed in the economic analysis.

Li-mediated NRR is fundamentally energy intensive due to the required presence of metallic Li, with an $E_{eq,0}$ of -3 V vs. SHE for Li-plating. This results in a thermodynamic minimum of 51 GJ per tNH_3 when Li-plating is combined with hydrogen oxidation (at 0 V vs. SHE), which is already 16 GJ per tNH_3 higher than electrified Haber-Bosch. Figure 3d shows that the actual energy input will be even more severe due to activation overpotentials and ohmic losses. Among the Li-salts, Li bis(trifluoromethanesulfonyl)imide (LiTFSI) and Li bis(fluorosulfonyl)imide (LiFSI) are reported as having the highest conductivities in organic solvents and contain fluorinated functional groups. Especially the latter is important for the formation of a stable and selective SEI.[26] By assuming 1M LiFSI dissolved in 0.1M EtOH/THF as electrolyte with a conductivity of 0.015 S cm^{-1} (electrolyte gap = 2 mm), the ohmic resistance becomes so significant, that ohmic losses starts to dominate E_{cell} at current densities > 0.3 A cm^{-2}. Unsurprisingly, the EE diagram in Figure 4d indicates that Li-NRR (including AEL for green H_2 production) has the lowest EE in comparison with other NRR electrolyzers.

5.3.2 Energy Losses in Sustainable NH_3 processes

The total energy inputs for the NH_3 production processes, including the electrolyzers, upstream and downstream unit operations, are illustrated in Figure 5. For comparison, the energy requirement of SMR Haber-Bosch is also included and was taken from previous literature reports.[8,31] The energy input of the AEL (28.4 GJ per tNH_3) and PEMEL (32.8 GJ per tNH_3) for the electrified Haber-Bosch process and indirect NRR pathways are based on commercially available models from Nel Hydrogen (A485) and Siemens Energy (Silyzer 300) with an EE of 75% and 65% (using the LHV of the stoichiometric amount of H_2).[20] The energy requirements for the NRR electrolyzers were calculated with our electrochemical model using the US DoE ARPA-e aspirational values (0.3 A cm^{-2} and 90% FE) as input parameters. The following highlights the main findings from our energy analysis and discusses several energy saving strategies.

The energy consumption in the synthesis loop is significantly higher in the methane fed Haber-Bosch process (6.45 GJ per tNH_3) than in the electrolysis based process.[8,31] These losses in SMR Haber-Bosch can be assigned to low efficiencies of the steam turbine cycles (42-48%) that drive the feed-gas, recycle and refrigeration compressors.[8] Additional losses of 1.7 GJ per tNH_3 are associated with the necessity to purge a part of the product mixture for the recycle loop. In electrified Haber-Bosch, the losses in the NH_3 synthesis loop are solely related to the compressor duty since there is no requirement for purging. Moreover, these compressors are are significantly more efficient because they are electrically-driven and have a driver efficiency up to 95%. Commercially available PEMEL systems have the ability to produce H_2 at 35-50 bar, which can save up to 56% of the compressor duty. After the synthesis loop, the $NH_3/N_2/H_2$ mixture is separated by condensation (typically at -5 °C and 145 bar).[32] Although the temperature gradient between the condenser and the synthesis reactor seems large, heat integration in the synthesis loop (see Appendix D

Supplemental Methods) recovers most of the heating and cooling duties. The energy input of the ASU is directly proportional to the stoichiometric demand of N_2 for the reactor because unreacted N_2 is separated and recycled back to the synthesis loop. Therefore, the ASU energy demand is limited to 1.3 GJ per tNH3. Although the electrified version of the Haber-Bosch is less energy efficient (33.9 GJ per tNH3) than the BAT (27.4-31.8 GJ per tNH3) due to the water electrolyzers, it is expected that innovations in the PEMEL system will improve the EE in the foreseeable future.[33]
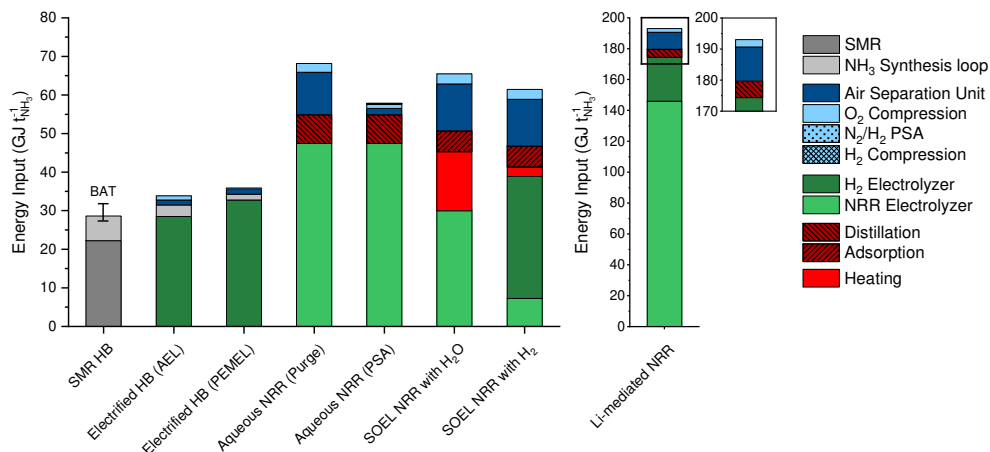
Figure 5. Indicative overview of the estimated energy input of each process. Values above the LHV of NH3 (18.6 GJ per tNH3) can be considered as energy losses. The energy input of the NRR electrolyzer was calculated at the aspirational values (j = 0.3 A cm^{-2} and FE = 90%). Generally, the energy losses will increase at FE < 90% and j > 0.3 A cm^{-2}.

The aqueous NRR electrolyzer consumes 47.4 GJ per tNH3, which accounts for 57% of the total energy loss. It is assumed that NH_3 dissolves directly into the electrolyte after electrosynthesis and has be separated downstream by distillation. The NH_3 feed composition plays an important role in determining the energy input of the distillation unit. Figure D7 shows that the reboiler duty decays exponentially with increasing NH_3 feed concentration, with a minimum at approximately 10 mol%. Even at 10 mol%, the duty of both the reboiler and condenser are still considerable (7.5 GJ per tNH3). Implementing a N_2 recycle stream can reduce the demand of "fresh" N_2 from the ASU. To study this effect, we considered two process design alternatives for the N_2/H_2 product stream, where the product stream is simply purged (Figure D2) or separated by a PSA with N_2 recycling and H_2 recovery (Figure D3). The purge scenario shows a 7-fold increase of the ASU duty (10.9 GJ per tNH3) with respect to the PSA scenario. This indicates the importance of a recycle stream in order to save up to -9.3 GJ per tNH3.

NRR SOEL with water oxidation is the most energy efficiency NRR electrolyzer (62%), meaning that the voltage losses at high temperature electrolysis are minimal. However, this

is a false minimum since roughly 15 GJ per tNH_3 of additional heat is necessary to sustain the NRR SOEL operational temperature (550 °C). Even though heat integration is included, there is a mismatch between the heat capacities of the reactants (N_2, $H_2O_{(g)}$) and products (N_2, NH_3, O_2). This implies that external heat must be supplied. By combining the additional heat and energy input of the SOEL, the EE decreases to 41%. Unfortunately, 3.8 GJ per tNH_3 of this heat is labelled as "high quality heat" (to raise the feed temperature to 550 °C), which is challenging to obtain by steam, but can be harnessed from electric heating or waste heat from neighbouring chemical plants.[34] For a stand-alone plant, a "green" furnace based on biogas or H_2 from water electrolysis are also considerable options. For now, it is assumed that the heat is imported from neighbouring chemical industries for the natural gas price. To save energy on the ASU (-10.2 GJ per tNH_3), the N_2 enriched waste stream from the separation step can in principle be recycled and mixed with the reactant stream. However, an additional 3.3 GJ per tNH_3 of high quality heat is necessary to elevate the recycle temperature from 200°C to 550°C. This means that there is a trade-off between the import of heat and ASU energy savings. For simplicity, the recycle stream is excluded from further analysis. Separating the low pressure N_2/H_2/NH_3 product mixture of the NRR SOEL by condensation is not economically attractive due to the excessive compressor costs.[8] While still in the research phase, adsorption with zeolites is a promising approach for low pressure NH_3 separation.[24,35] The energy input for separation by adsorption (5.5 GJ per tNH_3) depends on the heat of adsorption (2.76 GJ per tNH_3), feed compression (2.32 GJ per tNH_3) and desorption vacuum swing (0.46 GJ per tNH_3). The compression duty is required to overcome the large pressure gradient (around 2 bar) across the densely packed column. The heat of adsorption depends on the interaction strength between the adsorbent and adsorbate. Since NH_3 binds strongly to zeolites, a significant amount of heat must be supplied for desorption, although this is much less than would be required with metal halides.[24]

The enormous energy input of the Li-NRR electrolyzer (146 GJ per tNH_3) accounts for 84% of the process losses, which are inherently related to the Li-plating potential and the low conductive nature of organic Li-salt electrolytes. These specific physical properties cannot be improved, but the electrolyte gap between the electrodes can be minimized by implementing a zero-gap membrane electrode assembly (MEA).[36] Figure D11 indicates that the electrolyzer EE can be increased by 8% when the electrolyte gap is completely eliminated. An alternative strategy is to find an active mediator with a lower plating potential than Li. Ca has recently been identified as an active mediator besides Li.[37] However, the net energy gain of using Ca is limited since its plating potential only differs ~0.2 V from Li. Theoretical work of Bagger, Stephens and coworkers have proposed Mg and Al as promising alternatives.[38] An overview of the $E_{eq,0}$ and ΔG of these mediators paired with hydrogen oxidation are displayed in Figure D12. When assuming an $E_{eq,0}$ of -2.36 V vs. SHE for Mg plating and 0 V vs. SHE for hydrogen oxidation, the thermodynamic minimum of this electrolyzer would be 40.2 GJ per tNH_3, which is still significantly higher in comparison with other NRR electrolyzers. Al is in terms of its low plating potential the most propitious element, but remains yet to be experimentally explored and verified.

5.3.3 Economic Comparison of Methane-based versus Electrified Haber-Bosch

With the implementation of the base case assumptions, the LCOA of the small scale SMR Haber-Bosch plant is \$555 per tNH_3 as illustrated in Figure 6a and 6d, which is in line with previous literature reports.[16,60] These figures indicate that the price for grey ammonia (from SMR Haber-Bosch) remain considerably lower than ammonia from sustainable sources, such as the electrified Haber-Bosch process. The sensitivity analysis implies that the natural gas price and carbon tax are the main cost drivers for SMR Haber-Bosch (Figure D13). For a while, these plants have been benefitting from relatively low natural gas prices (~\$3 per GJ), but the 2022 energy crisis in Europe has shown that SMR Haber-Bosch can be vulnerable.[61] The US EIA states that natural gas prices can rise above \$5 per GJ by 2050 which will put a lot of pressure on conventional Haber-Bosch economics.[18] Additionally, societies demand more compensation for emitted greenhouse gases from the chemical industries in the form of an emission trading system or tax to stimulate the transition towards renewable alternatives. The latest IPCC report predicts that a carbon tax of \$58 per tCO_2 is necessary to incentivise the implementation of carbon capture and storage technologies by the chemical industry.[55] Other economists and climate scientists claim that the CO_2 tax should increase even further to \$174-417 per tCO_2.[62-64] Hence, a more conservative price scenario (\$175 per tCO_2, \$5.66 per GJ) is necessary to incentivise a shift towards carbon free NH_3.
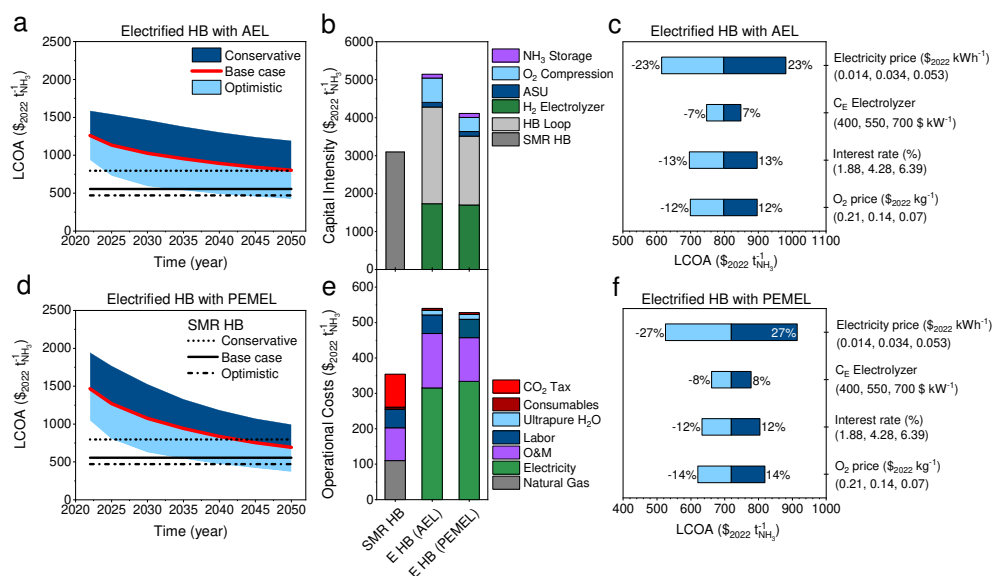
Figure 6. Economic analysis of electrified Haber-Bosch. (a) Levelized cost of ammonia (LCOA) of electrified Haber-Bosch with AEL at conservative, base case and conservative assumptions. (b) Capital intensity calculated with the base case assumption in 2050. (c) Sensitivity analysis of electrified Haber-Bosch with AEL. (d) LCOA of electrified Haber-Bosch with PEMEL at conservative, base case and conservative assumptions. (e) Operational costs estimated with the base case assumptions in 2050. (f) Sensitivity analysis of electrified Haber-Bosch with PEMEL. Black lines in (a,d) indicate the LCOA of SMR

HB calculated with optimistic (NG price = \$2.79 per GJ, CO_2 tax = \$23 per tCO2), base case (NG price = \$3.77 per GJ, CO_2 tax = \$58 per tCO2) and conservative (NG price = \$5.66 per GJ, CO_2 tax = \$175 per tCO2) price scenarios.

Figure 6a and 6d illustrate that electrified Haber-Bosch is too expensive under the current economic conditions (in 2022) compared with SMR Haber-Bosch, even when considering conservative price assumptions (~\$800 per tNH_3). The sensitivity analysis in Figure 6c and 6f show that the electricity price has the largest influence on the LCOA. By saving \$0.01 per kWh on the OPEX, the LCOA reduces with roughly \$100 per tNH_3 (electrified HB with PEMEL), while a cost reduction of \$100 per kW of the stack, lowers the LCOA with only \$60 per tNH_3 (approximately -5%). When considering the base case cost projection, electrified HB with PEMEL becomes cost competitive with SMR HB at \$615 per kW (PEMEL investment costs) and \$0.035 per kWh (electricity price). This means that the manufacturing of PEMEL systems and the cost of electricity has to be reduced by -68% and -38% within the upcoming decades. Other combinations of electrolyzer CAPEX and electricity prices can also lead to cost competitive ammonia production (see Figure D14b). Replacing PEMEL with AEL demands an additional investment of 29% for larger compressors because commercially available AELs deliver H_2 at atmospheric pressure. Therefore, PEMEL is in this context a more suitable source for H_2.

5.3.4 Economic Analysis of Aqueous NRR at Ambient Conditions

The LCOA of aqueous NRR at ambient conditions for the process scheme with a N_2/H_2 purge or PSA recovery unit are under the base case conditions not competitive with SMR Haber-Bosch, and require more optimistic price projections (see Figure 7a and d). The main economic issue with aqueous NRR is the relatively high operational costs (~\$450 per tNH_3) related to the electrolyzer due to unavoidable energy losses by activation overpotentials and ohmic losses. Consequently, Figure 7e indicates that approximately 70% of the electricity costs and 50% of the OPEX are associated with the electrolyzer's electrical input. The capital costs of the NRR electrolyzer comprises 55% of the total capital cost and is ~\$2000 per tNH_3 more expensive than a PEMEL. The latter is justifiable since a GDE-based system is more complex in operation and consumes more power per tNH_3. Therefore, the balance of plant (BoP) can be higher due to additional pressure regulators, rectifiers with a larger capacity, and miscellaneous auxiliary equipment.

The process design with a N_2/H_2 purge (Figure D2), hence without a N_2 recycle, consumes evidently more "fresh" N_2 feedstock from the ASU. Consequently, the CAPEX of the ASU (18% of total capital costs) is roughly \$1200 per tNH_3 more expensive than when a N_2 recycle is considered. For electrified Haber-Bosch, recycling N_2 or a N_2/H_2 mixture is more straightforward because N_2/H_2 can be re-compressed, mixed with the N_2/H_2 feedstock and fed into the synthesis reactor. A mixture of N_2/H_2 can in principle be used as feed for the NRR electrolyzer since H_2 is inert. But, if H_2 is not separated from the recycle loop, it will accumulate, cross-over to the anode and form an explosive mixture with O_2 or recombine

into water. To realize a H_2 separation step, an additional capital injection of 11% has to be invested into a N_2/H_2 PSA ($638 per tNH_3), storage infrastructure for recycle buffering ($1286 per tNH_3) and H_2 compressors ($488 per tNH_3) with a -4% gain of the OPEX. It becomes clear that by comparing the LCOA trend in Figure 7a and 7d, purging the N_2/H_2 product stream is from an economic point of view more attractive because N_2/H_2 separation is considered to be technically challenging, wherein a minimum feed composition of 60 mol% H_2/N_2 is typically required with very low H_2 recoveries (~50%).[22]
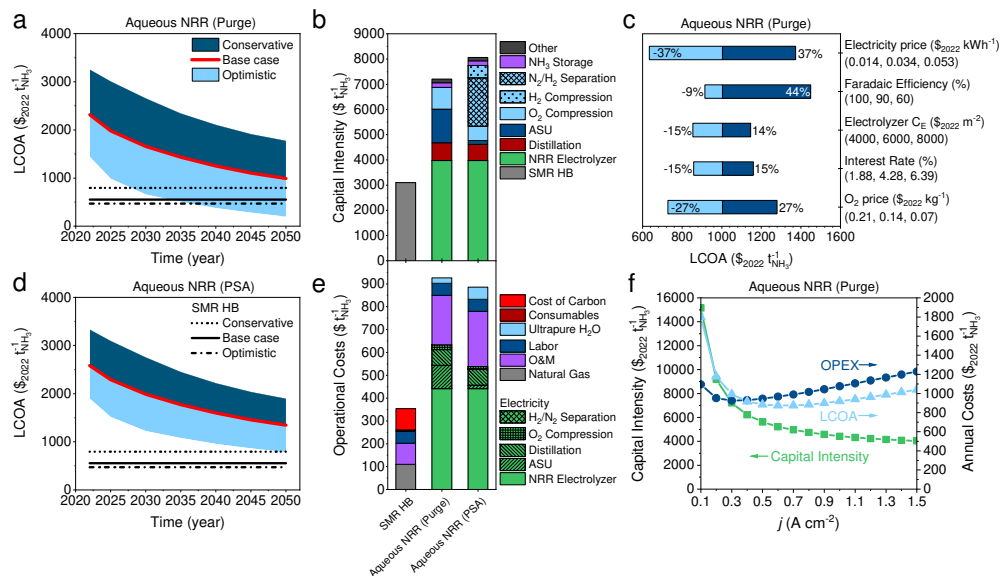
Figure 7. Economic analysis of aqueous NRR at ambient conditions. (a) LCOA of aqueous NRR with a H_2 purge. (b) Capital intensity calculated with the base case assumptions in 2050. (c) Sensitivity analysis of aqueous NRR (purge) at a constant j of 0.3 A cm^{-2}. (d) LCOA of aqueous NRR with H_2 recovery (PSA). (e) Operational costs using the base case assumptions in 2050. (f) Current density as a function of the capital intensity, OPEX and the LCOA for aqueous NRR (purge) at FE of 90% and base case assumptions in 2050. Black lines in (a,d) indicate the LCOA of SMR HB calculated with optimistic, base case and conservative price scenarios. (a,b,d,e) The ARPA-e electrolyzer aspirational values (FE = 90%, j = 0.3 A cm^{-2}) were used for the economic analysis.

Stirring towards H_2 production with NH_3 as a by product (FE < 50%) is not preferred because NH_3 has more intrinsic value, and H_2 can be produced more efficiently in a PEMEL or AEL. This indicates that steering towards a FE near unity is should be the main objective as is supported by our sensitivity analysis (Figure 7c). When considering the purge scenario, O_2 market price fluctuations have a substantial effect on the LCOA (±27%), especially in comparison with electrified Haber-Bosch (Figure 6c and 6f). This is related to the vast quantities of O_2 (230 tonnes per day) that are being produced by the cryogenic distillation unit due to the large demand for N_2. In case the location of the plant does not allow O_2 export to the market, the LCOA increases by ~$550 per tNH_3.

The necessary cost reductions to reach SMR Haber-Bosch parity (~$800 per tNH_3) are highlighted in Figure D14c. It becomes clear that very optimistic electrolyzer costs ($5600 per m^2) and electricity prices ($0.025 per kWh) has to be realized for cost competitive NH_3 production. Additionally, the LCOA is heavily influenced by the electrolyzer performance metrics. Figure 7f presents an optimal j window between 0.5-0.9 A cm^{-2}, where the LCOA is approaching its minima. By assuming an electrolyzer CAPEX of $5850 per m^2 (base case) and a very optimistic electricity price of $0.02 per kWh, a "minimum" FE as a function of the j can be estimated. The results are displayed in Figure D15 and highlights three regions: FE > 80% at 0.3 A cm^{-2}, FE > 70% at 0.4 A cm^{-2} and FE > 65% between 0.5-1 A cm^{-2}. Operating at j < 0.3 A cm^{-2} is not preferable because the capital costs increases exponentially with the electrode area. The earlier used aspirational values from the ARPA-e REFUEL program (90% FE, 0.3 A cm^{-2}) are reasonable and fall within the estimated range. Nevertheless, this analysis extends the aqueous NRR opportunity window and can be used as guidelines for experimentalists.

5.3.5 Economic Analysis of NRR at Elevated Temperatures

Figure 8a and 8c show that both NRR SOEL with water and with hydrogen pathways are under the base case assumptions not cost competitive with SMR Haber-Bosch, and require a more optimistic economic scenario. In contrast with aqueous NRR, the CAPEX and OPEX of the NRR SOEL unit are not dominating the plant costs. The majority of the investment is related to conventional process units, such as heat exchangers, air separation units and adsorption columns, which account for roughly 65% of the fixed capital costs. According to our analysis, NRR SOEL with hydrogen (containing two electrolyzers) is more cost effective than the NRR SOEL with water. This is counterintuitive, but can be explained based on differences in the heat integration and the electrolyzer capital costs. NRR SOEL with hydrogen has almost an ideal heat integration scenario, limiting the demand for high quality heat, which saves up to $100 per tNH_3 on the OPEX. Additionally, Figure 8b illustrates that the NRR SOEL unit with hydrogen oxidation is less capital intensive due to its lower power density (1.6 versus 5.9 kW per m^2 for NRR SOEL with water oxidation), which directly affects the BoP as discussed previously.

The sensitivity analysis in Figure 8e and D16 indicates that the electricity price has the largest effect on the feasibility. Unsurprisingly, the absence of a N_2 recycle in the high temperature process means that the ASU is producing large quantities of O_2, which has to be sold for additional revenue. At the ARPA-e REFUEL aspirational values (FE = 90%, j = 0.3 A cm^{-2}), Figure D14e illustrates that NRR SOEL with hydrogen only becomes competitive with SMR Haber-Bosch at very optimistic electricity prices (≤ $0.02 per kWh) and SOEL capital costs ($800 per m^2). We estimated new aspirational values for the NRR SOEL with hydrogen oxidation using the same approach as discussed for aqueous NRR. By assuming a NRR SOEL and AEL CAPEX of $1209 per m^2 and $564 per kW (base case assumptions in 2050) at an electricity price of $0.02 per kWh, the trend in Figure D17 can be divided into three

segments: FE > 90% at 0.4 A cm^{-2}, FE > 85% at 0.5 A cm^{-2} and FE > 80% between 0.6-1 A cm^{-2}. These performance requirements are significantly higher than for aqueous NRR because improvements in the CAPEX and OPEX of the NRR SOEL unit has only a limited effect on the plant's economics.
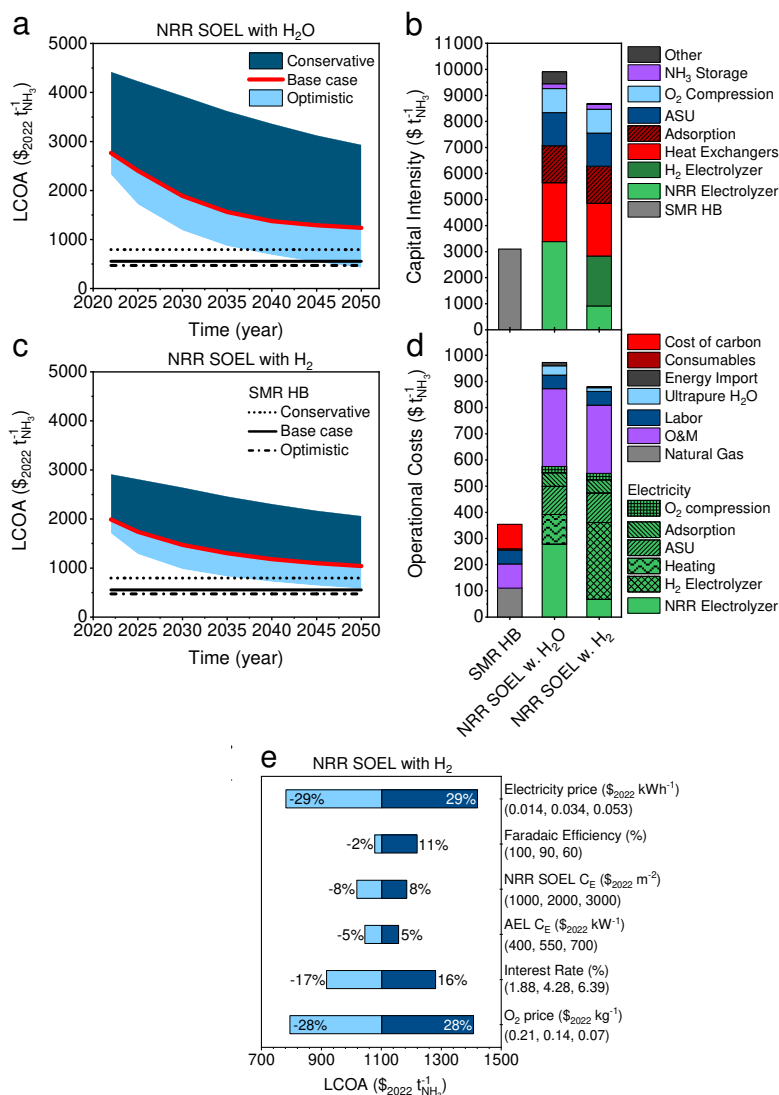
Figure 8. Economic analysis of high temperature NRR. (a) LCOA of NRR SOEL with water oxidation. (b) Capital intensity calculated with the base case assumptions in 2050. (c) LCOA of NRR SOEL with hydrogen oxidation. (d) Operational costs calculated with the base case assumptions in 2050. (e) Sensitivity analysis of NRR SOEL with hydrogen oxidation at a constant j of 0.3 A cm^{-2}. Black lines in (a,d) indicate the LCOA of SMR HB calculated with optimistic, base case and conservative price scenarios. (a-d) The ARPA-e electrolyzer aspirational values (FE = 90%, j = 0.3 A cm^{-2}) were used for the economic analysis.

NRR SOEL with water has even a smaller opportunity window, wherein electricity must decrease to unrealistic market prices (≤ $0.018 per kWh) at $3000 per m^2. Electricity prices up to $0.01 per kWh have been reported during peak periods of surplus renewable power.[65] An electrochemical NH_3 plant could theoretically operate along the volatile trend of low electricity market prices. The scale of the plant increases according to an assumed capacity factor, which results in higher investment costs. Wang et al. investigated the matter and observed an increase of the LCOA with $100 per tNH_3 at a 0.2-0.3 capacity factor.[16] Another issue is the compatibility with intermittent operation, which can especially be challenging for high temperature electrolysis, upstream and downstream units.

5.3.6 Economic Assessment of Li-mediated NRR

Among the assessed sustainable NH_3 pathways, Li-mediated NRR is the most expensive process and cannot become cost competitive with SMR Haber-Bosch even when considering the most optimistic cost factors (Figure 9a). Due to the complexity of the electrolyzer system (GDE-based, compatibility with organic electrolytes, moisture free operation) and significant power demand, the BoP will be excessive and comparable with other energy intensive electrochemical processes, such as chlor-alkali (~$30000 per m^2).[56] With a base case estimate of $18650 per m^2 (in 2050), approximately 75% of capital intensity is directly related to the electrolyzer system (Figure 9b). The operational costs in Figure 9c shows that the electricity consumption of the Li-NRR electrolyzer accounts for almost 50% of the total OPEX (~$1360 per tNH_3), mainly due to its low EE. By changing to a more compact cell design, a zero gap membrane electrode assembly without ohmic losses, the LCOA can be reduced by ~50% (Figure D18a), but is still not sufficient.

Another strategy is to find an alternative mediator with a significantly lower deposition potential. Although Ca has recently been identified as an active mediator besides Li,[37] its reduction potential differs only +0.2 V vs. Li, which results in a limited gain in the OPEX. We decided to do a preliminary techno-economic screening, whereby Mg and Al are implemented as potential mediators (+0.7 V and +1.37 vs. Li). We assume a zero-gap electrolyzer configuration with the Li-plating activation overpotential and the same upstream and downstream units as used in the Li-NRR process. Under the base case assumptions (in 2050), Mg-NRR or Al-NRR allow a LCOA reduction of -$262 and -$547 per tNH_3 with respect to Li-NRR in MEA configuration. These cost saving scenarios are insufficient and do not allow mediated NRR to compete with other sustainable ammonia processes (as illustrated in Figure D18). This incentivises the search for mediators beyond Al in order to enable mediated NRR as a compelling approach.
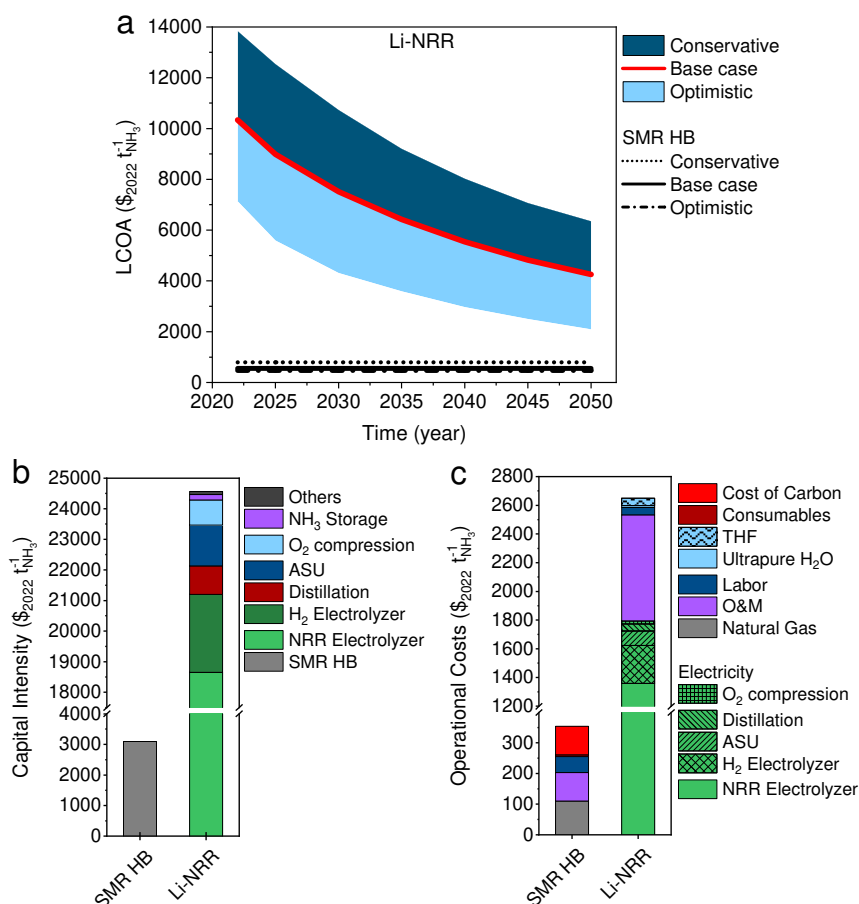
Figure 9. Economic analysis of Li-mediated NRR. (a) LCOA of Li-NRR. The black lines indicate the LCOA of SMR HB calculated with optimistic, base case and conservative price scenarios. (b) Capital intensity calculated with base case assumptions in 2050. (c) Operational costs calculated with the base case assumption in 2050. (a-c) The ARPA-e electrolyzer aspirational values (FE = 90%, j = 0.3 A cm^{-2}) were used for the economic analysis.

5.3.7 Future Outlook

SMR Haber-Bosch will be around for several decades until the technology can be phased out with a zero-emission alternative. The transition rate towards green ammonia will mainly depend on the level of inducible carbon tax by governmental policies, future levelized cost of renewable electricity and reductions in the electrolyzer manufacturing costs. Among the options for sustainable ammonia synthesis at a small scale plant (91 tonnes per day), electrified Haber-Bosch remains the most promising technology in terms of maturity, costs and energy efficiency (see Figure 10). Nonetheless, research exploration for alternative pathways must continue.
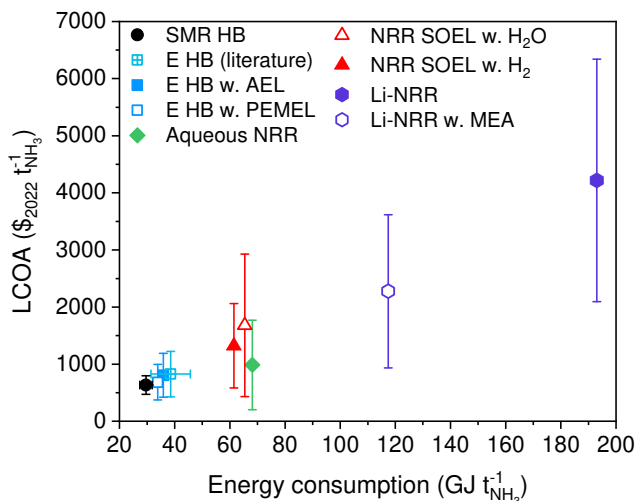
Figure 10. LCOA versus the energy consumption of the ammonia production routes discussed in this work. The y-error bars indicate the LCOA at optimistic and conservative cost scenarios in 2050 (from Table D16). The data points represent the average between the optimistic and conservative cost assumptions, and not necessarily the base case assumptions. The x-error bar of SMR HB (black) represents the BAT (27.4-31.8 GJ per tNH₃). The variation among the reported literature values on the LCOA ($827±398 per tNH₃) and energy input (38.6±7.1 GJ per tNH₃) of electrified HB at a similar production capacity were taken from ref. [8,66-68], and added for comparison (sapphire).

Aqueous NRR at ambient conditions is thermodynamically the most favorable approach, but the energy losses associated with activation overpotentials, ohmic losses, N_2 feedstock production and distillation are often overlooked and decrease the energy efficiency of the process significantly. The low single-pass conversion and inability to recycle unreacted N_2 demands an ASU with a large capacity, which will also produce vast quantities of O_2. Selling O_2 as a commodity is therefore essential to stimulate cash flow. Unfortunately, the current state of the aqueous NRR field is orders of magnitude away ($j < 0.001$ A cm^{-2}, FE < 1%) from reaching our newly defined electrolyzer aspirational values (FE > 80% at 0.3 A cm^{-2}, FE > 70% at 0.4 A cm^{-2} and FE > 65% between 0.5-1 A cm^{-2}). Moreover, numerous publications that claim to have activated N_2 are dubious and irreproducible,[69,70] which can mostly be assigned to extraneous sources of NH_3 or the electroreduction of NO_x species.[71] It remains to be seen if ambient NRR will ever be experimentally demonstrated unambiguously at the intended j and FE.

High temperature NRR combined with water oxidation is as challenging as aqueous NRR at room temperature, wherein reported j (< 0.01 A cm^{-2}) and FE (< 1%) remain at a bare minimum.[72] On the contrary, high temperature NRR with H_2 oxidation allows N_2 activation to be more selective (FE > 70%).[72] Yet, both the FE and the current densities obtained at lab scale do not meet with the bare minimum j and FE (FE > 90% at 0.4 A cm^{-2}), hence remain impractical for industrial applications. More progress has been made in the Li-NRR field,

where current densities of 1 A cm^{-2} and FEs near unity were reported,[26,27] continuous flow and membrane electrode assembly cells have been developed,[25,36,73] and Ca has been identified as an active N_2 mediator.[37] These achievements have progressed the mediated NRR field tremendously, but due to the fundamentally low energy efficiencies of the electrochemical conversion step and the overall complexity of the process, ammonia production at a competitive cost price will be a major challenge for its future application.

5.4 Conclusion

In this work, we designed detailed process models for the electrochemical production of NH_3 to gain insights into the main bottlenecks of the process and to understand what process conditions are required to reach economic parity with SMR Haber-Bosch. Electrified Haber-Bosch with PEMEL is so far the most attractive process. However, current PEMEL investment costs and electricity prices need to be reduced to $615 per kW and $0.035 per kWh, which can be achieved within two decades according to future price projections. Aqueous NRR at ambient conditions needs even more optimistic scenarios and only becomes promising if the electricity price drops below $0.024 per kWh at $522 per kW (electrolyzer CAPEX). In addition to this, the NRR performance has to be increased to FE > 80% and $j \geq 0.3$ A cm^{-2}, a daunting task when comparing to the current state of the field. On the contrary, numerous experimental reports show that NRR in a SOEL with hydrogen oxidation is more selective (FE > 70%), but current densities remain at industrially irrelevant scales. Additionally, we find that SOEL based processes tend to be more capital intensive due to the additional requirement of heat exchangers and more auxiliary equipment. Hence, high temperature NRR is only cost competitive at the most optimistic and perhaps unrealistic economic scenario (≤ $0.02 per kWh, ≤ $800 per m^2). Li-NRR has progressed tremendously over the last years in terms of scale, continuity, ammonia yield and selectivity. Unfortunately, the inherently low energy efficiency (<11%) of the electrolyzer causes disproportionally high operational costs. The EE can be improved by developing MEA-type electrolyzers to circumvent electrolyte conductivity losses or by implementing an alternative mediator with a more positive plating potential than Li, such as Mg or Al. For a small scale plant at 91 tonnes per day, Li-mediated NRR is under the most optimistic economic assumptions not economically feasible. This means that Li-NRR and also Ca-NRR remain interesting subjects for scientific research, but might never be integrated into a profitable application or process. Future research has to focus on the identification of mediators beyond Li and Ca. For now, electrified Haber-Bosch remains the only compelling electrolysis based pathway for sustainable ammonia production.

5.5 References

1   Food and Agriculture Organization of the United Nations. World Fertilizer Trends and Outlook to 2022. (2019).

2   IMARC. Ammonia Market: Global Industry Trends, Share, Size, Growth, Opportunity and Forecast 2023-2028. (2022).

3   International Energy Agency. Ammonia Technology Roadmap - Towards more sustainable nitrogen fertiliser production (2021).

4   Lim, J., Fernández, C. A., Lee, S. W. & Hatzell, M. C. Ammonia and nitric acid demands for fertilizer use in 2050. *ACS Energy Letters* **6**, 3676-3685 (2021).

5   Van Der Ham, C. J. M., Koper, M. T. M. & Hetterscheid, D. G. H. Challenges in reduction of dinitrogen by proton and electron transfer. *Chemical Society Reviews* **43**, 5183-5191 (2014). https://doi.org:10.1039/c4cs00085d

6   Soloveichik, G. Electrochemical synthesis of ammonia as a potential alternative to the Haber–Bosch process. *Nature Catalysis* **2**, 377-380 (2019).

7   Brown, T. *The capital intensity of small-scale ammonia plants*, <https://www.ammoniaenergy.org/articles/the-capital-intensity-of-small-scale-ammonia-plants/> (2018).

8   Smith, C., Hill, A. K. & Torrente-Murciano, L. Current and future role of Haber-Bosch ammonia in a carbon-free energy landscape. *Energy and Environmental Science* **13**, 331-344 (2020). https://doi.org:10.1039/c9ee02873k

9   Arias, P. *et al.* Climate Change 2021: the physical science basis. Contribution of Working Group I to the Sixth Assessment Report of the Intergovernmental Panel on Climate Change; technical summary. (2021).

10 Smolinka, T., Bergmann, H., Garche, J. & Kusnezoff, M. in *Electrochemical power sources: fundamentals, systems, and applications* 83-164 (Elsevier, 2022).

11 International Rewenable Energy Agency (IRENA). Renewable power generation costs in 2022. (2022).

12 Glenk, G. & Reichelstein, S. Economics of converting renewable power to hydrogen. *Nature Energy* **4**, 216-222 (2019).

13 Michael Nayak-Luke, R. & Bañ ares-Alcá ntara, R. Techno-economic viability of islanded green ammonia as a carbon-free energy vector and as a substitute for conventional production †. *Cite this: Energy Environ. Sci* **13**, 2957-2957 (2020). https://doi.org:10.1039/d0ee01707h

14 Cesaro, Z., Ives, M., Nayak-Luke, R., Mason, M. & Bañares-Alcántara, R. Ammonia to power: Forecasting the levelized cost of electricity from green ammonia in large-scale power plants. *Applied Energy* **282**, 116009-116009 (2021). https://doi.org:10.1016/J.APENERGY.2020.116009

15 MacFarlane, D. R. *et al.* A Roadmap to the Ammonia Economy. *Joule* **4**, 1186-1205 (2020). https://doi.org:10.1016/j.joule.2020.04.004

16 Wang, M. *et al.* Can sustainable ammonia synthesis pathways compete with fossil-fuel based Haber–Bosch processes? *Energy & Environmental Science* **14**, 2535-2548 (2021). https://doi.org:10.1039/d0ee03808c

5

17   Fernandez, C. A. & Hatzell, M. C. Editors' Choice-Economic Considerations for Low-Temperature Electrochemical Ammonia Production: Achieving Haber-Bosch Parity. (2020). https://doi.org:10.1149/1945-7111/abc35b

18   Hochman, G. *et al.* Potential Economic Feasibility of Direct Electrochemical Nitrogen Reduction as a Route to Ammonia. *ACS Sustainable Chemistry and Engineering* **8**, 8938-8948 (2020). https://doi.org:10.1021/acssuschemeng.0c01206

19   Sánchez, A. & Martín, M. Scale up and scale down issues of renewable ammonia plants: Towards modular design. *Sustainable Production and Consumption* **16**, 176-192 (2018). https://doi.org:10.1016/j.spc.2018.08.001

20   Buttler, A. & Spliethoff, H. Current status of water electrolysis for energy storage, grid balancing and sector coupling via power-to-gas and power-to-liquids: A review. *Renewable and Sustainable Energy Reviews* **82**, 2440-2454 (2018). https://doi.org:10.1016/j.rser.2017.09.003

21   International Chemical Safety Cards (ICSCs). *Ammonia (anhydrous) - Physical & Chemical Information*, <https://www.ilo.org/dyn/icsc/showcard.display?p_lang=en&p_card_id=0414&p_version=2> (2021).

22   Yáñez, M. *et al.* PSA purification of waste hydrogen from ammonia plants to fuel cell grade. *Separation and Purification Technology* **240**, 116334 (2020).

23   Miller, J. A. & Bowman, C. T. Mechanism and modeling of nitrogen chemistry in combustion. *Progress in energy and combustion science* **15**, 287-338 (1989).

24   Rouwenhorst, K. H., Van der Ham, A. G. & Lefferts, L. Beyond Haber-Bosch: the renaissance of the Claude process. *international journal of hydrogen energy* **46**, 21566-21579 (2021).

25   Fu, X. *et al.* Continuous-flow electrosynthesis of ammonia by nitrogen reduction and hydrogen oxidation. *Science* **379**, 707-712 (2023).

26   Li, S. *et al.* Electrosynthesis of ammonia with high selectivity and high rates via engineering of the solid-electrolyte interphase Electrosynthesis of ammonia with high selectivity and high rates via engineering. *Joule* **6**, 2083-2101 (2022). https://doi.org:10.1016/j.joule.2022.07.009

27   Du, H.-L. *et al.* Electroreduction of nitrogen at almost 100% current-to-ammonia efficiency. *Nature* **609**, 722-727 (2022). https://doi.org:10.1038/s41586-022-05108-y

28   Skúlason, E. *et al.* A theoretical evaluation of possible transition metal electro-catalysts for N2 reduction. *Physical Chemistry Chemical Physics* **14**, 1235-1245 (2012). https://doi.org:10.1039/c1cp22271f

29   Dražević, E. & Skúlason, E. Are There Any Overlooked Catalysts for Electrochemical NH3 Synthesis—New Insights from Analysis of Thermochemical Data. *iScience* **23**, 101803-101803 (2020). https://doi.org:10.1016/j.isci.2020.101803

30   Soloveichik, G. Renewable Energy to Fuels Through Utilization of Energy-Dense Liquids (REFUEL) Program Overview. 1-16 (2016).

31   Dybkjaer, I. in *Ammonia - Catalysis and Manufacturing*   (ed A Nielsen) 199-327 (Springer-Verlag, 1995).

32   Appl, M. *Ammonia: Principles and Industrial Practice*. (1999).

5

33   Chatenet, M. *et al.* Water electrolysis: from textbook knowledge to the latest scientific strategies and industrial developments. *Chemical Society Reviews* **51**, 4583-4762 (2022). https://doi.org:10.1039/d0cs01079k

34   Innovation for Cool Earth Forum (ICEF). Industrial Heat Decarbonization Roadmap. (2019).

35   Helminen, J., Helenius, J., Paatero, E. & Turunen, I. Comparison of sorbents and isotherm models for NH3‑gas separation by adsorption. *AIChE journal* **46**, 1541-1555 (2000).

36   Cai, X. *et al.* Membrane electrode assembly design for lithium-mediated electrochemical nitrogen reduction. *Energy & Environmental Science* (2023).

37   Fu, X. *et al.* Calcium-mediated nitrogen reduction for electrochemical ammonia synthesis. *Nature Materials*, 1-7 (2023).

38   Tort, R. *et al.* Searching for the Rules of Electrochemical Nitrogen Fixation. *ACS Catalysis* **13**, 14513-14522 (2023).

39   Towler, G. & Sinnott, R. *Chemical engineering design: principles, practice and economics of plant and process design*. (Butterworth-Heinemann, 2021).

40   Smith, R. *Chemical process: design and integration*. (John Wiley & Sons, 2005).

41   Ludwig, E. E. *Applied Process Design for Chemical and Petrochemical Plants: Volume 2*. Vol. 2 (gulf professional publishing, 1997).

42   Turton, R., Bailie, R. C., Whiting, W. B. & Shaeiwitz, J. A. *Analysis, synthesis and design of chemical processes*. (Pearson Education, 2008).

43   Morgan, E. R. *Techno-economic feasibility study of ammonia plants powered by offshore wind*. (University of Massachusetts Amherst, 2013).

44   Mivechian, A. & Pakizeh, M. Hydrogen recovery from Tehran refinery off-gas using pressure swing adsorption, gas absorption and membrane separation technologies: Simulation and economic evaluation. *Korean Journal of Chemical Engineering* **30**, 937-948 (2013).

45   Bañares-Alcántara, R. *et al.* Analysis of Islanded Ammonia-based Energy Storage Systems. *University of Oxford*, 1-150 (2015).

46   Marsidi, M. *Technology Factsheet - Electric Industrial Boiler*, <https://energy.nl/wp-content/uploads/electric-industrial-boiler-7.pdf> (2018).

47   Marc Marsidi, Luuk Beurskens & Uslu, A. The role of renewable heat technologies in industry - a review of Dutch sectoral industry roadmaps. (2018).

48   Lane, B., Reed, J., Shaffer, B. & Samuelsen, S. Forecasting renewable hydrogen production technology shares under cost uncertainty. *International Journal of Hydrogen Energy* **46**, 27293-27306 (2021).

49   International Rewenable Energy Agency (IRENA). Making The Breakthrough - Green hydrogen policies and technology costs. (2021).

50   International Rewenable Energy Agency (IRENA). Future of Solar Photovoltaic: Deployment, investment, technology, grid intergration and socio-economic aspects (A global Energy Transformation: paper). (2019).

51   Bogdanov, D. *et al.* Radical transformation pathway towards sustainable electricity via evolutionary steps. *Nature communications* **10**, 1-16 (2019).

52   INDEXBOX. EU - Oxygen - Market Analysis, Forecast, Size, Trends and Insights. (2022).

5

53   Administration, U. S. E. I. *Henry Hub Natural Gas Spot Price*, <https://www.eia.gov/dnav/ng/hist/rngwhhdm.htm> (2023).

54   Hausmann, J. N., Schlögl, R., Menezes, P. W. & Driess, M. Is direct seawater splitting economically meaningful? *Energy & Environmental Science* **14**, 3679-3685 (2021).

55   Bashmakov, I. A. *et al.* IPCC. Climate Change 2022: Mitigation of Climate Change. Industry. (2022).

56   Ramdin, M. *et al.* High-pressure electrochemical reduction of CO2 to formic acid/formate: effect of pH on the downstream separation process and economics. *Industrial & Engineering Chemistry Research* **58**, 22718-22740 (2019).

57   Ramdin, M. *et al.* Electroreduction of CO2/CO to C2 products: process modeling, downstream separation, system integration, and economic analysis. *Industrial & Engineering Chemistry Research* **60**, 17862-17880 (2021).

58   macrotrends. *Federal Funds Rate - 62 Year Historical Chart*, <https://www.macrotrends.net/2015/fed-funds-rate-historical-chart> (2023).

59   Spurgeon, J. M. & Kumar, B. A comparative technoeconomic analysis of pathways for commercial electrochemical CO 2 reduction to liquid products. *Energy & Environmental Science* **11**, 1536-1551 (2018).

60   Philibert, C. Producing ammonia and fertilizers: new opportunities from renewables. *IEA Rep*, 1-6 (2017).

61   Fertilizers Europe. *Europe's fertilizer industry victim of EU's energy chaos*, <https://www.fertilizerseurope.com/wp-content/uploads/2022/08/Fertilizers-Europe-Press-release_Europe-fert-industry-victim-of-EU-energy-chaos-1.pdf> (2022).

62   Pindyck, R. S. The social cost of carbon revisited. *Journal of Environmental Economics and Management* **94**, 140-160 (2019).

63   Ricke, K., Drouet, L., Caldeira, K. & Tavoni, M. Country-level social cost of carbon. *Nature Climate Change* **8**, 895-900 (2018).

64   Rennert, K. *et al.* Comprehensive evidence implies a higher social cost of CO2. *Nature* **610**, 687-692 (2022).

65   International Energy Agency (IEA). *Real-Time Electricity Tracker - United States*, <https://www.iea.org/data-and-statistics/data-tools/real-time-electricity-tracker?from=2023-4-9&to=2024-4-8&category=price&country=USA> (2022).

66   Nayak-Luke, R. M. & Bañares-Alcántara, R. Techno-economic viability of islanded green ammonia as a carbon-free energy vector and as a substitute for conventional production. *Energy & Environmental Science* **13**, 2957-2966 (2020).

67   Morgan, E. R., Manwell, J. F. & McGowan, J. G. Sustainable Ammonia Production from U.S. Offshore Wind Farms: A Techno-Economic Review. *ACS Sustainable Chemistry and Engineering* **5**, 9554-9567 (2017). https://doi.org:10.1021/acssuschemeng.7b02070

68   Institute for Sustainable Process Technology (ISPT). Power to Ammonia - Feasibility study for the value chains and business cases to produce CO2-free ammonia suitable for various market applications. (2017).

69   Choi, J. *et al.* Identification and elimination of false positives in electrochemical nitrogen reduction studies. *Nature Communications* **11**, 1-10 (2020). https://doi.org:10.1038/s41467-020-19130-z

5

70   Izelaar, B. *et al.* Revisiting the Electrochemical Nitrogen Reduction on Molybdenum and Iron Carbides: Promising Catalysts or False Positives? *ACS Catalysis* **13**, 1649-1661 (2023).

71   Izelaar, B. *et al.* Identification, Quantification, and Elimination of NO x and NH3 Impurities for Aqueous and Li-Mediated Nitrogen Reduction Experiments. *ACS Energy Letters* **8**, 3614-3620 (2023).

72   Kyriakou, V., Garagounis, I., Vasileiou, E., Vourros, A. & Stoukides, M. Progress in the Electrochemical Synthesis of Ammonia. *Catalysis Today* **286**, 2-13 (2017). https://doi.org:10.1016/j.cattod.2016.06.014

73   Li, S. *et al.* Long-term continuous ammonia electrosynthesis. *Nature*, 1-3 (2024).

5

Appendix D

Process Flow Diagrams, Stream Summary and Equipment List

Electrified Haber-Bosch
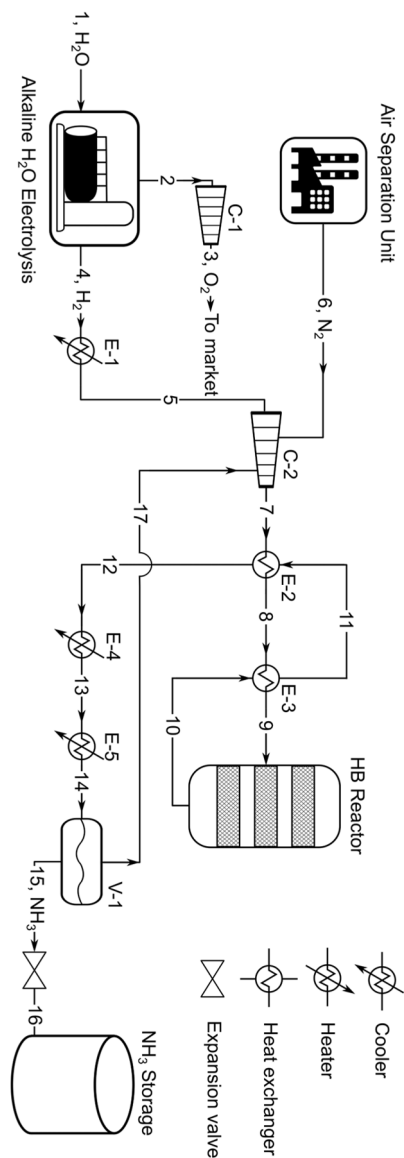
Figure D1. Process flow diagram of the electrified Haber-Bosch process with an alkaline water electrolyzer (AEL). The electrified Haber-Bosch with a proton exchange membrane electrolyzer (PEMEL) is identical, except that the feed-gas compressor (C-2) requires less compression stages.

Table D1. Stream summary of the electrified Haber-Bosch process with AEL (Figure D1).

Property	1	2	3	4	5	6	7
Temperature (°C)	25	80	40	80	40	25	40
Pressure (bar)	1.01	1.01	163	1.01	1.01	6	157
Mole flows (kmol h^{-1})	370.43	166.47	166.47	334.06	334.06	111.37	1830.5
NH$_3$ (kmol h^{-1})							54.835
H$_2$ (kmol h^{-1})				334.06	334.06		1331.75
N$_2$ (kmol h^{-1})						111.37	443.82
O$_2$ (kmol h^{-1})		166.47	166.47				
KOH (kmol h^{-1})							
H$_2$O (kmol h^{-1})	370.43						
Mole fractions							
NH$_3$							0.03
H$_2$				1	1		0.73
N$_2$						1	0.24
O$_2$		1	1				
KOH							
H$_2$O	1						
Mass flow (kg h^{-1})	6667.77	5326.69	5326.69	673.42	673.42	3119.75	16054.1
Property	**8**	**9**	**10**	**11**	**12**	**13**	**14**
Temperature (°C)	220	400	619	437	239	239	-5
Pressure (bar)	156	155	152	151	150	149	147
Mole flows (kmol h^{-1})	1830.5	1830.5	1608.54	1608.54	1608.54	1608.54	1608.54
NH$_3$ (kmol h^{-1})	54.835	54.835	276.79	276.79	276.79	276.79	276.79
H$_2$ (kmol h^{-1})	1331.75	1331.75	998.81	998.81	998.81	998.81	
N$_2$ (kmol h^{-1})	443.82	443.82	332.94	332.94	332.94	332.94	998.81
O$_2$ (kmol h^{-1})							332.94
KOH (kmol h^{-1})							
H$_2$O (kmol h^{-1})							
Mole fractions							
NH$_3$	0.03	0.03	0.17	0.17	0.17	0.17	0.17
H$_2$	0.73	0.73	0.62	0.62	0.62	0.62	0.62
N$_2$	0.24	0.24	0.21	0.21	0.21	0.21	0.21
O$_2$							
KOH							
H$_2$O							
Mass flow (kg h^{-1})	16054.1	16054.1	16054.1	16054.1	16054.1	16054.1	16054.1

5

Table D1 (continued). Stream summary of the electrified Haber-Bosch process with AEL (Figure D1).

Property	15	16	17
Temperature (°C)	-5	-34	-5
Pressure (bar)	145	1.01	145
Mole flows (kmol h^{-1})	223.25	223.25	1385.29
NH$_3$ (kmol h^{-1})	221.92	221.92	54.87
H$_2$ (kmol h^{-1})			
N$_2$ (kmol h^{-1})	0.34	0.34	997.83
O$_2$ (kmol h^{-1})	0.98	0.98	332.60
KOH (kmol h^{-1})			
H$_2$O (kmol h^{-1})			
Mole fractions			
NH$_3$	0.995	0.995	0.04
H$_2$	0.004	0.004	0.72
N$_2$	0.001	0.001	0.24
O$_2$			
KOH			
H$_2$O			
Mass flow (kg h^{-1})	3790.98	3790.98	12263.2

Table D2. Equipment list of the electrified Haber-Bosch process with AEL (Figure D1). CW: Cooling water.

Main Equipment	C-1	C-2	E-1	E-2	E-3	E-4
Type	6-stage compressor	6-stage compressor	Cooler	Heat Exchanger	Heat Exchanger	Cooler
Power (kW)	2701	1137.92				
Heat (kW)	2234 (intercoolers)	1184.12	108.5	2923	2776	3062
Area (m^2)	347 (intercoolers)	314.72	104	53.02	50.96	87.8
U (kW m^{-2})	-	-	42.2	310.4	287.4	574.1
Medium	CW	CW	CW			CW
Main Equipment	E-5	V-1	Air separation unit			
Type	Condensor	Flash drum	Pressure-swing adsorption			
Power (kW)			1372.03			
Heat (kW)	1746					
Area (m^2)	71.23					
U (kW m^{-2})	658.6					
Medium	Ammonia					

Table D3. Stream data modification when replacing AEL with PEMEL in the electrified HB process (referring to Figure D1).

Property	2	4	5
Temperature (°C)	80	80	40
Pressure (bar)	35	35	35
Mole flows (kmol h^{-1})	166.47	334.06	334.06
NH$_3$ (kmol h^{-1})			
H$_2$ (kmol h^{-1})		334.06	334.06
N$_2$ (kmol h^{-1})			
O$_2$ (kmol h^{-1})	166.47		
KOH (kmol h^{-1})			
H$_2$O (kmol h^{-1})			
Mole fractions			
NH$_3$			
H$_2$		1	1
N$_2$			
O$_2$	1		
KOH			
H$_2$O			
Mass flow (kg h^{-1})	5326.69	673.42	673.42

Table D4. Equipment data modifications when replacing AEL with PEMEL in the electrified HB process (referring to Figure D1).

Main Equipment	C-1	C-2	E-1
Type	2-stage compressor	4-stage compressor	Cooler
Power (kW)	333.2 kW	1203	
Heat (kW)	411.2 (intercoolers)	708 (intercoolers)	108
Area (m^2)	28.6 (intercoolers)	67.3 (intercoolers)	16.03
U (kW m^{-2})	-	-	276
Medium	CW	CW	CW

Aqueous NRR at Ambient Conditions
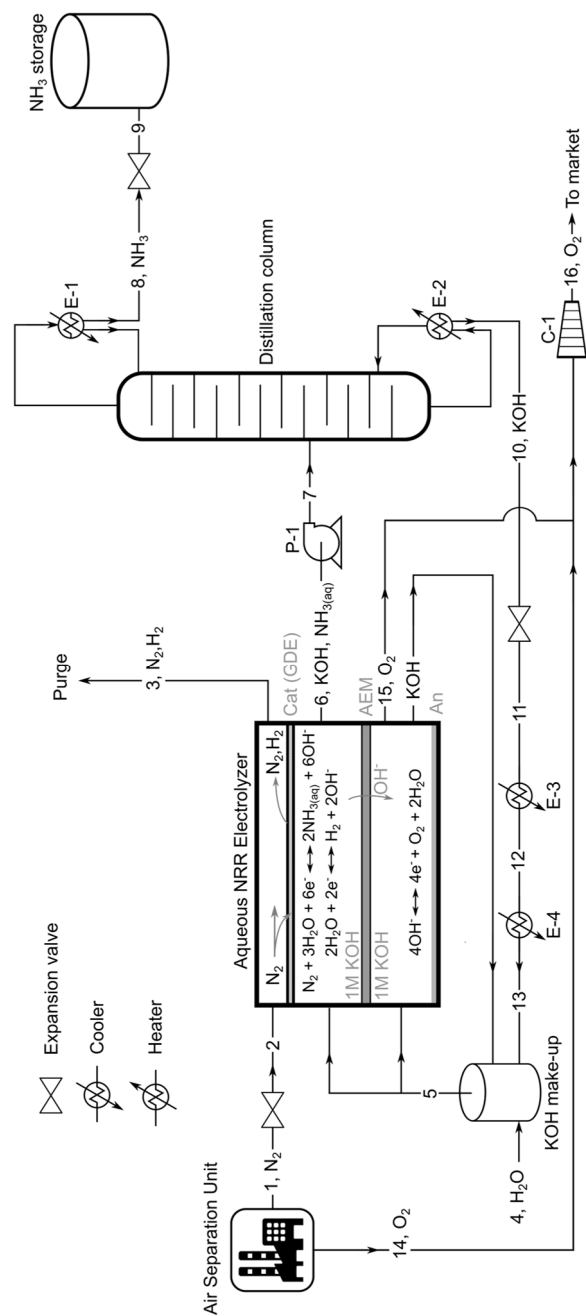
Figure D2. Process flow diagram of aqueous NRR at ambient conditions with a H_2 purge.

Table D5. Stream summary of the aqueous NRR process with a H2 purge at a FE of 90% (Figure D2).

Property	1	2	3	4	5	6	7	8
Temperature (°C)	25	25	25	25	25	25	25	-24.8
Pressure (bar)	6	1.01	1.01	1.01	1.01	1.01	3.5	3.5
Mole flows (kmol h^{-1})	1110.92	1110.92	1035.82	666.0	2665.72	2221.80	2221.80	223.07
NH$_3$ (kmol h^{-1})					0.218	222.18	222.18	221.96
H$_2$ (kmol h^{-1})			36.99					
N$_2$ (kmol h^{-1})	1109.81	1109.81	998.83					
O$_2$ (kmol h^{-1})	1.11	1.11						
KOH (kmol h^{-1})					39.58	39.58	39.58	
H$_2$O (kmol h^{-1})				666.0	2625.916	1960.03	1960.03	1.11
Mole fractions								
NH$_3$					0.00008	0.1	0.1	0.995
H$_2$			0.036					
N$_2$	1	1	0.964					
O$_2$	1	1	0.964					
KOH					39.58	0.0178	0.0178	
H$_2$O				1	2625.92	0.882	0.882	0.005
Mass flow (kg h^{-1})	31121.24	31121.24	28055.1	12016.11	49531.36	41315.2	41315.2	3800.16
Property	**9**	**10**	**11**	**12**	**13**	**14**	**15**	**16**
Temperature (°C)	-33	140	101	40	25	25	25	40
Pressure (bar)	1.01	3.5	1.01	1.01	1.01	6	1	163
Mole flows (kmol h^{-1})	222.08	2038.21	2038.21	2038.21	2038.21	298.79	166.47	465.27
NH$_3$ (kmol h^{-1})	221.96	0.218	0.218	0.218	0.218			
H$_2$ (kmol h^{-1})								
N$_2$ (kmol h^{-1})								
O$_2$ (kmol h^{-1})						298.79	166.47	465.27
KOH (kmol h^{-1})		39.58	39.58	39.58	39.58			
H$_2$O (kmol h^{-1})	1.11	1958.92	1958.92	1958.92	1958.92			
Mole fractions								
NH$_3$	0.995	0.0001	0.0001	0.0001	0.0001			
H$_2$								
N$_2$								
O$_2$						1	1	1
KOH		0.0194	0.0194	0.0194	0.0194			
H$_2$O	0.005	0.961	0.961	0.961	0.961			
Mass flow (kg h^{-1})	3800.16	37515.1	37515.1	37515.1	37515.1	9561.11	5326.9	14888.02

Table D6. Equipment list of the aqueous NRR process with a H_2 purge at a FE of 90% (Figure D2).

Main Equipment	P-1	E-1 (Distillation)	E-2 (Distillation)	E-3	E-4	C-1	Air separation Unit
Type	Pump	Condenser	Reboiler	Cooler	Cooler	6-stage compressor	Cryogenic Distillation
Power (kW)	3.489					2393.4	11490.66
Heat (kW)		-806.8	6967.4	-4062	-602.5	-2345.9 (intercoolers)	
Area (m^2)		71.93	44.69	43.65	10.32	498.7 (intercoolers)	
U (kW m^{-2})		497.7	5230.8	2139.9	1031.1		
Medium		Propylene	Steam	CW	Ammonia	CW	
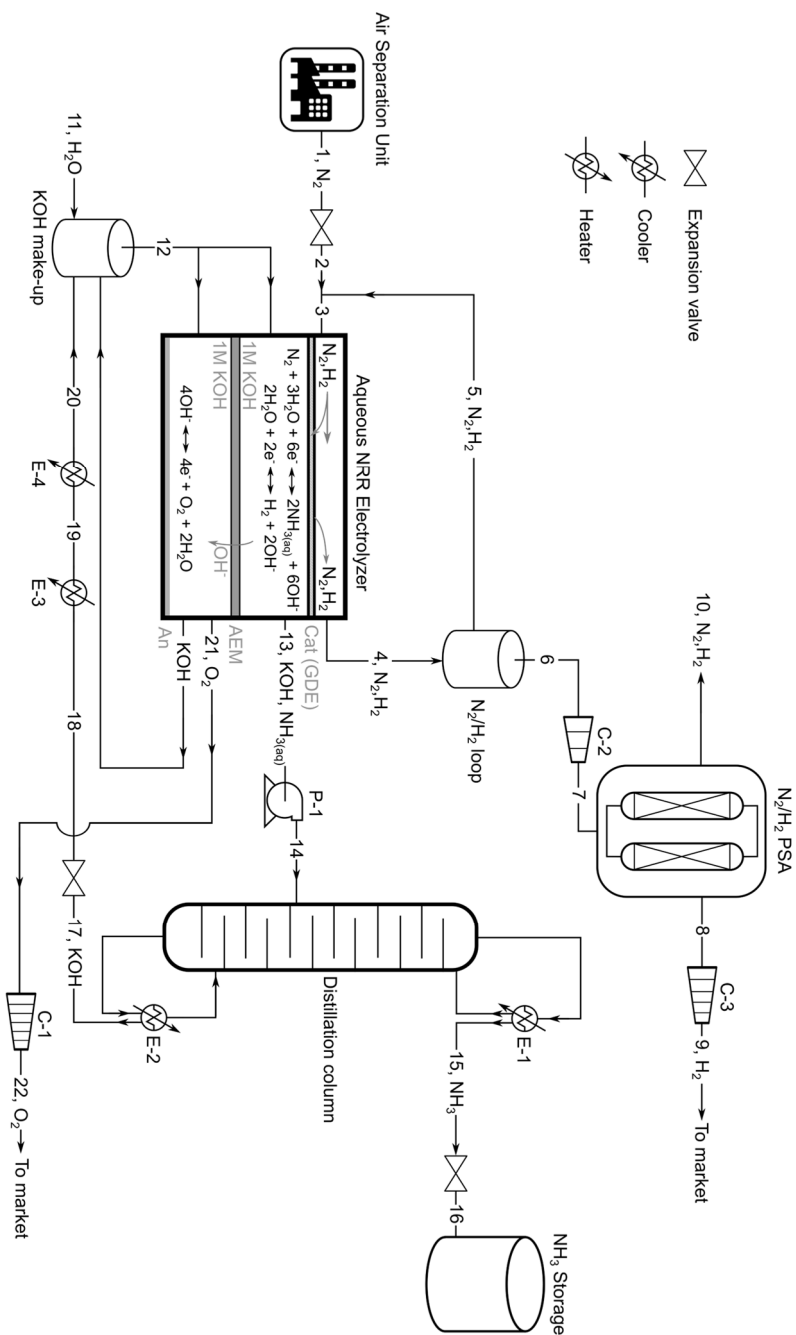
Figure D3. Process flow diagram of the aqueous NRR process at ambient conditions including a N2/H2 PSA separation step, N2 recycle stream and storage vessel.

Table D7. Stream summary of the aqueous NRR process at a FE of 90% with a N2/H2 PSA (Figure D3).

Property	1	2	3	4	5	6	7
Temperature (°C)	25	25	25	25	25	25	40
Pressure (bar)	6	1.01	1.01	1.01	1.01	1.01	7
Mole flows (kmol h^{-1})	135.64	135.64	2570.97	2495.98	2435.33	61.654	61.654
NH$_3$ (kmol h^{-1})							
H$_2$ (kmol h^{-1})			1461.2	1498.19	1461.20	36.99	36.99
N$_2$ (kmol h^{-1})	135.64	135.64	1109.77	998.79	974.13	24.66	24.66
O$_2$ (kmol h^{-1})							
KOH (kmol h^{-1})							
H$_2$O (kmol h^{-1})							
Mole fractions							
NH$_3$							
H$_2$	1	1	0.57	0.6	0.6	0.6	0.6
N$_2$			0.43	0.4	0.4	0.4	0.4
O$_2$							
KOH							
H$_2$O							
Mass flow (kg h^{-1})	3799.8	3799.8	34034.3	30999.9	30234.49	765.43	765.43

Property	8	9	10	11	12	13	14
Temperature (°C)	40	40	40	25	25	25	25
Pressure (bar)	6	350	6	1.01	1.01	1.01	3.5
Mole flows (kmol h^{-1})	18.64	18.64	43.02	666.0	2665.72	2221.80	2221.80
NH$_3$ (kmol h^{-1})					0.218	222.18	222.18
H$_2$ (kmol h^{-1})	18.50	18.50	18.50				
N$_2$ (kmol h^{-1})	0.14	0.14	24.52				
O$_2$ (kmol h^{-1})							
KOH (kmol h^{-1})					39.58	39.58	39.58
H$_2$O (kmol h^{-1})				666.0	2625.916	1960.03	1960.03
Mole fractions							
NH$_3$					0.00008	0.1	0.1
H$_2$	0.9925	0.9925					
N$_2$	0.0075	0.0075					
O$_2$							
KOH					39.58	0.0178	0.0178
H$_2$O				1	2625.92	0.882	0.882
Mass flow (kg h^{-1})	41.2	41.2	724.23	12016.1	49531.36	41315.2	41315.2

Table D7 (continued). Stream summary of the aqueous NRR process at a FE of 90% with a N2/H2 PSA (Figure D3).

Property	15	16	17	18	19	20	21	22
Temperature (°C)	-24.8	-33	140	101	40	25	25	40
Pressure (bar)	3.5	1.01	3.5	1.01	1.01	1.01	1	163
Mole flows (kmol h^{-1})	223.07	222.08	2038.21	2038.21	2038.21	2038.21	166.47	166.47
NH$_3$ (kmol h^{-1})	221.96	221.96	0.218	0.218	0.218	0.218		
H$_2$ (kmol h^{-1})								
N$_2$ (kmol h^{-1})								
O$_2$ (kmol h^{-1})							166.47	166.47
KOH (kmol h^{-1})			39.58	39.58	39.58	39.58		
H$_2$O (kmol h^{-1})	1.11	1.11	1958.92	1958.92	1958.92	1958.92		
Mole fractions								
NH$_3$	0.995	0.995	0.0001	0.0001	0.0001	0.0001		
H$_2$								
N$_2$								
O$_2$							1	1
KOH			0.0194	0.0194	0.0194	0.0194		
H$_2$O	0.005	0.005	0.961	0.961	0.961	0.961		
Mass flow (kg h^{-1})	3800.16	3800.16	37515.1	37515.1	37515.1	37515.1	5326.9	5326.9

Table D8. Equipment list of the aqueous NRR process at a FE of 90% with a N_2/H_2 PSA (Figure D3).

Main Equipment	P-1	E-1 (Distillation)	E-2 (Distillation)	E-3	E-4	C-1	C-2
Type	Pump	Condenser	Reboiler	Cooler	Cooler	6-stage compressor	3-stage compressor
Power (kW)	3.489					1093.14	169.48
Heat (kW)		-806.8	6967.4	-4062	-602.5	-1063.21 (intercoolers)	-155.45 (intercooler)
Area (m^2)		71.93	44.69	43.65	10.32	301.03 (intercooler)	43.73 (intercooler)
U (kW m^{-2})		497.7	5230.8	2139.9	1031.1		
Medium		Propylene	Steam	CW	Ammonia	CW	CW

Main Equipment	C-3	Air separation Unit
Type	6-stage compressor	Cryogenic Distillation
Power (kW)	93.37	1671.91
Heat (kW)	86.37 (intercooler)	
Area (m^2)	4.74 (intercooler)	
U (kW m^{-2})		
Medium	CW	

5

5

Figure D4. Process flow diagram of the NRR SOEL process with water oxidation.
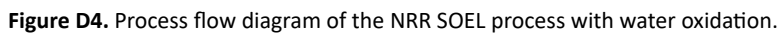
Table D9. Stream summary of the NRR SOEL process with water oxidation process at a FE of 90% (Figure D4).

Property	1	2	3	4	5	6	7
Temperature (°C)	25	25	540	550	550	167	40
Pressure (bar)	6	1.01	1.01	1.01	1.01	1.01	1.01
Mole flows (kmol h^{-1})	1233.1	1233.1	1233.1	1233.1	1397.51	1397.51	1397.51
NH$_3$ (kmol h^{-1})					246.62	246.62	246.62
H$_2$ (kmol h^{-1})					41.1	41.1	41.1
N$_2$ (kmol h^{-1})	1233.1	1233.1	1233.1	1233.1	1109.78	1109.78	1109.78
O$_2$ (kmol h^{-1})							
H$_2$O (kmol h^{-1})							
Mole fractions							
NH$_3$					0.176	0.176	0.176
H$_2$					0.029	0.029	0.029
N$_2$	1	1	1	1	0.794	0.794	0.794
O$_2$							
H$_2$O							
Mass flow (kg h^{-1})	34543.22	34543.22	34543.22	34543.22	35371.93	35371.93	35371.93

Property	8	9	10	11	12	13	14
Temperature (°C)	40	200	40	-33	200	25	98
Pressure (bar)	3.5	1.01	1.01	1.01	3.5	1.01	1.01
Mole flows (kmol h^{-1})	1397.51	223.07	223.07	223.07	1174.44	986.48	986.48
NH$_3$ (kmol h^{-1})	246.62	221.96	221.96	221.96	24.66		
H$_2$ (kmol h^{-1})	41.1	0.22	0.22	0.22	40.88		
N$_2$ (kmol h^{-1})	1109.78	0.89	0.89	0.89	1108.89		
O$_2$ (kmol h^{-1})							
H$_2$O (kmol h^{-1})						986.48	986.48
Mole fractions							
NH$_3$	0.176	0.995	0.995	0.995	0.021		
H$_2$	0.029	0.004	0.004	0.004	0.035		
N$_2$	0.794	0.001	0.001	0.001	0.94		
O$_2$							
H$_2$O						1	1
Mass flow (kg h^{-1})	35371.93	3805.6	3805.6	3805.6	31566.33	17771.66	17771.66

Table D9 (Continued). Stream summary of the NRR SOEL process with water oxidation process at a FE of 90% (Figure D4).

Property	15	16	17	18	19	20	21
Temperature (°C)	102	164	550	550	110	25	40
Pressure (bar)	1.01	1.01	1.01	1.01	1.01	6	163
Mole flows (kmol h^{-1})	986.48	986.48	986.48	184.96	184.96	331.99	516.95
NH$_3$ (kmol h^{-1})							
H$_2$ (kmol h^{-1})							
N$_2$ (kmol h^{-1})							
O$_2$ (kmol h^{-1})				184.96	184.96	331.99	516.95
H$_2$O (kmol h^{-1})	986.48	986.48	986.48				
Mole fractions							
NH$_3$							
H$_2$							
N$_2$							
O$_2$				1	1	1	1
H$_2$O	1	1	1				
Mass flow (kg h^{-1})	17771.66	17771.66	17771.66	5918.68	5918.68	10623.2	16531.9

Table D10. Equipment list of the NRR SOEL process with water oxidation process at a FE of 90% (Figure D4).

Main Equipment	E-1	E-2	E-3	E-4	E-5	E-6	E-7
Type	Heat Exchanger	Heat Exchanger	Heat Exchanger	Heat Exchanger	Heater	Heater	Cooler
Power (kW)							
Heat (kW)	5298	1635	724.6	108.1	11505	3894	-383.9
Area (m^2)	25000	2367	226.9	91.84	2865	1978	293.5
U (kW m^{-2})	5	22.9	18.6	6.2	51	5.3	21.5
Medium					MP Steam	Fired heat	CW

Main Equipment	E-8	C-1	C-2	Air separation Unit	Adsorption
Type	Cooler	2-stage compressor	6-stage compressor	Cryogenic Distillation	6-zeolite adsorbers
Power (kW)		2898	2713	12767	2927
Heat (kW)	-159.9	-2748 (intercoolers)	-2788.3 (intercooler)		
Area (m^2)	266.7	1537 (intercooler)	586.23 (intercooler)		
U (kW m^{-2})	20.5				
Medium	Propylene	CW	CW		

NRR SOEL with Hydrogen Oxidation
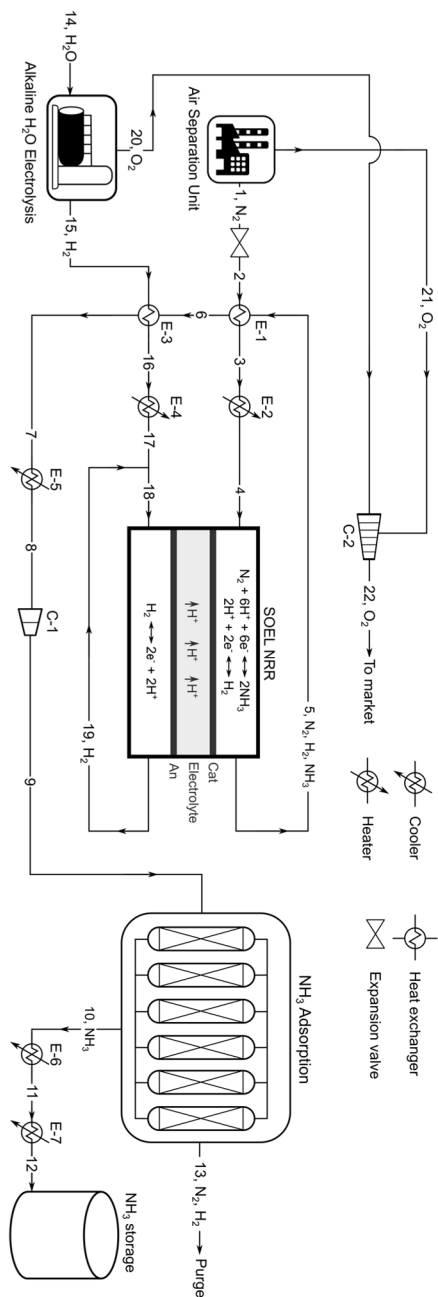
Figure D5. Process flow diagram of the NRR SOEL process with hydrogen oxidation including an additional alkaline water electrolyzer.

Table D11. Stream summary of the NRR SOEL process with hydrogen oxidation at a FE of 90% (Figure D5).

Property	1	2	3	4	5	6	7
Temperature (°C)	25	25	540	550	550	167	150
Pressure (bar)	6	1.01	1.01	1.01	1.01	1.01	1.01
Mole flows (kmol h^{-1})	1233.1	1233.1	1233.1	1233.1	1397.51	1397.51	1397.51
NH$_3$ (kmol h^{-1})					246.62	246.62	246.62
H$_2$ (kmol h^{-1})					41.1	41.1	41.1
N$_2$ (kmol h^{-1})	1233.1	1233.1	1233.1	1233.1	1109.78	1109.78	1109.78
O$_2$ (kmol h^{-1})							
H$_2$O (kmol h^{-1})							
Mole fractions							
NH$_3$					0.176	0.176	0.176
H$_2$					0.029	0.029	0.029
N$_2$	1	1	1	1	0.794	0.794	0.794
O$_2$							
H$_2$O							
Mass flow (kg h^{-1})	34543.22	34543.22	34543.22	34543.22	35371.93	35371.93	35371.93
Property	**8**	**9**	**10**	**11**	**12**	**13**	**14**
Temperature (°C)	40	40	200	40	-33	200	25
Pressure (bar)	1.01	3.5	1.01	1.01	1.01	3.5	1.01
Mole flows (kmol h^{-1})	1397.51	1397.51	223.07	223.07	223.07	1174.44	409.87
NH$_3$ (kmol h^{-1})	246.62	246.62	221.96	221.96	221.96	24.66	
H$_2$ (kmol h^{-1})	41.1	41.1	0.22	0.22	0.22	40.88	
N$_2$ (kmol h^{-1})	1109.78	1109.78	0.89	0.89	0.89	1108.89	
O$_2$ (kmol h^{-1})							
H$_2$O (kmol h^{-1})							409.87
Mole fractions							
NH$_3$	0.176	0.176	0.995	0.995	0.995	0.021	
H$_2$	0.029	0.029	0.004	0.004	0.004	0.035	
N$_2$	0.794	0.794	0.001	0.001	0.001	0.94	
O$_2$							
H$_2$O							1
Mass flow (kg h^{-1})	35371.93	35371.93	3805.6	3805.6	3805.6	31566.33	7442.85

5

Table D11 (Continued). Stream summary of the NRR SOEL process with hydrogen oxidation at a FE of 90% (Figure D5).

Property	15	16	17	18	19
Temperature (°C)	80	152	550	550	550
Pressure (bar)	1.01	1.01	1.01	1.01	1.01
Mole flows (kmol h^{-1})	369.93	369.93	369.93	3699.29	3329.36
NH$_3$ (kmol h^{-1})					
H$_2$ (kmol h^{-1})	369.93	369.93	369.93	3699.29	3329.36
N$_2$ (kmol h^{-1})					
O$_2$ (kmol h^{-1})					
H$_2$O (kmol h^{-1})					
Mole fractions					
NH$_3$					
H$_2$	1	1	1	1	
N$_2$					
O$_2$					1
H$_2$O					
Mass flow (kg h^{-1})	745.78	745.78	745.78	7457.77	6711.99
Property	**20**	**21**	**22**		
Temperature (°C)	80	25	40		
Pressure (bar)	1.01	6	163		
Mole flows (kmol h^{-1})	184.96	331.99	516.95		
NH$_3$ (kmol h^{-1})					
H$_2$ (kmol h^{-1})					
N$_2$ (kmol h^{-1})					
O$_2$ (kmol h^{-1})	184.96	331.99	516.95		
H$_2$O (kmol h^{-1})					
Mole fractions					
NH$_3$					
H$_2$					
N$_2$					
O$_2$	1	1	1		
H$_2$O					
Mass flow (kg h^{-1})	5918.7	10623.3	16541.9		

Table D12. Equipment list of the NRR SOEL process with hydrogen oxidation at a FE of 90% (Figure D5).

Main Equipment	E-1	E-2	E-3	E-4	E-5	E-6	E-7
Type	Heat Exchanger	Heat Exchanger	Heater	Heater	Cooler	Cooler	Cooler
Power (kW)							
Heat (kW)	5298	216.9	108.1	1200	1418	-383.9	-159.9
Area (m^2)	25000	1131	91.84	389.8	1350	293.5	266.7
U (kW m^{-2})	5	6.3	6.2	8.1	22.9	21.5	20.5
Medium			Fired heat	Fired heat	CW	CW	Propylene

| Main Equipment	C-1	C-2	Air separation Unit	Adsorption
Type	2-stage compressor	6-stage compressor	Cryogenic Distillation	6-zeolite adsorbers
Power (kW)	2883	2713	12767.17	2927.822
Heat (kW)	-2748 (intercoolers)	-2788.3 (intercooler)		
Area (m^2)	1537 (intercooler)	586.23 (intercooler)		
U (kW m^{-2})				
Medium	CW	CW		

Li-mediated NRR

Figure D6. Process flow diagram of the Li-mediated NRR process with hydrogen oxidation and an additional alkaline water electrolyzer.

Table D13. Stream summary of the Li-mediated NRR process at a FE of 90% (Figure D6).

Property	1	2	3	4	5	6	7
Temperature (°C)	25	25	25	25	80	40	80
Pressure (bar)	6	1.01	1.01	1.01	1.01	163	1.01
Mole flows (kmol h^{-1})	1109.78	1109.78	1035.80	371.83	166.47	166.47	332.94
NH$_3$ (kmol h^{-1})							
H$_2$ (kmol h^{-1})			36.99				332.94
N$_2$ (kmol h^{-1})	1109.78	1109.78	988.8				
O$_2$ (kmol h^{-1})					166.47	166.47	
THF (kmol h^{-1})							
LiFSI (kmol h^{-1})							
EtOH (kmol h^{-1})							
H$_2$O (kmol h^{-1})				371.83			
Mole fractions							
NH$_3$							
H$_2$			0.0357				1
N$_2$	1	1	0.964				
O$_2$					1	1	
THF							
LiFSI							
EtOH							
H$_2$O				1			
Mass flow (kg h^{-1})	31088.9	31088.9	28054.6	6711.99	5326.81	5326.81	671.20
Property	**8**	**9**	**10**	**11**	**12**	**13**	**14**
Temperature (°C)	25	25	25	25	25	25	-34
Pressure (bar)	1.01	1.01	1.01	1.01	1.01	1.01	1.01
Mole flows (kmol h^{-1})	332.94	3329.4	2996.42	1.0921	2009.77	2230.73	223.07
NH$_3$ (kmol h^{-1})					1.12	223.07	221.96
H$_2$ (kmol h^{-1})	332.94	3329.4	2996.4				
N$_2$ (kmol h^{-1})							
O$_2$ (kmol h^{-1})							
THF (kmol h^{-1})				1.0921	1849.58	1849.57	1.12
LiFSI (kmol h^{-1})					152.56	151.56	
EtOH (kmol h^{-1})					6.52	6.517	
H$_2$O (kmol h^{-1})							
Mole fractions							
NH$_3$					0.0006	0.1	0.995
H$_2$	1	1	1				
N$_2$							
O$_2$							
THF				1	0.92	0.829	0.005
LiFSI					0.076	0.0679	
EtOH					0.0032	0.0029	

H$_2$O							
Mass flow (kg h^{-1})	671.20	6711.0	6040.79	78.75	162230.0	165823	3860.36

Table D13 (Continued). Stream summary of the Li-mediated NRR process at a FE of 90% (Figure D6).

Property	15	16
Temperature (°C)	50	25
Pressure (bar)	1.01	1.01
Mole flows (kmol h^{-1})	2008.677	2008.677
NH$_3$ (kmol h^{-1})	1.12	1.12
H$_2$ (kmol h^{-1})		
N$_2$ (kmol h^{-1})		
O$_2$ (kmol h^{-1})		
THF (kmol h^{-1})	1848.49	1848.49
LiFSI (kmol h^{-1})	151.56	151.56
EtOH (kmol h^{-1})	6.517	6.517
H$_2$O (kmol h^{-1})		
Mole fractions		
NH$_3$	0.0006	0.0006
H$_2$		
N$_2$		
O$_2$		
THF	0.92	0.92
LiFSI	0.076	0.076
EtOH	0.0032	0.0032
H$_2$O		
Mass flow (kg h^{-1})	162151.3	162151.3

Table D14. Equipment list of the Li-mediated NRR process at a FE of 90% (Figure D6).

Main Equipment	E-1	E-2	E-3	E-4	C-1	Air separation Unit
Type	Cooler	Condenser	Reboiler	Cooler	6-stage compressor	Cryogenic Distillation
Power (kW)					2440.75	11484.96
Heat (kW)	145.2	-2963.82	4116.39	1881	-2502.52 (intercooler)	
Area (m^2)	45.59	279.8	286.1	49.44	524.1 (intercooler)	
U (kW m^{-2})	43.3	931.9	193.5	622.4		
Medium	Ammonia	Propylene	Electric heating	Propylene	CW	

Appendix Figures
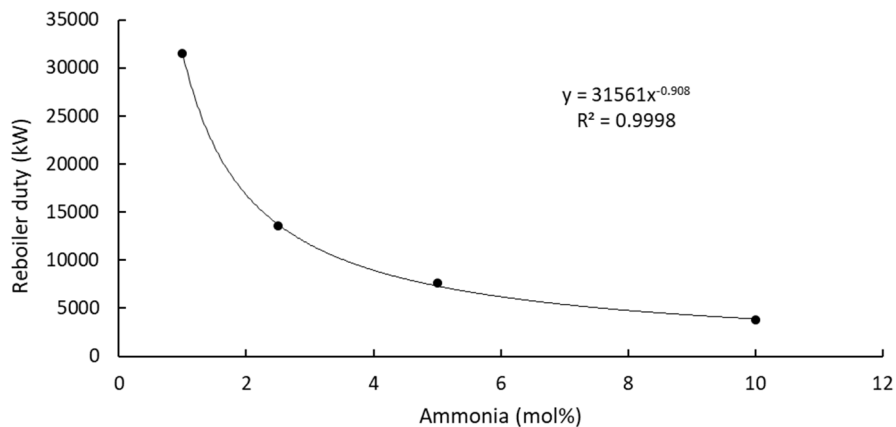
Figure D7. Reboiler duty as a function of the NH$_3$ mol fraction in the feed.
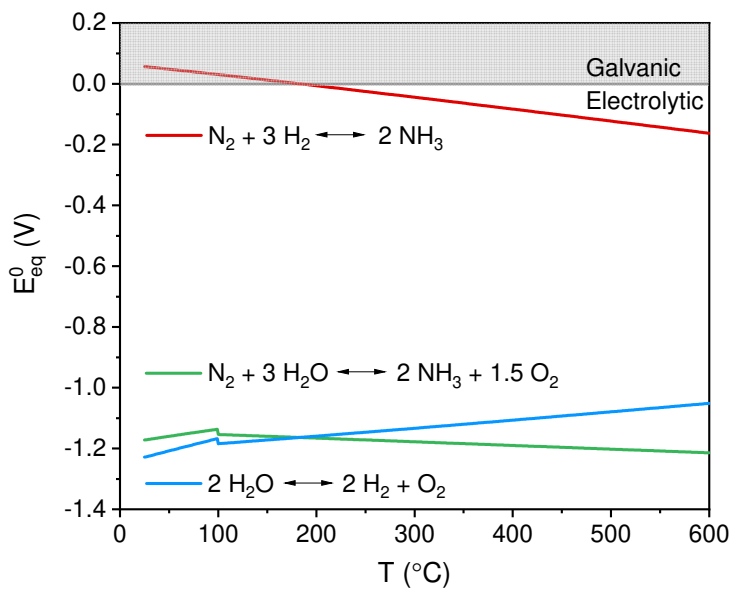
Figure D8. Standard equilibrium potentials for water electrolysis (blue), aqueous NRR (green) and indirect NRR (red) based on the Gibbs free energy.
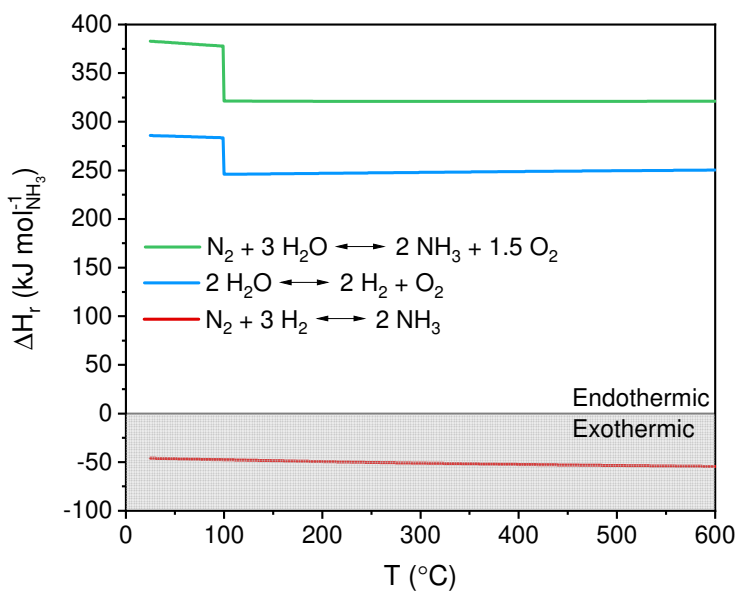
Figure D9. Reaction enthalpy diagram for water electrolysis (blue), aqueous NRR (green) and NRR with H_2 oxidation (red).
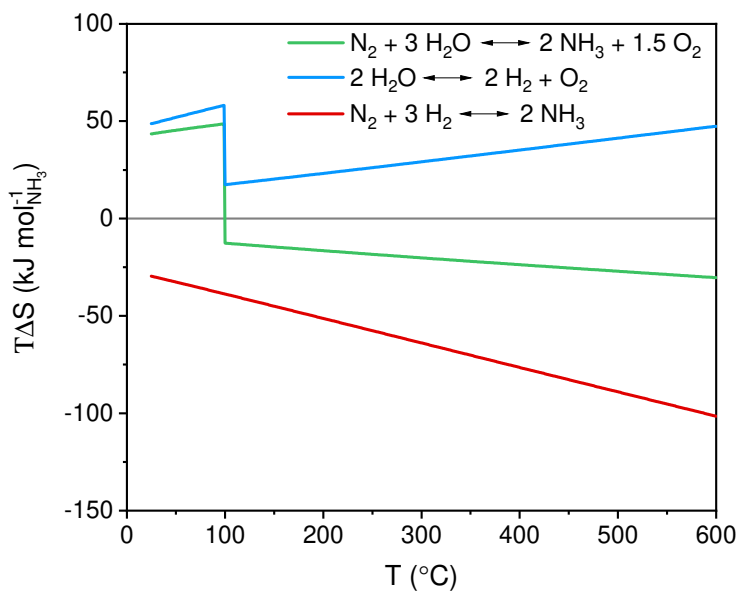
Figure D10. Reaction entropy diagram for water electrolysis (blue), aqueous NRR (green) and NRR with H$_2$ oxidation (red).
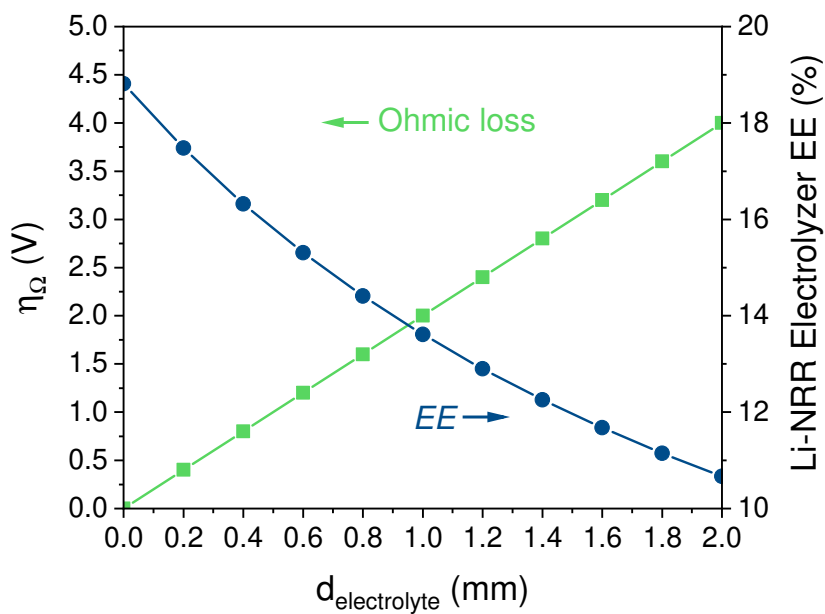
Figure D11. The Li-NRR electrolyzer energy efficiency at the aspirational values (0.3 A cm^{-2} and FE = 90%) including the energy input for H$_2$ production from water electrolysis.
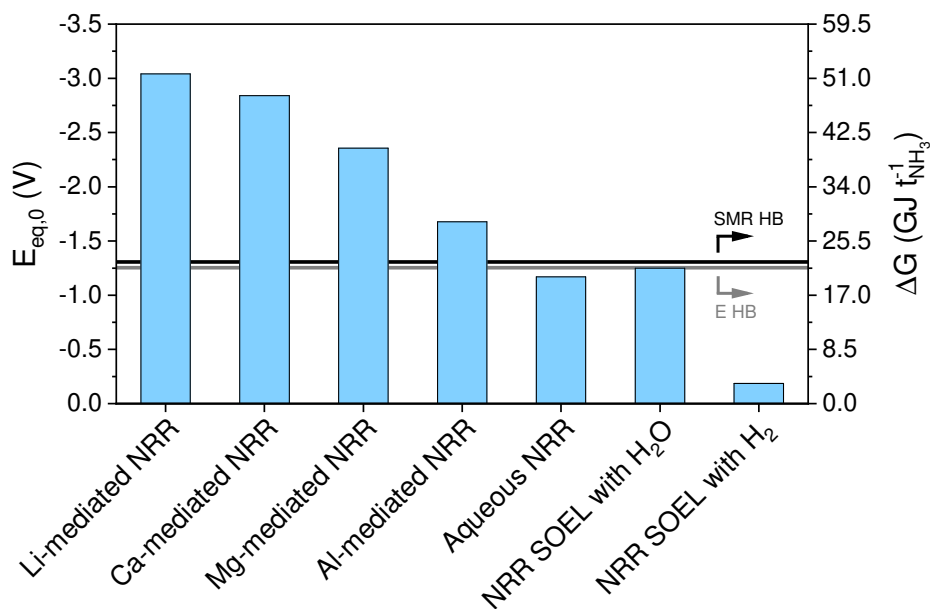
Figure D12. Standard equilibrium potentials and the Gibbs free energies for mediated NRR and other NRR electrolyzers. Additional energy input for H_2 production via water electrolysis is not included for indirect NRR electrolyzers. The thermodynamic minimum of electrified and SMR Haber-Bosch are also added for referencing. Standard equilibrium potentials for Li, Ca, Mg and Al plating are obtained from Bard & Faulkner. [1]
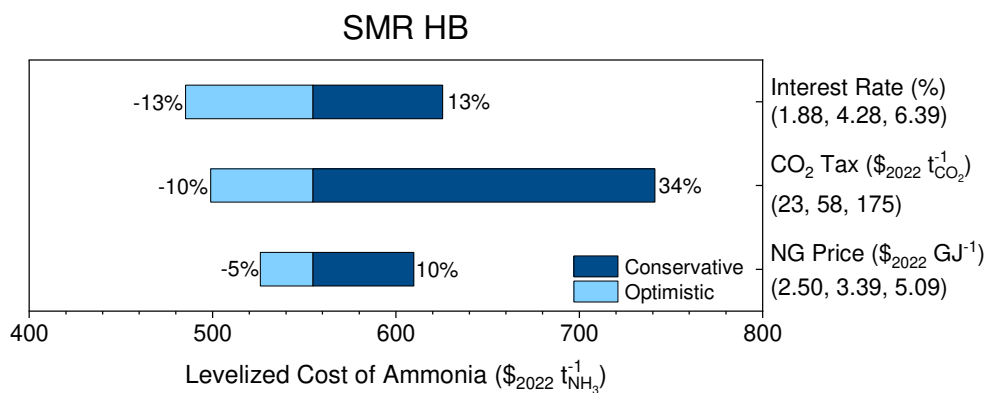
Figure D13. Sensitivity analysis of a small scale (91 tNH_3 per day) SMR HB plant.
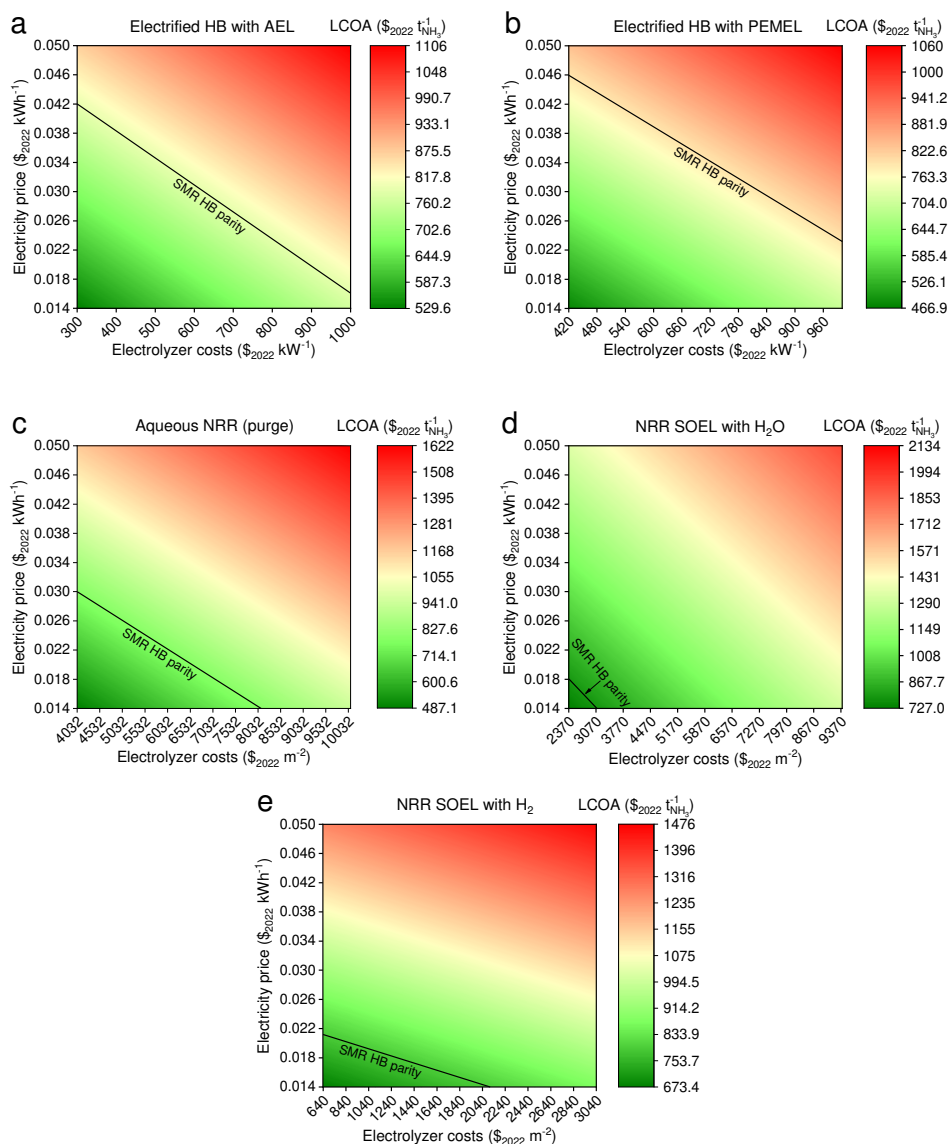
Figure D14. LCOA as a function of the electricity price and the electrolyzer costs for (a) electrified Haber-Bosch with AEL, (b) electrified Haber-Bosch with PEMEL, (c) aqueous NRR at ambient conditions with purge scenario, (d) NRR SOEL with water oxidation, (e) NRR SOEL with hydrogen oxidation. Base case assumptions for O_2, H_2O and energy import prices in 2050 are used. NRR electrolyzers operate at the ARPA-e aspirational values (0.3 A cm^{-2} and FE = 90%).
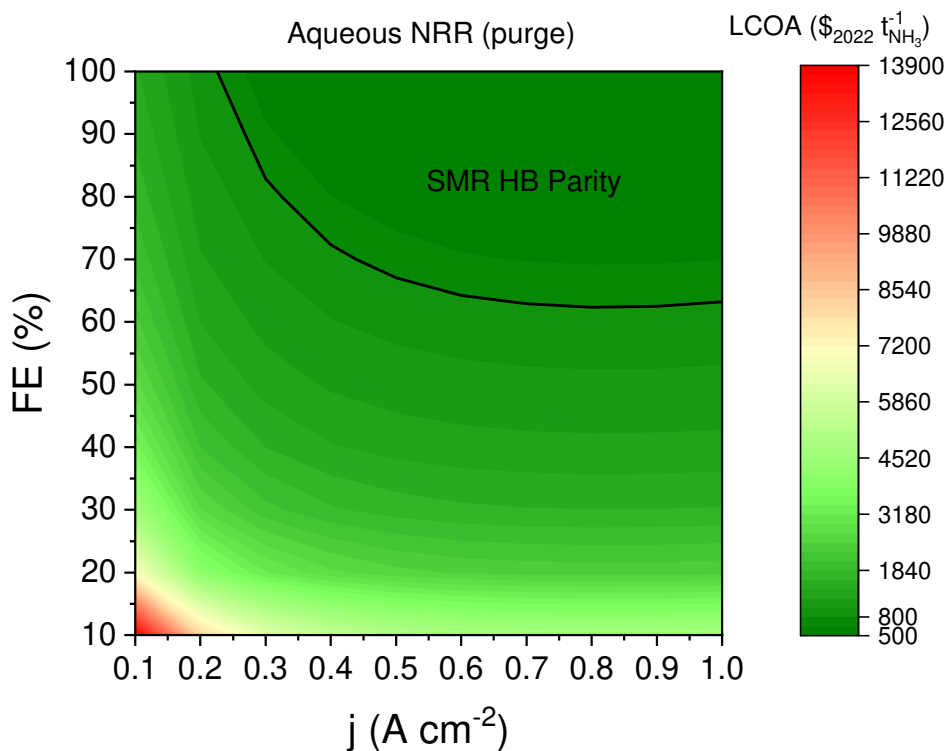
Figure D15. LCOA versus the FE and *j* for aqueous NRR at base case assumptions in 2050, using a more optimistic electricity price of $0.02 per kWh.
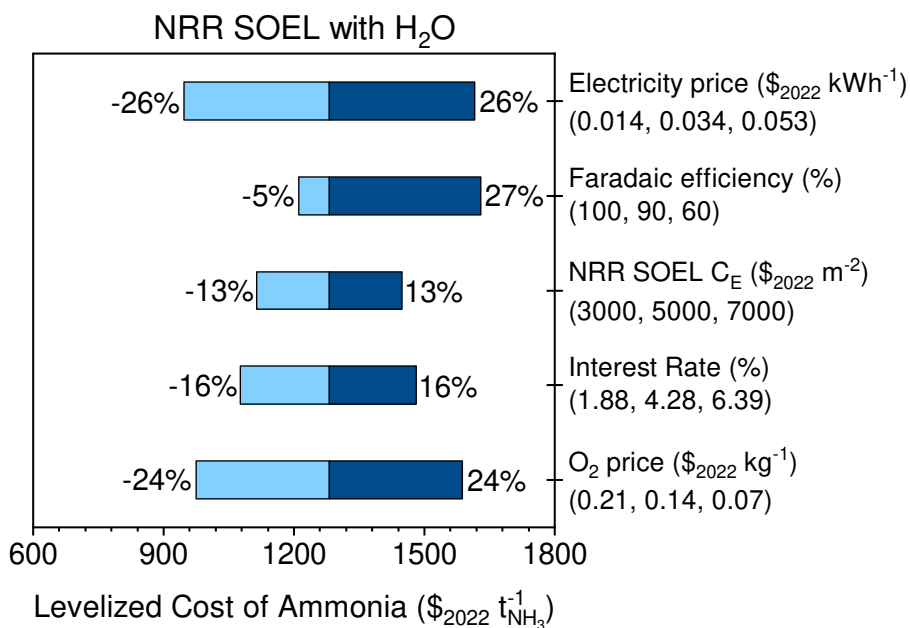
Figure D16. Sensitivity analysis of the NRR SOEL process with water oxidation at a constant *j* of 0.3 A cm^{-2}.
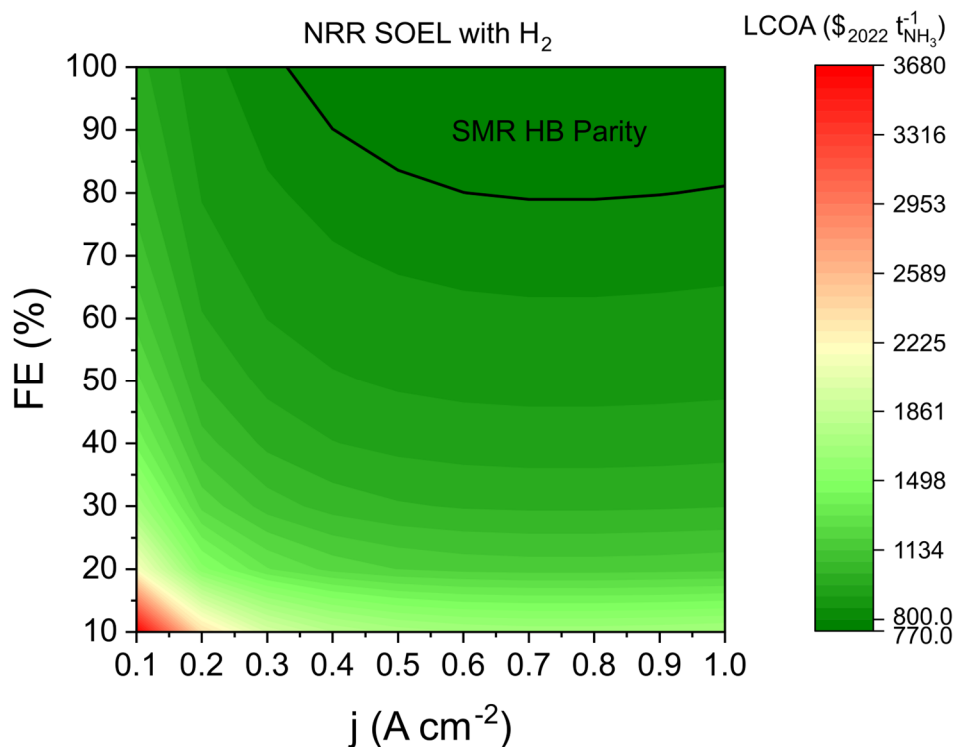
Figure D17. LCOA versus the FE and *j* for NRR SOEL with hydrogen oxidation at base case assumptions in 2050, using a more optimistic electricity price of $0.02 per kWh.
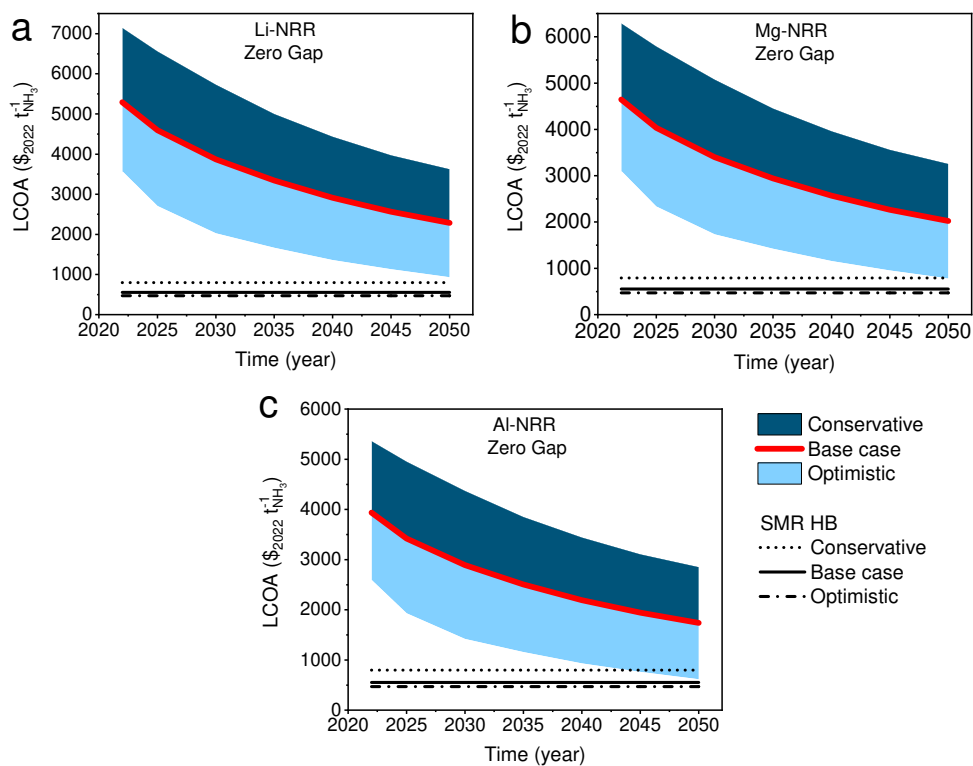
Figure D18. LCOA of mediated NRR processes using an "optimized" zero-gap membrane electrode assembly electrolyzer with (a) Li-NRR, (b) Mg-NRR and (c) Al-NRR.
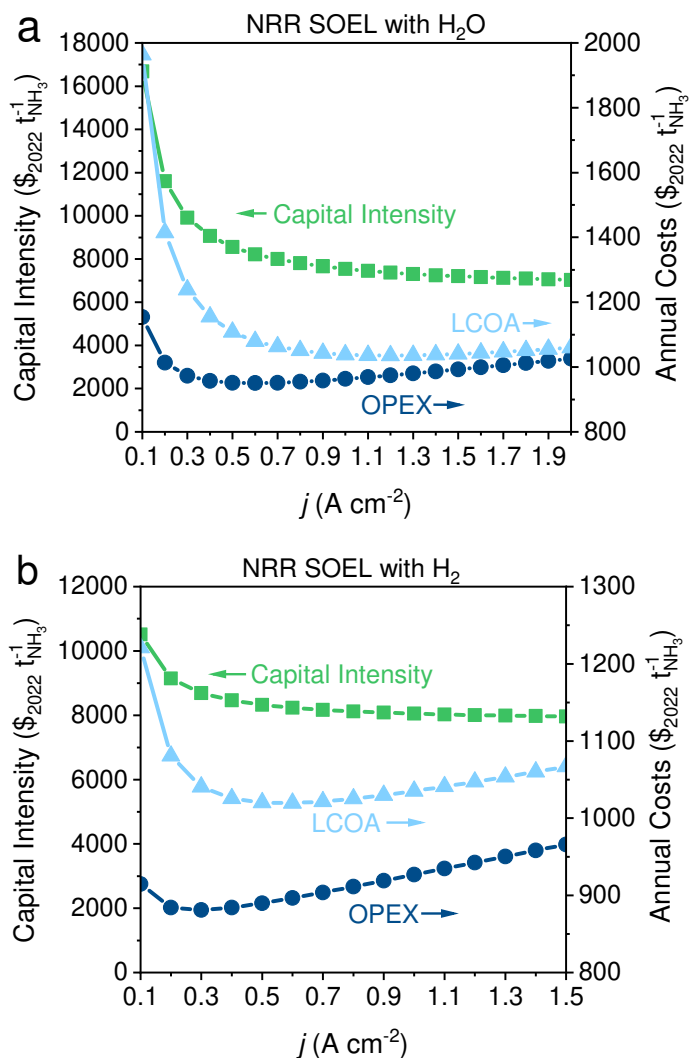
Figure D19. Current density as a function of the capital intensity, OPEX and LCOA for (a) NRR SOEL with water oxidation and (b) NRR SOEL with hydrogen oxidation at a FE of 90% using the base case assumption in 2050.

Appendix Tables

Table D15. Equipment cost data for conventional process units.[12-17]

Equipment	a	b	S_{units}	n	S_B	C_B ($)	K_1	K_2	K_3	Equation	Ref
Pump ($_{2010}$)	8000	240	0.2-126 L s^{-1}	0.9						S42	12
Compressor ($_{2010}$)	580000	20000	75-30000 kW	0.6						S42	12
Heat exchanger (U-tube and shell) ($_{2010}$)	28000	54	10-1000 m^2	1.2						S42	12
Vertical Pressure Vessels ($_{2010}$)	17400	79	120-250000 kg	0.85						S42	12
Vacuum pump (CEPCI 1000) ($_{2010}$)			3-1670 L s^{-1}		170 L s^{-1}	22000				S43	13
Rotary compressor ($_{2001}$)			18-950 kW				5.0355	-1.8002	0.8253	S44	14
Heat exchanger (plate and frame) ($_{2010}$)	1600	210	1-500 m^2	0.95						S42	12
Storage tank (fixed roof) ($_{2001}$)			90-30000 m^3				4.8509	-0.3973	0.1445	S44	14
Make-up tank ($_{2010}$)	5800	1600	10-4000 m^3	0.7						S42	12
Cryogenic Distillation ($_{2010}$)				0.6	250 tN$_2$ d^{-1}	1823620				S43	15
ASU PSA ($_{2014}$)				1	89.98 tN$_2$ d^{-1}	565000				S43	16
N$_2$/H$_2$ PSA ($_{2011}$) (Total fixed capital costs)				0.6	66.72 kmol$_{H2}$ h^{-1}	2050585				S43	17

5

235

Table D16. Cost projections for electrolyzers, electricity, feedstock and commodity prices for conservative, base case and optimistic scenarios. The large collection of AEL and PEMEL cost estimates reported by Glenk et al.,[18] were used for our analysis. Their exponential fitting through the data points was extrapolated until 2050 and used as the base case scenario (for AEL and PEMEL). A collection of their highest and lowest reported estimates were used to inter- and extrapolate a trend until 2050, which was implemented as conservative and optimistic price assumptions. The base case capital costs for water SOEL were taken from Bohm et al., who used technology learning curve models to predict reductions in the manufacturing cost trend over time.[19] Optimistic and conservative price scenarios were extrapolated from survey data from Schmidt et al.[20] The equipment costs of the NRR electrolyzers were derived from water electrolyzer data and converted from $ per unit power to $ per unit area via their respective power densities (more details discussed in the Supplemental Methods in Appendix D). The optimistic renewable electricity price is interpolated from utility solar PV price forcasts from ref [21,22]. The conservative scenario is adapted from Bogdanov et al. (North America).[23] The base case represents the average between the conservative and optimistic scenario. H_2 commodity pricing was extrapolated from ref [24]. The base case cost assumption for the O_2 price is the average Europe export tariff in 2021. [25] Optimistic cost price is the average O_2 price in Belgium in 2021.[25] Conservative O_2 price is assumed. Ultrapure H_2O price is 4-11 $ per m^3 based on Hausmann et al. by combining utility PV solar with reverse osmosis.[26] The natural gas price was derived by using statistical analysis from the Henry Hub historical data between 1997-2023. The first quartile (optimistic), median (base case) and third quartile (conservative) of the Henry Hub natural gas spot price historical data (1997-2023) were implemented for the scenarios.[27] The CO_2 tax is based on the IPCC 2022 mitigation report (chapter 11).[28] All data is inflation corrected to 2022.

Quantity	Scenario	2022	2025	2030	2035	2040	2045	2050	Unit
C_E water AEL[a]	Conservative	1773	1639	1439	1263	1108	973	854	$ per kW
	Base Case	1307	1194	1028	884	761	655	564	
	Optimistic	839	751	623	517	429	356	296	
C_E water PEMEL[a]	Conservative	2689	2237	1646	1211	891	656	482	$ per kW
	Base Case	1901	1641	1284	1005	787	615	482	
	Optimistic	1258	1120	922	760	626	515	425	
C_E water SOEL[b]	Conservative	5550	5166	4583	4067	3608	3201	2840	$ per kW
	Base Case	3095	2688	1830	1259	954	831	758	
	Optimistic	3081	2513	1789	1274	907	645	460	
C_E aqueous NRR[c]	Conservative	24985	21706	17273	13853	11196	9118	7482	$ per m^2
	Base Case	17963	15876	12946	10581	8667	7115	5854	
	Optimistic	11745	10474	8653	7149	5907	4880	4032	
C_E NRR SOEL with H_2O[d]	Conservative	32859	30583	27135	24076	21362	18954	16817	$ per m^2
	Base Case	18326	15912	10832	7451	5649	4921	4486	
	Optimistic	18241	14876	10591	7150	5368	3822	2721	
C_E NRR SOEL with H_2[e]	Conservative	8852	8239	7310	6486	5755	5106	4531	$ per m^2
	Base Case	4937	4287	2918	2007	1522	1326	1209	
	Optimistic	4914	4008	2853	1926	1446	1030	733	
C_E Li-NRR[f]	Conservative	79588	69142	55023	44127	35663	29045	23832	$ per m^2
	Base Case	57219	50572	41239	33704	27607	22664	18649	
	Optimistic	37413	33363	27564	22774	18816	15546	12845	
C_E Li-NRR[f] (MEA-type)	Conservative	33508	29111	23166	18579	15015	12229	10034	$ per m^2
	Base Case	24091	21292	17363	14190	11623	9542	7852	
	Optimistic	15752	14047	11605	9588	7922	6545	5408	
C_E	Conservative	27941	24273	19317	15491	12520	10197	8367	$ per m^2

Parameter	Scenario								Units
Mg-NRR[f] (MEA-type)	Base Case	20088	17754	14478	11832	9692	7957	6547	
	Optimistic	13134	11713	9677	7994	6606	5458	4509	
C_E Al-NRR[f] (MEA-type)	Conservative	21784	19003	15123	12128	9802	7983	6550	$ per m²
	Base Case	15726	13899	11334	9263	7588	6229	5125	
	Optimistic	10283	9170	7576	6259	5171	4273	3530	
Electricity price	Conservative	0.062	0.062	0.061	0.058	0.056	0.054	0.053	$ per kWh
	Base Case	0.056	0.046	0.041	0.038	0.036	0.0345	0.034	
	Optimistic	0.049	0.03	0.02	0.018	0.016	0.015	0.014	
H₂ price	Conservative	4.5	2.76	2.27	2.03	1.91	1.83	1.77	$ per kg
	Base Case	4	2.47	2.02	1.81	1.68	1.61	1.56	
	Optimistic	3.25	2.15	1.73	1.54	1.42	1.36	1.31	
O₂ price	Conservative	0.07	0.07	0.07	0.07	0.07	0.07	0.07	$ per kg
	Base Case	0.14	0.14	0.14	0.14	0.14	0.14	0.14	
	Optimistic	0.21	0.21	0.21	0.21	0.21	0.21	0.21	
Ultrapure H₂O	Conservative	11	11	11	11	11	11	11	$ per m³
	Base Case	7.5	7.5	7.5	7.5	7.5	7.5	7.5	
	Optimistic	4	4	4	4	4	4	4	
Natural gas	Conservative	5.66	5.66	5.66	5.66	5.66	5.66	5.66	$ per GJ
	Base Case	3.77	3.77	3.77	3.77	3.77	3.77	3.77	
	Optimistic	2.79	2.79	2.79	2.79	2.79	2.79	2.79	
CO₂ Tax	Conservative	175	175	175	175	175	175	175	$ per tCO₂
	Base Case	58	58	58	58	58	58	58	
	Optimistic	23	23	23	23	23	23	23	

[a] Extrapolated costs from Glenk et al.[18]

[b] Extrapolated costs from Schmidt et al and Bohm et al.[19,20]

[c] Average equipment cost between AEL and PEMEL. Converted to $ per area with a power density of 11.2 kW per m² (see Table D24).

[d] $ per kW price as a water SOEL. Converted to $ per area with a power density of 5.92 kW per m² (see Table D24).

[e] $ per kW price as a water SOEL. Converted to $ per area with a power density of 1.59 kW per m² (see Table D24).

[f] $ per kW price as aqueous NRR. Converted to $ per area with a power density of 35.7 kW per m² (see Table D24).

Table D17. Lang factors adapted from "Smith – Chemical Process Design and Integration".[29]

Inside Battery Limit (ISBL)		
	f_M	1 - 3.4[*]
	f_P	1 - 1.9[*]
	f_T	1 - 2.1[*]
	f_{pip}	0.7
	f_{erec}	0.4
	$f_{I\&C}$	0.2
	f_{elec}	0.1

$$C_{ISBL} = C_E \left(f_m f_p f_T \left(1 + f_{pip} \right) + f_{er} + f_{I\&C} + f_{elec} \right) \qquad (D1)$$

Outside Battery Limit (OSBL)		
	f_{util}	0.5
	$f_{off\text{-}sites}$	0.2
	f_{build}	0.2
	$f_{side\ prep}$	0.1

$$C_{OSBL} = C_E \left(f_{util} + f_{off-sites} + f_{build} + f_{side\ prep} \right) \qquad (D2)$$

Total fixed capital cost (TFC)		
	$f_{design\&eng}$	1
	f_{cont}	0.2

$$C_{TFC} = \frac{C_{ISBL} + C_{OSBL} + C_E f_{design\&eng}}{f_{cont}} \qquad (D3)$$

Total capital cost (TC)		
	$f_{work\ cap}$	0.2

$$C_{TC} = \frac{C_{TFC}}{f_{work\ cap}} \qquad (D4)$$

[*] Factors are process condition dependent.

Table D18. General assumptions for the OPEX.

Days of operation	333.3	days
Workers	22	
Annual work hours	1791	hours/year
Salary	71640	$/year
O&M	3 % of Total Capital [30]	$
SMR H-B Consumables	3 [30]	$/t NH_3
Interest rate	4.28	%

Table D19. An overview of the electrochemical model input parameters.

Quantity	Unit	Aqueous NRR (GDE)	NRR SOEL with OER	NRR SOEL with HOR	Li-NRR with HOR
E_{eq}^0	V	-1.17	-1.21	-0.14	-3.045
T	°C	25	550	550	25
P	atm	1	1	1	1
α_{cat}		0.5	0.5	0.5	0.4 [2]
α_{an}		0.5	0.5	0.5	0.5
n_{cat}	Electrons	6 (NRR)	6 (NRR)	6 (NRR)	1 (Li-plating)
n_{an}	Electrons	4 (OER)	4 (OER)	2 (HOR)	2 (HOR)
$j_{0,reduction}$	A cm^{-2}	10^{-22} [3] (NRR)	0.4 [4] (NRR)	0.4 [4] (NRR)	0.00001 [5] (Li)
$j_{0,oxidation}$	A cm^{-2}	10^{-12} [3] (OER)	0.13 [4] (OER)	0.53 [6] (HOR)	0.01 [7] (HOR)
R_{mem}	Ω cm	0.375 [8]	-	-	-
d_{mem}	mm	0.05 [8]	-	-	-
Electrolyte		1M KOH	$Ce_{0.8}Sm_{0.2}O_2$	$Ce_{0.8}Sm_{0.2}O_2$	1M LiFSI in THF
$\kappa_{electrolyte}$	S cm^{-1}	0.215 [9]	0.014 (650°C) [10]	0.014 (650°C) [10]	0.015 [11]
d_{gap}	mm	4	0.05 [10]	0.05 [10]	2

Supplemental Methods

NRR Electrolyzers: Gibbs Free Energy and the Equilibrium Potential

The following half-reactions were considered for direct and indirect electrochemical NH_3 synthesis.

$$N_2 + 6\,H_2O + 6\,e^- \rightarrow 2\,NH_3 + 6\,OH^- \quad \text{(NRR)} \tag{D5}$$

$$6\,OH^- \rightarrow \frac{3}{2}O_2 + 3\,H_2O + 6e^- \quad \text{(OER)} \tag{D6}$$

$$N_2 + 3\,H_2O \rightarrow 2\,NH_3 + \frac{3}{2}O_2 \quad \text{(Overall reaction)} \tag{D7}$$

$$N_2 + 6\,H^+ + 6\,e^- \rightarrow 2\,NH_3 \quad \text{(NRR)} \tag{D8}$$

$$3\,H_2 \rightarrow 6\,H^+ + 6e^- \quad \text{(HOR)} \tag{D9}$$

$$N_2 + 3\,H_2 \rightarrow 2\,NH_3 \quad \text{(Overall reaction)} \tag{D10}$$
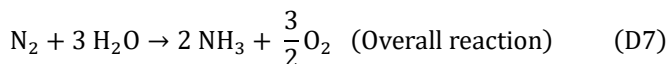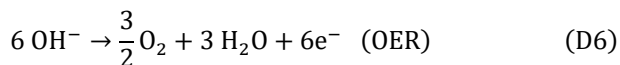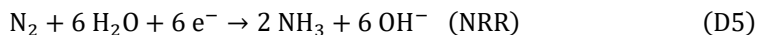
The standard Gibbs free energy is the thermodynamic minimum of the reaction (S7 and S10) and can be calculated by Equation D11 using tabulated standard enthalpies and entropies of formation (NIST database) and stoichiometric coefficients of each reactant and product. Equation D12 shows a calculation example for aqueous NRR.

$$\Delta G^0 = \Delta H^0 - T\Delta S^0 \tag{D11}$$

$$
\begin{aligned}
\Delta G^0 &= \left(\left[v_{O_2}\,\Delta H_f^{O_2} + v_{NH_3}\Delta H_f^{NH_3}\right] - \left[v_{N_2}\Delta H_f^{N_2} + v_{H_2O}\Delta H_f^{H_2O}\right]\right) \\
&\quad - T\cdot\left(\left[v_{O_2}\Delta S_f^{O_2} + v_{NH_3}\Delta S_f^{NH_3}\right] - \left[v_{N_2}\Delta S_f^{N_2} + v_{H_2O}\Delta S_f^{H_2O}\right]\right) \\
&= \left([1.5\cdot 0 + 2\cdot -45.9] - [1\cdot 0 + 3\cdot -285.83]\right) \\
&\quad -98\cdot\left([1.5\cdot 205.15 + 2\cdot 192.77] - [1\cdot 191.61 + 3\cdot 69.95]\right)\cdot 10^{-3} \\
&= (-91.8 + 857.49) - 298\cdot(693.265 - 401.46)\cdot 10^{-3} = 765.69 - 86.95789 \\
&= 678.73211\ \text{kJ} = 339.366\ \frac{\text{kJ}}{\text{mol NH}_3} = 19.928\ \frac{\text{GJ}}{\text{tNH}_3}
\end{aligned}
\tag{D12}
$$

The standard Gibbs free energy is related to the standard equilibrium potential via the Faraday constant (96485 C/mol). Three electrons are required to produce one mol of NH_3, thus for aqueous NRR:

$$E_{eq}^0 = -\frac{\Delta G^0}{nF} = -\frac{339366}{3\cdot 96485.33} = -1.172\ \text{V} \tag{D13}$$

The equilibrium potential is calculated via the Nernst law with N_2, O_2 and NH_3 partial pressures of 1, 1 and 0.1 atm, respectively:

$$E_{eq} = E_{eq}^0 - \frac{RT}{nF} \ln \left(\frac{p_{NH_3}^2}{p_{N_2} p_{O_2}^{1.5}} \right) \tag{D14}$$

NRR Electrolyzers: Activation Overpotentials and Ohmic Losses

An additional overpotential is required to overcome the activation barrier of an electrochemical reaction. It is estimated that the minimum overpotential for NRR must be at least 0.4 V.[31,32] The activation overpotential increases with the current density and can be estimated by approximations of the Buttler-Volmer equation. If the exchange current density (j_0) is relatively small with respect to j ($j/j_0 > 4$) the Tafel equation (Equation D15 and S16) can be considered. In case j_0 is large ($j/j_0 < 1$), which is often the case for high temperature electrolyzers, the hyperbolic sine approximation (Equation D17 and D18) is more appropriate.[33]

$$\eta_{cat} = -\frac{RT}{n_{cat}F\alpha} \ln \frac{j}{j_{0,c}} \tag{D15}$$

$$\eta_{an} = \frac{RT}{n_{an}F\alpha} \ln \frac{j}{j_{0,a}} \tag{D16}$$

$$\eta_{cat} = -\frac{RT}{n_{cat}F\alpha} sinh^{-1}\left(\frac{i}{i_0}\right) \tag{D17}$$

$$\eta_{an} = \frac{RT}{n_{an}F\alpha} sinh^{-1}\left(\frac{i}{i_0}\right) \tag{D18}$$

The ohmic losses are associated with the transport of ions in the membrane (Equation D19) and the electrolyte (Equation D20). The membrane transport losses are usually small because they are < 1 mm. On the contrary, the gap between the working and the counter electrode (d_{gap}) in liquid electrolyzers can be up to a few mm thick. This means that electrolytes with a poor conductivity will have a large influence on the overall cell voltage. The concentration overpotential due to mass transport limitations is not considered in this work.

$$\eta_{mem} = j \cdot d_{mem} \cdot R_{mem} \tag{D19}$$

$$\eta_{\Omega} = \frac{j \cdot d_{gap}}{\kappa} \tag{D20}$$

H$_2$ Electrolyzers

The energy consumption of the AEL and PEMEL for electrified Haber-Bosch and the indirect NRR processes are based on commercially available models from Nel (A485) and Siemens (Silyzer 300), respectively.[34] All relevant details are listed in Table D20.

Table D20. H$_2$ electrolyzer operating conditions based on commercially available electrolyzers. Data acquired from ref [34-36].

Quantity	Unit	AEL (Nel A485)	PEMEL (Siemens Silyzer 300)
E_{system}	kWh $Nm_{H_2}^{-3}$	4	4.59
EE_{LHV}[a]	%	75	65
T	C	80	80
P	Bar	1.013	35
H$_2$O Consumption	L_{H_2O} $kg_{H_2}^{-1}$	10	10

[a] based on the LHV of H$_2$ (3 kWh Nm^{-3})

Air Separation Unit

Pressure swing adsorption (PSA) for air separation is economically attractive at N$_2$ capacities < 500 t per day.[37] The energy consumption of a PSA ASU depends on the purity of the N$_2$ product stream, which can very between $1.12 - 1.584$ GJ per tN$_2$ with corresponding purities between $98 - 99.9$ vol% N$_2$.[38] Vast quantities of O$_2$ can effect the current efficiency, therefore it is desired to have the highest possible N$_2$ feed purity. Hence, we assume a PSA energy consumption of 1.584 kJ per tN$_2$. The energy consumption of the cryogenic distillation unit can vary between $0.44 - 1.33$ GJ per tN$_2$, which depends mainly on the N$_2$ capacity and final gas pressure.[38] The N$_2$ demand for our process is relatively small compared to a industrial scale Haber-Bosch plant, therefore we assume a single cryogenic column, which is less capital intensive, but consumes more energy (1.33 GJ per tN$_2$).

Heat Exchangers, Compressors and Pumps

The necessary heating or cooling duties of all exchangers are calculated in Aspen Plus, which uses the first law of thermodynamics. The actual energy input in the form of work depends on the exchange medium, wherein steam (from an electric boiler) was used for hot utilities, cooling water (CW) for cold utilities up to 35 °C, and various refrigerants for cold utilities < 35 °C. The energy input of the electric steam boiler can simply be calculated with Equation D21 implementing a boiler efficiency of 0.95.[39,40]

$$W_{boiler} = \frac{Q_{demand}}{\eta_{boiler}} \tag{D21}$$

The amount of required cooling water for the intercoolers is calculated by:

$$Q_{intercooler} = \dot{m}_{CW} \cdot C_{P,H_2O} \cdot \Delta T \tag{D22}$$

Where Q is obtained from Aspen and a ΔT of 10 °C is assumed. Additional work input is required for the cooling water pumps, which can be calculated by the following heuristic:[41]

$$W_{CW} = \frac{0.0972 \cdot \dot{m}_{CW} \cdot \Delta P}{\eta_{pump}} \tag{D23}$$

With $\dot{m}_{CW}$, the cooling water mass flow obtained from Q_{cool}, ΔP is the pressure drop in the tubing (assumed to be 2 bar) and η_{pump} is 85% for a reciprocating pump.

The cold utilities < 35 °C are based on a Carnot refrigeration cycle, in which the duty of the compressor can be calculated by the coefficient of performance (COP):

$$COP = \frac{Q}{W_{comp}} = \frac{0.6 T_{evap}}{(T_{cond} - T_{evap})} \tag{D24}$$

Where T_{evap} is the evaporation temperature of the selected refrigerant and T_{cond} is the temperature of the condenser. We assume a minimum temperature difference of 10 °C between the hot and cold stream (for all heat exchangers). Therefore, T_{cond} is atleast -10 °C lower than the temperature of the hot stream.

The area of all exchangers were obtained from Aspen Plus, which calculates the overall heat transfer coefficient and the logarithmic mean temperature difference between the hot and cold streams (Equation D25). A U-tube and shell type is considered in case $A > 10$ m^2. A plate and frame model is selected for smaller heat exchangers. The equipment cost of pumps and refrigeration compressors are also included in the total capital costs.

$$Q = U \cdot A \cdot \Delta T_{LM} \tag{D25}$$

All compressors are simulated in Aspen Plus as polytropic using the ASME calculation method. The pressure ratio is 2.5. The polytropic and mechanical efficiencies are 0.75 and 0.95, respectively. The pressure ratio determines the required compressor stages to reach the desired final pressure. As an example, O_2 needs to be pressurized up to 163 bar to reach market requirements. Therefore, a six multistage compressor including intercoolers is implemented (see Figure D20). We assumed that the 1st intercooler has no ΔP, the 2nd intercooler a ΔP = 0.5 psi, and the 3rd intercooler a ΔP of 1 psi or 1 bar in case the pressure > 15 bar. The total energy input of a multistage compressor can be expressed as:

$$W_{comp} = \sum_{i=1}^{No. \ stages}(W_{stage,i} + W_{CW,i}) \tag{D26}$$

The total equipment cost of the compressor unit includes the individual compressor stages, U-tube and shell intercoolers and CW pumps.
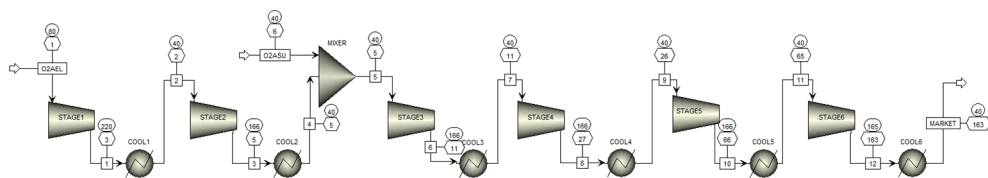
Figure D20. Aspen simulation of a multistage O_2 compressor with intercooling.

Distillation

Distillation columns were designed in Aspen Plus using the RADFRAC model. The column was optimized at an NH_3 distillate purity of 99.5% and NH_3 recovery of 99.9%. Figure D7 shows that the NH_3 feed composition has a significant influence on the reboiler duty. We assume a NH_3 feed composition of 10 mol% to minimize the reboiler duty. In general, a minimum amount of stages is required to ensure the desired distillate purity. Beyond this minimum, the number of stages is a trade-off between the equipment and operational costs, since more stages reduce the energy input of the condenser and reboiler. Herein, we focused particularly on minimizing the energy input. The column design specs are illustrated in Figure D21.
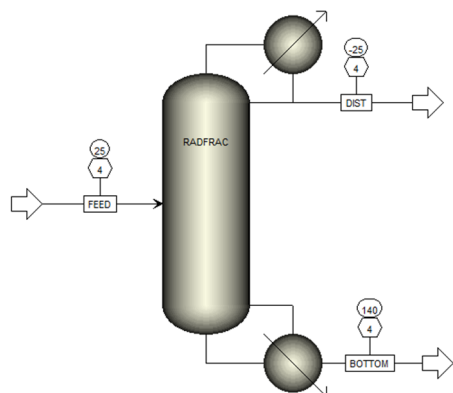
Quantity	Unit	Aqueous NRR (ambient)	Li-NRR
$N_{theoretical}$	#	17	14
Feed stage	#	8	9
Top stage T	C	-24.8	-33.6
Bottom stage T	C	140.16	49.9
Condenser Duty	kW	-806.8	-2963.8
Reboiler Duty	kW	6967	4116.4
Reflux Ratio		0.826	1.02
Boilup Ratio		0.31	0.24
N_{actual}	#	20	16
L_C	m	10	8
D_C	m	1.322	3.427

Figure D21. Example of the RADFRAC model in Aspen Plus (left) and its design specs (right). ELECNRTL was used as the property package.

The column sizing was based on standard methods available in chemical engineering textbooks, such as "Towler and Sinnot – Chemical Engineering Design".[12] The actual number of stages to estimate the column length is calculated via the plate efficiency:

$$N_{\text{actual}} = \frac{N_{\text{theoretical}}}{\eta_{\text{plate}}} \tag{D27}$$

$$\eta_{\text{plate}} = \frac{\log\left(1 + \eta_{\text{mw}}\left(\frac{mV}{L} - 1\right)\right)}{\log\left(\frac{mV}{L}\right)} \tag{D28}$$

$$L_{\text{C}} = \frac{N_{\text{actual}}}{l_{\text{plate}}} \tag{D29}$$

With a murphy plate efficiency (η_{mw}) of 0.9 for an ammonia-water mixture,[12] m the slope of the equilibrium line, l_{plate} the plate spacing of 0.5 m, V and L the molar vapor and liquid flow rate, respectively. The diameter of the column is obtained with the vapor flow rate and the maximum allowable superficial velocity (u_{v}) using the Souders-Brown equation:

$$D_{\text{c}} = \sqrt{\frac{4V_{\text{w}}}{\pi \rho_{\text{v}} u_{\text{v}}}} = 3.43 \text{ m} \tag{D30}$$

$$u_{\text{v}} = \left(-0.171 l_{\text{plate}}^2 + 0.27 l_{\text{plate}} - 0.047\right)\left[\frac{\rho_{\text{L}} - \rho_{\text{v}}}{\rho_{\text{v}}}\right]^{0.5} \tag{D31}$$

Where V_{w} is the mass vapor flow rate, ρ_{v} the distillate density and ρ_{L} the bottom liquid density. The wall thickness is related to the maximum allowable stress (σ_{max}), D_{c}, and the pressure:

$$\sigma_{\text{max}} = \frac{PD_{\text{c}} + 1.2t_{\text{wall}}P}{2t_{\text{wall}}} \tag{D32}$$

The design pressure is assumed to be 10% above the working pressure. Values for σ_{max} are tabulated for different steels and temperatures, which can be used to extract t_{wall}. In our case, the column is made from stainless steel grade 304. The head and closure of the column are assumed to have a hemicircular shape and require 60% of the column wall thickness. The sum of the column, condenser and reboiler represent the total equipment cost of the distillation unit.

Adsorption

The adsorption column was designed and optimized in Aspen Adsorption. The adsorption cycle consists of adsorption, column regeneration by heating under vacuum and cooling.

Zeolite 13x is selected as adsorbent material. The gas adsorption equilibrium isotherms were modelled with the Langmuir approach:

$$q = \frac{q_s \cdot b \cdot p}{1 + b \cdot p} \tag{D33}$$

Where, q is the adsorbed gas concentration, q_s is the saturation sorbate concentration, b is the adsorption equilibrium constant. The kinetics of the adsorption and desorption process is also influenced by temperature. Therefore, the adsorption equilibrium constant for NH_3 is expanded in the form of the van 't Hoff equation; [42]

$$b_{NH_3} = b_{0,NH_3} \cdot e^{\left(-\frac{\Delta H_{ads,NH_3}}{RT}\right)} \tag{D34}$$

Table D21. Adsorption equilibrium isotherm data acquired from Helminen et al. and Park et al.[42,43]

Quantity		Unit
q_s	7.51 [42] (NH_3) 3.16 [43] (N_2) 4.15 [43] (H_2)	mmol g-1
b_{NH_3}	0.735 [42] (NH_3)	kPa-1
b_{0,NH_3}	1.2·10-3 [43] (N_2) 5.34·10-5 [43] (H_2)	kPa-1
ΔH_{ads}	63.3 [42] (NH_3)	kJ mol-1

With ΔH_{ads} representing the heat of adsorption that is specific for the adsorbent material. T_{ads} is set to 313 K in order to minimize the cooling cost from the SOEL product stream and regeneration step. The adsorption capacity is generally higher at room temperature. The adsorbed gas concentration N_2 and H_2 are to some extent inert to the zeolite, hence Equation D34 is not included in the Langmuir model for N_2 and H_2. The adsorption time, t_{ads}, was set to 600 s, which is slightly before NH_3 breakthrough occurs as shown in Figure D22. The fixed bed mass transfer coefficients for the gases (Equation D35) can be derived from the Colburn-Chilton correlations for the diffusion mass transport (Equation D36 and D37), where v_s is the superficial velocity.[44]

$$k = 1.17 \cdot v_s \cdot Re^{-0.415} Sc^{-0.667} \tag{D35}$$

$$j_D = \frac{k}{v_s} \cdot Sc^{0.667} \tag{D36}$$

$$j_D = 1.17 Re^{-0.415} \quad 10 < Re < 2500 \tag{D37}$$

Aspen Adsorption uses time-dependent partial differential equations (PDEs) to solve the mass, momentum and energy balances during the dynamic simulation. The first-order upwind difference scheme (UDS1) with 40 nodes in 1D was used to discretize the PDEs. The material balance equations govern the adsorption kinetics and the mass transfer coefficients which are solved via a linear lumped resistance model. For the momentum balance, the

pressure drop is calculated via the Ergun equation.[45] It is assumed that the column is isothermal. By using the model input parameters of Table D21 and D22, the optimal length (3 m) and diameter (2 m) of the column were obtained from Aspen Adsorption.
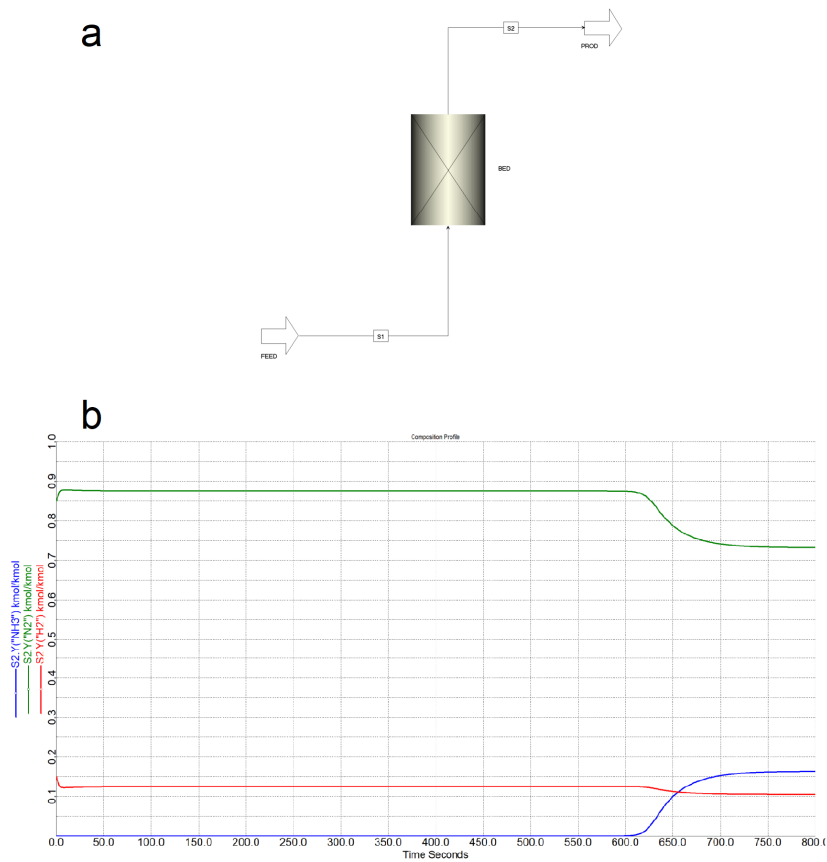

Figure D22. (a) Example of the model in the Aspen Adsorption simulation environment. (b) Obtained NH$_3$ breakthrough curve.

Table D22. A summary of the Aspen Adsorption model parameters.

Quantity		Unit
D_{bed}	2	m
h_{bed}	3	m
$d_{zeolite13x}$	2 [42]	mm
$\rho_{zeolite13x}$	647 [42]	kg m^{-3}
$C_{p,zeolite13x}$	943 [46]	J kg^{-1} K^{-1}
SF	1	
ε_i	0.35	
ε_p	0.6	
T_{ads}	313.15	K
v_s	0.42 [45]	m s^{-1}
p_i	56.98 (NH$_3$) 256.40 (H$_2$) 36.63 (N$_2$)	kPa
μ	9.815·10^{-6} (NH$_3$) 1.746·10^{-5} (N$_2$) 8.743·10^{-6} (H$_2$)	cP
ρ_{gas}	0.398 (NH$_3$) 2.948 (N$_2$) 0.030 (H$_2$)	kg m^{-3}
D_{gas}	2.28·10^{-5} [47] (NH$_3$) 2.19·10^{-5} [48] (N$_2$) 8.5·10^{-5} [49] (H$_2$)	m^2 s^{-1}
K	0.031 (NH$_3$) 0.041 (N$_2$) 0.044 (H$_2$)	s^{-1}

Although not modelled, it is assumed that the fixed bed is heated internally by steam during the regeneration step. Since the volume is relatively large, we assume that t_{reg} is 1500 s. The heat input can be estimated by rewriting the heat balance over the column during the regeneration step:[50]

$$Q_{reg} = \frac{m_{zeolite}\left(C_{p,zeolite} \cdot (T_{reg} - T_{ads}) + \Delta H_{ads} \cdot \left(q_{ads} - q_{reg}\right)\right)}{t_{reg}} \tag{D38}$$

Where, q_{ads}–q_{reg} is the work capacity of the fixed bed and T_{reg} = 473.15 K. It is not possible to desorb all NH$_3$, therefore a 90% recovery is assumed. The heat is supplied by steam from an electric boiler with an efficiency of 95%.[39] The vacuum pump power is calculated via the following heuristic:[51]

$$W_{vacuum} = 21.4 \cdot (SF)^{0.924} \tag{D39}$$

$$SF = \frac{\frac{1}{2}\dot{m}_{NH_3} \cdot \sqrt{273.15 + T_{reg}} \cdot 28.96}{293.15 \cdot Mw_{NH_3} \cdot P_{vacuum}} \quad 0.02 < SF < 16 \tag{D40}$$

Where SF is the size factor and $\dot{m}_{NH3}$ is the NH_3 mass flow leaving the column. To calculate the cooling duty in order to reach T_{ads}, the heat of adsorption can be excluded from the heat balance:

$$Q_{cool} = \frac{m_{zeolite} \cdot C_{p,zeolite} \cdot (T_{reg} - T_{ads})}{t_{cool}} \tag{D41}$$

With t_{cool} = 1100 s (assumed). Nonetheless, the usage of cooling water will only include the work of the cooling pump as explained earlier in subsection "Heat Exchangers, Compressors and Pumps". Hence, the total energy input for the adsorption column is:

$$W_{ads} = W_{compression} + \frac{Q_{reg}}{\eta_{steam}} + W_{vacuum} + W_{CW} \tag{D42}$$

By combing the adsorption, regeneration and cooling time in an adsorption schedule (Figure D23), six adsorption columns are required to enable continuous operation. Thus, the equipment cost of the adsorption unit consist of 6 columns, 1 compressor, 1 vacuum pump and a CW pump.
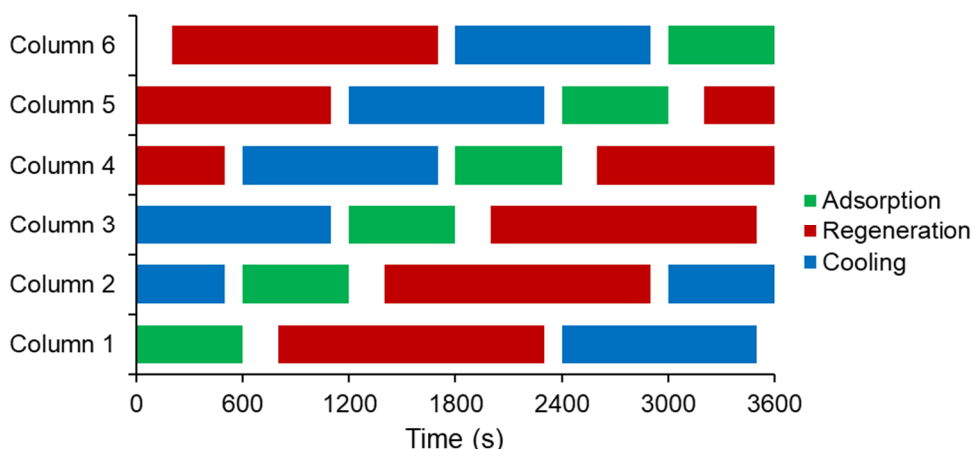
Figure D231. Adsorption, regeneration and cooling schedule of six adsorption columns.

Storage tanks

NH_3 is stored at -33 °C and 1 atm in a refrigerated double walled storage tank. The capacity of the storage tank is designed to accommodate 30 days of continuous production plus 10% freeboard.[15] The internal tank has a total volume of 4400 m^3 when taking a liquid NH_3 density of 682 kg per m^3. The internal tank is sized by D_{int}/H_{int} = 0.75 as a heuristic. The diameter of the external tank is 2 m wider than $D_{internal}$, while keeping the height constant. An additional refrigeration cycle is designed to reduce NH_3 boil-off losses, which are assumed to be 0.04% of the production capacity.[15]
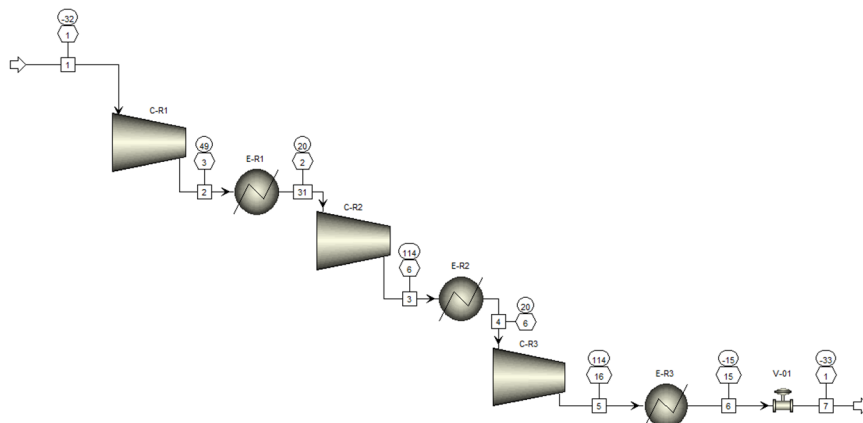
Figure D24. Refrigeration loop to recycle the NH$_3$ boil-off gasses.

Haber-Bosch synthesis loop

For the electrified Haber-Bosch process with AEL, the feed gas compressor is simulated as a 6th stage compressor with CW intercoolers. The recycle stream enters the multistage compressor in the 6th stage (see Figure D1), but is simulated separately in Aspen (Figure D25).
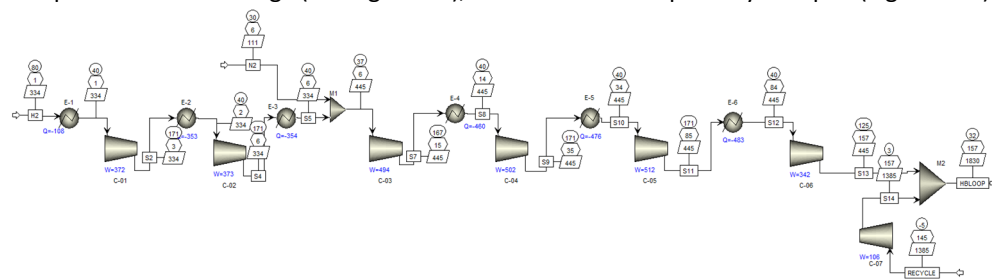
Figure D25. Aspen Plus simulation of the feed gas compressor in the electrified Haber-Bosch process.

Figure D26 shows the synthesis loop with heat integration, the reactor, condensation and a flash drum. The heat exchangers, including the coolers have a pressure drop of 1 bar. The Haber-Bosch reactor is modelled as a stoichiometric reactor (RStoic) at 400 °C and 155 bar with reaction S43.

$$N_2 + 3\,H_2 \rightarrow 2\,NH_3 \qquad (D43)$$

The Haber-Bosch reaction is exothermic, thus for convenience, the heat of reaction (53.8 kJ per mol) was added separately to the product stream. The product stream was used in the heat exchanger network for heat transfer to the reactant stream. Although not implemented

here, it is possible to produce additional low pressure (1.57 GJ per tNH_3) or medium pressure steam (0.87 GJ per tNH_3) from the remaining heat for energy export.

The reactor is sized based on the catalyst bed. The total amount of required catalyst is calculated via Temkin-Pyzhev kinetics given by Equations S44-S46.[15] The input parameters are summarized in Table D23.

$$r_{NH_3} = 2 \cdot Mw_{NH_3} \frac{f}{\rho_{cat}} \left(k_1 \cdot \frac{p_{N_2} \cdot p_{H_2}^{1.5}}{p_{NH_3}} - k_2 \frac{p_{NH_3}}{p_{H_2}^{1.5}} \right) \left[\frac{kg\ NH_3}{kg\ cat\ hr} \right] \tag{D44}$$

$$k_1 = 1.79 \cdot 10^4 \cdot e^{-\frac{20800}{RT}} \tag{D45}$$

$$k_2 = 2.57 \cdot 10^{16} \cdot e^{-\frac{47400}{RT}} \tag{D46}$$

Table D23. Haber-Bosch reaction kinetic data.

Quantity	Unit	
p_{N_2}	bar	37.589
p_{H_2}	bar	112.767
p_{NH_3}	bar	4.64
f (activity factor)		2
R	cal mol^{-1} K^{-1}	1.9872
ρ_{cat}	kg m^{-3}	2650

The dimensions of the catalyst bed can be scaled according to a reference reactor as is further discussed in Morgan et al. (page 142). Using this method, the height and diameter of the bed is 6.98 m and 0.58 m, respectively. Catalyst costs are categorized as consumables, which are listed as operational costs (see Table D18).

The flash drum has a 5 min half-full hold-up time,[52] thus with a liquid NH_3 stream of 123 L per min, the necessary volume is 1.23 m^3. As a heuristic, we assume an optimal L/D of 3, which can range between 2.5-5 m.[52] Thus, D and L are 0.8 m and 2.4 m, respectively. The wall thickness of both the reactor and the flash drum is calculated with a similar approach as the distillation column for the equipment cost.
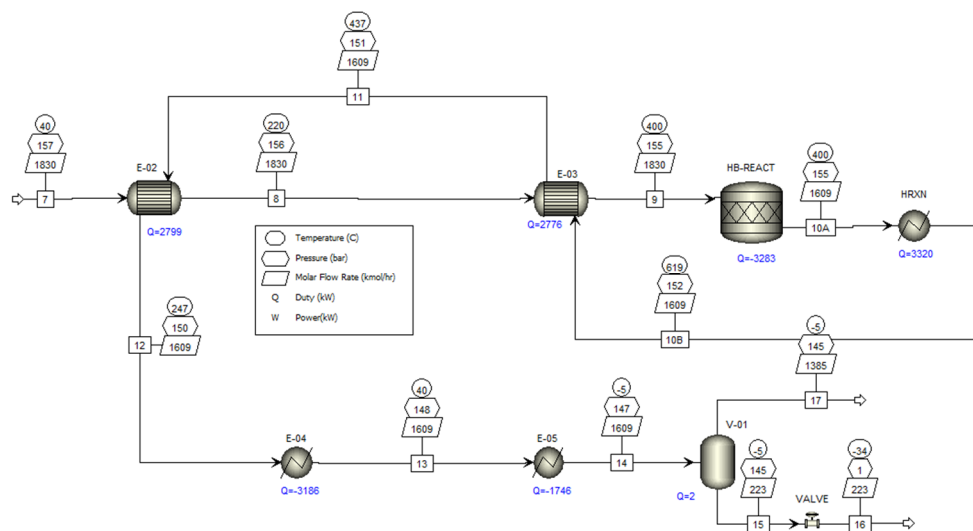
Figure D26. Aspen Plus simulation of the Haber-Bosch synthesis loop. RKS-BM was used as the property package.

Techno-economic assumptions

The capital costs of the NRR electrolyzers were derived from cost projections of commercial H_2O electrolyzers. Since these are given in $ per unit power ($ per kW), we used this metric as a base price. For the aqueous NRR and the Li-NRR electrolyzer, we assumed that their respective price is somewhere between the AEL and PEMEL, thus $C_{E,NRR} = (C_{E,AEL} + C_{E,PEMEL})/2$. The costs (in $ per kW) of the NRR SOEL are assumed to be the same as a water SOEL. The power density (kW per m^2) is used to convert $ per kW to $ per m^2. The latter is more useful if the j is used for the sensitivity analysis. Figure D27 shows that the $ per kW metric is insensitive to changes in the j because it is related to the electrolyzer power, which increases linearly with respect to the j, while the required electrode area decays exponentially with the j. For water electrolyzers, this issue is less relevant because the cost metrics ($ per kW) are already based on their performance criteria (0.4 A cm^{-2} for AEL and 2 A cm^{-2} for PEMEL).[20,34] Estimating the power density is somewhat arbitrary because its value depends strongly on the selected j and E_{cell}. To be consistent, a j of 0.4 A cm^{-2} (based on commercial AEL) was selected for all electrolyzers. The corresponding E_{cell} for AEL and PEMEL were taken from Buttler and Spliethoff.[34] The E_{cell} (at 0.4 A cm^{-2}) of the NRR electrolyzers were calculated with our electrochemical model.
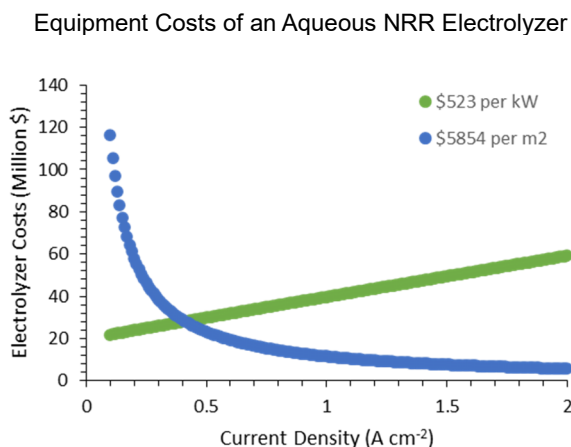
Equipment Costs of an Aqueous NRR Electrolyzer

Figure D27. Comparison between two different methods for calculating the electrolyzer equipment cost. The Aqueous NRR electrolyzer is used as an example with cost data from Table D24.

The capital cost estimates of the electrolyzers for 2025 and 2050 are listed in Table D24. The capital costs of the AEL in 2025 ($8119 per m^2) are similar to earlier reported estimates ($5250 and $7800 per m^2).[20,53,54] It is evident that PEMEL ($10502 per m^2) is currently (2025) more expensive than AEL due to the requirement of expensive metals, such as Pt and IrO_x. Even higher estimates of ~$30000 per m^2 for PEMEL were reported elsewhere.[55] The stack of the AEL and PEMEL are usually around 40-50% of the total costs. The other 50-60% are system related equipment (balance of plant), such as rectifiers, heat exchangers, compressors, gas purifiers and storage facilities.[56] This means that the balance of plant (BoP) is different for each electrolyzer system.

The aqueous NRR electrolyzer is roughly 1.5 times more expensive ($15876 per m^2) than the PEMEL, which is justifiable because of the increased complexity of a GDE-type system. H_2O SOEL capital costs in the literature vary between $5600-16000 per m^2 with a more optimistic estimate from Schmidt et al. ($5600 per m^2),[20] and more conservative from Ramdin et al. (~$16000 per m^2).[54] In our case, the capital costs of the NRR SOEL with water ($15912 per m^2) is more comparable with the conservative estimate, while the NRR SOEL with H_2 ($4287 per m^2) is more similar to the estimate from Schmidt et al. NRR SOEL with H_2 oxidation is generally more stable and has a lower voltage drop across the ceramic material. This could mean that less reinforcement material is required with respect to NRR SOEL with H_2O oxidation, leading to a relatively lower stack cost. Additionally, the NRR SOEL with H_2 consumes less power, which can indicate that smaller and cheaper rectifiers are necessary.

The capital costs of the Li-NRR electrolyzer (~$50000 per m^2) is somewhat comparable to the chlor-alkali process (~$30000 per m^2),[53] which is known to be capital intensive. Our cost of merit is reasonable considering the complexity of the Li-NRR system (GDE-based, organic

electrolyte, moisture free operation, etc) and the fact that the power density is higher than the chlor-alkali electrolyzer (35.7 vs. 15 kW per m^2).

At last, it is expected that future electrolyzers will become significantly cheaper due to constant investment in research & development and scale-up of the manufacturing capacity.[20] This is reflected in our capital cost estimates for 2050, which allowed us to investigate the relationship between electrolyzer costs and the LCOA, but also to estimate the necessary cost reductions to achieve SMR Haber-Bosch parity.

Table D24. Electrolyzer equipment cost estimation.

Quantity	Unit	AEL	PEMEL	Aqueous NRR	NRR SOEL with H$_2$O	NRR SOEL with H$_2$	Li-NRR
j	A cm^{-2}	0.4	0.4	0.4	0.4	0.4	0.4
E_{cell} [a]	V	1.7 [34]	1.6 [34]	2.8	1.5	0.4	8.9
$P_{density}$	kW m^{-2}	6.8	6.4	11.2	5.92	1.59	35.7
C_E (2025)	$_{2022}$ kW^{-1}	1194	1641	1418	2688	2688	1418
C_E (2050)	$_{2022}$ kW^{-1}	564 [18]	482 [18]	523 [b]	758 [c]	758 [c]	523 [b]
C_E (2025)	$_{2022}$ m^{-2}	8119	10502	15876	15912	4287	50572
C_E (2050)	$_{2022}$ m^{-2}	3835	3085	5854	4486	1209	18649
Quantity	**Unit**	**Li-NRR (MEA)**	**Mg-NRR (MEA)**	**Al-NRR (MEA)**			
j	A cm^{-2}	0.4	0.4	0.4			
E_{cell} [a]	V	3.8	3.1	2.5			
$P_{density}$	kW m^{-2}	15	12.5	9.8			
C_E (2025)	$_{2022}$ kW^{-1}	1418	1418	1418			
C_E (2050)	$_{2022}$ kW^{-1}	523 [b]	523 [b]	523 [b]			
C_E (2025)	$_{2022}$ m^{-2}	21270	17725	13896			
C_E (2050)	$_{2022}$ m^{-2}	7845	6538	5125			

[a] E_{cell} for the NRR electrolyzers are calculated at 0.4 A cm^{-2} using the assumptions from Table D19. [b] Average between AEL and PEMEL. [c] Assumed same price as a water SOEL.[20] MEA stands for membrane electrode assembly.

The following set of equations are used to calculate the levelized cost of ammonia (LCOA), which is the NH_3 selling price at which the end-of-life net present value (NPV) is equal to zero:

$$\text{Revenue} = \text{LCOA} \cdot NH_3 \text{ capacity} + H_2 \text{ price} \cdot H_2 \text{ capacity} + O_2 \text{ price} \cdot O_2 \text{ capacity} \quad \text{(D47)}$$

$$\text{Gross profit} = \text{Revenue} - \text{OPEX} \quad \text{(D48)}$$

$$\text{Net profit} = \text{Gross profit} - (\text{Gross profit} - \text{Depreciation}) \cdot \text{Tax rate} \quad \text{(D49)}$$

$$\text{Depreciation} = \frac{\text{Total equipment cost} - \text{Salvage value} \cdot \text{Total equipment cost}}{\text{Plant years}} \quad \text{(D50)}$$

$$\text{Cash Flow} = \text{Net profit} + \text{Depreciation} \quad \text{(D51)}$$

$$\text{NPV} = 0 = \sum_{t=1}^{n} \frac{\text{Cash Flow}}{(1 + \text{interest rate})^t} - \text{total capital costs} \quad \text{(D52)}$$

In the 0th year (t = 0), the total capital costs are invested into the construction of the plant, while there is no revenue nor operational expenses. It is assumed that the plant is fully operational in year one (t ≥ 1). We used 25% tax rate, 25% salvage value and 4.28% interest rate with a linear depreciation scheme.

5

Appendix References

1   Bard, A. J., Faulkner, L. R. & White, H. S. *Electrochemical methods: fundamentals and applications*. (John Wiley & Sons, 2022).

2   Akolkar, R. Mathematical model of the dendritic growth during lithium electrodeposition. *Journal of Power Sources* **232**, 23-28 (2013).

3   Kugler, K., Ohs, B., Scholz, M. & Wessling, M. Towards a carbon independent and CO2-free electrochemical membrane process for NH3 synthesis. *Physical Chemistry Chemical Physics* **16**, 6129-6138 (2014). https://doi.org:10.1039/c4cp00173g

4   Ni, M., Leung, M. K. & Leung, D. Y. Electrochemical modeling of hydrogen production by proton-conducting solid oxide steam electrolyzer. *International Journal of Hydrogen Energy* **33**, 4040-4047 (2008).

5   Liu, Y. *et al.* Insight into the critical role of exchange current density on electrodeposition behavior of lithium metal. *Advanced Science* **8**, 2003301 (2021).

6   Ni, M. Modeling of SOFC running on partially pre-reformed gas mixture. *International Journal of Hydrogen Energy* **37**, 1731-1745 (2012).

7   Fu, X. *et al.* Continuous-flow electrosynthesis of ammonia by nitrogen reduction and hydrogen oxidation. *Science* **379**, 707-712 (2023).

8   Dioxide Materials. *Sustainion Anion Exchange Membranes*, <https://dioxidematerials.com/technology/sustainion-membranes/> (2023).

9   Gilliam, R., Graydon, J., Kirk, D. & Thorpe, S. A review of specific conductivities of potassium hydroxide solutions for various concentrations and temperatures. *International Journal of Hydrogen Energy* **32**, 359-364 (2007).

10   Fernandez, C. A. *et al.* Opportunities for intermediate temperature renewable ammonia electrosynthesis. *Journal of Materials Chemistry A* **8**, 15591-15606 (2020). https://doi.org:10.1039/d0ta03753b

11   Du, H.-L. *et al.* Electroreduction of nitrogen with almost 100% current-to-ammonia efficiency. *Nature 2022 609:7928* **609**, 722-727 (2022). https://doi.org:10.1038/s41586-022-05108-y

12   Towler, G. & Sinnott, R. *Chemical engineering design: principles, practice and economics of plant and process design*. (Butterworth-Heinemann, 2021).

13   Woods, D. R. *Rules of thumb in engineering practice*. (John Wiley & Sons, 2007).

14   Turton, R., Bailie, R. C., Whiting, W. B. & Shaeiwitz, J. A. *Analysis, synthesis and design of chemical processes*. (Pearson Education, 2008).

15   Morgan, E. R. *Techno-economic feasibility study of ammonia plants powered by offshore wind*. (University of Massachusetts Amherst, 2013).

16   Bañares-Alcántara, R. *et al.* Analysis of Islanded Ammonia-based Energy Storage Systems. *University of Oxford*, 1-150 (2015).

17 Mivechian, A. & Pakizeh, M. Hydrogen recovery from Tehran refinery off-gas using pressure swing adsorption, gas absorption and membrane separation technologies: Simulation and economic evaluation. *Korean Journal of Chemical Engineering* **30**, 937-948 (2013).

18 Glenk, G. & Reichelstein, S. Economics of converting renewable power to hydrogen. *Nature Energy* **4**, 216-222 (2019).

19 Böhm, H., Zauner, A., Rosenfeld, D. C. & Tichler, R. Projecting cost development for future large-scale power-to-gas implementations by scaling effects. *Applied Energy* **264**, 114780 (2020).

20 Schmidt, O. *et al.* Future cost and performance of water electrolysis: An expert elicitation study. *International journal of hydrogen energy* **42**, 30470-30492 (2017).

21 International Rewenable Energy Agency (IRENA). Renewable power generation costs in 2022. (2022).

22 International Rewenable Energy Agency (IRENA). Future of Solar Photovoltaic: Deployment, investment, technology, grid intergration and socio-economic aspects (A global Energy Transformation: paper). (2019).

23 Bogdanov, D. *et al.* Radical transformation pathway towards sustainable electricity via evolutionary steps. *Nature communications* **10**, 1-16 (2019).

24 International Rewenable Energy Agency (IRENA). Making The Breakthrough - Green hydrogen policies and technology costs. (2021).

25 INDEXBOX. EU - Oxygen - Market Analysis, Forecast, Size, Trends and Insights. (2022).

26 Hausmann, J. N., Schlögl, R., Menezes, P. W. & Driess, M. Is direct seawater splitting economically meaningful? *Energy & Environmental Science* **14**, 3679-3685 (2021).

27 Administration, U. S. E. I. *Henry Hub Natural Gas Spot Price*, <https://www.eia.gov/dnav/ng/hist/rngwhhdm.htm> (2023).

28 Bashmakov, I. A. *et al.* IPCC. Climate Change 2022: Mitigation of Climate Change. Industry. (2022).

29 Smith, R. *Chemical process: design and integration*. (John Wiley & Sons, 2005).

30 Appl, M. *Ammonia: Principles and Industrial Practice*. (1999).

31 Van Der Ham, C. J. M., Koper, M. T. M. & Hetterscheid, D. G. H. Challenges in reduction of dinitrogen by proton and electron transfer. *Chemical Society Reviews* **43**, 5183-5191 (2014). https://doi.org:10.1039/c4cs00085d

32 Skúlason, E. *et al.* A theoretical evaluation of possible transition metal electro-catalysts for N2 reduction. *Physical Chemistry Chemical Physics* **14**, 1235-1245 (2012). https://doi.org:10.1039/c1cp22271f

5

33   Noren, D. & Hoffman, M. A. Clarifying the Butler–Volmer equation and related approximations for calculating activation losses in solid oxide fuel cell models. *Journal of Power Sources* **152**, 175-181 (2005).

34   Buttler, A. & Spliethoff, H. Current status of water electrolysis for energy storage, grid balancing and sector coupling via power-to-gas and power-to-liquids: A review. *Renewable and Sustainable Energy Reviews* **82**, 2440-2454 (2018). https://doi.org:10.1016/j.rser.2017.09.003

35   Nel Hydrogen. *Nel Hydrogen Electrolyzers - The World's Most Efficient and Reliabel Electrolyzers*, <https://nelhydrogen.com/wp-content/uploads/2020/03/Electrolysers-Brochure-Rev-D.pdf> (2020).

36   Siemens Energy. *Overview of the PEM Silyzer Family*, <https://4echile.cl/wp-content/uploads/2020/10/20200930-SE-NEB-PEM-Electrolyzer-and-Applications_EW.pdf> (2020).

37   Sánchez, A. & Martín, M. Scale up and scale down issues of renewable ammonia plants: Towards modular design. *Sustainable Production and Consumption* **16**, 176-192 (2018). https://doi.org:10.1016/j.spc.2018.08.001

38   Bocker, N. & Grahl, M. Nitrogen - Air separation technology. *Ullmann's Encyclopedia of Industrial chemistry* (2013).

39   Marsidi, M. *Technology Factsheet - Electric Industrial Boiler*, <https://energy.nl/wp-content/uploads/electric-industrial-boiler-7.pdf> (2018).

40   Marc Marsidi, Luuk Beurskens & Uslu, A. The role of renewable heat technologies in industry - a review of Dutch sectoral industry roadmaps. (2018).

41   Lin, B., Wiesner, T. & Malmali, M. Performance of a Small-Scale Haber Process: A Techno-Economic Analysis. *ACS Sustainable Chemistry & Engineering* **8**, 15517-15531 (2020). https://doi.org:10.1021/ACSSUSCHEMENG.0C04313

42   Helminen, J., Helenius, J., Paatero, E. & Turunen, I. Comparison of sorbents and isotherm models for NH3-gas separation by adsorption. *AIChE journal* **46**, 1541-1555 (2000).

43   Park, Y., Ju, Y., Park, D. & Lee, C.-H. Adsorption equilibria and kinetics of six pure gases on pelletized zeolite 13X up to 1.0 MPa: CO2, CO, N2, CH4, Ar and H2. *Chemical Engineering Journal* **292**, 348-365 (2016).

44   Knaebel, K. S. A "How to" guide for adsorber design. *Adsorption Research, Inc. Dublin, Ohio* **43016** (2007).

45   Ntiamoah, A., Ling, J., Xiao, P., Webley, P. A. & Zhai, Y. CO2 capture by temperature swing adsorption: use of hot CO2-rich gas for regeneration. *Industrial & Engineering Chemistry Research* **55**, 703-713 (2016).

46   Sciuller, E., Dutournié, P., Zbair, M. & Bennici, S. New Approach for Measuring the Specific Heat Capacity of Reactive Adsorbents Using Calorimetry. *Journal of Chemical & Engineering Data* **68**, 1865-1871 (2023).

5

47   Spiller, L. L. Determination of ammonia/air diffusion coefficient using nafion lined tube. *Analytical letters* **22**, 2561-2573 (1989).

48   Winn, E. B. The temperature dependence of the self-diffusion coefficients of argon, neon, nitrogen, oxygen, carbon dioxide, and methane. *Physical review* **80**, 1024 (1950).

49   The Engineering Toolbox. *Air - Diffusion Coefficients fo Gases in Excess of Air*, <https://www.engineeringtoolbox.com/air-diffusion-coefficient-gas-mixture-temperature-d_2010.htm> (2018).

50   Salomone, F. *et al.* Process simulation and energy analysis of synthetic natural gas production from water electrolysis and CO2 capture in a waste incinerator. *Applied Energy* **343**, 121200 (2023).

51   Bannwarth, H. *Liquid ring vacuum pumps, compressors and systems: conventional and hermetic design*. (John Wiley & Sons, 2006).

52   Coker, A. K. & Ludwig, E. E. Ludwig's applied process design for chemical and petrochemical plants. *Applied process design for chemical and petrochemical plants* (2007).

53   Ramdin, M. *et al.* High-pressure electrochemical reduction of CO2 to formic acid/formate: effect of pH on the downstream separation process and economics. *Industrial & Engineering Chemistry Research* **58**, 22718-22740 (2019).

54   Ramdin, M. *et al.* Electroreduction of CO2/CO to C2 products: process modeling, downstream separation, system integration, and economic analysis. *Industrial & Engineering Chemistry Research* **60**, 17862-17880 (2021).

55   Spurgeon, J. M. & Kumar, B. A comparative technoeconomic analysis of pathways for commercial electrochemical CO 2 reduction to liquid products. *Energy & Environmental Science* **11**, 1536-1551 (2018).

56   International Rewenable Energy Agency (IRENA). Green Hydrogen Cost Reduction - Scaling up electrolysers to meet the 1.5 degree C climate goal. (2020).

5

5

6

Conclusions and Recommendations

6.1 Conclusions

Electrochemical ammonia synthesis was experimentally explored via the aqueous nitrogen reduction reaction (NRR) and non-aqueous Li-mediated NRR at ambient conditions. For aqueous NRR, a strict experimental protocol was developed to avoid the influence of external labile N-species on the NH_3 quantification process. This protocol was used to revisit a promising class of Fe and Mo-based carbide materials as NRR electrocatalyst (**Chapter 2**). Fe and Mo carbide nanoparticles were successfully synthesized by well-known carburization methods as was confirmed by physical characterization methods, such as X-ray diffraction, X-ray photoelectron spectroscopy (XPS), Mossbauer spectroscopy and electron microscopy. The current-potential relationship of the carbide materials only showed a typical trend for the hydrogen evolution reaction and there were no signs of any peaks associated with the NRR. Two-hour potentiostatic measurements at different potentials did not result in NH_3 concentrations exceeding the background level. This means that Fe and Mo-carbides are not active NRR catalysts and that previous literature reports on the subject matter were facing N contamination in their systems. This emphasizes the importance of sophisticated experimental design to avoid reporting false positives to the field.

An extensive screening of NH_3 and NO_x impurities was presented in **Chapter 3**. New sources were identified and strategies to avoid or eliminate them were discussed. Accumulation of atmospheric NH_3 and NO_x species on ambient exposed cell components, chemicals and lab ware is likely the most troubling source. The optimal cleaning procedure is material dependent and includes alkaline washing for membranes and electrodes, heat treatment for Pt and rinsing lab ware with water. Chemicals should be stored in a desiccator due to the difficulty of purifying them. We noticed that commonly used high purity N_2 and Ar gases do not contain any labile N species, as was earlier suggested by literature reports. Hence, they do not require further purification. Only isotope labelled N_2 that is typically available at lower purities can contain 9.8 ppm $^{15}NH_3$ and 1.03 ppm $^{15}NO_x$. Therefore, commercially certified gas purifiers are advised to install upstream of the electrochemical cell if isotope labelled experiments are performed. Li-salts may contain nitrate species, therefore it is good practise to determine the NO_3^- background level of the salt by dual-wavelength UV spectroscopy because purification is not always possible. These guidelines and tools allow the experimentalist to perform more reliable NRR measurements.

A partially delithiated sheet of Li_xFePO_4 was used as a reliable non-aqueous reference electrode to investigate the potential dependency of the Li-mediated NRR on important performance parameters, such as the current stability, Faradaic efficiency (FE) and NH_3 production rate (in **Chapter 4**). Cyclic voltammetry measurements were also performed with 2 M LiTFSI under Ar, N_2 with or without EtOH and only revealed Li plating or stripping peaks. Hence, the N_2 activation and protonation are chemical reaction steps. With 2 M LiTFSI dissolved in 0.1 M EtOH/THF, the current response during chronoamperometry measurements were stable at potentials >-3.23 V vs. SHE but resulted in FEs lower than 15%.

The FE increased to approximately 50% at more negative potentials (<-3.43 V vs. SHE). Below -3.74 V vs. SHE, the current density was very unstable and affected the NH_3 production rate negatively, while the FE remained at ~50%. The composition of the SEIs was analysed post-mortem by XPS and were mostly enriched with LiF. The ratio between inorganic and organic species varied with the applied potential but does not solely explain the trend between the Li-NRR performance parameters and the potential. The FE and NH_3 production rate were significantly lower when the salt concentration was reduced to 1 M LiTFSI. The XPS analysis revealed that more organic species were present in the SEI, which is related to the lower availability of anions in the Li^+ solvation environment and explains a relatively poor Li-NRR performance. Changes in the surface morphology were not investigated in the present work but might give more insights into the true effect of the applied potential.

The techno-economic feasibility of the different electrochemical ammonia synthesis pathways was discussed in **Chapter 5**. Detailed process models were designed for the electrified version of the Haber-Bosch process, aqueous NRR at ambient and high temperature conditions, both with water or hydrogen oxidation, and Li-mediated NRR. Among the sustainable ammonia production pathways, the electrified Haber-Bosch is currently the most cost-effective, mature and energy efficient option. Aqueous NRR at ambient conditions needs an electricity price of $0.024 per kWh and an electrolyzer CAPEX of $522 per kW to become cost competitive, only if the FE and the current density are higher than 80% and 0.3 A cm^{-2}, which is a daunting task in comparison with the current state of the field. High temperature NRR in combination with hydrogen oxidation in a SOEL is technically possible but very capital intensive due to additional heat exchangers and seems to be only cost competitive under unrealistic economic assumptions (electricity price ≤ $0.02 per kWh, electrolyzer CAPEX ≤ $500 per kW). The inherently low energy efficiency of the Li-NRR electrolyzer (<11%) increases the operational costs of the process tremendously. Other electrolyzer configurations based on a zero-electrolyte-gap and switching to other mediators beyond Li may improve the energy efficiency, but it remains difficult to become cost competitive with electrified Haber-Bosch. Currently, the SMR Haber-Bosch process is the most cost-effective and energy efficient pathway to make ammonia on an industrial scale. High natural gas prices and a carbon tax above $175 per tNH_3 will steer the industry to invest into greener alternatives.

6.2 Recommendations

Chapter 2 addresses the value of reporting inactive materials towards the NRR, which is especially important in the aqueous NRR field plagued by false positive results. Therefore, it is highly encouraged to report irreproducible results from earlier publications to initiate a debate on whether a material is N_2 active and to be excluded from future research. This is especially important for researchers new to the field, who are often overwhelmed by the large amount of literature reports claiming to have found an active catalyst. To the best of my knowledge, there is currently no reproducible experimental evidence of a material that can electrochemically activate N_2 while the catalytic surface is in contact with aqueous media.

First principles Density Functional Theory calculations can be used as a tool to obtain information about the N and H binding energy of materials favoring NRR over HER. Nørskov and coworkers screened numerous transition metals and concluded that catalysts with an optimum N binding energy, such as Fe, Rh, Ru, Ir, Co, Ni and to some extent Mo have a higher affinity towards H-binding, thus favoring the HER (see **Section 1.2.1**). Sc, Y, Ti and Zr seem to favor N binding over H binding, but at the cost of a higher overpotential. Dražević et al. poised post transition metals, such as In, Mn and Al as promising NRR catalysts because they are inferior towards the hydrogen evolution and show a favorable N-binding at alkaline pH.[1] These materials could function as a starting point for future aqueous NRR research.

The extremely low N_2 solubility in aqueous electrolytes is perhaps another reason why NRR activation is difficult to detect due to the low N_2 concentration at the electrocatalyst surface. The N_2 mass transport can be improved by implementing a gas-diffusion electrode cell.[2] Carrying out such experiments are generally more challenging because more cell components are involved, which will require more sophisticated cleaning procedures and control experiments. An alternative to increase the N_2 solubility and therefore the mass transport is by performing electrochemistry at elevated N_2 pressures in an autoclave cell.

Li-mediated NRR is a more successful approach in terms of N_2 activation. In **Chapter 4**, the relationship between the applied potential, the system's stability and selectivity of the reaction are clearly established. The composition of the SEIs was characterized by XPS and varied to some extent among the tested potentials. Although XPS depth profiling gives a good estimate of the chemical species present in the SEI, solid state NMR can also be used as a complementary technique. Primarily, to identify the composition of specific Li and F species, and to validate the XPS analysis. Nonetheless, induced SEI structural and morphological changes by the applied potential can also be valuable to better understand the potential dependency on the Li-NRR performance. This can be visualized by ex-situ (cryogenic) electron microscopy techniques and in-situ neutron reflectometry as discussed in previous literature reports.[3,4] The three-electrode autoclave system develop for the Li-NRR experiments did not allow correction of the ohmic potential drop. Hence, the actual potential of the working electrode will be slightly more positive. To minimize the ohmic

potential drop, the cell design has to be further improved by reducing the distance between the reference and the working electrode via a Luggin capillary and increasing the geometric surface area of the working electrode.

Chapter 5 concludes that a process based on Li-NRR is not cost competitive due to the inherently low energy efficiency of the electrolyzer unit, which is mainly caused by the highly negative Li-plating potential, the low conductivity of organic Li^+ electrolytes, next to the energy investment in a necessary hydrogen source. Future research efforts must focus on the identification of N_2 active mediators with a significantly less negative potential than Li/Li^+. The development of membrane electrode assemblies for mediated NRR can drastically improve the overall energy efficiency, especially at industrially relevant current densities. Cai et al. demonstrated a proof of concept for Li-NRR which can be used as an initial design for future development.[5]

6.3 References

1   Dražević, E. & Skúlason, E. Are There Any Overlooked Catalysts for Electrochemical NH3 Synthesis—New Insights from Analysis of Thermochemical Data. *iScience* **23**, 101803-101803 (2020).
2   Kolen, M., Ripepi, D., Smith, W. A., Burdyny, T. & Mulder, F. M. Overcoming nitrogen reduction to ammonia detection challenges: the case for leapfrogging to gas diffusion electrode platforms. *ACS catalysis* **12**, 5726-5735 (2022).
3   Steinberg, K. *et al.* Imaging nitrogen fixation at lithium solid electrolyte interphases via cryo-electron microscopy. (2022).
4   Blair, S. J. *et al.* Combined, time-resolved, in situ neutron reflectometry and X-ray diffraction analysis of dynamic SEI formation during electrochemical N2 reduction. *Energy & Environmental Science* **16**, 3391-3406 (2023).
5   Cai, X. *et al.* Membrane electrode assembly design for lithium-mediated electrochemical nitrogen reduction. *Energy & Environmental Science* (2023).

Acknowledgements

The unforgettable experience of my PhD journey has come to an end. Obtaining a doctorate is not only about becoming an expert in a particular research field, but it also tests your mental resilience to overcome the major hurdles and setbacks along the way. Luckily, I was not alone and could not have done it without the invaluable support of my dear colleagues, friends and family.

First of all, I would like to show my deepest gratitude to my supervision team, **Dr. Ruud Kortlever**, **Prof. Dr. Ir. Wiebren de Jong** and **Prof. Dr. Fokko M. Mulder**, who guided me throughout the PhD and taught me how to become an independent researcher. I am especially grateful to **Ruud** and **Wiebren** who gave me the opportunity to pursue a PhD in the first place and believed in me from the beginning. The bi-weekly (and later monthly) meeting sessions with **Ruud** were always helpful to shape my research projects, setting directions, discuss the planning and the latest results. Besides work, we also had great fun with the whole group at the annual ISE conference in Lyon and Montreal, the NCCC conferences in Noordwijkerhout, the curling event in The Hague and many group dinners! I would like to thank **Wiebren** for all his help, especially with the techno-economic feasibility study, wherein we had numerous discussions about classical process engineering topics, such as separation technologies and heat integrations. During the first two years, we had dedicated ammonia meetings with **Fokko** and his PhD students, which created the opportunity to setup fruitful collaborations. In a later stage, **Fokko** also allowed me to build a setup in his lab, perform experiments and make use of his glovebox. Many thanks for that! Our interactions became more occasionally in a later stage, but when the door was open, I could always walk in for a discussion.

I would like to thank the independent members of my thesis committee, **Prof. Dr. Guido Mul**, **Prof. Dr. Ir. Atushi Urakawa**, **Prof. Dr. Ir. Andrea G. Ramirez-Ramirez**, **Dr. Peter Ngene** and **Prof. Dr. Ir. Rene Pecnik** for providing their invaluable feedback on the dissertation and participate in the thesis defence ceremony. Further, I sincerely thank all the members of the Electron to Carbon Bonds consortium, where I have a lot of gratitude for **Prof. Dr. Bernard Dam** and **John Nijenhuis** for initiating and leading the consortium. Also, the short stays in Garderen (including archery) and Bergen were scientifically engaging and fun! A big thanks to **Roos** and **Leslie** for organising this.

I will always carry a warm heart towards my colleagues from the LSES group who made working in the lab and office enjoyable. **Shilong**, I admire your work ethic, precision, and dedication to your experiments, which had a positive impact on my own lab work, so thank you for that. I also liked our collaborations and time together at national and international conferences. **Daniël**, I always enjoyed our time in the lab (especially your taste for classic rock music) and our discussions on Dutch politics in between the experiments and during

the lunch breaks. **Nandalal**, you always created a humoristic atmosphere in the office and in the lab. I remember that we worked out in the sketchy gym down in the basement, which suddenly closed overnight. They still owe me money! **Iris**, I will remember our numerous lunch breaks, the soccer matches and the fun time in Lyon. **Katie**, I am glad we finally share the same office again! I also enjoyed our time during the training for the video pitch, where mine was never released. For my own benefit I suppose. **Asvin**, my friend, always too kind and eager to help everybody to organise things in the lab and especially me with the process modelling. **Ahmed**, your fundamental knowledge of electrochemistry and experience were very valuable to me. Thank you for all our discussions. **Hengameh**, you taught me a lot about Persian culture and showed me to appreciate other things in life besides research. **Aleksandra**, I always enjoyed our collaborations and conservations together in the office, lab and even in the TEM room. **Simone**, I am amazed how fast you learned yourself the Dutch language. Thank you for all your help with the SEM, Raman and FT-IR. **Shahid**, you inspired me to pursue an international post-doctoral fellowship and provided me valuable insights into the application process. Many thanks for that! **Katherine**, your colorful character is a great addition to the group and our office. Your organisational talents inspired me to take more initiative in organizing activities with colleagues, friends and family. **Sohan**, I enjoyed the sporadic lunch and coffee breaks together, our discussions on hydrogen peroxide, and our time in Lyon. **Min**, it was nice to collaborate with you on your urea electrosynthesis project, which seems to be even more challenging than ammonia production. **Ming**, it was always fun to interact with you in and outside the lab. Thank you for sharing your very interesting ALD experience with me. **Dr. Mahinder Ramdin** thank you for all your guidance related to the process design and engineering part of this thesis. I also liked our chats about ammonia research and countless rides in bus 40 from and to Rotterdam. **Dr. Luis Cutz**, thank you for all our fun interactions during my PhD and I am happy for you that you became promoted to assistant professor in the group. **Michel**, I am very grateful for all your technical support in the lab during my PhD. I big thank you goes to all the hard-working MSc and BSc students: **Deanne**, **Dylan**, **Alexander**, **Niels**, and **Lies** whom I supervised during their thesis work. I am also grateful to the former members of the LSES group: **Andrea**, **Hamid**, **Marilia**, **Sevgi**, **Mara** and **Christos**.

I am also thankful for the hospitality of the MECS group during the last 1.5 year of my PhD journey which always felt like a second home. There are so many people I need to thank, but I would like to start with **Davide**, who turned out to be one of my best collaborators and good friend. I enjoyed working together on the impurity project and the synchrotron work we did in Barcelona. I hope that our paths once cross again. **Dylan** and **Peter**, the epic duo with whom I was in the infamous research line 4 on nitrogen activation. It was great to interact with you during the E2CB outings, MECS coffee and lunch breaks. **Pranav**, I am in great dept for all the material characterization you did for me and the night shifts you took during our work with Davide in the synchrotron. You are a very reliable collaborator, and I admire your work endurance. **Mark W**, thank you so much for sharing your knowledge on Li-ion batteries with me, which were of good use for my own research project. **Herman** and

Joost, the two pillars of the MECS group. I am very thankful for the numerous times I could disturb you for technical advice regarding my setup and the glovebox. **Dr. Tom Burdyny**, thank you for all your free career advise, useful discussions and friendly conservations. I am amazed how fast you became a well-established name in the electrochemistry field. It is unfortunate that we never collaborated professionally. Perhaps in the future when I transition to CO_2 reduction or you to N_2 reduction. **Siddhartha**, it was great to hang out with you in and outside the lab from time to time. I really enjoyed your PhD graduation dinner and felt honoured to be invited. **Santosh** I am grateful for your help with SEM imaging and our countless interactions in the lab. Furthermore, I would like to thank the other members of the MECS groups, **Jasper**, **Nikita**, **Henri**, **Elena**, **Gerard** and **Julia**. Additionally, I want to acknowledge the former members of the MECS group with whom I interacted during my PhD, **Vineesh**, **Maryam**, **Erdem**, **Sanjana**, **Nienke**, **Marijn**, **Kailun**, **Hugo**, **Mengran**, **Mark S**, **Martin** and **Robin**.

I am very grateful for the support of **Hans**, **Dr. Amarante Böttger**, and **Ruud H** from the MSE department and **Dr. Iulian Dugulan** from the reactor institute for helping me out with the synthesis and characterization of the metal carbides I needed for my first research projects. **Dr. Mar Pérez-Fortes**, thank you so much for all the help with the process modelling work. **Arash**, although our collaboration was short, I really enjoyed working together with you on the same topic and to share my experience. I am grateful that you helped me out with so many experiments. I am confident that you will be able to finish your research work during your visit in Delft.

I am very lucky to have so many friends outside the TU Delft umbrella to rely on and help me to relax afterwork and in the weekends. I acknowledge **Ruben**, **Bregje**, **Tim**, **Emilia**, **Bas**, **Dunya**, **Wouter**, **Corwin**, **Marijn**, **Nieke**, **Roland**, **Lars**, **Daisy**, and countless others. I also enjoyed company of my friends from the "buddy band": **Joeri**, **Sander**, **Mitchell**, **Naomi**, **Jara**, **Anne**, **Ruud** and **Clair**, where I know most of you for more than a decade. I will not forget all the great beers and dinners we shared, the music festivals we went to and the countless boardgames we played.

My deepest gratitude goes to my family for their loyal support. Especially I would like to thank **Leo**, **Lara**, **Robbe**, and **Liewe** for believing in me and always show their kind interest in my research activities. **Tirza**, it is great to have you as a sister. I always admire your creativity, view on life and talent for cooking and baking. I tried to apply most of your color-coding tips on most of the key figures in the dissertation. I hope I didn't disappoint you! Thanks for helping me out with the cover design, it looks fabulous. Also, I really enjoyed our trips together with **Jurre** to Val Thorens and Berlin. It is such a pity that you are not playing Twilight Imperium with me, **Jurre** and his friends. **Dad**, I am thankful for believing in me throughout my studies and PhD trajectory. You also stimulated me to work hard and not to give up when matters are going side-ways. I might have inherited your humour and entrepreneurial spirit, but that is for others to judge. **Mom**, I always know that I can count on you in times of need, which gives me great comfort. You also inspired me to adapt to a

more active and healthier lifestyle, which made me, together with all your other valuable life lessons, more resilient towards all the stressors from the past four years. **Rosa**, my soulmate, I am so grateful to share my life with you and that I obtain your unconditional love and support through the ups and downs of life. I am excited about the many adventures that lie ahead of us.

Boaz

Delft, Oktober 2024

Curriculum Vitae

Boaz Izelaar was born in Dirksland, the Netherlands on July 12th, 1993. He obtained his BSc degree in Chemical Engineering from the "Hoge School Rotterdam" in 2015. During his BSc program, he obtained hands on working experience in the industry at Rubis Terminal in the port of Rotterdam, where he identified the major energy losses in the terminal and developed energy saving strategies accordingly. He performed his BSc thesis at the engineering consultancy firm "Iv Group" in Papendrecht and worked on strategies to avoid gas flaring during crude oil production. In 2019, he obtained his MSc degree in Chemical Engineering from Delft University of Technology. He did his MSc thesis project in the lab of prof. dr. Wilson Smith and studied ion transport behaviour in monopolar and bipolar membranes using electrochemical impedance spectroscopy with the primary goal to improve electrolysis based systems. Early 2020, he joined the Large Scale Energy Storage (LSES) research group at the faculty of Mechanical Engineering of the Delft University of Technology as a PhD student under the supervision of dr. Ruud Kortlever under co-supervision of prof. dr. ir. Wiebren de Jong and prof. dr. Fokko M. Mulder. His PhD project focused on electrochemical N_2 activation in aqueous electrolytes via electrocatalysis and in non-aqueous electrolytes via lithium as an activation mediator. The results of his doctorate research are presented in this thesis. He is currently working as a post-doctoral researcher in the same group to continue his research on non-aqueous electrochemical N_2 reduction, and to work on other electrochemical conversion reactions, such as CO_2 reduction and C-N coupling for urea synthesis.

List of Publications

Karanth, P., Weijers, M., Labrinenko, A., **Izelaar, B.**, Ganapathy, S., Kortlever, R., Wagemaker., Mulder, F. M., Rational Design of Safe, Fluorine-free Dual Salt Electrolytes for Lithium Metal Batteries, *in preparation*.

Weijers, M., Karanth, P., Homann, G., Kondakova, A., **Izelaar, B.**, Ganapathy, S., Kortlever, R., Battaglia, C., Mulder, F. M., Constructive Movement: Assessment of Effective Lithium Diffusivity in High Lithium Concentration Ternary Polymer Ionic Liquids, *in submission*.

Izelaar, B., Karanth., P., Toghraei, A., Girichandran,. N., Weijers, M., Hendrikx, R. W. A., Mulder., F. M., Kortlever., R., The Effect of Potential on the Li-mediated NRR Performance, *in preparation*.

Fu, S., **Izelaar, B.**, Li, M., An, Q., Li, M., de Jong, W., Kortlever, R., Ni-N-C Catalysts for CO_2 Electrochemical Reduction to CO: The Effects of Carbon Support., *in submission*.

Kumar., A. S., Fu, S., Mohamed, A., Saedy, S., **Izelaar, B.**, Ramdin, M., de Jong, W., Kortlever, R., Potential Dependent Effect of Sulphur-based Gaseous Contaminants on Electrochemical CO_2 reduction to C_{2+} products, *in submission*.

Izelaar, B., Ramdin, M., Vlierboom, A., Pérez-Fortes, M., van der Slikke, D., Kumar, A. S., de Jong, W., Mulder, F. M., Kortlever, R., Techno-economic Assessment of Different Small-scale Electrochemical NH_3 Production Plants, *Energy and Environmental Science*, 2024.

Van den Berg, D., **Izelaar, B.**, Fu, S., Kortlever, R. The effect of surface conditions on the electrochemical CO2 reduction performance of bimetallic AuPd electrocatalysts, *Catal. Sci. Technol.*, 2024, 14, 555-561.

Izelaar, B., Ripepi, D., van Noordenne, D. D., Jungbacker, P., Kortlever, R., Mulder, F. M., Identification, Quantification, and Elimination of NO_x and NH_3 Impurities for Aqueous and Li-Mediated Nitrogen Reduction Experiments, *ACS Energy Lett.*, 2023, 8, 8, 3614-3620

Izelaar, B., Ripepi, D., Asperti, S., Dugulan, I. A., Hendrikx, R. W. A., Böttger, A. J., Mulder, F. M., Kortlever, R., Revisiting the Electrochemical Nitrogen Reduction on Molybdenum and Iron Carbides: Promising Catalysts or False Positives? *ACS Catal.*, 2023, 13, 3, 1649-1661.

Ripepi, D., **Izelaar, B.**, van Noordenne, D. D., Jungbacker, P., Kolen, M., Karanth, P., Cruz, D., Zeller, P., Pérez-Dieste, V., Villar-Garcia, I. J., Smith, W. A., Mulder, F. M., In Situ Study of Hydrogen Permeable Electrodes for Electrolytic Ammonia Synthesis Using Near Ambient Pressure XPS, *ACS. Catal.*, 2022, 12, 21, 13781-13791

Blommaert, M. A., Vermaas, D. A., **Izelaar, B.**, in 't Veen, B., Smith, W. A., Electrochemical impedance spectroscopy as a performance indicator of water dissociation in bipolar membranes, *j. Mater. Chem. A.*, 2019, 7, 19060-19069.